



**HAL**  
open science

# Quantum information processing using a molecular magnet single nuclear spin qudit

Clément Godfrin

► **To cite this version:**

Clément Godfrin. Quantum information processing using a molecular magnet single nuclear spin qudit. Quantum Physics [quant-ph]. Université Grenoble Alpes, 2017. English. NNT : 2017GREAY015 . tel-01648035

**HAL Id: tel-01648035**

**<https://theses.hal.science/tel-01648035>**

Submitted on 24 Nov 2017

**HAL** is a multi-disciplinary open access archive for the deposit and dissemination of scientific research documents, whether they are published or not. The documents may come from teaching and research institutions in France or abroad, or from public or private research centers.

L'archive ouverte pluridisciplinaire **HAL**, est destinée au dépôt et à la diffusion de documents scientifiques de niveau recherche, publiés ou non, émanant des établissements d'enseignement et de recherche français ou étrangers, des laboratoires publics ou privés.

## THÈSE

Pour obtenir le grade de

### **DOCTEUR DE LA COMMUNAUTÉ UNIVERSITÉ GRENOBLE ALPES**

Spécialité : **Physique**

Arrêté ministériel : 25 mai 2016

Présentée par

**Clément Godfrin**

Thèse dirigée par **Wolfgang WERNSDORFER**  
et codirigée par **Franck BALESTRO**

préparée au sein **Institut Néel, CNRS/UGA**  
et de **Ecole Doctorale de Physique, Grenoble**

## **Quantum information processing using a molecular magnet single nuclear spin qudit**

Thèse soutenue publiquement le **21 Avril 2017**,  
devant le jury composé de :

**Prof. Wiebke GUICHARD**

Professeure, Institut Néel-CNRS, Présidente

**Prof. Michel PIORO-LADRIRE**

Professeur, Université de Sherbrooke, Rapporteur

**Dr. Patrice BERTET**

Chargé de recherche, CEA Saclay, Rapporteur

**Dr. Xavier WAITAL**

Directeur de recherche, CEA Grenoble, Examineur

**Prof. Wolfgang WERNSDORFER**

Directeur de recherche, Karlsruhe Institute of Technology, Directeur de thèse

**Dr. Franck BALESTRO**

Maître de conférences, Institut Néel-CNRS/UGA, Co-Directeur de thèse

**Dr. Rafik BALLOU**

Directeur de recherche, Institut Néel-CNRS, Invité





## Acknowledgements

Une thèse est avant tout une aventure collective. Je tiens donc ici à remercier sincèrement toutes ces personnes qui m'ont permis de garder un équilibre indispensable pour mener à bien une thèse.

Mes premiers remerciements vont tout naturellement à Franck Balestro. Merci de m'avoir accordé ta confiance il y a un peu plus de trois ans en m'offrant la possibilité de travailler dans l'équipe Nanospin. Merci pour tout le temps que tu as pris au début de ma thèse pour que je puisse devenir autonome en salle blanche et sur les manip'. Pour tous ces cafés, moment d'échange scientifique et humain indispensables au bon déroulement de cette thèse. Pour ces matinées à la frontale dans la salle de manip à maintenir en vie "la molécule". Merci pour la grande liberté que tu m'as laissée, merci d'avoir pris le temps de relire ce manuscrit et enfin merci de m'avoir offert la possibilité de courir en Chartreuse un certain week-end d'Août ! Cette anecdote me permet, sans transition, de dire un grand merci à Wolfgang Wernsdorfer. Ta grande force, pour un étudiant ayant la chance de travailler à tes côtés, réside dans ta capacité à renormaliser la difficulté d'une épreuve à surmonter. Que ce soit pour garder un échantillon à froid pendant 4 ans, réaliser un algorithme quantique avec le noyau d'un atome ou bien même traverser Belledune d'une traite (j'ai encore quelques doutes sur ce dernier point) tout cela paraît simple et naturelle. Cela m'a permis de ne jamais perdre espoir et de traverser les épreuves que réserve une thèse. Vous formez un duo remarquable pour encadrer des étudiants et j'espère que cela durera encore longtemps ! Je souhaite également remercier Rafik Ballou. Evidemment parce que tu as pris beaucoup de temps pour relire ce manuscrit et pour m'aider à mieux comprendre les mécanismes en jeu dans mon expérience. Mais je tiens aussi et surtout à te remercier pour la vision que tu portes sur le monde de la recherche et tes qualités humaines dont l'élégance transparait au cœur de tes raisonnements scientifiques. Je tiens à remercier Karim Ferhat. Tu as été la rencontre de cette thèse. Je souhaite à toute personne d'avoir la chance de se promener en toute décontraction dans les théories physiques autour d'un verre ou d'un ordinateur avec un ami. Longue vie à Tic&Tac ;) !

Je tiens à remercier Patrice Bertet, Michel Piore-Ladrière et Xavier Waintal d'avoir fait partie de mon jury de thèse ainsi que Wiebke Guichard pour avoir acceptée d'en être la présidente. Vos retours et questions furent d'un grand intérêt à la fois pour moi mais aussi pour la suite du projet. Merci à l'équipe Nanospin, à commencer par Christophe et Edgar pour le précieux développement informatique que vous avez fait. Un grand merci à Stefan Thiele, pour ton accueil, ton sourire permanent et bien entendu pour avoir développé l'expérience sur laquelle j'ai pu m'amuser pendant cette thèse, vivement qu'on réchauffe pour qu'on puisse libérer le petit hamster ! Merci aussi aux anciens thésards du groupe, Nicolas, Romain, Mathias et Marc, cette thèse est la suite d'un chemin que vous avez initié. Merci aux thésards actuels, Joachim, Hugo et Stefano, bon courage à vous pour la suite, que la chance soit avec vous ! Enfin merci aux étudiants: Michael pour tous ces stages, entre verres au Denfert et enfer dans le Vercors ;) et Nard, j'ai hâte de goûter la Carapils, bonne continuation à vous deux ! Merci à l'équipe de Modène, à commencer par Andrea (encore désolé d'avoir tourné la diluette) merci Filippo de t'être battu et avoir compris plus en détail le retournement de ce spin !

Bien souvent pendant ma thèse je me suis senti comme un enfant à qui on donne un jouet, mon seul "travail" étant de jouer avec ! Comme tout enfant qui joue, il m'est arrivé d'abimer le jeu ou simplement de vouloir l'améliorer pour y ajouter de nouvelles fonctionnalités. Dans ces moments-là, j'ai eu la chance d'interagir avec les différents pôle de l'institut. Je veux donc remercier ici la team Nanofab, Thierry et Thierry, Jef, Seb, Bruno Gwen et la nouvelle recrue Latifa, grâce à vous tous "la panne Godfrin" ne m'a pas totalement rendu fou (encore que...). Un grand merci à toute l'équipe du rez-de-chaussée des bâtiments K et D, Éric pour tes opérations à cœur ouvert sur la manip et ton amour de la Bretagne, Didier, Yves, David et Loulou! Je suis aussi contraint et forcé de remercier un Normand :) merci Daniel pour les fantastiques boîtes et le porte échantillon que tu nous à fabriqués et dessinés. Merci à toi Christophe d'avoir toujours résolu mes soucis de RF et pour tous tes précieux conseils. Merci enfin à l'équipe du liquef qui m'a fourni 200L d'Hélium par semaine.

L'institut Néel est un microcosme propice aux rencontres et discussion (Vive la K-fette!). Un grand merci à Benjamin, coéquipier de trail et de tour de piste, tout comme Jan, merci d'avoir bien balisé le sentier après l'Arselle. Merci à Olivier, Benjamin, Francesco (mais pas à Laure parce que je dois te remercier plus loin) pour les cafés très enrichissant. Un grand merci à ma marraine de thèse, Virginie, tu as pris ton rôle très à cœur en étant toujours à l'écoute. Merci à Pierre pour ta gestion du café mais surtout pour l'énergie que tu mets à la diffusion de la science ! Merci aussi au duo de la com', Lilian et Florence, d'avoir soutenu

---

toutes nos initiatives. Merci enfin à l'équipe cohérence quantique dans son ensemble de nous accepter aux réunions d'équipe, séminaire informel ou les idées et les personnalités s'affrontent toujours dans la bienveillance.

La majorité de mon temps de thèse fut consacré à « parler » avec un spin nucléaire, cependant une thèse ne se limite pas à un seul projet. Je tiens donc à remercier Véronique Fanchon et les classes de 3<sup>ème</sup> du Lycée Champollion avec lesquelles j'ai eu plaisir à interagir. Merci également à mes collègues d'enseignement et tout particulièrement à Alain Drillat. Merci à l'ESAD de Grenoble, en particulier à Simone Frangi de m'avoir accueilli avec bienveillance dans son univers. Merci à toute l'équipe de MT180, Cesar, Souad, Sergi et Marion, les lyonnais nous ont battu mais au fond on était les meilleurs ! Merci à Laetitia, Pierre, Muriel et l'ensemble de la SFP Rhône-Alpes de nous avoir laissé une grande liberté tout en nous assurant un fort soutien dans l'organisation de ce qui est en train de devenir le grand rendez-vous des jeunes chercheurs grenoblois, les RJPs. Enfin, un immense merci à toute la "webteam", vive Drupal et les croissants !!

Tout naturellement après cette webteam, j'en viens à remercier l'ensemble des thésards avec qui j'ai eu la chance d'interagir. Vous êtes bien plus que des compagnons de galère ! Merci donc à (désolé ça fait un peu mailing list) Ketty, Karim, Marin, Yann, mon grand seigneur Al le chacal et ma petite sœur Laure, Olivier, Emilie, Chloé, Nicolas, Alexis, Sylvain, Béatrix, Elie, Pauline, Valentin, Mathias, mes co-bureau, Moana l'experte du point triple adiabatique et à tout ce que j'oublie. Pour ces derniers, je m'engage à leur payer une mousse ! Au passage, merci aux bars grenoblois ! Un immense merci à tous mes amis non-Néelien, à commencer par Marine, merci pour tout :). Merci à la coloc : Nours, Maélenne, Valval et les Schtroumpfs mais aussi à la coloc'nel : Jéjé, Madec et Gunt! Merci à la troupe de l'Est: Mika et Pow, Xav, Totoy et Antho. Merci à la grande randonneuse Nadia, Anais (on est à 1631 vues !) et Alexis (sans oublier Gérard et Jean !). Merci à Coralie, Alice, Morgan et l'asso photon ! Merci Adri, Le 22 et Melow ! Merci au Brest Volley et surtout au tournoi d'Ouessant !

L'idée de faire une thèse naît petit à petit dans l'esprit, au fil de rencontres qui marquent une vie. Un immense merci donc à Benoît Daré, Jean-Luc Hermann et André Brahic. Merci également à la famille dans son ensemble. Merci aux cousins pour toutes les conneries faites à Kernouës. Un grand merci à toi Vincent, pour ton écoute, tes conseils et surtout pour toutes ces tranches de vie, merci à Isabelle et bien sûr un immense merci au plus beau de tous, j'ai nommé Gabriel ! De belles années nous attendent :) ! Je finis ces remerciements par ceux qui

ont commencé cette thèse avant même que j'en sois conscient de par leur travail d'éducation : mes parents. Merci de ne pas m'avoir laissé regarder trop la télé et surtout merci pour votre soutien pendant toutes ces années.

Enfin merci et bonne lecture à toi qui lit cette thèse.

## Abstract

The application of quantum physics to the information theory turns out to be full of promises for our information society. Aware of this potential, groups of scientists all around the world have this common goal to create the quantum version of the computer. The first step of this ambitious project is the realization of the basic block that encodes the quantum information, the qubit. Among all existing qubits, spin based devices are very attractive since they reveal electrical read-out and coherent manipulation. Beyond this, the more isolated a system is, the longer its quantum behaviour remains, making of the nuclear spin a serious candidate for exhibiting long coherence time and consequently high numbers of quantum operation.

In this context I worked on a molecular spin transistor consisting of a TbPc<sub>2</sub> single-molecule magnet coupled to electrodes (source, drain and gate) and a microwave antenna. This setup enabled us to read-out electrically both the electronic and the nuclear spin states and to coherently manipulate the nuclear spin of the Terbium ion. I focused during my Ph.D. on the study of the spins dynamic and mainly the 3/2 nuclear spin under the influence of a microwave pulse. The first step was to measure the energy difference between these states leading in a second time to the coherent manipulation of the three nuclear spin transitions using only a microwave electric field. To further characterize the decoherence processes that break the phase of the nuclear spin states, I performed Ramsey and Hahn-echo measurements. These preliminary results show that we were in presence of three qubits with figure of merit higher than two thousands, thus meeting the expectations aroused by the use of a nuclear spin as the basic block of quantum information.

More than demonstrating the qubit dynamic, I demonstrated that a nuclear spin embedded in the molecular magnet transistor is a four quantum states system that can be fully controlled, a qudit. Theoretical proposal demonstrated that quantum information processing such as quantum gates and algorithms could be implemented using a 3/2 spin. I focused on a research algorithm which is a succession of an Hadamard gate, that creates a coherent superposition of all the nuclear spin states, and an unitary evolution, that amplified the amplitude of a desired state. It allows a quadratic speed-up to find an element in an unordered list compared to

classical algorithm. During my Ph.D., I demonstrated the experimental proof of feasibility of this Grover like algorithm applied to a multi-levels system. The first step was to experimentally create coherent superposition of two, three and four states. Then I measured coherent oscillations in between a 3 state superposition and a selected state which is the signature of the research algorithm implementation.

In summary, this Ph.D. exposed the first quantum search algorithm on a single-molecule magnet based qudit. These results combined to the great versatility of molecular magnet holds a lot of promises for the next challenge: building up a scalable molecular based quantum computer.

---

## Résumé

La physique quantique appliquée à la théorie de l'information se révèle être pleine de promesses pour notre société. Conscients de ce potentiel, des groupes de scientifiques du monde entier ont pour objectif commun de créer un ordinateur utilisant les principes de la mécanique quantique. La première étape de cet ambitieux cheminement menant à l'ordinateur quantique est la réalisation du bloc de base de l'encodage quantique de l'information, le qubit. Dans le large choix de qubits existants, ceux utilisant un spin sont très attrayants puisqu'ils peuvent être lus et manipulés de façon cohérente uniquement en utilisant des champs électriques. Enfin, plus un système est isolé, plus son comportement demeure quantique, ce qui fait du spin nucléaire un sérieux candidat dans la course au long temps de cohérence et donc aux grands nombres d'opérations quantiques.

Dans ce contexte, j'ai étudié un transistor de spin moléculaire. Ce dispositif, placé dans un réfrigérateur à dilution assurant des mesures à 40mK, est composé d'une molécule magnétique TbPc<sub>2</sub> couplée à des électrodes (source, drain et grille) et à une antenne hyperfréquence. Il nous a permis de lire à l'aide d'une mesure de conductance, à la fois l'état de spin électronique et nucléaire de l'ion Terbium. Ma thèse se focalise sur l'étude de la dynamique de ces spins et plus particulièrement celle du spin nucléaire 3/2 sous l'influence d'un champ micro-onde. La première étape consiste à mesurer la différence d'énergie entre ces quatre états de spin nucléaire pour ensuite parvenir à manipuler de façon cohérente ses trois transitions en utilisant uniquement un champ électrique. Pour caractériser davantage les processus de décohérence à l'origine de la perte de phase des états quantiques, j'ai réalisé des mesures Ramsey et Hahn-echo révélant des temps de cohérence de l'ordre de 0.3ms. Ces résultats préliminaires montrent que nous sommes en présence de 3 qubits ayant une figure de mérite supérieure à deux mille, répondant ainsi aux attentes suscitées par l'utilisation d'un spin nucléaire comme bloc de base de l'information quantique.

Plus que démontrer expérimentalement la dynamique de trois qubits, ces mesures nous prouvent qu'un spin nucléaire intégré dans une géométrie de type transistor à aimant moléculaire est un système à quatre états contrôlé de façon cohérente. Des propositions théoriques démontrent qu'un traitement quantique de l'information, telle que l'application de portes quantiques et la réalisation d'algorithmes, peut être implémenté sur un tel système. Je me suis concentré sur un algorithme de recherche. Il s'agit de la succession d'une porte Hadamard, qui crée une superposition cohérente de tous les états de spin nucléaire, et une évolution

unitaire qui amplifie l'amplitude d'un état désiré. Il permet une accélération quadratique de la recherche d'un élément dans une liste non ordonnée comparée à un algorithme classique. Pendant ma thèse, j'ai apporté la preuve expérimentale de la faisabilité de cet algorithme de Grover sur un système à plusieurs niveaux. La première étape a été de créer une superposition cohérente de deux, trois et quatre états par l'application d'une impulsion radio-fréquence. Enfin, j'ai mesuré une oscillation cohérente entre une superposition de trois états et un état sélectionné qui est la signature de l'implémentation de l'algorithme de recherche.

En résumé, cette thèse expose la première implémentation d'un algorithme quantique de recherche sur un qudit de type aimant moléculaire. Ces résultats, combinés à la grande polyvalence des molécules magnétiques, sont autant de promesses pour la suite de ce défi scientifique qu'est la construction d'un ordinateur quantique moléculaire.

# Table of contents

<b>1</b>	<b>Introduction to quantum information</b>	<b>1</b>
1.1	Motivation . . . . .	1
1.2	Qubit System . . . . .	2
1.3	Quantum Information Processing . . . . .	8
1.3.1	Quantum gates . . . . .	8
1.3.2	Quantum algorithm . . . . .	11
1.4	Thesis outline . . . . .	14
<b>2</b>	<b>TbPc<sub>2</sub> Molecular Magnet</b>	<b>17</b>
2.1	Composition and structure . . . . .	17
2.2	Tb <sup>3+</sup> ion . . . . .	18
2.3	Internal interaction . . . . .	18
2.3.1	Electron-electron . . . . .	19
2.3.2	Spin-orbit . . . . .	20
2.3.3	Ligand field . . . . .	21
2.3.4	Hyperfine . . . . .	23
2.4	External field interaction . . . . .	25
2.4.1	Magnetic: Zeeman . . . . .	26
2.4.2	Electric: Stark . . . . .	28
<b>3</b>	<b>Experimental setup</b>	<b>29</b>
3.1	Inverse dilution refrigerator . . . . .	29
3.2	Sample Holder . . . . .	33
3.3	DC measurement circuit . . . . .	35
3.3.1	Filtering . . . . .	35
3.3.2	Signal transducer . . . . .	36
3.3.3	Real time data acquisition . . . . .	37
3.4	Magnetic field generation . . . . .	39

3.5	Microwave generation . . . . .	41
3.5.1	Equipment . . . . .	41
3.5.2	Monochromatic pulse . . . . .	42
3.5.3	Constant frequencies multi-chromatic pulse . . . . .	43
3.5.4	Multi-chromatic with frequency modulation . . . . .	44
<b>4</b>	<b>Single molecular magnet transistor</b>	<b>47</b>
4.1	Sample nanofabrication process . . . . .	48
4.1.1	Type 1 sample . . . . .	48
4.1.2	Type 1 bis sample. . . . .	55
4.1.3	Type 2 sample . . . . .	55
4.2	Molecular deposition and electromigration . . . . .	63
4.3	Transport measurement . . . . .	66
<b>5</b>	<b>Spins read-out and life time</b>	<b>73</b>
5.1	Electronic spin . . . . .	73
5.1.1	Direct read-out . . . . .	73
5.1.2	Relaxation time . . . . .	81
5.2	Nuclear spin . . . . .	82
5.2.1	Indirect read-out : Quantum Tunnelling of Magnetization . . . . .	82
5.2.2	Nuclear spin lifetime . . . . .	92
<b>6</b>	<b>Nuclear spin transitions coherent manipulation</b>	<b>95</b>
6.1	Magnetic Field-Qubit interaction . . . . .	95
6.2	From magnetic to electric manipulation: Stark effect . . . . .	100
6.2.1	Magnetic dipole hyperfine field Stark effect . . . . .	102
6.2.2	Discussion on the Hyperfine interaction modulation . . . . .	108
6.3	Experimental protocol . . . . .	109
6.4	Nuclear spin dynamic . . . . .	110
6.4.1	Frequency calibration . . . . .	110
6.4.2	Rabi Oscillation . . . . .	114
6.5	Nuclear spin coherence time . . . . .	121
6.5.1	Coherence time $T_2^R$ : Ramsey fringes . . . . .	121
6.5.2	Investigation of decoherence process : Hahn-echo . . . . .	125
6.6	From qubit to multi level system: Coherent pump-probe . . . . .	133
6.6.1	3 states coherent pump probe: single pump . . . . .	133
6.6.2	4 states coherent pump probe: double pump . . . . .	135

---

<b>7</b>	<b>Grover algorithm implementation</b>	<b>139</b>
7.1	Microwave pulse - multi-states interaction . . . . .	140
7.2	Hadamard Gate . . . . .	142
7.2.1	Theory . . . . .	142
7.2.2	Experimental realisation . . . . .	145
7.2.3	Ramsey fringes generalised to N states . . . . .	147
7.3	Grover's unitary evolution . . . . .	150
7.3.1	Amplitude amplification . . . . .	151
7.3.2	Experimental Implementation . . . . .	152
<b>8</b>	<b>Conclusion and outlook</b>	<b>161</b>
	<b>References</b>	<b>165</b>
	<b>Appendix A Stevens operators</b>	<b>175</b>



# Chapter 1

## Introduction to quantum information

### 1.1 Motivation

As explained by Richard Feynman [1], taking the example of a room position, the easiest way to encode an information is the use of a two states system. These two states can be either a colour, a water flow, an electronic flow, a magnetic moment or whatever you can imagine. When the information is encoded, you want to control it in different ways: storing, reading, manipulating or transmitting it. Nowadays computers are based on this idea and use different physical two classical states systems to play with the information depending on what we want to do with. For example, to store the information, you will prefer a magnetic moment because of its memory properties whereas you will prefer an electrons flow to perform fast operation because of their speed. All information processes of today computers can be explained using classical mechanic while since 1900 [2] we now that quantum theory offers a much better description of Nature than the classical one. In the 80's, pioneers of quantum information [1, 3, 4] start to think about this idea: What about using the power of quantum mechanic to treat the information [5] ? The idea of this new information theory is to generalize the Church-Turing hypothesis [6] to its quantum level : " A quantum Turing machine can efficiently simulate any realistic model of computation" [7]. More than accelerating calculations by decreasing the complexity of a given problem, the quantum computer might be able to solve problems that are unbreakable for a classical computer with finite time and resources [8]. The power of a quantum computer lies in its capability to be in all states simultaneously by using superposition principles (a quantum operation influences the complete superposition of states) and to create quantum interferences. The realization of an operational quantum computer is one of the most ambitious technological goals of today's scientist. Even if the will of drawing a predefined road for fundamental research is a strange idea, the community

defined seven steps to reach this goal [9].

The first step is to develop the basic element of this new computer, a two quantum states system, the so-called qubit. As for the classical computer, because a two states system is the most fundamental system you can find, one can imagine many of them. In section 1.2, we will make a brief overview of these systems that experimentally demonstrate to be suited qubit, trying to understand the advantages and drawbacks of each one to perform quantum operations and to build a quantum machine. After identifying the new information media, we will examine the second step along this road : the treatment of it using quantum algorithm to solve concrete problems (section 1.3). I will not treat the other steps that are mainly dealing with error code correction [10]: quantum non destructive measurements for error code correction, logical memory with longer lifetime than physical qubits, operations on single logical qubits, algorithms on multiple logical qubits to finish with a fault-tolerant quantum computation.

## 1.2 Qubit System

A qubit is a quantum system which can be described by a two-dimensional Hilbert space. The basis states are  $|\uparrow\rangle$  and  $|\downarrow\rangle$  and a pure qubit states can be put in any arbitrary linear superposition of this basis, represented as  $|\psi\rangle = \alpha|\uparrow\rangle + \beta|\downarrow\rangle$ , where  $(\alpha, \beta) \in \mathbb{C}$  with the normalization  $|\alpha|^2 + |\beta|^2 = 1$ . As a result, every pure qubit state can be written as:

$$|\psi\rangle = e^{i\gamma} \left\{ \cos\left(\frac{\theta}{2}\right) |\uparrow\rangle + e^{i\phi} \sin\left(\frac{\theta}{2}\right) |\downarrow\rangle \right\} \quad (1.1)$$

The global phase  $\gamma$  can be ignored and set arbitrarily to zero being irrelevant to the qubit manipulation. All the dynamic can be then expressed using two angles  $(\theta, \phi)$ , enabling a graphical representation of this pure state on the so-called Bloch-sphere (figure 1.1). On this sphere, the north (south) pole represents the  $|\uparrow\rangle$  ( $|\downarrow\rangle$ ) state and the equator represents an equal superposition of the two states:  $\frac{1}{\sqrt{2}}(|\uparrow\rangle + e^{i\phi} |\downarrow\rangle)$ .

Many fields of physics are concerned by the realization of a qubit: atomic and molecular physics, quantum optics, nuclear and electron magnetic resonance spectroscopy, superconducting electronics, quantum-dot physics... In order to decide whether or not a quantum mechanical system is suited, DiVincenzo formulated five criteria [11].

- *A scalable physical system with well characterized qubits* : The state must be described as a normalized superposition of two states and the internal Hamiltonian of the system must be

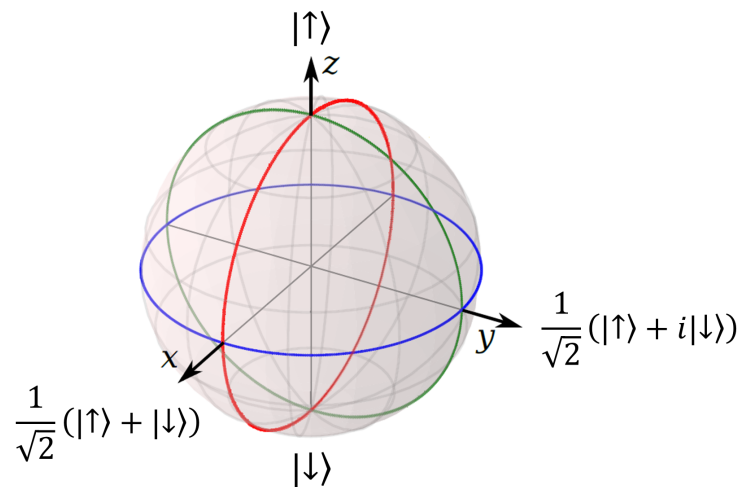


Fig. 1.1 Bloch sphere representation of a quantum bit. Eq. 1.1 show that only 2 parameters ( $\theta, \phi$ ) are needed to identify a qubit states, as a results any quantum superposition of two states can be visualized as a point on the surface of the sphere. The north pole and the south pole are the two levels of the qubit  $|\uparrow\rangle$  and  $|\downarrow\rangle$ .

known.

- *The ability to initialize the state of the qubits to a simple fiducial state:* the state of the qubit has to be prepared before each computation.
- *Long relevant decoherence times:* the qubit must be protected from decoherence by isolation from the environment.
- *A universal set of quantum gate :* the manipulation of a quantum state must be performed with reasonable precision and much faster than the decoherence time.
- *A qubit specific measurement capability:* the final state of the qubit must be read-out with a sufficiently high precision.

He also gives two other criteria relating to the communication of quantum information. In brief a good qubit is a two states quantum system that can be initialized, manipulated faster than its decoherence time and read-out. In this sentence, the main difficulty of quantum computation is exposed. On one hand we want a well isolated system to preserve the coherence and on another hand we want a system that can be manipulated and read-out. Several systems met the criteria, the idea of this section is not to provide an exhaustive list of all these qubits but to understand our line of thought, starting from the ion trap and finishing with molecular magnet.

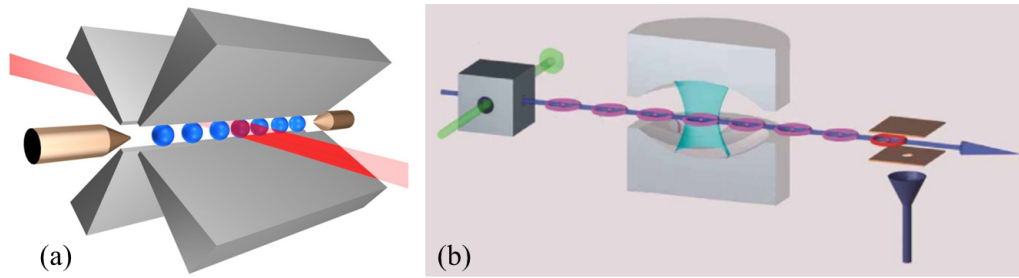


Fig. 1.2 Quantum information pioneers experiments. In 1996, Wineland's group, working on ion traps (a), create the first experimental Schrödinger cat [12] and Haroche's group study the decoherence processes (b) using photons in a cavity [13]

One of the experimental pioneers of quantum information is the group of David Wineland. In 1978 they cooled down a  $\text{Mg}^{2+}$  ion confined in a Penning trap using the radiation-pressure techniques [14] and they produced there first Schrödinger cat in 1996 [12]. The same year, the group of Serge Haroche observed Rabi oscillation of Rydberg atoms in the vacuum and in small coherent fields stored in a cavity [15]. They also did the first measurement of the decoherence process time [13]. Both Wineland and Haroche were awarded the Nobel Prize in physics in 2012. These fantastic experiments demonstrate the fundamental possibility of performing basic quantum calculation and are still ongoing active research domain. Nevertheless, both systems are experimentally very demanding and at the same time nano-fabrication techniques develop, opening the road to the solid state qubit systems which offer more perspective for scalability.

A nano-fabricated promising candidate to realize a qubit is superconducting quantum circuit based on Josephson junctions. This innovative idea of using macroscopic electrical circuit to do quantum manipulation comes from Anthony James Legget [18]. The electronic dynamics in this SIS junction is described by the Cooper-pair number and the phase difference across the junction which are conjugate observables. Depending on its design, it is possible to fix one variable resulting in a "charge" or a "phase" qubit. In 1985, the quantification of the phase difference across the junction was observed [19]. Few years latter, in 1999, Nakamura managed to perform coherent manipulation of these macroscopic states in a charge qubit [16]. Great progress in this field have been done in term of coherence time to go from  $3ns$ , for the first Nakamura qubit, to  $0.1ms$  using transmon qubit [17] and in term of geometry by entangling three qubits [20, 21]. The main intrinsic limitation of this qubit is

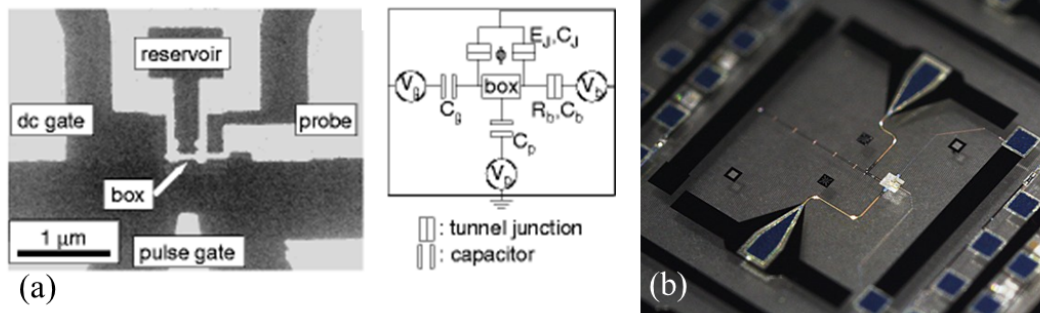


Fig. 1.3 Superconducting qubit. (a) In 1999 Nakamura *et al.* measured the first coherent manipulation of a qubit using a superconducting macroscopic circuit [16]. Nowadays, people coupled this qubit to structure such as cavity or resonator to increase the qubit properties [17]. (b) Here is a picture from Martinis website, showing a superconducting qubit coupled to a resonator.

their typical size of several  $\mu m$  that makes them extremely sensitive to external noise.

To decouple the qubit from its environment, the first idea is to decrease its typical size. Loss in 1998 proposed [24] the idea of using the spin of an electron inside a quantum dot as a two states quantum system. Since they are much smaller than superconducting circuits, they couple less strongly to the environment, but at the same time they are also harder to measure. A 2D confinement of the electron is obtained thanks to the electronics properties in *GaAs/AlGaAs* heterostructure. It is then possible to form quantum dots in this two-dimensional electron gas by applying negative voltages to metallic surface gates. The first single-shot read-out of an electron spin inside a quantum dot was reported in 2004 [25]. Two years later the coherent manipulation of an electron spin in a GaAs quantum dot was presented by Koppens *et al.* [26] using magnetic field and by Pioro-Ladrière *et al.* using only an electric field [27]. The intrinsic spin bath of host nuclear spins in these materials, coupled through the hyperfine interaction to the electronic spin of the quantum dot, was the primary limit to achieve long spin coherence times in these systems (inhomogeneous dephasing time of few tens of ns in GaAs [28]). This limitation has been reduced through the use of dynamical decoupling protocols measurements that can extend the useful coherence time up to  $200\mu s$  [29]. The geometry of these quantum dot are 2D scalable by building array of qubits. In 2012 Shulman *et al.* [23] demonstrated the entanglement of two qubits in such a structure.

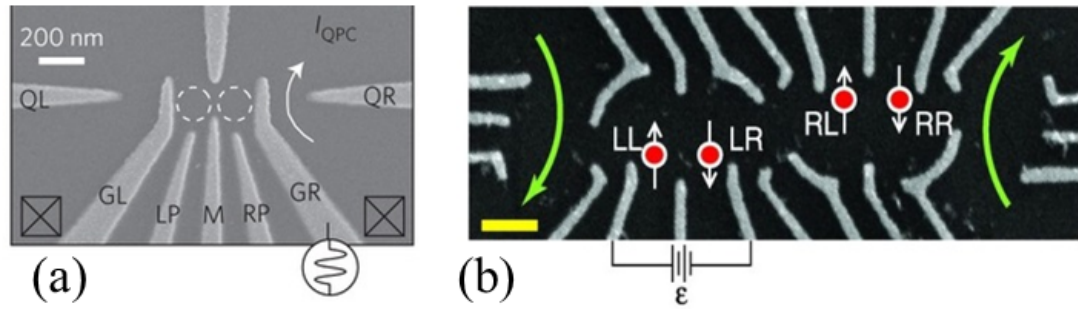


Fig. 1.4 Electronic spin qubit in quantum dot. (a) SEM photograph of a double quantum dot with a microwave excitation that ensure a coherent manipulation of the qubit [22]. (b) SEM photograph of the structure that showed the first entangled electronic spin qubit [23].

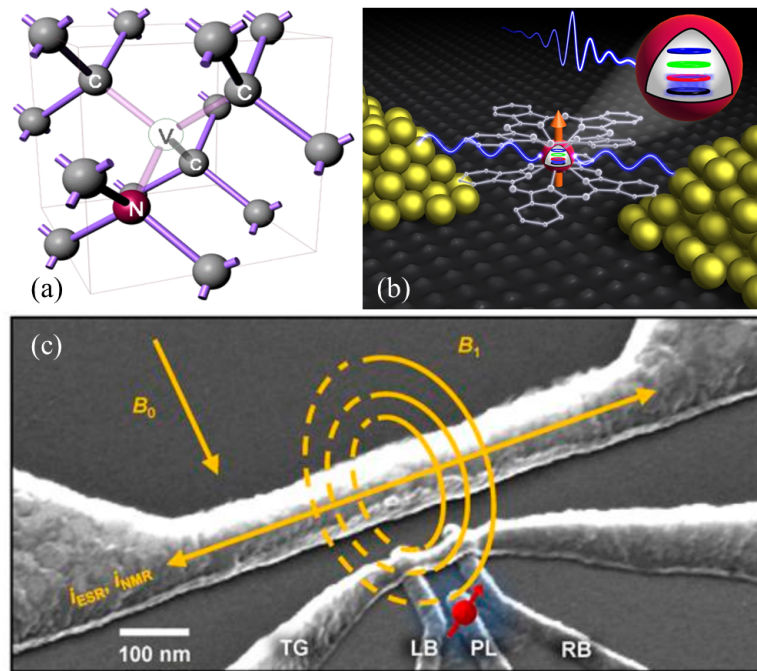


Fig. 1.5 Nuclear spin qubit. (a) Nitrogen-Vacancy system structure representation [30]. (b) Single molecular magnet transistor picture, this system demonstrate the first manipulation of a nuclear spin using an electrical field [31]. (c) SEM photograph of a microwave line use to manipulate a  $^{31}\text{P}$  donor in silicon nuclear spin qubit [32].

Another material for electronic spin manipulation is diamond. It supports a plethora of optically active point defects, many of which are paramagnetic and could therefore serve as spin qubits. In 1997, nitrogen-vacancy (NV) defect in diamond, consisting of a substitutional nitrogen atom adjacent to a vacancy in the diamond crystal, was observed [33] and gained much interest in experimental quantum physics because it behaves much like a single ion in a robust solid-state not strongly interacting environment. The NV centre, in its negatively charged ground state, is an electron spin triplet, the state of which can be initialized and measured simply through optical excitation and fluorescence detection, respectively [30]. The properties of this material, an extremely high Debye temperature and the large band gap, endow NV centre spins with remarkable coherence properties that persist up to room temperature. Nowadays, fast manipulation (sub-nanosecond) of this electronic spin [34] enables more than one million coherent operations within the NV centre's spin coherence time.

A key feature of NV centre spin qubits is to enable access not only to the electronic spin state but also to the individual nuclear spins of the intrinsic nitrogen atom and proximal  $^{13}\text{C}$  nuclei. Indeed, when some of the quantum information community tries to increase the quality of the electronic spin environment, using spinless material like  $^{28}\text{Si}$  or  $^{12}\text{C}$  [35–37], others try to use a spin which is much less coupled to its environment: the nuclear spin which has a magnetic moment 3 orders of magnitude smaller than the electronic one [38]. Here again, more isolated means harder to detect. The fundamental idea is the same for all these systems: an indirect measurement of the nuclear spin states through the hyperfine coupling to an electronic spin. For NV centre, they demonstrated that this nuclear spin qubits can be initialized [39], measured non-destructively in a single shot [40], and even entangled [41]. Scientists demonstrated operating spin [42] and nuclear [32, 43] spin qubits also in silicon based devices, using  $^{31}\text{P}$  impurity. Finally, and here is the subject of this thesis, read-out [44, 45] and coherent control of a nuclear spin was demonstrated in single-molecule magnet using electrically driven resonance [31]. We focus our study on the  $\text{TbPc}_2$  in a transistor system. In this molecule the Pc ligands work as a read-out dot under the influence of the Terbium ion spin. In addition, the specific geometric and electronic properties of it offer interesting manipulation and coherence times. Moreover, the great diversity of molecules in addition to their massively parallel synthesis are full of promises for scalable quantum information processing.

The above non exhaustive list of qubit systems show how prolific were the two past decades in term of fundamental research. I do not want to compare and classify them to know which one is the best to build the first quantum computer for two distinct reasons. First, the

list of criteria is so large (figure of merit, scalability, difficulties of production, information transfer, working temperature...) and hard to weight. Second point, the number of different system we use today to play with the classical information is the best example to call for a diversified research in term of quantum information system. Each system could be the best for a specific quantum application: fast calculation, long memory, simulation, sensing *etc.*

### 1.3 Quantum Information Processing

The main objective of Quantum Information Processing (QIP) is to implement coherent control on qubits with quantum gates. In the previous part we have seen how different are the investigating qubits. As a result, the physical phenomena used to achieve the desired manipulation of a quantum state can be also very varied. For example, if qubits are encoded in spins, the manipulation is performed by varying an applied magnetic or electric field. If the qubit is encoded in an internal excitation state of an ion, the gate operation can be achieved by varying the irradiation time of a laser beam. The common point of all these systems is that they are governed by Schrödinger's equation:

$$i\hbar \frac{\delta |\psi\rangle}{\delta t} = H |\psi\rangle \quad (1.2)$$

To preserve the normalization of the state during the operation, the evolution must be unitary *i.e.* described by a time independent Hamiltonian. QIP is a succession of unitary matrices  $U$  describing quantum gates which are related to the physical processes by which they are achieved *via* the equation  $U = e^{-\frac{iHt}{\hbar}}$ . Here is an other promising fundamental thermodynamic gain for the future of computation: if we use only reversible gates, no energy needs to be dissipated to perform those gate operations.

#### 1.3.1 Quantum gates

The first example of non-trivial single qubit gates are the Pauli matrices,  $\sigma_x$ ,  $\sigma_y$  and  $\sigma_z$  (eq. 1.3). These matrices represent the rotation of the vector in the Bloch sphere respectively around the x, y and z axis.

$$\sigma_x = \begin{pmatrix} 0 & 1 \\ 1 & 0 \end{pmatrix} \quad \sigma_y = \begin{pmatrix} 0 & -i \\ i & 0 \end{pmatrix} \quad \sigma_z = \begin{pmatrix} 1 & 0 \\ 0 & -1 \end{pmatrix} \quad (1.3)$$

The application of the  $\sigma_x$  flips the qubit state,  $\sigma_y$  does the same with an additional phase when  $\sigma_z$  flips the phase. These transformations are experimentally performed for all the systems described in section 1.2 and will be explained in details in section 6.1. Pauli matrices form, with the identity, a basis for the vector space of  $2 \times 2$  Hermitian matrices. These, with the standard multiplication law for matrices, form a group isomorphic to  $SU(2)$ . As a result, every single qubit gate  $G$  can be decomposed on these matrices:

$$G = \frac{1}{2} (Tr[G]Id + Tr[G\sigma_x]\sigma_x + Tr[G\sigma_y]\sigma_y + Tr[G\sigma_z]\sigma_z) \quad (1.4)$$

In this context the use of the Bloch sphere reveals itself extremely helpful. This is easily illustrated by examining the effect of  $\sigma_x$ . As an introduction with this concept of rotation in the Bloch-sphere, it is interesting to see if  $\sigma_x$  is a quantum NOT gate? The NOT gate has the effect of mapping a state at the North pole of the Bloch sphere into a state at the South pole and vice versa. It is natural to extend the definition of a NOT gate to be the operation that maps a qubit  $|\psi\rangle$  into its antipodal state  $|\psi^\perp\rangle$ :

$$|\psi\rangle = \cos\left(\frac{\theta}{2}\right)|\uparrow\rangle + e^{i\phi}\sin\left(\frac{\theta}{2}\right)|\downarrow\rangle \quad (1.5)$$

$$\begin{aligned} |\psi^\perp\rangle &= \cos\left(\frac{\pi-\theta}{2}\right)|\uparrow\rangle + e^{i(\phi+\pi)}\sin\left(\frac{\pi-\theta}{2}\right)|\downarrow\rangle \\ &= \sin\left(\frac{\theta}{2}\right)|\uparrow\rangle - e^{i\phi}\cos\left(\frac{\theta}{2}\right)|\downarrow\rangle \end{aligned} \quad (1.6)$$

Now that we have the expression of antipodal state we can compare it with the state after a  $\sigma_x$  gate:

$$\sigma_x|\psi\rangle = \begin{pmatrix} 0 & 1 \\ 1 & 0 \end{pmatrix} \cdot \begin{pmatrix} \cos(\frac{\theta}{2}) \\ e^{i\phi}\sin(\frac{\theta}{2}) \end{pmatrix} = \sin\left(\frac{\theta}{2}\right)|\uparrow\rangle + e^{-i\phi}\cos\left(\frac{\theta}{2}\right)|\downarrow\rangle \neq |\psi^\perp\rangle \quad (1.7)$$

One thus observed that  $\sigma_x$  is the quantum analog of the NOT gate for the states  $|\uparrow\rangle$  or  $|\downarrow\rangle$  but not for an arbitrary pure quantum state. A deeper investigation of this question shows that there is no quantum analog to the NOT gate, another example on how caution we should be when using classical vocabulary to describe the quantum world.

A single qubit gate of great interest, with no classical analog, is the Hadamard gate. When operating on one of the basis states  $|\uparrow\rangle$  or  $|\downarrow\rangle$  it sends it to the equatorial plane of the Bloch sphere. Because of the reversibility, on subsequent application, we obtain the original

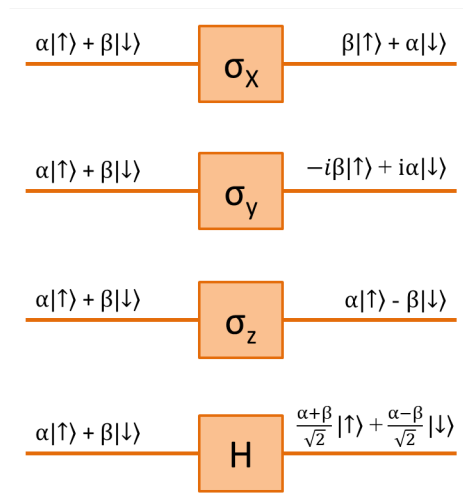


Fig. 1.6 Non exhaustive list of single qubit gate showing how they transform an input state.

state. The Hadamard gate is written in the matrix form as

$$H = \frac{1}{\sqrt{2}} \begin{pmatrix} 1 & 1 \\ 1 & -1 \end{pmatrix} \quad (1.8)$$

This rather simple gate is one of the most useful in quantum computation. Indeed, starting from a basis state, the Hadamard gate creates a coherent superposition of all states and makes possible the use of quantum parallelism.

Complex QIP requires bigger Hilbert space than the one provided by a single qubit. The most naive idea to increase the dimension of a Hilbert space is to increase the number of states of the system. If you coherently control all the transition of a  $N$  states system, so that you can create a coherent superposition of all these states, you can apply complex gates. This solution is the one I used during my thesis, playing with a single  $3/2$  nuclear spin. These relatively large spin systems are of great interest as proof of feasibility for quantum operation. Nevertheless the Hilbert space dimension increasing as  $2n + 1$ , where  $n$  is the spin value. This linear evolution may be a strong limitation if another quantum property is not accessible. Indeed an exponential growth is possible by mixing several qubits. Considering a two qubits system, its Hilbert space is:

$$\xi_s = \xi_1 \otimes \xi_1 \quad (1.9)$$

*i.e.* the tensor product of the qubit 1 Hilbert space  $\xi_1$  and qubit 2 Hilbert space  $\xi_2$ . One can demonstrate that the four eigenstates of this Hilbert space are

$$\frac{(|\uparrow, \downarrow\rangle - |\downarrow, \uparrow\rangle)}{\sqrt{2}} \quad (1.10)$$

that corresponds to the singlet state:  $|0, 0\rangle$  in the  $|S, m_s\rangle$  representation and

$$|\downarrow, \downarrow\rangle ; \frac{|\uparrow, \downarrow\rangle + |\downarrow, \uparrow\rangle}{\sqrt{2}} ; |\uparrow, \uparrow\rangle \quad (1.11)$$

that corresponds to the triplet state:  $|1, -1\rangle ; |1, 0\rangle ; |1, 1\rangle$  in the  $|S, m_s\rangle$  representation. As a result, a state of the system will be a linear superposition of these four states:

$$|\Psi\rangle = \alpha \frac{(|\uparrow, \downarrow\rangle - |\downarrow, \uparrow\rangle)}{\sqrt{2}} + \beta |\downarrow, \downarrow\rangle + \gamma \frac{|\uparrow, \downarrow\rangle + |\downarrow, \uparrow\rangle}{\sqrt{2}} + \delta |\uparrow, \uparrow\rangle \quad (1.12)$$

Where a classical computer encodes two informations with two bits (value of bit 1, value of bit 2) a quantum computer encodes four informations in two qubits ( $\alpha, \beta, \gamma, \delta$ ). A generalization at  $n$  qubit leads to an Hilbert space dimension of  $2^n$  that is growing exponentially.

Get back to the Hadamard single qubit gate: If you prepare  $n$  qubit in their fundamental states  $|\uparrow\rangle$  and apply to each qubit in parallel its own Hadamard gate, then the state produced is an equal superposition of  $2^n - 1$  states :

$$H|\uparrow\rangle \otimes H|\uparrow\rangle \otimes \dots \otimes H|\uparrow\rangle = \frac{1}{\sqrt{2^n}} \sum |x\rangle \quad (1.13)$$

Where  $|x\rangle$  stand for the basis of the full system Hilbert space. Equation 1.13 shows how, by applying simultaneously a Hadamard gate to each qubit of the basis, a coherent  $n$ -qubits superposition, containing  $2^n$  eigenstates, can be created. It is one of the most important tricks of quantum computing as it gives the ability to load exponentially many indices using only polynomial operations.

Even if I could present other quantum gates operating on a  $2^n$  states system, the aim of this introduction is not to give an exhaustive list. Thus, I will present in the following how from a massively superposed state, we would solve concrete problem using massively parallel algorithms.

### 1.3.2 Quantum algorithm

In 1985, David Deutsch [5] proposed the first quantum algorithm. It is a finite succession of gate applied to an input state that can be implement on a quantum computer. Since this proposition, a lot of efforts have been devoted to the realization of a working quantum computer. In order to better understand how powerful this quantum treatment of the information could be, I will present in the following a simple example.

There exists a rigorous way of defining what makes an algorithm fast or slow [46]. This relies on how does the computation time increases with increasing size of the input. If the time taken to execute the algorithm increases not faster than a polynomial function of the size of the input, then it is said to be fast. A naive example can illustrate this idea: if one is asked to solve the two following problems:

$$3 \times 5 = ? \quad (1.14)$$

$$? \times ? = 21 \quad (1.15)$$

One instantaneously finds the solution. When now one is asked to solve:

$$421 \times 307 = ? \quad (1.16)$$

$$? \times ? = 160451 \quad (1.17)$$

The first will take certainly less than one minute when the second might take an hour. This is because we know fast algorithms for multiplication, but we do not know fast algorithm for factorization. As a result when the complexity of the problem increases, performing a multiplication is still possible but factorization becomes much more tricky. We do not know if a fast classical algorithm exists for factorization problem even if there is much interest in finding. Indeed, the problem of factorization underpins the security of many public key. Nowadays after two years of calculation, a classical algorithm manages to factorize a 232-digit numbers [47]. What we know is that a quantum algorithm can solve this problem exponentially faster. This is the so-called Shor's Algorithm [48, 49] which is well detailed in [50]. It is mainly based on number theorem that states that there exists a relation between the periodicity of a particular function and the factor of an integer. Where Shor's algorithm is more efficient than a classical one is to find out this periodicity. It is a great example of quantum algorithm because it is based both on quantum superposition and interferences to reduce the complexity of the problem from exponential to polynomial. This discovery attracted considerable attention from banks and security agencies. Indeed the promise of an implementation of this algorithm is huge: breaking the RSA cryptosystem [51] or any other

form of secret informations. IBM group of California presented the first proof of feasibility of this algorithm in 2001 by factorizing  $15 = 5 \times 3$  using nuclear magnetic resonance (NMR) on seven spin  $1/2$  embedded in a molecule [52]. Other groups performed the same factorization [53–55] and more recently, an experiment went one step further: using photonic qubit, they factorized 21 [56]. Nowadays, the main goal of the different groups working in this field is to implement architectures with at least 50 qubits. Indeed, when dealing with factorization, a quantum computer integrating 20 to 30 qubits can be simulated on a modern classical computer [57].

Searching an element in an unordered list is another concrete problem that can be solved by a quantum computer. A classical computer would take  $O(N)$  operations to search an object among  $N$ , whereas, a quantum search algorithm could find it in  $O(\sqrt{N})$  operations. This algorithm was first formulated by Lov Kumar Grover [58, 59]. Using  $n$  qubits, he demonstrated that, by encoding the information on the phase of one state and applying quantum gates, he could find an element in a unordered list of  $2^n$  elements faster than any classical algorithm. It is maybe the easiest one to understand and different lectures demonstrate it so I will not explain here in details the succession of quantum gates that one need to apply to the system. The general idea is to increase, at each iteration, the population of the searched element which, at the beginning, is labelled by having a different phase from the others. After  $\sqrt{N}$  iterations, the full state gets close to the desired state, so that when you measure the final state system you find it with the largest probability. In 1998, Edward Farhi [60], presented another method where the search element is no more marked with a different phase but a different energy from the others. The second important difference comes from the process that increases the population of the desired state. Instead of applying  $\sqrt{N}$  iterations of duration independent of  $N$ , we apply at once a unitary evolution that is  $\sqrt{N}$  time dependent. This last quantum gate induces a coherent oscillation between the fully superposed state and the desired state. Few years later, Michael Leuenberger and Daniel Loss [61] presented the possibility to use this analog Grover's algorithm on a nuclear spin  $n$  ( $N = 2n + 1$  elements list), which I will experimentally demonstrate in section 7 of this thesis. It is important to note that other groups solved this problem using NMR implementation [62, 63]. Today, the size list record is  $N=8$  [64], showing once again the scalability problem of quantum computation.

There exist two others algorithm that have been implemented: the quantum annealing which solves Ising spin model problem [65] using the D-Wave system and the HHL algorithm that solves linear equation. This last algorithm has been implemented both in bulk optic system with photon qubit [66, 67] and on a 4 qubits NMR experiment [68]. These three

experiments showed the feasibility of solving a  $2 \times 2$  linear equation system. Moreover, there has been rapid progress in discovering quantum algorithms with varied applications such as eigenvalue and Gauss sum estimation [69, 70], boson sampling [71], numerical gradient estimation [72] *etc...* Showing, if necessary, that besides the fact that this research field is a fantastic playground to test and understand quantum experiments, it is also always evolving to find the most optimized quantum algorithm and quantum systems.

## 1.4 Thesis outline

My Ph.D. work was dedicated to the study of the read-out and manipulation of an isolated nuclear spin embedded in a single-molecule magnet in order to implement the Grover search algorithm. We made use of a three terminal transistor geometry, in which the nuclear spin is electrically detected using a read-out quantum dot and electrically manipulated *via* AC Stark effect. The idea of my thesis outline is to present the different experimental and theoretical mandatory steps forward the demonstration of the Grover's algorithm.

- In chapter 2, I will concentrate on the heart of the system, the TbPc<sub>2</sub> single-molecule magnet. After a brief description of the composition and the structure, the interactions responsible for the observed magnetic properties of the device will be discussed. We shall see how these properties can be tuned using external magnetic and electrical fields.
- In chapter 3, I will describe the setup that enabled all the experimental results shown after. Starting from the dilution refrigerator, I will explain each important part of the experiment which was added to this refrigerator in order to fabricate and measure a molecular spin-transistor: measurement lines, 3D-vector magnet, sample holder and microwave generators.
- In chapter 4, I will detail the fabrication process in order to realize a single molecular magnet transistor. The nanofabrication processes as well as the molecular deposition and the electromigration technique will be presented. I will mainly focus on the sample I have been measuring to prove the Grover's algorithm but also on the sample I developed for the next generation of an all electrically and magnetic controlled single nuclear transistor. The final part of this chapter will be devoted to the presentation of the different measurements we usually perform to ensure the realization of a single molecular magnet spin transistor.

- 
- In chapter 5, I shall present the scheme of the direct read-out of a single electronic spin leading to the indirect read-out of a single nuclear spin. This technique enables to record the nuclear spin trajectory giving access to the life time of this single quantum object. The life time of the electronic spin will be also investigated as a function of the magnetic field applied to the system.
  - In chapter 6, I will focus on our ability to control each nuclear spin transition. Rabi, Ramsey and Hahn-echo measurement will be presented using an RF electrical field. A model will be presented to explain our limitation ( $300\mu\text{s}$ ) in the coherence of the system. Finally, to demonstrate that we can fully control the four levels nuclear spin, I will present single and double coherent pump-probe measurements.
  - In chapter 7, the Grover's algorithm will be discussed in details. In a theoretical part we will see that it consists of two quantum gates that have to be implement on a fully coherent controlled system. I will then present the experimental realization of these gates, demonstrating the first implementation of the Grover's algorithm using a single nuclear spin.



# Chapter 2

## TbPc<sub>2</sub> Molecular Magnet

In this chapter, I present the physical properties of the metal-organic complex called bisphthalocyaninato terbium(III), in order to understand how the different interactions induced by its structure and the external environment make this molecule a system of great interest for application in nano-spintronics [73] and quantum information processing [61].

### 2.1 Composition and structure

The terbium double-decker is a lanthanide Single Molecular Magnet (SMM) that derives its name from its resemblance to the double-decker air-plane: an ion trapped in between two phthalocyanine (Pc) ligands. The magnetic moment of the molecule arises from a single terbium ion (Tb<sup>3+</sup>) located in the centre of the molecule. This ion is 8-fold coordinated to

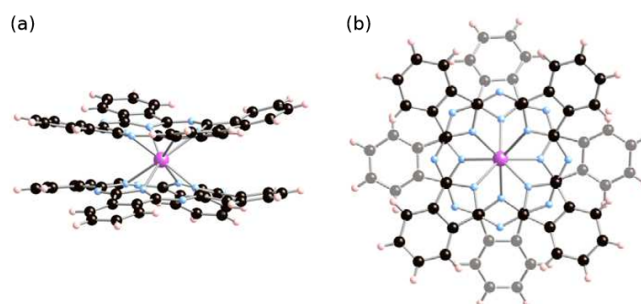


Fig. 2.1 Side view (a) and top view (b) of the TbPc<sub>2</sub>. The pink atom is the Tb<sup>3+</sup> ion, which is 8-fold coordinated to the nitrogen atoms (blue). The black and the white atoms are respectively the carbon and the hydrogen.

the nitrogen atoms that are part of the Pc. Each Pc plan is composed of 8 nitrogen atoms and 32 carbon atoms. The two Pc ligands are structurally rotated from each other by an angle  $45^\circ \pm 2^\circ$  so that in a first approximation the symmetry in the vicinity of the Tb<sup>3+</sup> ion is C<sub>4</sub>. We will see in the section 2.3.3 that this angle is crucial for the Tb<sup>3+</sup> electronic spin properties. The fact that the ligands encapsulate the Tb<sup>3+</sup> is of great interest to conserve both the structural integrity as well as the magnetic properties even when sublimated at 820 K on a copper surface [74].

## 2.2 Tb<sup>3+</sup> ion

Naturally attained <sup>159</sup>Tb is one of the 22 elements with only one natural abundant isotope. With an atomic number of 65, it is situated within the lanthanide series in the periodic table of elements. The electronic structure of Tb is [Xe]4f<sup>9</sup>6s<sup>2</sup>. The 4f shell is not completely filled and is responsible for its paramagnetism. It is located inside the 6s, 5s, and 5p shell and therefore well protected from the environment. Like most of the lanthanides, Tb releases three electrons to form chemical bonds. These three electrons consist of two 6s electrons, which are on the outer most shell and therefore easy to remove, and one 4f electron. 4f electrons are most of the time inside the 5s and 5p shell, but they cannot come very close to the core neither, resulting in a smaller ionization energy than for 5s and 5p electrons. Thus, the electronic structure of the Tb<sup>3+</sup> is [Xe]4f<sup>8</sup>. The nucleus is stable and composed of 65 protons and 94 neutrons resulting in a nuclear spin I= 3/2.

The energetic position of the different orbits and levels of the terbium ion is affected by several interactions, namely, the electron-electron interaction  $H_{ee}$ , the spin orbit coupling  $H_{so}$ , the ligand field potential  $H_{lf}$ , the exchange interaction  $H_{ex}$  and the hyperfine-coupling  $H_{hf}$ . Moreover, the properties of the SMM will be affected by external fields: the magnetic field will directly play on the electronic spin energy when the electric field will tune the hyperfine coupling. We will investigate these different interactions in the following part.

## 2.3 Internal interaction

We investigate the effect of the different interactions in the TbPc<sub>2</sub>. The summary of the different energy scale involved in Tab. 2.1, shows that the intensity of these interactions cover 4 orders of magnitude. I will present them from the most to the less intense.

Interaction	Typical energy		
Electron-electron	30 THz	1500 K	120 meV
Spin-orbit	3 THz	150 K	12 meV
Ligand-field	300 GHz	15 K	1.2 meV
Exchange	30 Ghz	1.5 K	120 $\mu$ eV
Hyperfine	3 GHz	150 mK	12 $\mu$ eV

Table 2.1 Energy scale of the different internal interactions involved in the  $\text{Tb}^{3+}$ .

### 2.3.1 Electron-electron

The electron-electron interaction is the strongest of all interactions and is mainly responsible for the orbital energies and the shell filling. The latter is well explained by the three Hund's rules:

1. The first rules can be understood in terms of Coulomb repulsion: electrons with the same spin have to be in different orbitals due to the Pauli principle. Since they are in different orbitals, they are in average further apart from each other, resulting in a reduced Coulomb repulsion. *The electrons within a shell are arranged such that their total spin  $S$  is maximized.*
2. The second rule also originates from the Coulomb repulsion. Electrons with similar angular momentum are revolving more synchronous and avoiding each other therefore more effectively. *For a given spin, the electrons are arranged within the shell such that their total angular momentum  $L$  is maximized.*
3. The third rules arises from minimizing the spin-orbit coupling energy and cannot be explained easily with hand-waving arguments. *For less than half-filled sub-shells the total angular momentum  $J = |L - S|$ , whereas for more than half-filled sub-shells the total angular momentum  $J = |L + S|$ .*

In order to fill up the 4f shell of  $\text{Tb}^{3+}$  we start with rule number one by putting seven electrons with spin up in the seven different orbitals and therefore maximize the spin  $S$ . The last electron is put in the  $m_l = 3$  state according to the second rule. This already results in the final shell filling with a total spin  $S = 7 \times 1/2 - 1/2 = 3$  and an angular momentum  $L = 3 + 2 + 1 + 0 - 1 - 2 - 3 + 3 = 3$ .

$$\begin{array}{ccccccc}
m_l = & 3 & 2 & 1 & 0 & -1 & -2 & -3 \\
& \boxed{\uparrow\downarrow} & \boxed{\uparrow} & \boxed{\uparrow} & \boxed{\uparrow} & \boxed{\uparrow} & \boxed{\uparrow} & \boxed{\uparrow} \\
m_s = & +\frac{1}{2}-\frac{1}{2} & +\frac{1}{2} & +\frac{1}{2} & +\frac{1}{2} & +\frac{1}{2} & +\frac{1}{2} & +\frac{1}{2}
\end{array}$$

Fig. 2.2 Electronic configuration of the 4f shell resulting from the Hund's rules  $L = S = 3$ .

### 2.3.2 Spin-orbit

The spin-orbit interaction is the coupling of the electron's spin  $\mathbf{s}$  with its orbital motion about the nucleus. In the semi-classical picture, owing to its orbital motion, the electron experiences in its frame a magnetic field  $\mathbf{B}_1 \propto \mathbf{l}$  proportional to the electric field of the nucleus and the orbital moment  $\mu_l = \mu_B \mathbf{l}$  of the electron associated with its intrinsic spin. Applying the correspondence principle leads to the spin-orbit Hamiltonian  $H_{so} = \zeta l s$ , where  $\zeta$  is the one-electron spin-orbit coupling parameter.

Since  $\text{Tb}^{3+}$  has eight electrons in the 4f shell we have to consider more than just one spin and orbital momentum. If, however, the coupling between different orbital momenta  $H_{l_i-l_j} = a_{ij} l_i l_j$  and the different spins  $H_{s_i-s_j} = b_{ij} s_i s_j$  is large compared to the spin-orbit coupling  $H_{l_i s_i}$ , the momenta themselves couple first to form a total spin  $S = \sum_i s_i$  and a total orbital momentum  $L = \sum_i l_i$ , then these couple to yield the total momentum  $J = L + S$ . The Hamiltonian then simplifies to:

$$H_{so} = \lambda(r) \mathbf{L} \mathbf{S} \quad (2.1)$$

This Hamiltonian lifts the degeneracy of  $|\mathbf{L} \mathbf{M}_S\rangle$  spectral terms into multiplets  $|\mathbf{L} \mathbf{S} \mathbf{J} \mathbf{M}_J\rangle$  with  $|\mathbf{L} - \mathbf{S}| \leq \mathbf{J} \leq \mathbf{L} + \mathbf{S}$ . According to the sign of  $\lambda$  the ground multiplet is either  $|\mathbf{L} - \mathbf{S}|$  of  $\mathbf{L} + \mathbf{S}$  (3<sup>rd</sup> Hund's rules). In case of  $\text{Tb}^{3+}$  the ground multiplet is  $(\mathbf{L} = 3, \mathbf{S} = 3, \mathbf{J} = \mathbf{L} + \mathbf{S} = 6)$  which is  $2J + 1 = 13$  times degenerate. Since the spin-orbit contribution to the electron energy is small with respect to the electron-electron interaction, first-order perturbation theory can be applied. The calculation detailed in [75] gives the final expression of the spin-orbit Hamiltonian:

$$H_{so} = \zeta [L_z S_z + \frac{1}{2}(L_+ S_- + L_- S_+)] \quad (2.2)$$

Calculation of  $\zeta$  gives  $\zeta = -336K$  and diagonalizing the Hamiltonian results in the eigenvalues as shown in figure 2.3. The calculated eigenvalues and the experimentally obtained ones [76] fit very well except for  $J=6$ , where higher order perturbation theory is necessary. The important information here is the observation of a large energy splitting between the new ground state  $J=6$  and the new first excited state  $J=5$  of 2900 K [77]. Due to this large gap in energy, one can simplify the calculation of the magnetic properties by only considering the

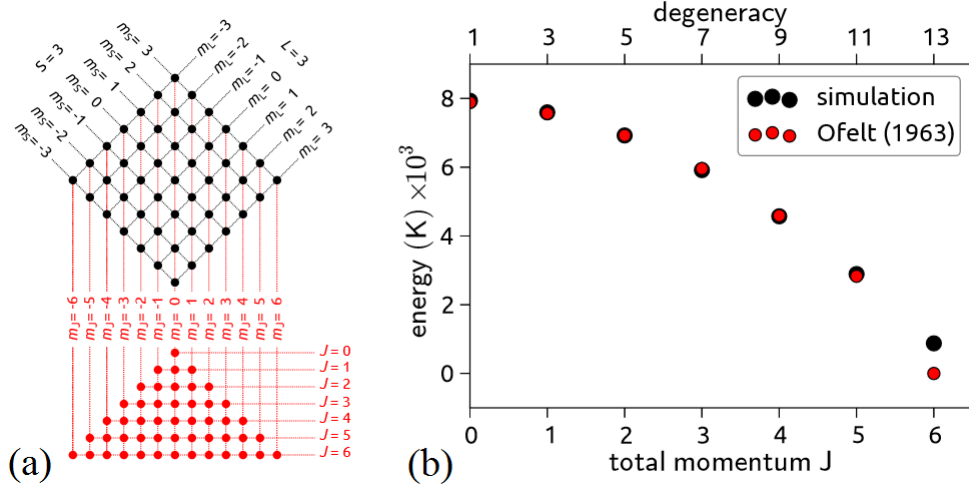


Fig. 2.3 (a) Due to spin orbit coupling, the total spin  $S$  couples to the total orbital momentum  $L$ , resulting in a total momentum  $J = L + S$  with  $(2S + 1)(2L + 1)$  states. (b) Calculated and measured eigenvalues with  $\zeta = -336K$ . The simulated values were shifted vertically to coincide with the values taken from [76]. The spin-orbit coupling lifts the degeneracy of the 49 states resulting in seven different multiplets with  $J = 6$  as a new ground state.

13 ground states. The large splitting between the ground state and the first excited state is a general property of rare earth ions and increases with the atomic number [78].

### 2.3.3 Ligand field

The ligand-field theory describes the electrostatic interaction between the coordination centre of a complex and its ligands, leading to a modification of the electronic states of the former. Since the 4f shell of the lanthanide is situated inside the 5s and 5p shell, it is to a large part protected from its surrounding environment. However, the effect on the energy levels is still of the order of a few hundred Kelvin and acts as a perturbation on the spin-orbit coupling. The calculation detailed in [75] starts from the general expression of the electrostatic potential created by the ligand and introduces Stevens operators to finally gives the expression of the ligand-field Hamiltonian:

$$H_{lf} = \sum_{k=0}^{\infty} \sum_{q=-k}^k A_k^q \langle r^k \rangle u_k O_k^q \quad (2.3)$$

The Stevens operators  $O_k^q$  are linear combinations of the total angular momentum operators and are detailed in appendix A. The symmetry of the  $O_k^q$  is identical to the spherical harmonics  $Y_k^q$ , where  $k - q$  is the number of nodes in the polar direction and  $q$  the number of

$u_2$	$u_4$	$u_6$			
$\frac{-1}{99}$	$\frac{2}{16335}$	$\frac{-1}{891891}$			
$A_2^0 \langle r^2 \rangle$	$A_4^0 \langle r^4 \rangle$	$A_4^4 \langle r^4 \rangle$	$A_6^0 \langle r^6 \rangle$	$A_6^4 \langle r^6 \rangle$	
595.7K	-328.1K	14.4K	47.5K	0K	

Table 2.2 The Stevens factors and the ligand-field parameters for TbPc<sub>2</sub> [80] [81].

nodes in the azimuthal direction with  $-k \leq q \leq k$ . The matrices for  $q = 0$  have only diagonal elements, whereas for  $q \neq 0$  off-diagonal elements occur, introducing a coupling between different states of the ground multiplet. The term  $O_0^0$  has spherical symmetry and gives rise to a constant potential which can be omitted.

Now we turn to the case of TbPc<sub>2</sub>. Since all f-electron states are parity odd, only even  $k$  values are allowed. The value of  $k$  are limited to 6 since matrix elements of  $Y_k^q$  between electron states are orbital quantum numbers  $l$  and  $l'$  are non zero solely for  $|l - l'| \leq k \leq l + l'$ . In our case,  $l = l' = 3$ , we can limit the allowed  $k$  values to 2, 4, and 6. Furthermore, due to the local approximate  $C_4$  symmetry of TbPc<sub>2</sub> the only remaining  $q$  values are  $q = 0, 4$ . With these considerations the ligand field Hamiltonian of the TbPc<sub>2</sub> becomes:

$$\begin{aligned}
 H_{lf}^{TbPc_2} = & \langle r^2 \rangle u_2 A_2^0 O_2^0 \\
 & + \langle r^4 \rangle u_4 (A_4^0 O_4^0 + A_4^4 O_4^4) \\
 & + \langle r^6 \rangle u_6 (A_6^0 O_6^0 + A_6^4 O_6^4)
 \end{aligned} \tag{2.4}$$

The set of ligand-field parameters that reproduces both the NMR and the magnetic susceptibility experimental data [79] is presented in Table 2.2.

The operators  $O_k^0$  contains the operator  $J_z$  up to the power of  $k$  and introduces a strong uniaxial anisotropy in the  $z$ -direction. As a result, the degeneracy between  $|J, m_j\rangle$  and  $|J, m_{j\pm n}\rangle$  is lifted, whereas due to the even powers of  $J_z$  the  $|J, m_j\rangle$  and  $|J, -m_j\rangle$  states remains degenerate. The ligand field induces an energy gap of a few hundred Kelvin between the ground state  $|6, \pm 6\rangle$  and the first excited state  $|6, \pm 5\rangle$ . Therefore, already at liquid nitrogen temperature, the magnetic properties of this complex are almost exclusively determined by the new ground state doublet  $|6, \pm 6\rangle$ . If we replace the terbium ion by another rare earth ion like Dy<sup>3+</sup>, Ho<sup>3+</sup>, Er<sup>3+</sup>, Tm<sup>3+</sup>, or Yb<sup>3+</sup>, this energy gap decreases depending on the ion under investigation (figure 2.5).

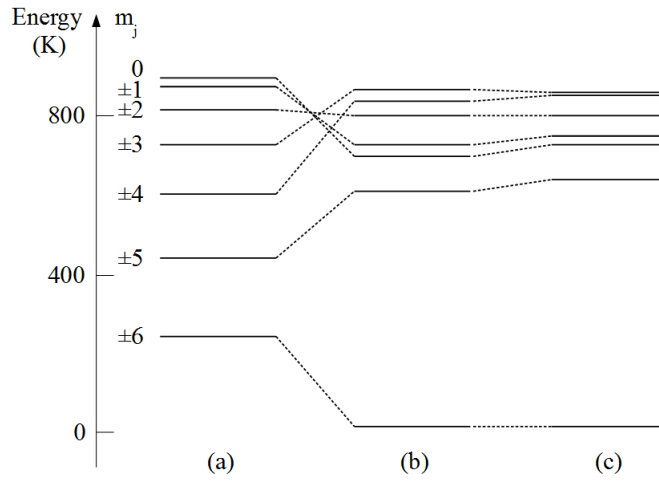


Fig. 2.4 Energy evolution of the  $|J = 6, m_j\rangle$  states as the function of the  $k$  term in the ligand field Hamiltonian, (a)  $k=2$ , (b)  $k=2, 4$  and (c)  $k=2, 4, 6$ . The energy is set to zero for  $|6, \pm 6\rangle$  with the full Hamiltonian.

The off-diagonal terms  $O_4^4$  and  $O_6^4$  emerge from the slight misalignment between the two phthalocyanine ligands, which are not exactly rotated by 45 degrees (section 2.1). The term  $O_4^4$  contains the operators  $J_4^+$  and  $J_4^-$ , which mixes the ground state doublet and lift their degeneracy by  $\Delta \simeq 1\mu K$ . This so-called avoided level crossing gives rise to quantum tunnelling of the magnetization, which will be developed in section 5.1.

### 2.3.4 Hyperfine

As explained in section 2.2, the nucleus of the terbium ion possesses an inherent angular momentum  $I = 3/2$ , resulting in an additional magnetic dipole moment:

$$\mu_I = g_I \mu_N \mathbf{I} \quad (2.5)$$

with  $g_I = 1.352$  the Landé factor of the nucleus [82] and  $\mu_N$  the nuclear magneton. This magnetic moment interacts *via* dipole coupling with the magnetic moment  $\mu_J$  created by the total angular momentum  $J$ . The Hamiltonian accounting for this interaction is formulated as:

$$H_{hf-dip} = A \mathbf{I} \mathbf{J} \quad (2.6)$$

$$= A \left[ \mathbf{I}_z \mathbf{J}_z + \frac{1}{2} (\mathbf{I}_+ \mathbf{J}_- + \mathbf{I}_- \mathbf{J}_+) \right] \quad (2.7)$$

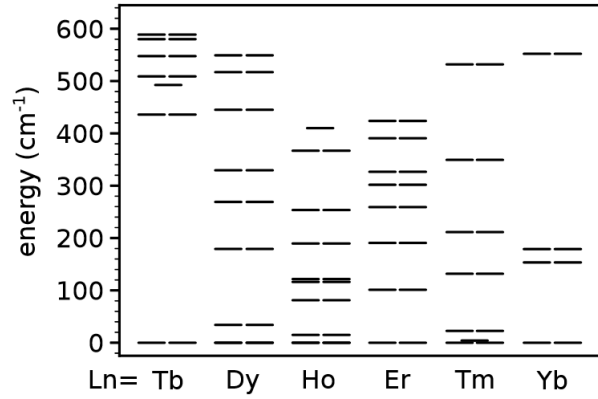


Fig. 2.5  $|6, m_j\rangle$  energy depending on the lanthanide of the molecule.

with  $A$  being the hyperfine constant. To second order, the nuclear spin possesses an electric quadrupole moment which makes it sensitive to electric field inhomogeneities, such as produced by the electrons in the 4f orbitals. The Hamiltonian which accounts for this interaction can be written as:

$$H_{hf-quad} = P (\mathbf{I}\mathbf{J})^2 \quad (2.8)$$

$$= P \left[ I_z J_z + \frac{1}{2} (I_+ J_- + I_- J_+) \right]^2 \quad (2.9)$$

with  $P$  being the hyperfine quadrupole constant. Neglecting the higher terms contribution, the hyperfine Hamiltonian is now simply the sum of the magnetic dipole interaction and the electric quadrupole contribution.

$$H_{hf} = A \mathbf{I}\mathbf{J} + P (\mathbf{I}\mathbf{J})^2 \quad (2.10)$$

For the terbium ion, the two parameters  $A$  and  $P$  have been determined on an assembly *via*  $\mu$ -SQUID measurements [81] and at the single molecular magnet level as presented in Sect. 6. These two results are presented in Tab. 2.3. Due to the hyperfine interaction each electronic ground state is split into four. The splitting of the electronic levels are unequal due to the quadrupole contribution of the hyperfine interaction and calculated as 2.448 GHz, 3.129 GHz and 3.811 GHz as depicted in section 2.6.

From these two independent measurements, on an assembly and on a single TbPc<sub>2</sub>, we can draw these two conclusions:

	A	P
Assembly (Micro-SQUID)	24.5 mK	14.4 mK
Single (SMMT)	25.03 mK	16.35 mK

Table 2.3 Magnetic dipole and electric quadrupole hyperfine constant for the terbium ion according to [81] ( $\mu$ -SQUID) and to Sect. 6 (SMMT).

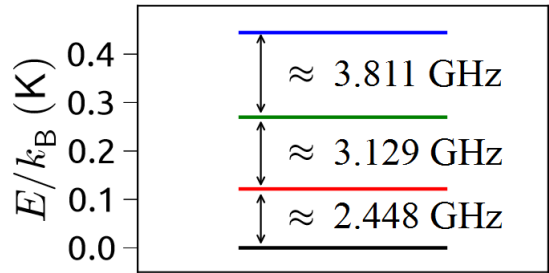


Fig. 2.6 Energy spacing between the 4 nuclear spin states.

- values of A and P are comparable ( $\pm 6\%$ ), showing that these hyperfine constants are robust.
- The value of the quadrupole term is large, resulting in a strong anharmonicity of these three different nuclear spin resonances, which is of great interest for quantum information processing as we will see in section 6.

## 2.4 External field interaction

All the internal interaction being presented, we will see how the energy of the different quantum states depend on the external fields we can apply. External magnetic fields are generated using a home-made 3D-vector magnet (Sect. 3.4). The maximum magnitude is of the order of 2T in each direction. The electric field is applied *via* the local back gate of the sample or *via* the source and drain electrodes and its typical intensity is  $1V/nm$  for the back gate (inducing DC Stark effect, section 6.4.2) and  $1mV/nm$  for the source and drain (inducing AC Stark effect, section 6.4.2). The energies obtained with these intensities are given in Tab. 2.4 and have to be compared with the values of the internal interaction of Tab. 2.1.

Interaction	Typical Energy		
Zeeman at 1 T	15 GHz	700 mK	60 $\mu$ eV
DC Stark 1 V.nm <sup>-1</sup>	1 MHz	50 $\mu$ K	4 neV
AC Stark 1 mV.nm <sup>-1</sup>	300 kHz	12 $\mu$ K	1 neV

Table 2.4 Energy scale of the different external interactions involved in the Tb<sup>3+</sup>.

### 2.4.1 Magnetic: Zeeman

From classical mechanics it is known that a magnetic moment  $\boldsymbol{\mu}$  exposed to an external magnetic field  $\mathbf{B}$  will change its potential energy by  $E_{pot} = -\boldsymbol{\mu}\mathbf{B}$ . The quantum mechanical equivalent is called the Zeeman effect. To calculate the Zeeman energy we write down the Hamiltonian:

$$H_{Zee} = g\mu_B\mathbf{J}\mathbf{B} \quad (2.11)$$

where  $g$  is the Landé factor,  $\mu_B = e\hbar/2m_e$  the Bohr magneton, and  $\mathbf{J} = \mathbf{L} + \mathbf{S}$  the total angular momentum of the system. In the case of a free electron with  $\mathbf{J} = \mathbf{S}$  and  $\mathbf{B} = (0, 0, B_z)$ , the Zeeman Hamiltonian becomes:

$$H_{Zee} = g\mu_B S_z B_z \quad (2.12)$$

with  $S_z$  being the Pauli matrix. Diagonalizing this Hamiltonian at different magnetic fields results in figure 2.7 (a), which is referred to as the Zeeman diagram. The important information here is that the spin degeneracy is lifted at  $\mathbf{B} \neq \mathbf{0}$ .

As explained in section 2.3, in the case of the terbium double-decker, the electron are no more free but subject to internal interaction. Because of the electronic configuration and the large spin-orbit coupling, the Zeeman diagram is obtained by diagonalizing  $H_{full}$  in the  $|J = 6, m_j\rangle$  basis:

$$H_{full} = H_{lf} + H_{hf} + H_{Zee} \quad (2.13)$$

The result of this diagonalization for different magnetic fields parallel to the quantification axes is presented in figure 2.7 (b).

As the nuclear spin magnetic momentum is much lower than the electronic one ( $\mu_N \approx \mu_B/1836$ ), the energy difference in between the nuclear spin state for a given electronic state is nearly constant ( $\approx 1$  mK for 1T) as shown in figure 2.7 (c).

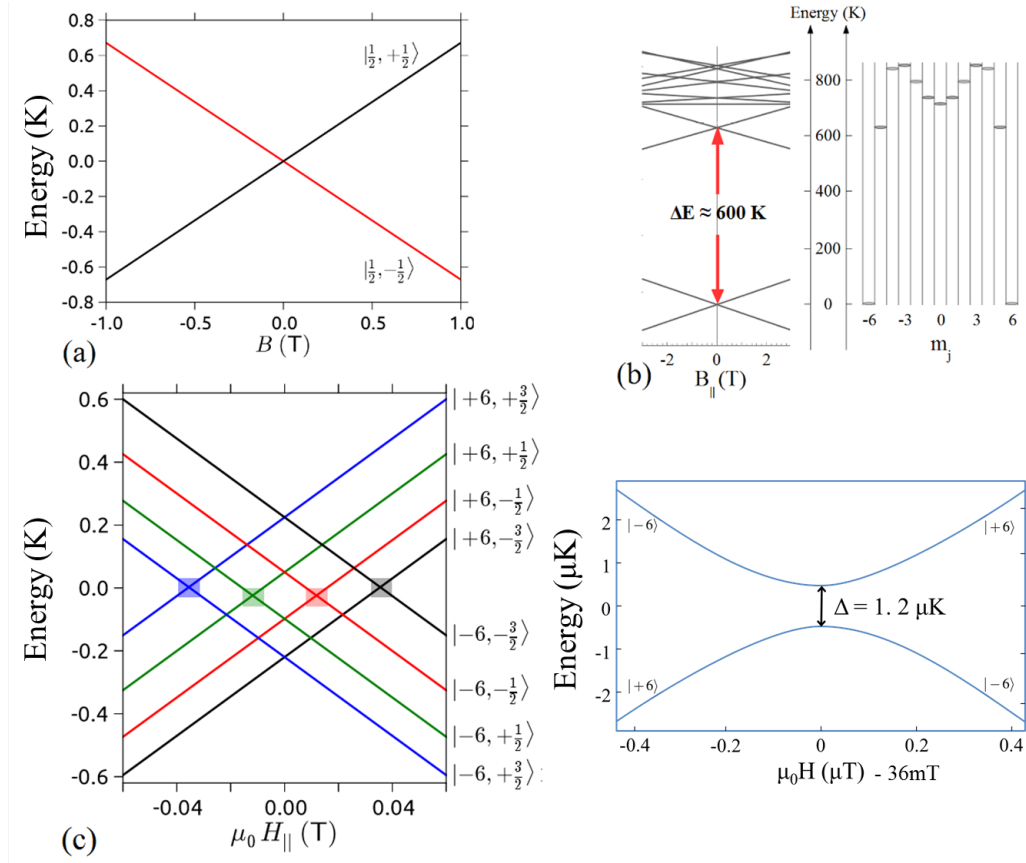


Fig. 2.7 Zeeman diagram for a free electron (a) and for the  $|6, m_j\rangle$  states of the  $\text{TbPc}_2$  (b). We clearly observe the large energy gap in between  $|6, \pm 6\rangle$  and  $|6, \pm 5\rangle$  states leading to an Ising spin model at cryogenic temperature. (c) Zeeman diagram for the lower electronic states  $|J=6, m_j = \pm 6, n\rangle$ . (d): Zoom on the blue square of (c), due to the off-diagonal term in the ligand field Hamiltonian, for a given nuclear spin state, the wave-function is slightly mixed leading to an anti-crossing  $\Delta = 1.2 \mu\text{K}$ .

### 2.4.2 Electric: Stark

The Stark effect is the electric analogue to the Zeeman effect, a particle carrying an electric dipole moment will change its potential energy by  $E_{pot} = -\boldsymbol{\mu}_e \mathbf{E}$ . To calculate the Stark energy we write down the Hamiltonian:

$$H_{St} = -\boldsymbol{\mu}_e \mathbf{E} \quad (2.14)$$

For the molecular magnet, this interaction will mainly impact the hyperfine coupling constant  $A$ . Even if this effect will be presented in details in section 6, I would like here to briefly introduce the different steps we have to take into account to derive the influence of  $\mathbf{E}$  on  $A$ . First, from the isolated  $\text{Tb}^{3+}$  ion, we consider the effect of the ligand field as a perturbation on the electronic configuration. Then, the Stark effect is treated as a perturbation on the ligand field ground states. Thus, an expression connecting the mixing of the ground states wave-function with  $\mathbf{E}$  can be obtained. Afterwards, we evaluate the hyperfine interaction with the mixed ground states. Finally, we derive the expression correlating the electric field  $\mathbf{E}$  with the change of the hyperfine constant  $A$ . This effect have two different outcomes depending on the frequency domain we investigate:

- the DC Stark effect tunes the resonance.
- The AC Stark effect drives the resonance.

# Chapter 3

## Experimental setup

During my Ph.D. I often asked myself: what "difficult" means in experimental physics? Many answers are possible, but one is: "working at the limits of your experimental setup". All the results presented in sections 5, 6 and 7 were obtained thanks to experimental techniques mainly developed by Eric Eyraud and Wolfgang Wernsdorfer for the dilution refrigerator part (section 3.1), Christophe Lepoittevin and Franck Balestro for the DC measurement circuit (section 3.3), Christophe Hoarau, Stefan Thiele and I for the microwave generation (section 3.5), Stefan Thiele and Yves Deschanel for the 3D vector magnet (section 3.4) and Didier Dufeu, Julien Jarreau, Stefan Thiele, Wolfgang Wernsdorfer and I for the sample holder (section 3.2). Thanks to this coordinated work, we managed to keep at 40mK a single molecular magnet transistor during more than 4 years, performing transport measurements and applying DC and AC fields with a great stability. I worked on four different setups during my Ph.D. I will only focus on the one with which I could acquire the main results I will present in the next chapters. An overview of this experiment is presented in figure 3.1 and I will now develop the main parts starting with the inverse dilution refrigerator.

### 3.1 Inverse dilution refrigerator

To explore the quantum properties of a molecular spin transistor, the effective temperature of the electrons going through the device has to be much lower than the typical energy of the molecular system. As explained in the previous section, the typical energy scale of the different interactions occurring in the system is below 1K. Besides this low working temperature, we need a setup that cools down as fast as possible, for statistic reasons, and provides a spacious low temperature stage. All these constraints make indispensable the use of a home-made Inverse Dilution Refrigerator (IDR) that offers a 20cm stage at 40mK in less than 3 hours with a cooling power of  $200\mu\text{W}$ . The basic working principle of this IDR is

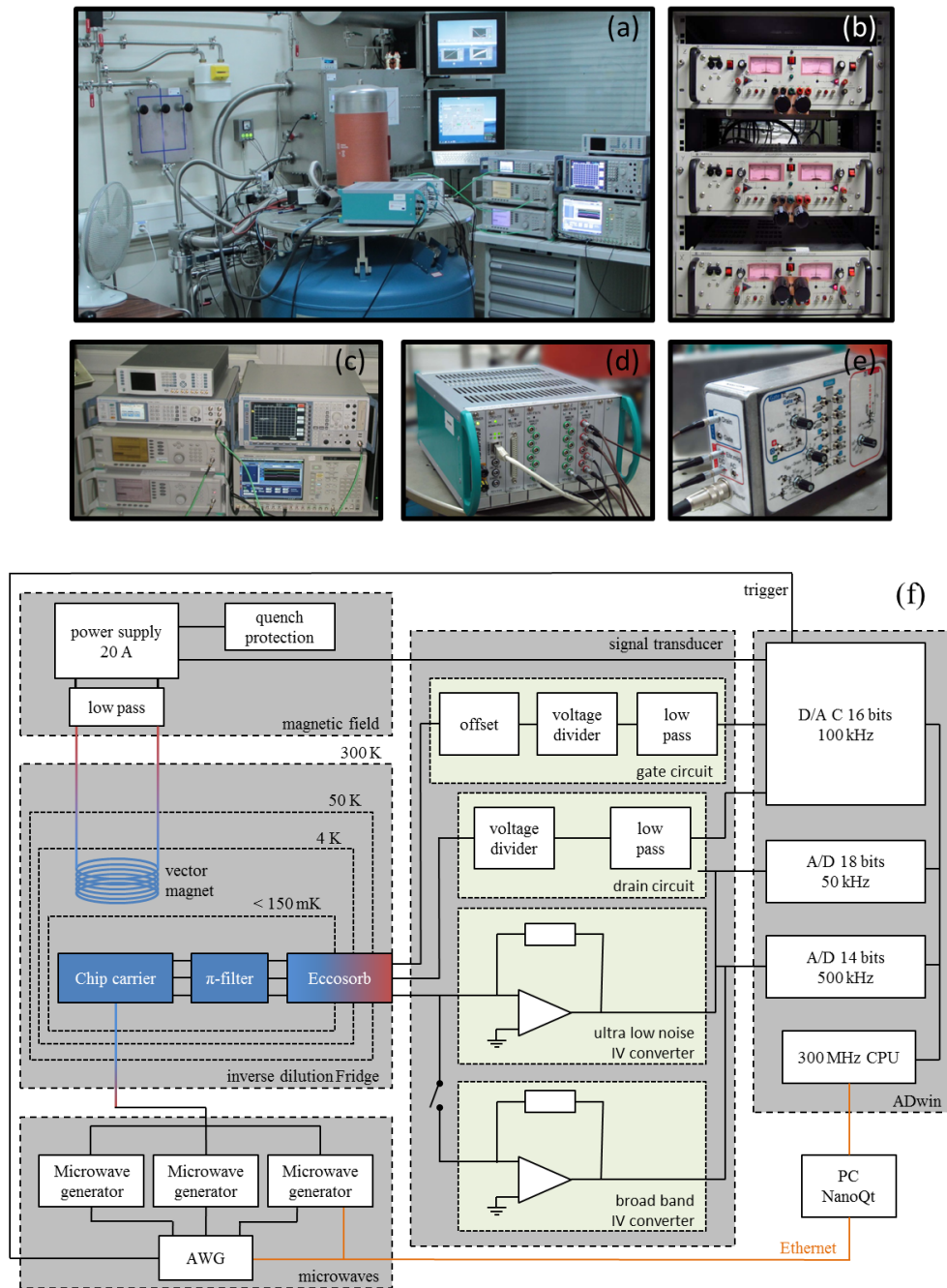


Fig. 3.1 Photographies and schematic of the experimental setup. The inverse dilution refrigerator (a), the power supplies of the vector magnets (b), the microwave generation part (c) the voltage source and measurement Adwin (d) and the signal transducer (e). These different elements are connected as shown in the schematic of the experiment (f).

explained in the following paragraphs.

The IDR consists of six different thermal stages, each encapsulated by another with higher temperature. Vacuum isolates one level from another so that each stage is a radiation shield for the next inner lying. To cool down the IDR, two independent cooling circuits operate simultaneously.

The secondary open cycle cooling circuit replaces the liquid  $^4\text{He}$  bath of conventional cryostat. It operates with liquid  $^4\text{He}$ , which is injected from a dewar underneath the IDR into the so-called 4K box. Since the dewar is slightly over pressured, a sufficiently large  $^4\text{He}$  circulation is established to guarantee a steady state operation. An additional pump inside the circuit is only needed during the cool down from room temperature, since high cooling power and hence high flow rates are necessary. The liquid helium inside the 4K box is used to cool the 4K stage, whereas the vapour created by the boiling liquid  $^4\text{He}$  is ejected into a spiral counter-flow heat-exchanger. While leaving the cryostat, it gradually cools down the primary cooling circuit as well as the 20K and the 100K stages. The 170L dewar providing  $^4\text{He}$  to this secondary open cycle needs approximately to be refilled every nine days.

The primary cooling circuit is a closed cycle, containing a mixture of  $\simeq 20\%$  of  $^3\text{He}$  and  $\simeq 80\%$  of  $^4\text{He}$ . It is subdivided into a fast and slow injection, both entering the IDR *via* the counter-flow heat exchanger. Due to the cooling power extracted from the secondary circuit  $^4\text{He}$  coming from the 4K box, the gas is gradually cooled down to 4.2K. Afterwards, the fast injection is directly thermalized onto the 1K stage and leaves the cryostat *via* the mixing chamber, the discrete exchangers, and the still. It has a larger cross section than the slow injection and is used to have a fast precooling of the colder parts of the cryostat to 4.2K during the cool down from room temperature. The slow injection on the other hand is used for the condensation of the mixture followed by the steady state operation. In order to condense the mixture, an external compressor pressurizes the gas to 4Bar before injecting it into the heat exchanger of the cryostat. Leaving the latter at a temperature of 4.2K, it passes through a second heat exchanger, which is terminated by a flow impedance. The resulting pressure gradient leads to a Joule-Thomson expansion and lowers the temperature of the gas by  $\approx 2\text{K}$  before entering the still. Then, the mixture flows through a set of continuous and discrete heat exchangers before being injected into the mixing chamber.

External primary pump and roots decrease the pressure inside the mixing chamber below 0.1mbar, allowing for another adiabatic expansion, which results in the condensation of the

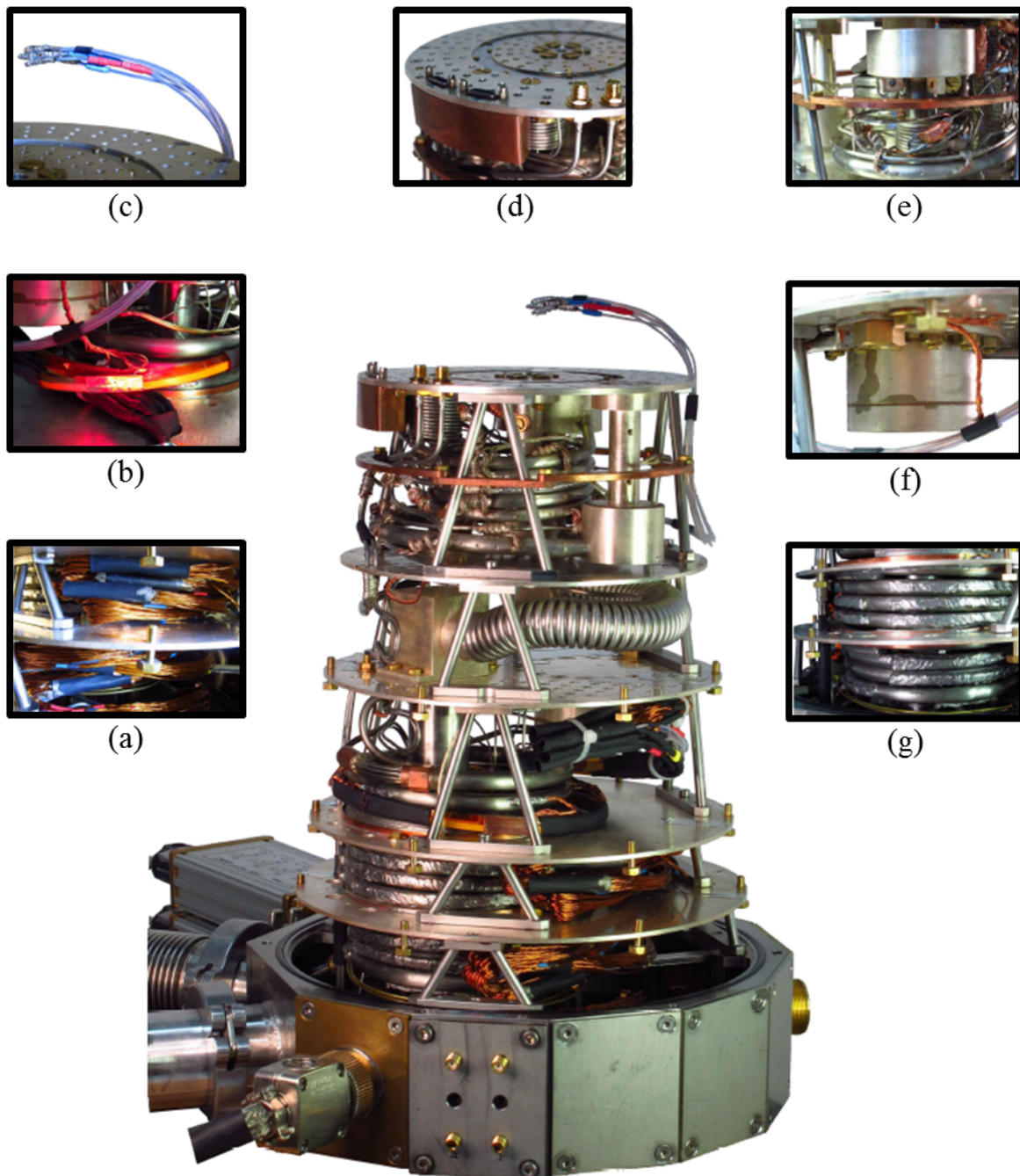


Fig. 3.2 (center) Photography of the fully wired inverse dilution refrigerator. (a-c) Current leads for the superconducting vector magnet consisting of copper (a), high temperature superconducting (b), and low temperature superconducting cables (c). (d) Cold stage showing the DC and microwave connectors. The sample holder (not shown) is situated in the centre of the cold stage. (e-g) Important parts of the primary and secondary cooling circuit showing the still (e), the 4K box (f), and the counter flow heat exchanger (g) [75].

mixture. The cold gas evaporating from the liquid is pumped out through the numerous heat-exchangers to cool down the incoming mixture. Hence, more and more gas condenses, gradually filling up every part from the mixing chamber to the still with liquid. At a temperature of  $\simeq 800\text{mK}$ , a phase separation into a lighter  $^3\text{He}$  rich phase and heavier  $^3\text{He}$  dilute phase takes place inside the mixing chamber. The diluted phase expands from the bottom of the mixing chamber to the still. It contains mainly super-fluid  $^4\text{He}$ , which can be viewed as inert and noninteracting with the  $^3\text{He}$ . Nevertheless, the vapour inside the still contains, despite the high concentration of  $^4\text{He}$ , 97% of  $^3\text{He}$  due to its low boiling point. By pumping on the still and re-injecting the gas in the  $^3\text{He}$  rich phase, a  $^3\text{He}$  circulation is established. In order to maintain the equilibrium concentration,  $^3\text{He}$  from the rich phase is pushed into the diluted phase. This is an endothermic process, providing the cooling power to cool down to mK temperatures. This process can also be viewed as an evaporation of liquid  $^3\text{He}$  from the rich into the diluted phase since the  $^4\text{He}$ , which requires heat and continues even to the lowest temperatures since the concentration of  $^3\text{He}$  in the diluted phase remains finite. The base temperature of the cryostat is only determined by residual heat leaks and remains usually lower than 20mK for most of the IDRs.

## 3.2 Sample Holder

The sample holder is the link between the sample and the cryostat. As presented in figure 3.3 (a), it consists of three parts:

- the chip carrier that has to be removable to glue and microbound the sample.
- The connectors in order to plug in the chip carrier
- The radiative shield that covers the chip carrier.

Here I will describe in the following the sample holder I designed during my Ph.D. It is inspired from the one used in the setup of Stefan Thiele [75]. This new chip carrier was designed to have:

- twenty-four DC lines: they are connected to the DC measurement lines *via* a modified 36 Pin PCI Express connector. We use only 28 pins, 14 of each side of the chip carrier. I chose to keep the PCI Express because it shows a good stability in time even with a lot of cooling cycles all over my Ph.D.
- Three  $50\Omega$  matched broadband waveguides: they are connected *via* 3 SMP connectors mounted in between the 2 PCI express connectors. This clip like connector ensures a

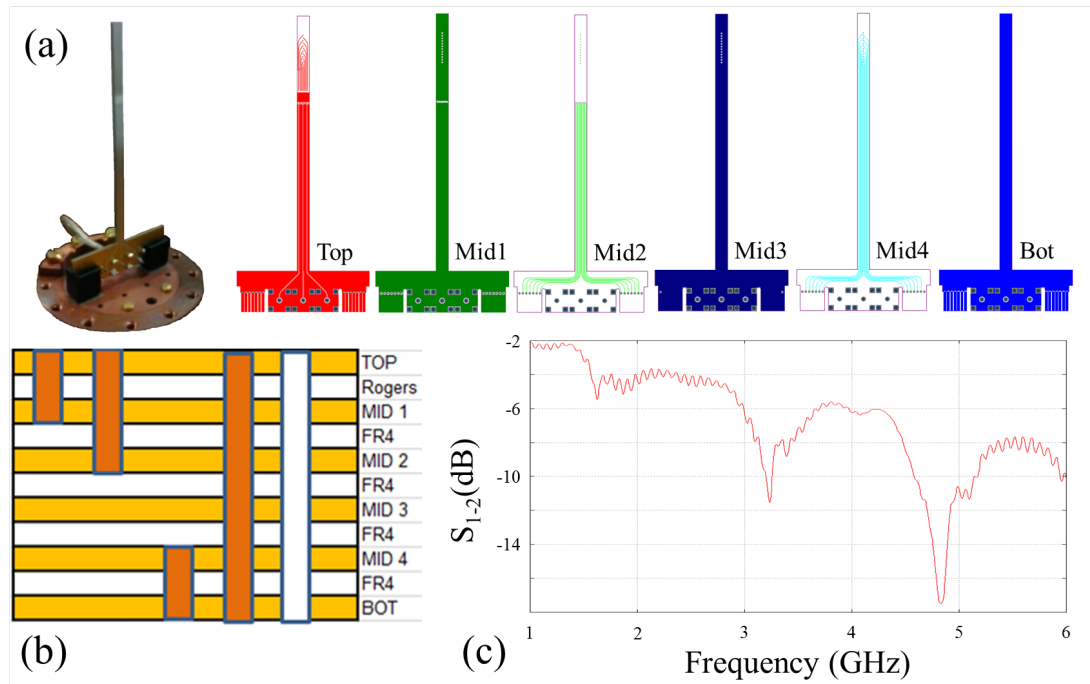


Fig. 3.3 The chip carrier consisting of six independent layers. The top layers contain 3 Microwaves coplanar lines and the others layer provides 24DC lines (a). The different layers are connected as show in the schematic using copper filed LASER drilling represented in orange in (b). The transmission  $s_{1-2}$ , measurement from the two SMA connector of the two external line, shows a minimum of transmission of  $-18dBm$ , this loss mainly comes from the microbonding that connect the two  $50\Omega$  matched lines.

transmission from DC to 26.5GHz and a convenient connection to the sample holder. Finally, 3 SMP-SMA wires are trapped in between the two parts of the radiative shield and make the connection from the SMP chip carrier to the SMA connector of the IDR.

In order to fit with the 3D vector magnet, the width of the chip carrier has to be less than 3.6mm. Moreover, it consists of three coplanar waveguides and twenty four DC lines. To integrate all these lines as close as possible to the sample and thereby minimize aluminium bonding length, we use a multi-layer chip carrier. The top layer is used for the three coplanar waveguides. A  $\epsilon_r = 10.2$  dielectric (Rogers in 3.3 (b)) minimizes the dimension of the lines while maintaining a  $50\Omega$  impedance. 12 DC lines come from the layer MID2 and 12 others *via* the layer MID4. All these lines come out close to the sample on the TOP layer using copper filled LASER drilling. Each layer is isolated from the other using ground layer (MID1, MID2 and MID3) and FR4 dielectric. It results in a 1.4mm thick 3.6mm wide at the top part and 3.9cm wide at the bottom part chip carrier. This latter dimension is the minimum size to adjust 2 PCI express and 3 SMP connectors. The different layers of the

chip carrier are presented in figure 3.3 (a). It can be easily clip to the radiative shield and the mechanical stability is ensured by the PCI connectors. Finally a home-made connector electrically connects the PCI express to the Canon like connectors of the IDR.

## 3.3 DC measurement circuit

One of the funniest thing of my thesis was to "see" and to manipulate quantum properties "only" by performing conductance measurements. Starting from the sample holder, I will then describe the DC measurement circuit to finish with *Adwin*, a real time data acquisition and voltage generator.

### 3.3.1 Filtering

We want to minimize the noise that goes to the sample in order to enhance the lifetime and coherence time but we also want to minimize the noise of the out-coming signal to maximize the visibility of the physical phenomenon. It exists three main noise sources interfering with the experiment:

- the electro-magnetic radiation: it is produced by any wireless communication system (Wifi, mobile phones, television, GPS etc) or by improperly shielded power sources like any switching power supply or transformer. Its typical frequency ranges from few Hz to GHz.
- The Johnson-Nyquist thermal noise: it is the electrical equivalent of Planck's black-body radiation. The noise power in Watts is given by  $P = k_B T \Delta f$ , where  $k_B$  is the Boltzmann constant,  $T$  the temperature and  $\Delta f$  the frequency bandwidth.
- The vibrational noise: produced mainly by pumps and environment. It can be minimized by vibrational low pass filters like concrete or T-shape metal plate. Its typical frequency ranges from Hz to hundreds of Hz.

For the DC measurement, we have to filter the 24 lines coming from the sample holder. Two kinds of filter are used:

- the discrete low temperature  $\Pi$ -filters. They attenuate the remaining electromagnetic noise and should have a negligible series resistance in order to be compatible with the electromigration (see section 4.2). Their cut-off frequency  $f_0$  is around 1MHz at cryogenic temperatures. It ensures enough bandwidth for the electromigration

technique. Since they will be mounted inside the cryostat, their size should of course be as small as possible. Finally a good stability over the cooling cycle is needed. We selected the  $\Pi$ -filter from EMI Inc. with the X7R dielectric.

- The continuous Eccosorb filters from low temperature to 300K. Above 1GHz discrete filters become transparent due to parasitic effects and continuous filters are required. Many different types of high frequency low pass filter exist, the fine-grain metal powder filters, thin coaxial cables, or lithographically fabricated meander lines. Recently, wires surrounded by Eccosorb, which is a microwave absorbing material, were tested under cryogenic conditions [83]. Based on the space-efficiency of this last technique and its filtering properties [75] we chose Eccosorb coated wires as high frequency attenuators. The filter was made out of 24 superconducting wires (to keep a low series resistance) made out of NbTi filaments embedded in a constantan matrix. They were coated with Eccosorb, and enclosed in a CuNi tube of 1.5mm external diameter. The first meter of the tube is gradually thermalized from 300K down to 40mK, while the rest is thermalized to the 40mK stage to attenuate all thermal noise sources.

### 3.3.2 Signal transducer

A way to curtail electromagnetic radiation and vibrations noise is to use short cables and avoid connectors wherever it is possible. Therefore, we wanted to unify the commonly used room temperature switch boxes, amplifiers, voltage dividers, and low pass filters in one signal transducer. The development was done in close collaboration with Daniel Lepoittevin from the electronics service of the Néel Institute. We developed two generations of signal transducer, the one I used during my thesis and the one we improved for the next experiments, resulting from our background.

The signal transducer was designed to be compatible with the standard dilution fridge interface (12 pins Jaeger connector) and the batches of electromigration junctions, which have a common source and gate (see section 4.1). Due to the geometry of the 12 pins Jaeger connector, we ended up with 10 selectable signal injections lines (drains), one signal output line (source), and one gate. To prevent large discharge currents during the installation of the chip carrier in the cryostat, which are caused by a potential difference between the junctions and the dilution fridge, there are switches to select the different drain terminals: ground, 100k $\Omega$  *via* ground or floating. The first two positions are used when connecting the sample to the cryostat, whereas the latter is used during the experiment. The drain and gate lines have additional voltage dividers in order to increase the resolution of the data acquisition unit. In addition, an offset of  $\pm 2.5V$  or  $\pm 5V$  can be superimposed to the divided gate signal in order

to shift the measuring range by keeping the resolution constant. In the second generation of signal transducer, this offset can be tuned with a 0.1V step, giving the possibility of dividing the gate signal at least by a factor 200. To avoid sharp transitions between different offsets or in case of electrical shut-down, a low pass filter with a time constant of 1 s is added to the summing amplifier. Furthermore, all inputs are equipped with low pass filters to reject the incoming noise. Thereby the drain inputs have a cut-off frequency of 500Hz and the gate input a cut-off frequency of 200Hz. The higher value of the drain inputs was needed in order to transmit the lock-in signal, which can be modulated up to a few hundred Hz.

The signal transducer contains two home made I/V convertors. An ultra low input bias current amplifier, that provides four selectable gains  $10^6$  to  $10^9$ , is used for the electrical transport measurements. A second I/V converter is used for electromigration measurement. Its large bandwidth of 75MHz, ensures a fast feed back loop. Its gain is selectable between  $10^2$  or  $10^3$ , which is the optimum range for the electromigration respectively on graphen or on gold junction. A complete characterization of this signal transducer and amplifier are given in [75]. A way to increase these amplification characteristics could be the use of low temperature amplifiers. The IDR has two 12 pins Jaeger connectors allowing to cool down 20 junctions using two transducers (20 drains, 2 sources and 2 gates). A real time acquisition system (Adwin) allows the generation and data acquisition as presented in the following.

### 3.3.3 Real time data acquisition

#### Motivation

The presented real-time data acquisition system allows to generate multiple signals with only one rack, which significantly reduces the number of ground loops and therefore the signal noise compared to a standard setup with multiple generators interfaced in parallel. In addition, one can generate a periodic signal with frequencies in the range of 10Hz to 10kHz. This enables the implementation of a numerical lock-in detection and makes a physical lock-in detector unnecessary. Due to the fast response time of the digital signal processor, one can reduce the measurement time by a factor 1000 compared to a standard setup controlled by a computer platform which is of great interest for the electromigration process. Finally the use of this single data acquisition allows synchronization with a precision of the order of 3ns with the different equipments of the experiment (voltage source, magnetic fields, microwaves pulses), mandatory for our nuclear spin read-out and manipulation protocols.

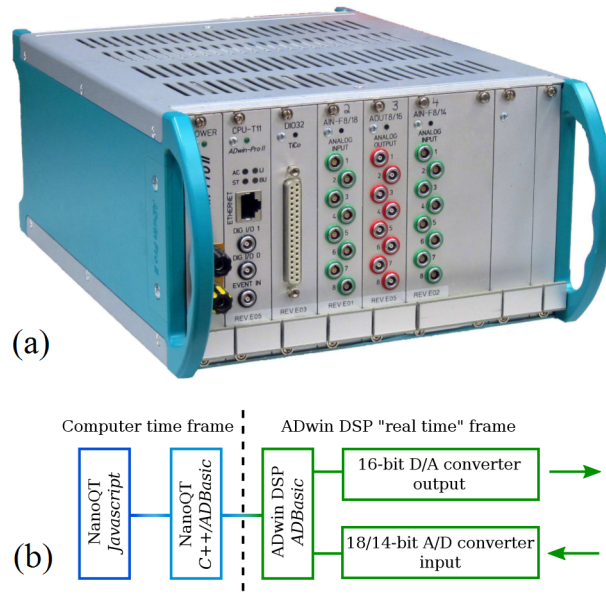


Fig. 3.4 Photography of the ADwin automat showing the front panel with a 18 and 14 bit analog input cards and a 16 bit analog output card (a). Schematic of the real-time data acquisition system (b).

## Presentation

It combines analog and digital inputs and outputs with a dedicated real-time processor and real-time operation system. It has a 16 bits output card with an integrated digital/analog converter. Its voltage range is  $\pm 10$  V resulting in a step size of  $20\text{V}/2^{16} = 305\mu\text{V}$ . The input card has a resolution of 18 bits and an analog/digital converter with readout voltages ranging from  $-10\text{V}$  and  $+10\text{V}$  resulting in a resolution of  $20\text{V}/2^{18} = 75\mu\text{V}$ . An additional 14 bits input card with a clock frequency of 50MHz was added to perform the electromigration using a fast feedback loop. All cards are controlled by a 300MHz digital signal processor, which performs tasks with a precision of 3ns. The response time in the feedback loop of the electromigration is  $1.5\mu\text{s}$  due to the execution of several lines of code. The ADwin is linked to a standard PC *via* an Ethernet connection that ensures datum and orders transmission. It can be programmed using NanoQt, a home-made software working on Linux, developed in our group by E. Bonet, C. Thirion and R. Picquerel. Its user interface is based on the JavaScript language and allows for the execution of user defined scripts. The great stability of this software was essential for the safety of the setup and therefore of the sample.

	x-coil	y-coil	z-coil
$I_{max}$	15 A	14 A	18 A
B at 10 A	0.9 T	0.8 T	1.1 T
$(dB/dt)_{max}$	$\approx 1$ T/s	$\approx 1$ T/s	$\approx 10$ T/s

Table 3.1 Characteristics of the 3 different coils.

## 3.4 Magnetic field generation

### 3D vector magnet

A single-molecule magnet carries a single magnetic moment which is at the heart of a molecular spin transistor. To measure and manipulate this single spin, external magnetic fields in arbitrary directions are needed. A way to create three dimensional fields is the use of three coils mounted in a way that provide magnetic fields perpendicular to each others, like the axes of a coordinate system. The orientation and magnitude of the magnetic field is controlled by adjusting the current through each coil so that the resulting field is the vector sum of the three respective fields.

Conventional state of the art 3D vector magnets consist of a cylindrical coil surrounded by two Helmholtz coils. In our experiment we have more constraints that compel us to develop a new design of 3D vector magnet:

- a well balance maximum field amplitude in each direction.
- A high sweeping rate.
- A compact design well adapted to the IDR but still considering enough space for the sample.
- A low inductance to reduce the Helium consumption.

The design and characteristics of the 3D magnet developed by Stefan Thiele and Yves Deschanel, represented in Table 3.1, result in a compact 3D vector magnet.

### Current leads

The current leads are the electrical link between the superconducting vector magnet and the room temperature connections outside the cryostat. Ideally, the material should be a

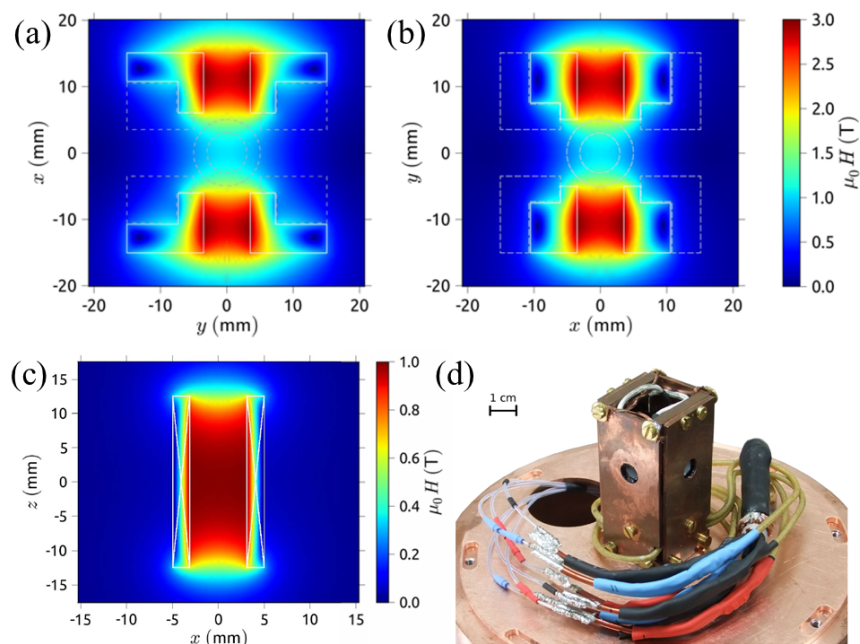


Fig. 3.5 Cross-section of the magnetic field distribution of the x-coil (a), y-coil (b) and x-coil (c). Photography of the fully mounted vector magnet (d).

very good electrical conductor but a very bad thermal conductor. Knowing this, for the low temperature part of the cryostat, *i.e.* at temperatures below 77K, high temperature superconductors were used as current leads. Since superconductors are both perfect electrical conductors and very poor thermal conductors, they represent the material of choice. The high temperature part of the current leads was made of copper wires. Since the resistivity and thermal conductivity of copper varies with temperature, a design study was carried out to determine the optimal geometry. To guarantee a stable operation, an equilibrium between the wire the diameter ( $D$ ), the length ( $L$ ) and the thermalization length ( $T_l$ ) had to be found. Calculations lead to the results presented in Table 3.2.

Finally these current leads are connected to 3 different  $\pm 20A$  current suppliers KEPCO BOP20-20M controlled *via* an input  $\pm 10V$  command generated by the ADwin. The efficiency of each coil was calculated in order to know the input voltage / field scale. For this experiment values are 2T/V, 1.8T/V and 1.6T/V respectively for x, y and z direction.

T ( $^{\circ}K$ )	L (cm)	D ( $mm^2$ )	T <sub>l</sub> (cm)
300 - 200	30	1.5	20
200 - 100	25	0.75	12
> 100	25	0.5	16

Table 3.2 Wire length L, diameter D and thermalization length T<sub>l</sub> for different temperature ranges.

## 3.5 Microwave generation

In chapter 6 and 7, depending on the experiment we want to perform, we will synthesized different microwaves sequences. I will present in the following the different apparatus and circuit used for microwave generation.

### 3.5.1 Equipment

We are not working in the strong coupling regime between our system and the microwave pulse. Indeed, the microwave pulses are generated to the sample through a microbounded antenna close to the device. The IDR transmission line is a coaxial line which external shield is thermalized on each stage *via* copper welding. In addition to the previously presented Adwin DAC (see section 3.3.3), we use microwave equipment to synthesized desired pulses. We can classify them into three different categories:

- **Microwave Source Generator:** I used three different sources. One R&S SMA 100A (from 9kHz to 6 GHz), one Anritsu MG3694A (from 0.1Hz to 40GHz) and one Anritsu MG3692 (from 2GHz to 20GHz) as shown in figure 3.6. These sources generate a monochromatic microwave of tunable frequency  $f$  and amplitude  $A$ . I used an external pulse to switch on (giving the amplitude  $A$ ) and off (giving the amplitude  $A-80dBm$ ) the signal.
- **Arbitrary Wave Generator:** I used two different AWGs. One Tektronix AWG 5014C shown in figure 3.6 (1.2GHz sampling rate, 4 channels) and one Tektronix AWG 7122B (12GHz sampling rate, 2 channels or 1 channel at 24GHz sampling rate). These generators are high frequency digital analog converter that provides a microwave signal from a table of value. They enable a "dot by dot" synthetization of the signal.
- **Microwave transmitter:** I used a Hubersuhner SF104 SMA/SMA cable and home-made capacitive RF dividers to transmit and mix the different microwave signals.

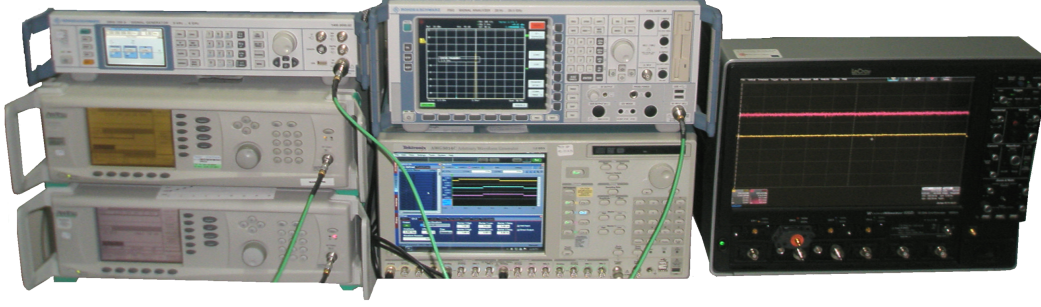


Fig. 3.6 Microwave generation and characterization equipments. On the left from top to down. Three RF sources: R&S SMA 100A (from 9kHz to 6GHz), Anritsu MG3694A (from 0.1Hz to 40GHz) and Anritsu MG3692 (from 2GHz to 20GHz). On the middle a R&S FSQ signal analyser (from 20Hz to 26.5GHz) and a Tektronix AWG 5014C 1.2GHz sampling rate. Finally on the right a Lecroy fast oscilloscope (30Ghz sampling rate).

- Characterization: I used a R&S FSQ signal analyser (from 20Hz to 26.5GHz) and a Lecroy fast oscilloscope (30Ghz sampling rate) to characterize the signals both in the frequency and in the time domain before transmitting them to the sample.

With these equipments, depending on the manipulation I wanted to apply to the nuclear spin, I built up different microwave circuits as presented in figure 3.7.

### 3.5.2 Monochromatic pulse

To manipulate one qubit (only one transition) a single frequency is necessary. To tune the width and the number of pulse trains per sequence, the microwave signal  $S(t)$  must be switched on and off with a precision of the order of 1ns.

$$S(t) = \sum_i H(t - t_i)H(t - t_i - \tau_i)A\sin(\omega t) \quad (3.1)$$

Where  $H$  is the Heaviside function,  $\tau_n$  and  $t_n$  respectively the duration and the starting time of the  $i^{th}$  train. All the trains have the same amplitude  $A$ . To produce this pulse, I use the circuit (a) of figure 3.7. The SMA generator is pulsed modulated by one channel of the AWG 5014. This pulse modulation ensures a power output up to 15dBm in the "on" state and of -80dBm in the "off" state. The resolution of this modulation is of the order of 1ns, which is one order of magnitude below our typical smaller manipulation time. The main limitation comes from the AWG sampling rate that defined one point every 0.83ns. Before the measurement, *via* the Ethernet connexion, NanoQt transmits to the AWG the table of values corresponding to the Heaviside part of equation 3.1 and 3.2. NanoQt also defines the power and the frequency

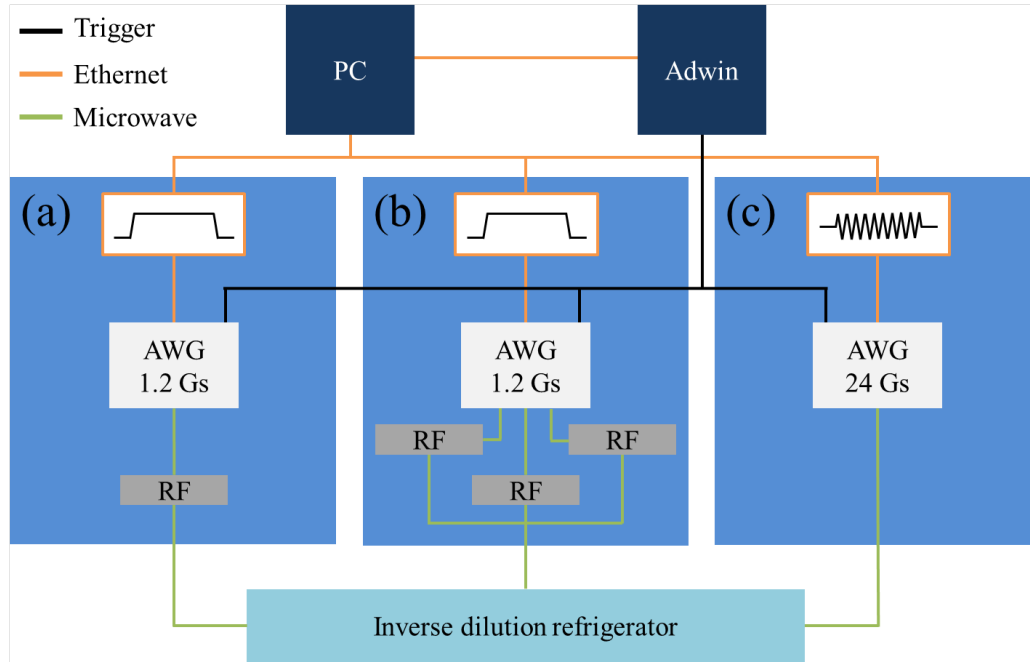


Fig. 3.7 Schematic of the three different configurations used to generate mmicrowave pulse sequences.

to the SMA generator. During the measurement, each time I need to send a pulse, Adwin triggers the AWG with a 2V pulse. This trigger tells to the AWG to generated the previously define waveform to the microwave generator. Finally the output of the SMA generator is directly connected to the IDR microwave line.

### 3.5.3 Constant frequencies multi-chromatic pulse

To manipulate several transitions in a same pulse sequence, pulses of different transitions can be generate simultaneously or at distinct times. Therefore, the width and the number of pulse trains per frequency and per sequence must be tunable with a precision of the order of 1ns.

$$S(t) = \sum_{n,i} H(t - t_{n,i})H(t - t_{n,i} - \tau_{n,i})A_n \sin(\omega_n t) \quad (3.2)$$

$\tau_{n,i}$  and  $t_{n,i}$  being respectively the duration and the starting time of the  $i^{th}$  train of pulsation  $\omega_n$ . Trains of the  $n^{th}$  transition have the same amplitude  $A_n$ . To produce this pulse, I use the circuit (b) of figure 3.7. Each microwave generator is pulsed modulated by one channel of the AWG 5014. As for the previous circuit, this pulse modulation ensures a power output up to 15dBm in the "on" state and of -80dBm in the "off" state and the resolution of this modulation

is of the order of 1ns. Before the measurement, *via* the Ethernet connexion, NanoQt transmits to the AWG the table of value corresponding to the Heaviside part of equation 3.1 and 3.2. The power and the frequency are define manually on the Anritsu. Because of the response time of each microwave generator, the windows offset time will be slightly different (16ns) for the Anritsu and for the R&S channels in order to have 3 synchronize pulses before the injection in the IDR. During the measurement, each time I need to send a pulse, Adwin trigger the AWG using a 2V pulse. This trigger signal starts the AWG waveform generation to the microwave generator. Finally a home made power divider mixes the signal coming from the microwave generator before injecting it in the IDR microwave line. The main advantages of this circuit are the high quality in the frequencies definition coming from the analog generator and the large flexibility of shapes we can synthesized. The main drawback, that forces us to use the second circuit, is the impossibility to change the generator frequency during a same pulse and to control the phase of each frequency pulse components.

### 3.5.4 Multi-chromatic with frequency modulation

We will see in section 7.3.1 that to implement the Grover algorithm we need to generate two pulse trains composed of all the transition frequencies. The only changing parameter between them is a frequency detuning  $\delta_n$  on the  $n^{th}$  transition.

$$S(t) = A \sum_n H(t)H(t - \tau_n^{Had})\sin(\omega_n t) + H(t - \tau_n^{Had})H(t - \tau_n^{Had} - \tau_n^{Gro})\sin([\omega_n + 2\pi\delta_n]t) \quad (3.3)$$

Where  $\tau_n^{Had}$  and  $\tau_n^{Gro}$  are respectively the width of the first and the second pulse train. The amplitude of this pulse sequence is constant and equal to A. Notice that the phase of the second pulse train has to be equal to the one of the first. This circuit ((c) in figure 3.7) is the easiest one because it makes use only of a single channel 24GHz sampling AWG 7122 that directly synthesis the pulse from a numerical definition. Before the measurement, NanoQt calculates the pulse value every 41ps and send this waveform *via* the Ethernet connexion to the AWG. From this numerical waveform, each time NanoQt generates a 2V trigger pulse, the AWG applies this waveform directly in the IDF microwave line. This is the most flexible way to generate microwave signals because you just have to mathematically define your waveform. Nevertheless, one can find two drawbacks. First, because the sampling rate is finite, the quality definition of an harmonic in the frequency domain is lower than an analog microwave source. It was a surprise to see that a coherent manipulation of a nuclear spin

---

was possible at 3.8GHz with this generator. Second point is the power limitation. The maximum amplitude is 1Vpp, corresponding to 4dBm. If you only use one harmonic it is enough but it can start to be a problem if you want to use  $n$  harmonics, resulting in a  $1/n$  Vpp for each harmonic. In my case  $n = 3$  was resulting in a power for each harmonic  $\approx 0$ dBm.



# Chapter 4

## Single molecular magnet transistor

Our nuclear spin detection scheme is based on a low temperature conductance measurement through a molecular magnet. To perform these measurements, one needs at least two terminals contacting the object, one for the source electrode and the other for the drain. When for a macroscopic object, a commercial circuit is good enough to perform a connexion, for much smaller objects one needs to use electrodes that are fabricated by standard lithography techniques. However, to connect a single molecule which typical diameter is about 1nm, even the most advanced electron-beam lithography techniques fail to create gaps at this scale between two electrodes. People have then developed various experimental techniques for wiring up single molecules:

- Scanning Tunnelling Microscope (STM) (figure 4.1 (a)). After a clean deposition of molecules on a conducting surface, a STM can perform transport measurement through a single molecule by probing it [84] [85].
- Mechanical break junction (figure 4.1 (b)). This techniques enables a nanometric precision on the gap size [86]. This is of great interest to tune the coupling in between the electrodes and the molecule.
- Electromigrated break junction. A well controlled current is generated through a nanowire. The electron wind momentum is transferred to the wire's atoms and creates a nano constriction on it. This technique, used during my thesis, is developed in section 4.2. With this method, it is easy to bring close to the molecule a third terminal. This is of great interest because more than contacting a single molecule, we want to control its electromagnetic environment to tune its chemical potential and study different charge states of it.

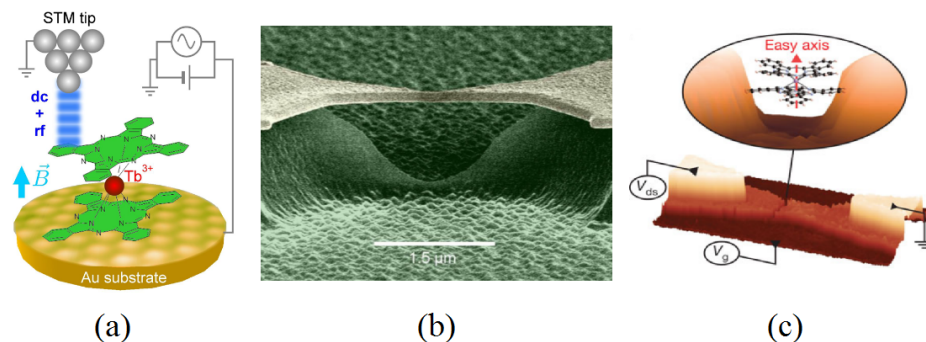


Fig. 4.1 Scanning tunnelling microscope (a) [85], break junction (b) (IRAMIS CEA website) and electromigration (c) are the main techniques to connect a single molecule to the macroscopic world.

In this chapter, we will discuss the device fabrication and the single molecular magnet characterization. First, the nanofabrication procedure for metallic nanowires with local back-gate and microwave line will be described. Then, the electromigration technique which is used to form a nanometer-sized gap in the wire, will be explained. Finally, discussions on the characterization of the single molecular magnet transistor *via* usual quantum transport measurements will be given.

## 4.1 Sample nanofabrication process

To start with the fabrication of a single molecular spin transistor using the electromigration technique, I will first present the nanofabrication process. Two different processes are detailed. First the one developed previously by Nicolas Roch [87] and Romain Vincent [88]. This first generation of sample (type 1 in the following) is at the heart of the experimental results regarding to single nuclear spin manipulation. The second generation (type 2 in the following) includes a microwave line on chip and have been developed in a strong collaboration with Thierry Crozes, from the NanoFab group of the Néel Institute.

### 4.1.1 Type 1 sample

First of all, let us remind ourselves the main component of the sample and the constraints we have

- One metallic wire. The total resistance of this wire has to be minimized except where we want to open the nanogap. At this precise point, the wire dimensions have to be of

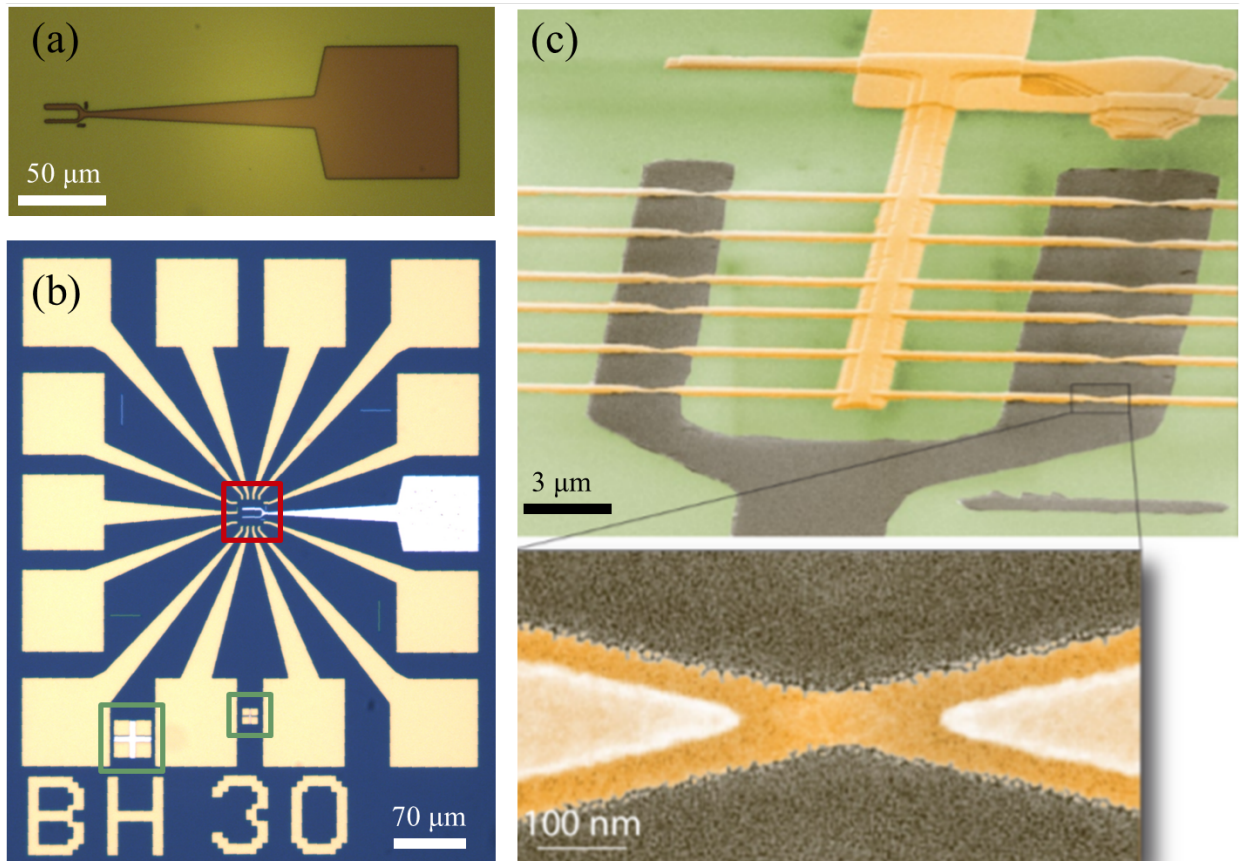


Fig. 4.2 (a) Optical picture of the sample after the first step showing the diapacon like back-gate. (b) Optical picture of the sample after the third step. We clearly see the colour difference in between the gate (white) and the supply line (yellow) due to the 8nm  $\text{HfO}_2$  deposition. One can see the alignment marks in the green square. The cross, deposited during the first step, has to be adjusted in the middle of the four squares to ensure a good alignment. Each chip has an identification number related to its coordinated in the wafer. (c) Colored SEM image of (b) picture red square after the fourth step. Each drain electrode is connected to a common source electrodes resulting in twelve gold-junctions evaporated on the back-gate. A zoom in one of the junction highlights the shadow evaporation results.

the order of 100nm large and 10nm high. The extremity of this wire will be connected to the measurement line using micro-bouding.

- One gate oxide. On one hand, it needs to be located very close to the molecule to produce a large gate capacitance. On the other hand, we want to apply large voltages meaning that we need a high quality insulator and a gate oxide region as small as possible to avoid gate leakage. Here again, the extremity of the gate have to be large enough to be micro-bounded to the sample holder.
- A large statistic. The fact that there is no direct way to control the molecular position implies a random process in the fabrication of the molecular magnet transistor. Hence, during the nano-fabrication process we always maximize the number of junctions per sample and the number of samples we can fabricated during the same nanofabrication step.

To fulfil these main points, we will first evaporate the metallic back gate, isolated it from the nano-wire using atomic layer deposition of  $\text{HfO}_2$ . Finally the nanowires will be evaporated with a given geometry that ensures a nanogap opening point on the top of the back-gate during the electromigration process.

### **Local back gate**

As explained in the introduction, I want to apply an electric field to the molecular magnet in order to tune its chemical potential. A possible way to do so is to fabricate a local gate near the junction. A local back-gate is preferred to top-gate or lateral gate for feasibility and efficiency reasons. A diapason like back-gate was chosen. A deep UV-lithography process is possible because the minimum size of this back gate is  $3\mu\text{m}$ , much higher than the deep UV-lithography resolution limit ( $\approx 1\mu\text{m}$ ). Finally flat-edge are insured using a bi-layer resist.

### 1<sup>st</sup> step process: Local-back-gate

- Take a 2 inch Si/SiO<sub>2</sub> wafer, clean it with a 1min oxygen plasma and warm it 5min at 200°C to remove carbonic dirt and water from the surface.
- First resist deposition: LOR3A spin coat, 30sec at 2000r.min<sup>-1</sup> and 2000r.min<sup>-2</sup> (400nm), anneal 1min at 200°C.
- Second resist deposition: UV3 spin coat, 30sec at 4000r.min<sup>-1</sup> and 2000r.min<sup>-2</sup> (490nm), anneal 1min at 130°C.
- Insolation: dUV aligner, 50sec at a power of 0.3mW.cm<sup>-2</sup>.
- Anneal: 1min at 130°C.
- Development: MF26A 35sec and deionized water 1min.
- Rinse: acetone, ethanol, isopropanol and nitrogen blowing.
- Optical microscope validation.
- Metal deposition: Titanium (3nm at 0.03nm.sec<sup>-1</sup>) and gold (35nm at 0.1nm.sec<sup>-1</sup>).
- Lift off: Minimum 2 hours in PG remover at 80°C. Ultrasonic bath 5sec at 20% of maximum power.

## Hafnium deposition

Parameters of the oxide insulator deposition are determined by two requirements already explained in the introduction: a large coupling with the molecule without leakage. In a first approximation, the expression of the gate capacitance is:

$$C_g = \epsilon_0 \epsilon_r A / e \quad (4.1)$$

where  $\epsilon_0$  and  $\epsilon_r$  are respectively the air permittivity and the oxide relative permittivity,  $A$  the molecule-gate facing surface and  $e$  the insulator thickness. To increase this coupling a thin high  $\kappa$  oxide is the best choice. We chose an Atomic Layer Deposition (ALD) of 8nm thick HfO<sub>2</sub>. Its permittivity of 24 is much higher than the Si/SiO<sub>2</sub> ( $\epsilon_r = 3.9$ ) and Al<sub>2</sub>O<sub>3</sub> ( $\epsilon_r = 9$ ).

### **2<sup>nd</sup> step process: hafnium atomic layer deposition**

- Take the 2 inch Si/SiO<sub>2</sub> wafer, clean it using 30sec oxygen plasma and perform the HfO<sub>2</sub> deposition using ALD.
- Temperature: HfO<sub>2</sub> 90°C, valve 150°C, chamber 200°C and below chamber 150°C.
- Cycle: HfO<sub>2</sub> (15ms), wait (120sec), water (15ms) and wait (120sec)
- Number of Cycle: 80

### **Supply line**

The electrical connexion of the sample to the measurement line is accomplished *via* a micro-bounding wire of 30 $\mu$ m diameter in between the sample holder (section 3.2) and the sample. These supply lines consist of a 70 per 70 $\mu$ m pad, to do the micro-bounding, connected to a line that goes to the centre of the chip. Because of the size of this structure (tens of  $\mu$ m) we used dUV-Lithography. The alignment of this third layer with respect to the first, ensured by the alignment cross (figure 4.2), has to be better than 0.5 $\mu$ m to ensure a good position of the metallic junction on the back-gate.

### **3<sup>rd</sup> step process: Supply line**

- First resist deposition: LOR3A spin coat, 30sec at 6000r.min<sup>-1</sup> and 4000r.min<sup>-2</sup> (250nm), anneal 1min at 200°C.
- Second resist deposition: UV3 spin coat, 30sec at 6000r.min<sup>-1</sup> and 4000r.min<sup>-2</sup> (430nm), anneal 1min at 115°C.
- Insolation: dUV aligner, 50sec at a power of 0.3mW.cm<sup>-2</sup>.
- Anneal: 1min at 130°C.
- Development: MF26A 35sec and deionized water 1min.
- Rinse: acetone, ethanol, isopropanol and nitrogen blowing.
- Optical microscope validation.
- Metal deposition: Titanium (3nm at 0.03nm.sec<sup>-1</sup>) and gold (80nm at 0.1nm.sec<sup>-1</sup>).
- Lift off: Minimum 2 hours in PG remover at 80°C. Ultrasonic bath 5sec at 20% of maximum power.

## Junctions

Now that the back-gate, the micro-bonding pads and the supply lines are fabricated, the earth of the sample can be realized: the metallic junctions. In order to have an optimal electromigration (section 4.2), the design is submitted to two constraints:

- the junction's cross section has to be of the order of  $10^3 \text{nm}^2$  at the thinnest position. This surface ensures a good nanometre gap and is large enough to avoid unwanted breaking during the sample mounting and cooling.
- The electric resistivity of the wire before and after this junction has to be as low as possible to ensure voltage dropping at the really junction neighbouring.

The solution we chose is an electronic bilayer resist [89] resulting in a bridge that provides, using a shadow evaporation, a 20nm per 80nm gold junction (figure 4.3). The thickness of the junction and the evaporation angles have to be adjusted at each electronic lithography: after the resist development, I always did a test evaporation for few chips, performed electromigration measurements to get the average breaking voltage for 20 junctions and, when the parameters ensured a high success rate, I evaporated many chips at the same time.

### 4<sup>st</sup> step process: Junction

- First resist deposition: PMAA-MAA 33% spin coat, 30sec at  $4000 \text{r.min}^{-1}$  and  $2000 \text{r.min}^{-2}$  (290nm), anneal 5min at  $200^\circ\text{C}$ .
- Second resist deposition: PMAA 2% spin coat, 30sec at  $1400 \text{r.min}^{-1}$  and  $2000 \text{r.min}^{-2}$  (110nm), anneal 5min at  $180^\circ\text{C}$ .
- Insolation: e-Beam "Leo" 20kV,  $250 \mu\text{C.cm}^{-1}$ .
- Development: MIBKA-IPA 30sec, IPA 5sec and IPA 1min.
- Optical microscope validation.
- Metal deposition: titanium (3nm speed  $0.03 \text{nm.sec}^{-1}$  at  $0^\circ$ ), gold (9nm speed  $0.03 \text{nm.sec}^{-1}$  at  $-30^\circ$ ), gold (9 nm at  $0.03 \text{nm.sec}^{-1}$  at  $+30^\circ$ ) and gold (80nm at  $0.1 \text{nm.sec}^{-1}$  at  $0^\circ$ ).
- Lift off: Minimum 2 hours in Acetone. Ultrasonic bath 5sec at 20% of maximum power.

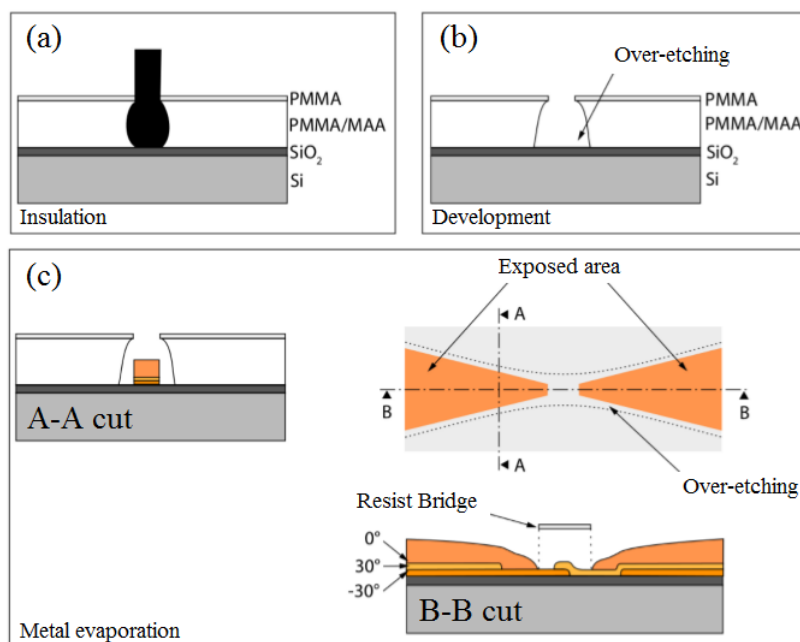


Fig. 4.3 Shadow evaporation technique illustrating sketch. (a) Bi-layer resist electronic insulation: because of a higher sensitivity and backscattered electron, the PMMA/MAA layer is more insulated than the PMMA one. (b) Resists profile after the development step. We clearly see the PMMA/MAA over-etching. (c) Shadow evaporation step to fabricate the junction. Near the two facing tips, a PMMA bridge is formed due to the PMMA/MAA over-etching process. The different colours represent the three evaporations angles.

### 4.1.2 Type 1 bis sample.

At the beginning of my Ph.D., I developed a new 5 terminals sample by adding 2 lateral gates in the vicinity of each junction. The main idea was to measure the effective coupling of this lateral gate to the molecular system in order to generate an RF electrical field to perform AC Stark manipulation. The drawback of this lateral-gate is the large distance to the molecule (8nm for the back gate and 50nm for the lateral-gate), resulting in a lower coupling. Indeed the respective slope in the stability diagram presented in figure 4.4 shows a coupling 100 times less efficient. However, even with this low coupling, calculations performed using the theory developed in section 4.3 demonstrated a good efficiency. With voltage amplitude of 10V applied on the lateral gate we could then obtain electrical field of the order of  $1\text{mV.nm}^{-1}$  which is sufficiently high to do nuclear spin manipulation as explain in section 6.1.

### 4.1.3 Type 2 sample

The development of this new sample was done in collaboration with Christophe Hoarau and Thierry Crozes. The use of "we" in this section refer to them and I. This new generation of sample originates from the desire to better control the electro-magnetic environment of the molecular magnet transistor in the Gigahertz regime. As we want to investigate deeper the origin of the nuclear spin manipulation we decided to modify the design of the sample to provide to the molecular transistor an AC magnetic field as well as two perpendicular directions of AC electric field. To separately study the influence of each excitation, we have to decouple them as much as possible. Keeping in mind that we have to maximize the number of junctions per chip, we chose for the AC magnetic field to design an on chip coplanar wave-guide, ground short-cut as close as possible to the junction. This coplanar wave-guide design already demonstrated nuclear spin manipulation in silicon based sample [32]. For the electric fields, we chose to use first the local back gate. However, the gate line is low pass filtered, a micro-wave injected through this line would result in a weak signal in the vicinity of the junction. It is the reason why we chose to design an on chip pad, capacitively coupled to the back gate. Finally, we decided to keep the micro-bounded antenna. It is inductively coupled to the source and drain circuit providing the electric field in the perpendicular direction. A sketch of this new design is presented in figure 4.5. In the following, I will present each nanofabrication step to obtain the final sample presented in figure 4.9.

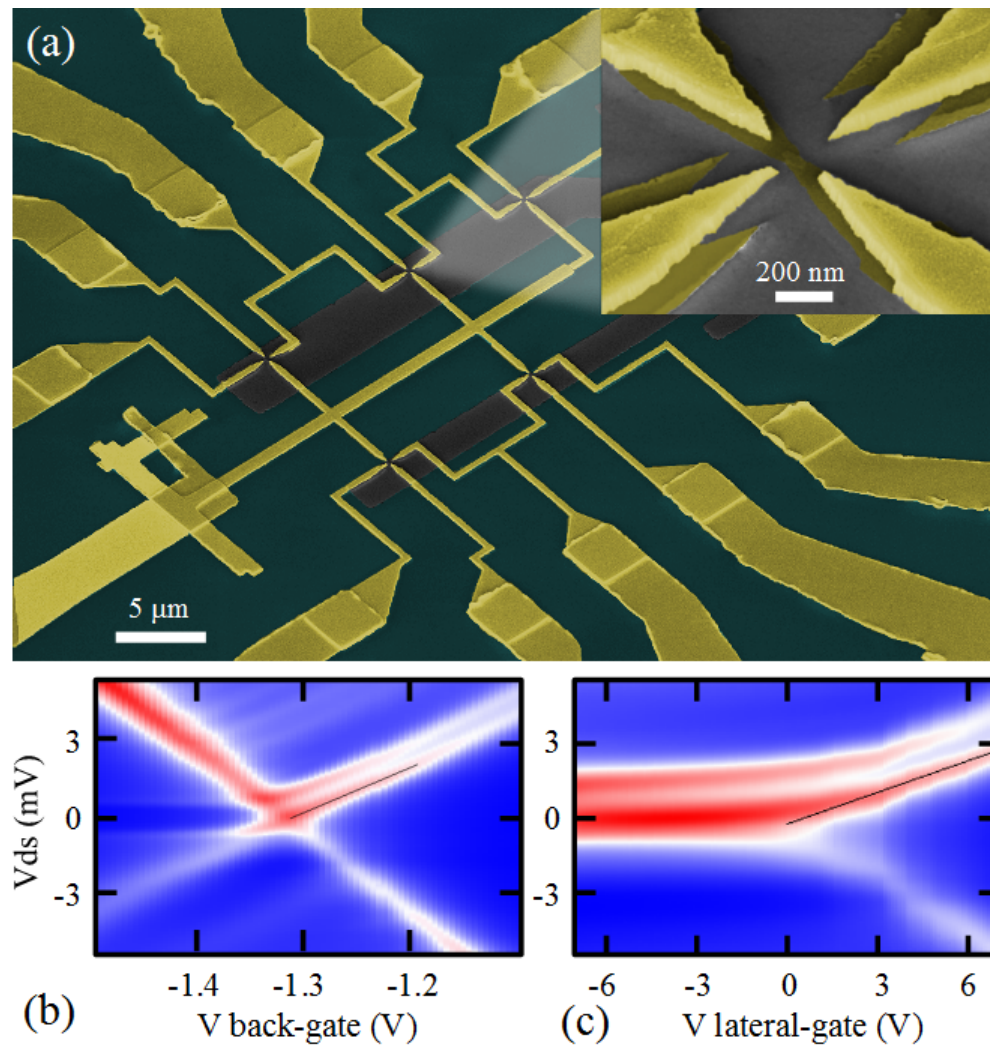


Fig. 4.4 Type 1 bis sample;. (a) Coloured SEM photography of the sample. Each chip possess six junctions. A zoom shows that the typical lateral-gate distance from the junction is below 100nm. Coulomb map (details about this measurement are given in section 4.3) using the back-gate (b) and the lateral-gate (c) of the same degeneracy point. It reveals that the back gate is 2 orders of magnitude more efficient than the lateral one.

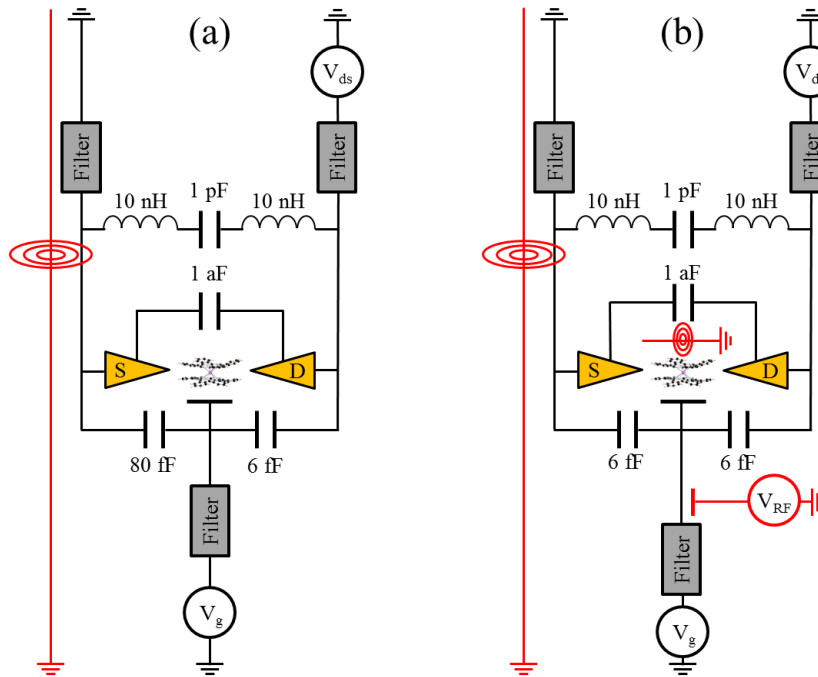


Fig. 4.5 Sample one (a) and two (b) equivalent circuit sketch. The red wires are the micro-waves lines

### RF line

For the first step, the idea is to fabricate a wave-guide in order to generate an AC magnetic field with amplitudes as high as possible in the frequency domain of the nuclear spin transition (from 2GHz to 10 GHz). Different designs ensure a  $50\Omega$  microwave transmission in this domain such as stripline, microstrip or coplanar wave-guide. Because we need to connect the junctions with DC lines, the design has to take only one half of the plan. Then the design needs to provide the same magnetic field to a large number of junctions. A coplanar waveguide with a short-cut in between its two lateral ground and its central line figure 4.6 ensures a magnetic field of the order of 10mT [90] and let enough space to bring 8 junctions close to this line. The resistivity, the loss, the dimension and the nature of substrate used are in direct relation [91]. Taking this into account we chose a sapphire substrate, its large relative permittivity ( $\epsilon_r=9$ ) ensures a micrometer typical size design. We decided to use an optical lithography process and more precisely a LASER lithography which enables a flexibility of design of great interest when we develop a new design.

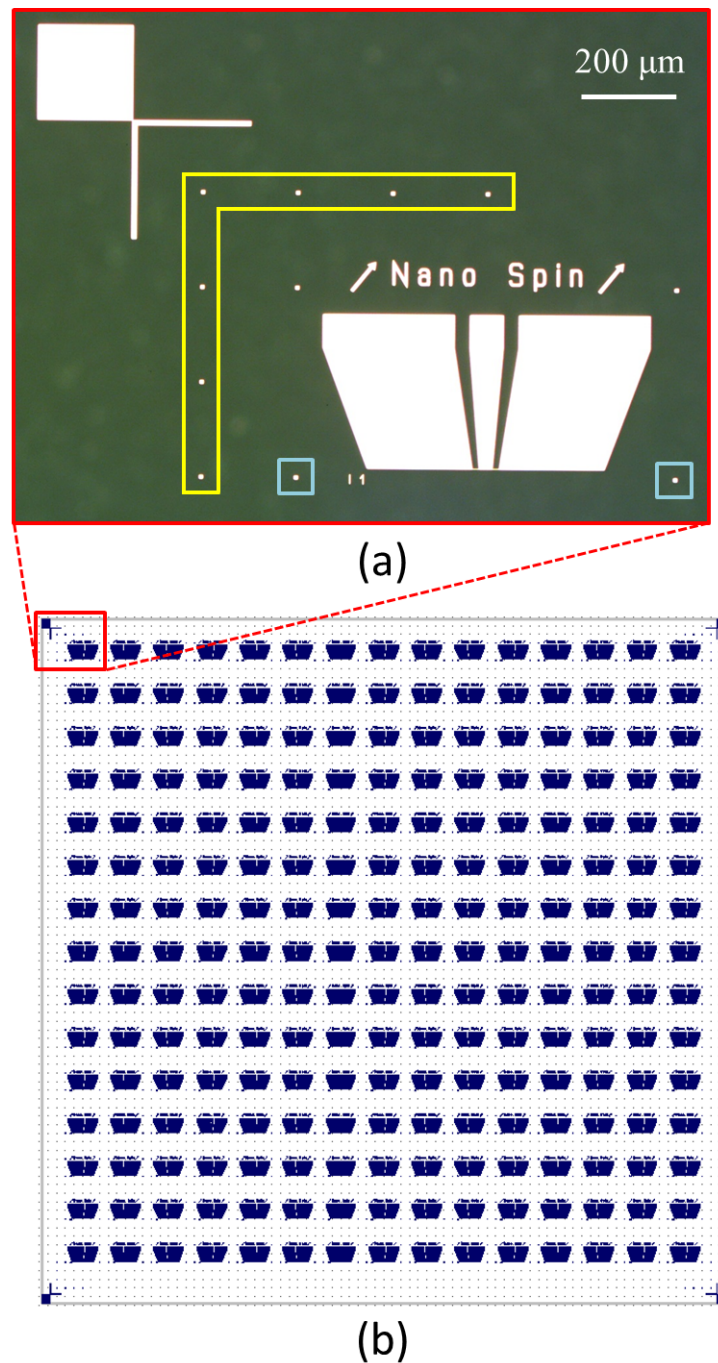


Fig. 4.6 In this first step a 15 per 15 coplanar wave-guide matrix is fabricated. This size is well calibrated for the electron beam lithography that is used during the 2<sup>nd</sup> and 4<sup>th</sup> step and can be reproduced 4 times on the 2 inch substrate. We draw two different types of alignment mark, global one (yellow) on the squares of the matrix and local one (blue) near each coplanar wave-guide.

### 1<sup>st</sup> step process: RF line

- Take a 2 inch  $330\mu\text{m}$  thick sapphire wafer, clean it with a 1min oxygen plasma and warm it 5min at  $200^\circ\text{C}$  to remove carbonic dirt and water from the surface.
- First resist deposition: LOR3A spin coat, 30sec at  $6000\text{r}\cdot\text{min}^{-1}$  and  $4000\text{r}\cdot\text{min}^{-2}$  (210nm), anneal 2min at  $200^\circ\text{C}$ .
- Second resist deposition: S1805 spin coat, 30sec at  $6000\text{r}\cdot\text{min}^{-1}$  and  $4000\text{r}\cdot\text{min}^{-2}$  (400nm), anneal 1min at  $115^\circ\text{C}$ .
- Insolation: Lazer Lithography at 56% of the maximum power.
- Development: MF26A 1min and deionized water 1min.
- Rinse: acetone, ethanol, isopropanol and nitrogen blowing.
- Optical microscope validation.
- Metal deposition: Titanium ( $3\text{nm}$  at  $0.03\text{nm}\cdot\text{sec}^{-1}$ ) and gold ( $150\text{nm}$  at  $0.1\text{nm}\cdot\text{sec}^{-1}$ ).
- Lift off: Minimum 2 hours in PG remover at  $80^\circ\text{C}$ . Ultrasonic bath 5sec at 20% of maximum power.

### Local-back-gate

The second nano-fabrication step concerns the realization of the local back-gate in the close vicinity of the previous RF line. There are two main goals:

- tuning the chemical potential of the molecular magnet.
- Providing a radio-frequency pad, capacitively coupled to this local gate to create an AC electric field *via* the local back-gate.

Because of the high precision of the realignment procedure of the Nanobeam apparatus used for this electron beam lithography step, the width of the local back-gate can be significantly decreased compare to the type one sample ( $300\text{nm}$  compared to  $3\mu\text{m}$ ). This is an important point in order to apply larger voltage to this gate without leakage to the source and drain terminals. In a first step development, we chose to bring this local gate at  $500\text{nm}$  from the microwave line (figure 4.7 (b)). This distance should be decreased in the future. We chose to insulate during the same step the radio-frequency contact pad at  $100\text{nm}$  from the back gate. The length of this RF line is  $250\mu\text{m}$  (figure 4.7 (b)) resulting in a calculated coupling of  $10^{-13}\text{F}$ . If this coupling appears to be too low, we will fabricate this RF line in another e-beam step, after deposition of the insulator. It will then be deposited on top of the local back-gate, resulting in a larger facing surface with a  $8\text{nm}$  thickness of dielectric in

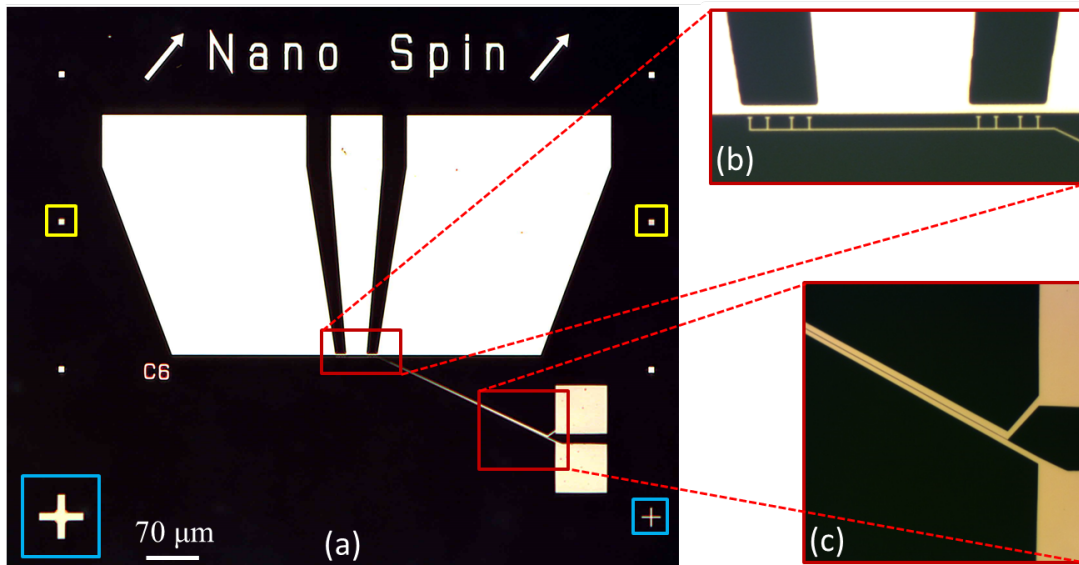


Fig. 4.7 Optical photography of the sample after the  $2^{nd}$  layer deposition. (a) To ensure a perfect alignment with the fourth layer we draw a  $3\mu\text{m}$  and  $1\mu\text{m}$  cross (blue square) and with the fifth layer we draw two  $8\text{nm}$  squares (yellow square). (b) Zoom on the local back-gate part of the sample, we see the 8 contacts going near ( $500\text{nm}$ ) the microwave line. (c) Zoom on the  $100\text{nm}$  gap between the gate line and the radio-frequency pad.

between this RF line and the gate.

This e-beam step is aligned using the blue squared mark displayed in figure 4.6. To align the  $4^{th}$  ( $5^{th}$ ) layer, with respect to this gate, we also insolate cross (square) in the bottom (middle) edge part of the sample as shown in the blue (yellow) square of figure 4.7. Last point about this layer insolation: because the sapphire substrate is an insulator it will charge itself during the electron beam lithography, resulting in so-called "charging effects" which is a deviation of the incident electron. As a consequence it will insolate a distorted image of the initial drawing. In order to avoid this drawback, we deposited  $15\text{nm}$  of gold on top of the resist. An electric connection is ensured between this thin gold layer and the stage *via* the clip that maintains the sample on the stage. We tried to do an aluminium deposition but the aluminium etching (MF26A) was also etching the resist, conversely the gold etch leaves unchanged the resist.

### **2<sup>nd</sup> step process: Local-back-gate**

- Resist deposition: PMMA 3% spin coat, 60sec at 4000r.min<sup>-1</sup> and 2000r.min<sup>-2</sup> (160nm), anneal 5min at 180°C.
- Metal deposition: gold (15nm at 0.1nm.sec<sup>-1</sup>).
- Insolation: electron beam, 80kV, 1nA, dose 13.
- Metal etching: gold etch, 5sec and deionized water 1min.
- Development: MIBKA-IPA 1min, IPA 5sec and IPA 1min.
- Rinse: acetone, ethanol, isopropanol and nitrogen blowing.
- Optical microscope validation.
- Metal deposition: titanium (3nm at 0.03nm.sec<sup>-1</sup>) and gold (35nm at 0.1nm.sec<sup>-1</sup>).
- Lift off: Minimum 2 hours in acetone. Ultrasonic bath 5sec at 20% of maximum power.

### **Dielectric deposition**

We chose to keep the same process as the sample one. Because of the decrease of the surface facing between the local back-gate and the source and drain terminal, a reduction of the HfO<sub>2</sub> thickness could be done in the future in order to keep the leakage voltage to 10V and increase the gate-molecular magnet coupling constant.

### **3<sup>rd</sup> step process: Hafnium atomic layer deposition**

- Take the 2 inch sapphire wafer, clean it with a 30sec oxygen plasma and do the HfO<sub>2</sub> deposition using ALD.
- Temperature: HfO<sub>2</sub> 90°C, valve 150°C, chamber 200°C and below chamber 150°C.
- Cycle: HfO<sub>2</sub> (15ms), wait (120sec), water (15ms) and wait (120sec)
- Number of cycles: 80

### **DC lines**

The technique used for this layer is the same as the one described for the 3<sup>rd</sup> layer of the first sample: a bi-layer resist optical lithography. These lines provide 8 drains and 4 connected sources resulting in a common source as for the previous sample. The alignment with respect to the gate layer is obtained with the two 4 squares like alignment mark (yellow square in figure 4.8). We used a dUV quartz mask of 15 per 15 chips.

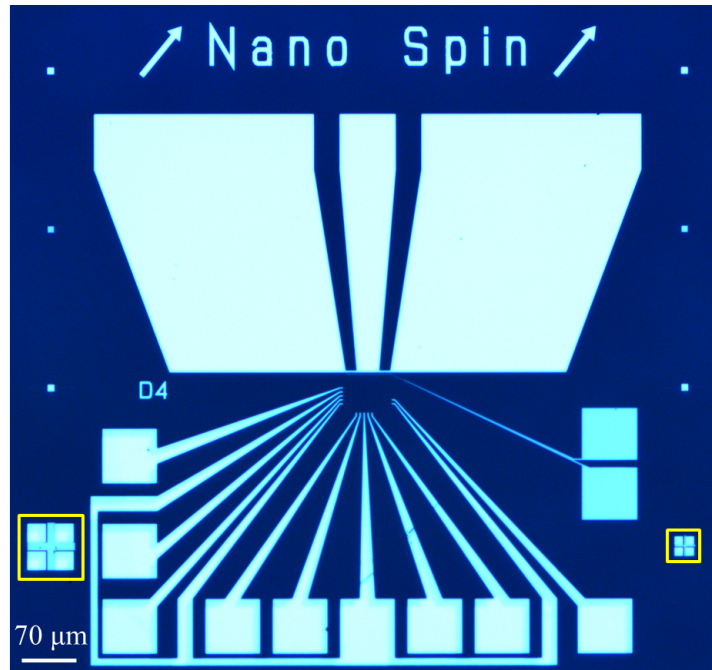


Fig. 4.8 Optical photography of the sample after the 4<sup>th</sup> layer deposition. It is aligned with respect to the gate layer *via* the marks in the yellow squares

#### 4<sup>th</sup> step process: DC lines

- First resist deposition: LOR3A spin coat, 30sec at  $6000\text{r}\cdot\text{min}^{-1}$  and  $4000\text{r}\cdot\text{min}^{-2}$  (400nm), anneal 1min at  $200^\circ\text{C}$ .
- Second resist deposition: UV3 spin coat, 30sec at  $6000\text{r}\cdot\text{min}^{-1}$  and  $4000\text{r}\cdot\text{min}^{-2}$  (490nm), anneal 1min at  $115^\circ\text{C}$ .
- Insolation: dUV aligner, 50sec at a power of  $0.3\text{mW}\cdot\text{cm}^{-2}$ .
- Anneal: 1min at  $130^\circ\text{C}$ .
- Development: MF26A 35sec and deionized water 1min.
- Rinse: acetone, ethanol, isopropanol and nitrogen blowing.
- Optical microscope validation.
- Metal deposition: titanium ( $3\text{nm}$  at  $0.03\text{nm}\cdot\text{sec}^{-1}$ ) and gold ( $80\text{nm}$  at  $0.1\text{nm}\cdot\text{sec}^{-1}$ ).
- Lift off: Minimum 2 hours in PG remover at  $80^\circ\text{C}$ . Ultrasonic bath 5sec at 20% of maximum power.

## Junctions

Here again we chose the same technique as the one described for sample one to create the junctions: a bi-layer resist and an under shadow evaporation. As for the second step of this sample, we need to deposit 15nm of gold on top of the resist to avoid charging effects. In order to minimize the inductive crosstalk between the microwave line and the source-drain loop we reduced the surface of this loop. The final result is presented in figure 4.9.

### 5<sup>th</sup> step process: Junctions

- First resist deposition: PMMA 33% spin coat, 30sec at  $4000\text{r.min}^{-1}$  and  $2000\text{r.min}^{-2}$  (290nm), anneal 5min at  $200^{\circ}\text{C}$ .
- Second resist deposition: PMMA 3% spin coat, 30sec at  $6000\text{r.min}^{-1}$  and  $4000\text{r.min}^{-2}$  (140nm), anneal 5min at  $180^{\circ}\text{C}$ .
- Metal deposition: gold (15nm at  $0.1\text{nm.sec}^{-1}$ ).
- Insolation: electron beam, 80kV, 1nA, dose 13.
- Metal etching: gold etch, 5sec and deionized water 1min.
- Development: MIBKA-IPA 1min, IPA 5sec and IPA 1min.
- Rinse: acetone, ethanol, isopropanol and nitrogen blowing.
- Optical microscope validation.
- Metal deposition: titanium (3nm speed  $0.03\text{nm.sec}^{-1}$  at  $0^{\circ}$ ), gold (9nm speed  $0.03\text{nm.sec}^{-1}$  at  $-12^{\circ}$ ), gold (9nm at  $0.03\text{nm.sec}^{-1}$  at  $+12^{\circ}$ ) and gold (80nm at  $0.1\text{nm.sec}^{-1}$  at  $0^{\circ}$ ).
- Lift off: minimum 2 hours in acetone. Ultrasonic bath 5sec at 20% of maximum power.

## 4.2 Molecular deposition and electromigration

After the sample nanofabrication, we cleave the substrate in order to keep only one chip. In the first step, we cleaned the nanowires from organic residues using acetone and isopropanol, followed by an exposure to oxygen plasma for 2 minutes. Subsequently, we dissolved 3 mg of TbPc<sub>2</sub> crystals into 5 g dichloromethane and sonicated the solution at low power for one hour. This ensures that the remaining TbPc<sub>2</sub> clusters are completely dissolved. Afterwards, some droplets of the solution were deposited on the nanowire chip and blow dried with nitrogen. In the next step, we glued the chip on the sample holder and established the electrical connections to the chip by microbonding aluminium wires. Subsequently, the sample was mounted inside a dilution refrigerator and cooled down. Once the sample was

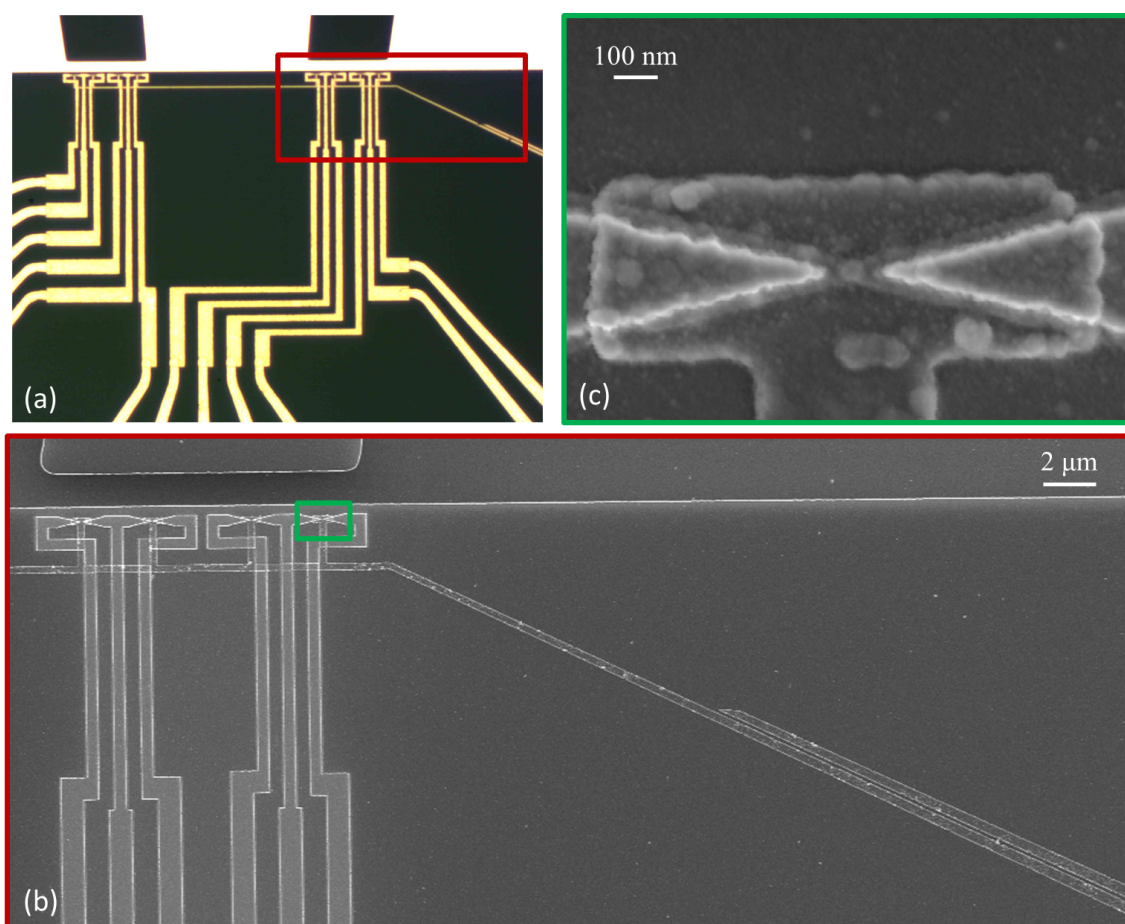


Fig. 4.9 Photography of the sample at the end of the nanofabrication process. (a) Optical photography zoom in the centre of the sample. (b) SEM photography zoom on the red square of image (a) we both see the small gate-microwave pad and gate-microwave line gap. (c) Zoom on the green square of image (b), the alignment with the local back gate is perfect and the shadow evaporation ensures a thin junction. To do a SEM image on an insulated wafer, you need to deposit a thin layer of metal to avoid charging effect, here I evaporated 20nm of aluminium which is responsible of the residues on the surface as observed on the photography.

cold, we started the electromigration to craft a nanometre gap into the nanowire.

The phenomenon of electromigration gained a lot of interest since it was found to be a reason for failure of micro-electronic devices [92]. It is a phenomenon of metal ions diffusion under the exposure of large electric fields [93]. The force applied to each metal ion can be written as:

$$\mathbf{F} = Z^* e \mathbf{E} \quad (4.2)$$

where  $Z^*$  is the effective charge of the ion during the electromigration and can be decomposed into:

$$Z^* = Z_{el} + Z_{wind} \quad (4.3)$$

where  $Z_{el}$  can be seen as the nominal charge of the ion and  $Z_{wind}$  the momentum exchange effect between electrons and the ion, commonly also referred to as the electron wind [93]. In metals, only the latter contribution is responsible for the diffusion of the ion and not the electric field. Therefore, the diffusion happens in the direction of the electric current. Our electromigration procedure is inspired from the method of Park [89]: We ramp the bias voltage applied to the junction in order to get the electromigration of it. When the junction resistivity becomes higher than a certain limit (generally the quantum of resistance value  $R_0 = h/(2e^2)$ ) the voltage is quickly setted back to 0V. The fact that we polarize the break junction with a voltage instead of a current is to limit the Joule heating during the electromigration. The increasing resistance, which is expected during the migration of the metal, thus, leads to a power reduction ( $U^2/R$ ) instead of a power increase ( $I^2R$ ). Furthermore, it was shown that a large serie resistance leads to an increase of power dissipation during the electromigration [94] [95] [96], which results in larger gaps or even the complete destruction of the device. The use of superconducting wires inside the cryostat (section 3.3) reduces the total series resistance (120Ω measured from one connector outside the cryostat to another). Moreover, we made use of the ADwin system to establish a fast feedback loop. It continuously reads-out the resistance of the wire and turns off the polarizing voltage within 1.5μs. Since the typical time constant of the electromigration is of the order of 100μs [97], we are able to control the size of the nanogap formation at the atomic level.

The conductance-voltage characteristic recorded during the electromigration typically looks like figure 4.10. It shows a first decrease of the conductance due to Joule heating of the metal. The subsequent increase of the conductance is caused by a rearrangement of the metallic grain boundaries, which enlarges the average grain size and therefore reduces the scattering at the grain boundaries. The following sharp drop in the conductance curve is

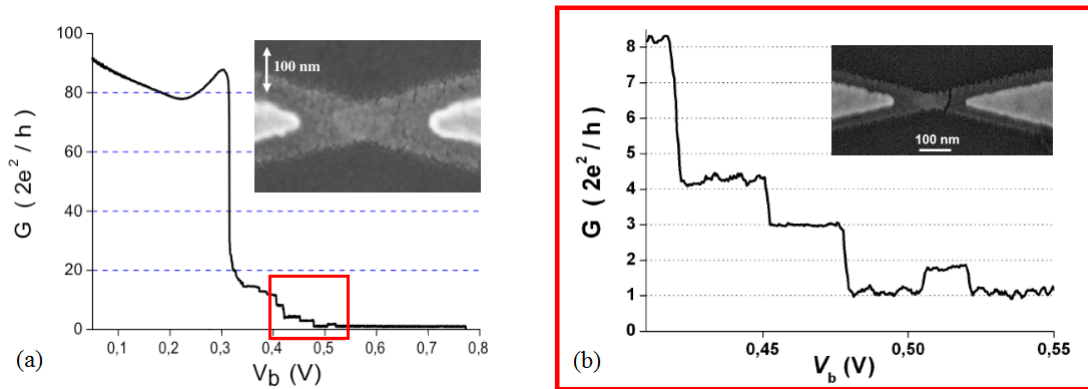


Fig. 4.10 (a) Conductance of the break junction during the electromigration showing the different regime (phonon resistivity, recrystallization and junction breaking) with a SEM photography of a junction before the procedure. (b) Zoom into the red square of (a) showing quantized conductance steps and a SEM photography of a nanogap after the electromigration.

caused by the migration of the gold ions, leading to the formation of a nm sized gap. During the last seconds of the electromigration (figure 4.10 (b)), we are often able to see quantized conductance steps, which arise from the current transport through the last remaining gold atoms. A scanning electron microscope photography before (figure 4.10 (a)) and after (figure 4.10 (a)) the electromigration of the junction is presented and shows the nanometer sized gap.

### 4.3 Transport measurement

To claim the building of a single molecular magnet transistor, we need to be sure that we trap a molecular magnet inside the nanogap. To do so we need to perform transport measurements through this junction. We will first see the equivalent circuit that models this single electron transistor to see its quantum transport measurement properties. Then, to be sure that we trap a molecular magnet, we will search a magnetic signature.

#### Equivalent circuit

A single electron transistor consists of a conducting island or quantum dot, which is tunnel-coupled to the source and drain leads. Due to the small size of the dot the electronic energy levels  $E_n$  are discretized. In order to observe the characteristic single electron tunnelling through the device, the resistance  $R_t$  of the tunnel barriers should be much higher than the quantum of resistance:

$$R_t \gg \frac{h}{2e^2} \quad (4.4)$$

where  $h$  is the Planck constant and  $e$  the elementary charge. This condition ensures that only one electron at the time is tunnelling in or out of the quantum dot. A simple model to describe the electron transport through the dot was developed by Korotkov et al. [98], and reviewed by Kouwenhoven [99], and Hanson [100]. Therein, the quantum dot is coupled *via* constant source, drain, and gate capacitors ( $C_s, C_d, C_g$ ) to the three terminals as shown in figure 4.11. By applying a voltage to the three different terminals, the electrostatic potential  $U_{es}$  of the quantum dot is modified as:

$$U_{es} = \frac{(C_s V_s + C_d V_d + C_g V_g)^2}{2C_\Sigma} \quad (4.5)$$

with  $C_\Sigma = C_s + C_d + C_g$  and  $V_s, V_d$ , and  $V_g$  being the source, drain, and gate voltages, respectively. Furthermore, due to the Coulomb repulsion, adding an electron to the quantum dot with  $N$  electrons will cost an additional energy:

$$U_c = \frac{E_c}{2} = \frac{e^2}{2C_\Sigma} \quad (4.6)$$

with  $E_c$  being the charging energy. Accordingly, to observe single electron tunnelling, temperatures smaller than  $E_c$  are required since, otherwise, the tunnel process can be activated thermally.

$$E_c \gg k_B T \quad (4.7)$$

Putting all contributions together results in the total energy  $U$  of the quantum dot with  $N$  electrons:

$$U(N) = \frac{(-e(N - N_0) + C_s V_s + C_d V_d + C_g V_g)^2}{2C_\Sigma} \quad (4.8)$$

where  $N_0$  is the offset charge. Experimentally, it is more convenient to work with the chemical potential, defined as the energy difference between two subsequent charge states:

$$\begin{aligned} \mu_{dot}(N) &= U(N) - U(N-1) \\ &= \left(N - \frac{1}{2}\right)E_c - \frac{E_c}{|e|} (C_s V_s + C_d V_d + C_g V_g) \end{aligned} \quad (4.9)$$

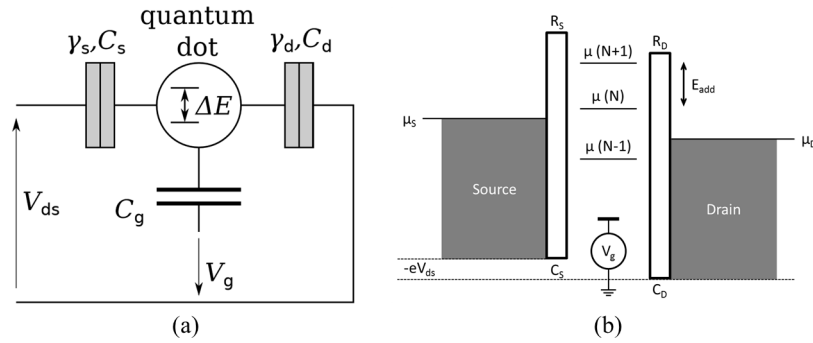


Fig. 4.11 (a) Equivalent circuit of a SET. The electrostatic behaviour of the dot is modelled by capacitors to the source, drain, and gate terminals. (b) Representation of the different chemical potential of a quantum dot couple to a source and drain *via* tunnel junction and a gate *via* a capacitive coupling.

with  $E_N$  being the energy of the  $N^{\text{th}}$  electron in the quantum dot. Notice that the chemical potential depends linearly on the gate voltage, whereas the total energy shows a quadratic dependence. Therefore, the energy difference between the chemical potentials of different charge states remains constant for any applied voltages. The energy to add an electron to the quantum dot is called addition energy  $E_{add}$  and is defined as the difference between two subsequent chemical potentials.

$$E_{add}(N) = \mu(N+1) - \mu(N) = E_c + \Delta E \quad (4.10)$$

This energy is the sum of two distinct parts:

- the charging energy ( $E_c$ ) which is purely electrostatic.
- The discrete energy of the quantum dot which is directly link to its spectrum, with  $\Delta E$  being the energy spacing between two discrete energy levels.

### Coulomb blockade

The transport through the quantum dot is very sensitive to the alignment of the chemical potential  $\mu$  inside the dot with respect to those of the source  $\mu_s$  and drain  $\mu_d$ . If we neglect the level broadening of the quantum dot, then the transport through the SET can be explained with figure 4.12 (a). Notice that  $V_{ds}$  and  $V_g$  are in arbitrary units and  $V_g = 0$  when  $\mu_{dot} = \mu_s = \mu_d$ .

First we want to discuss what happens for  $V_{ds}=0$ . In this configuration, if  $V_g < 0$ , the chemical potential of the dot is larger than the leads one, and the SET is in its off state. Increasing  $V_g$  to zero will align the three chemical potentials. Electrons can tunnel in and out of the dot from both sides leading to a finite conductance and a charge fluctuation between  $N$  and  $N + 1$ . This particular working regime is called the charge degeneracy point. A further increase of  $V_g$  will push the chemical potential of the dot below the ones of source and drain, and the SET is again in its off state, but having  $N + 1$  electrons on the dot. Whenever the charge of the dot is fixed, the SET is in the Coulomb blockade regime since adding another electron would cost energy to overcome the electron-electron repulsion.

If we now increase the bias voltage to  $V_{ds} \neq 0$ , we shift the chemical potential between source and drain and open an energy or bias window of  $\mu_s - \mu_d = -eV_{ds}$ , and a current can be observed even for  $V_g \neq 0$ . The red line in figure 4.12 (a) corresponds to the situation where the chemical potential of the dot is aligned with  $\mu_s$ . Crossing this line will turn the SET on or off, resulting in a conductance step along the line. The slope can be calculated from the equivalent circuit by setting the potential difference between dot and source to zero and is given by  $-C_g/(C_g + C_s)$ . On the other hand, if  $\mu_{dot}$  is aligned with the drain chemical potential, the SET turns also on or off, resulting in another conductance step (blue line in figure 4.12 (a)). Its slope is of opposite sign and calculated by setting the potential difference between drain and dot to zero, resulting in  $C_g/C_d$ . Therefore, inside the white region the transistor is turned on, whereas inside the grey region the SET is Coulomb blocked.

The experimental measurement of this stability diagram on the sample studied in [44] is presented in figure 4.12 (b). We clearly see a gate dependence of the conductance which shows that a quantum dot is capacitively coupled to the back-gate. Then the bias voltage dependence of this conductance exhibits diamond lines corresponding to the blue and red line of figure 4.12 (a). Because of a non symmetric coupling between the source and the drain the slopes of these lines are different.

### Magnetic signature

After the stability diagram measurement we can pretend to know how to fabricate a SET but we are not sure that it is a molecular magnet transistor. In fact, during the electromigration process we do not control the position of the molecular magnet, so it is impossible to know if during the stability diagram measurement we are doing transport through a molecular magnet or a nanometre sized impurity such as a gold nanoparticule.

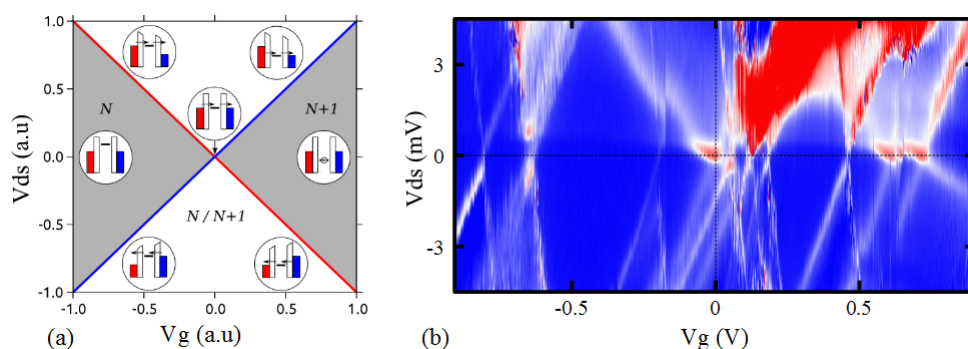


Fig. 4.12 Theoretical (a) and experimental (b) stability diagrams for a quantum dot. (a) Inside the grey regions the charge of the quantum dot is fixed, leading to the Coulomb blockade. Likewise, inside the white area electrons can tunnel in and out of the quantum dot. (b) Conductance measurement of a molecular magnet transistor as the function of the applied gate voltage and bias voltage. The blue (red) region define a low (large) conductance area, one clearly see the Coulomb blockade regime and the different charge degeneracy points.

A calculation of the charging energy  $E_c$  of the quantum dot gives a first clue. This energy can easily gives an order of magnitude of its size: the higher the charging energy, the higher the charge confinement, so the smaller the quantum dot. The charging energy of a single TbPc<sub>2</sub> ( $\approx 5\text{keV}$ ), which has a typical size of  $1\text{nm}$  (Sect. 2.1), is much higher than the one of a few tens of nanometre gold nanoparticle ( $\approx 1\text{eV}$ ), but those value depends also on the coupling to the source and drain electrodes.

Therefore, the only result that ensures the fabrication of a molecular magnet transistor is the presence of an hysteresis signal in the conductance as the function of the external magnetic field. As it will be explained in section 5.1, the electronic spin state has an influence on the quantum transport *via* an exchange coupling between this spin and the spin of the read-out dot. The main result of this effect is a bi-stable conductance value: one for the state  $|+6\rangle$  and another for the state  $|-6\rangle$ . In addition, as explained in section 2.3.3, the TbPc<sub>2</sub> electronic spin as a strong anisotropy and is oriented along the axis perpendicular to the two Pc plan. This axis is the so-called "easy axis" because along it, the necessary magnetic field amplitude to reverse the spin is the lower. To find this easy axis, we fixed  $V_{ds}=0\text{V}$  and  $V_g$  at a value close to the charge degeneracy point. It is where we expect the largest sensitivity as a slight variation of the quantum dot's chemical potential results in a strong modification of the conductance. Afterwards, we sweep the external magnetic field from negative to positive values (trace) and back again (retrace) while recording the conductance through the quantum dot. Thanks to the 3D vector magnet we can do this trace and retrace measurements

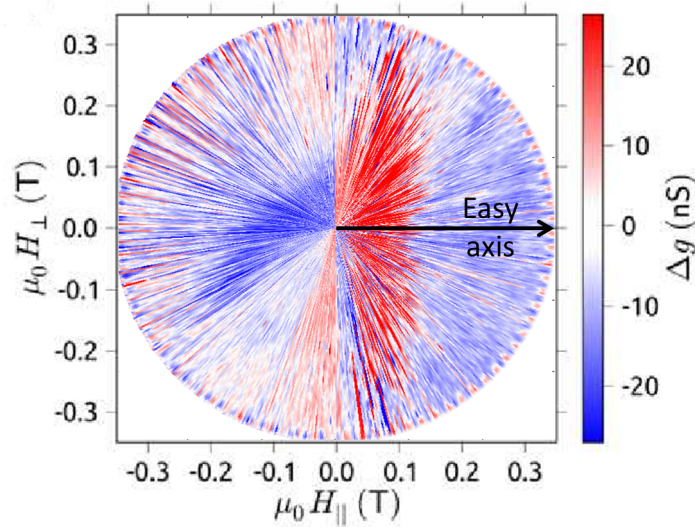


Fig. 4.13 Conductance difference between trace and retrace magnetic field sweep ( $\Delta g$ ) for different sweeping angles. This clearly exhibits an anisotropy and gives access to the easy axis of the molecular magnet trapped in the nanogap. It is the proof that we are in presence of a molecular magnet transistor.

along any direction. Figure 4.13 presents the conductance difference between the trace and retrace of such a measurement performed along different directions of a chosen plan with an angular step of  $0.5^\circ$ . By looking at the angular dependence of the reversal it is evident that it becomes harder to reverse the spin, as we turn the magnetic field from  $H_{\parallel}$  towards  $H_{\perp}$ . After this measurement we can conclude that we are performing quantum transport through a nanosized magnetically highly anisotrope object: a molecular magnet.



# Chapter 5

## Spins read-out and life time

A single electronic spin carries a magnetic moment of few  $\mu_B$  making its detection an experimental challenge. The use of standard magnetometer on molecular magnet assembly is not suited. In this chapter I present and investigate how to directly read-out a single electronic spin using a conductance measurement through a molecular magnet transistor. A nuclear spin carries a magnetic moment three orders of magnitude smaller than an electronic one. Despite this, the specific Zeeman diagram of the  $\text{TbPc}_2$  presented in section 2.4.1 shows how we have access to an indirect nuclear spin state measurement through the electronic spin flip position as a function of the applied magnetic field.

### 5.1 Electronic spin

#### 5.1.1 Direct read-out

The general spin transistor detection scheme can be split into two coupled quantum systems:

- the electronic spin arising from the 4f electrons of the terbium  $\text{Tb}^{3+}$  ion. We saw in section 2.3 that, due to a strong spin-orbit coupling and the ligand field, this electronic spin can be treated as a  $|\pm 6\rangle$  Ising spin in our experiment.
- A read-out quantum dot created by the Pc ligands. The  $\text{TbPc}_2$  has a spin  $S = 1/2$  radical electron delocalised over the Pc ligands planes which is close in energy to the Tb-4f states [101].

A delocalised p-electron of the Pc ligands is tunnel-coupled to the source and drain terminals, creating a quantum dot in the vicinity of the electronic spin carried by the  $\text{Tb}^{3+}$  ion, without affecting its magnetic properties. Furthermore, an overlap of the delocalised

p-electron system with the terbium's 4f wave functions gives rise to a strong exchange coupling between the read-out quantum dot and the electronic spin, as demonstrated in the following. Because of this coupling between the two systems, the conductance through the read-out quantum dot is spin dependent, enabling an electrical and non-destructive read-out of the single electronic spin.

A fast introduction to quantum transport measurement was given in section 4.3. Here we characterize our single molecular magnet spin transistor. Notice that two other samples on which we were able to read-out the electronic spin will not be described here. The measurement of the differential conductance as a function of the source drain voltage  $V_{ds}$  and the gate voltage  $V_g$  exhibits the stability diagram presented in figure 5.2. Regions coloured in red and blue are respectively high and low differential conductance values. From the general characteristics of the Coulomb diamond in figure 5.2, we obtained a conversion factor  $\alpha = \delta V_{ds} / \Delta V_g \approx 1/8$ , resulting in a low estimation of the charging energy  $E_C \approx 100 meV$  of the quantum dot. First, this large value is consistent with the claim that the quantum dot is created by the single TbPc<sub>2</sub> molecular magnet. Moreover, it was shown by Zhu *et al.* [102] that up to the fifth reduction and second oxidation of the TbPc<sub>2</sub> molecule, electrons are only added to the organic ligands, conserving the charge state and therefore the magnetic properties of the Tb<sup>3+</sup> ion. On these accounts, the read-out quantum dot is most likely created by the Pc ligands.

On the right part of the charge degeneracy point, one can see the usual spin  $S=1/2$  Kondo effect observed in others single molecule transistors [103, 104]. When Pc ligands are filled with an odd number of electrons, its total spin  $S = 1/2$  makes it an artificial magnetic impurity. If, furthermore, the coupling between the dot and the leads is large enough (tunnel resistances below  $1M\Omega$ ), electrons from the leads try to screen the artificial impurity by continuously flipping its spin *via* a tunnel process. This allows an hybridization between the leads and the quantum dot, resulting in the appearance of two peaks in the quantum dot's density of states: one at Fermi level of the source and one at the Fermi level of the drain. The conductance through the quantum dot can be explained by the convolution of the two peaks. Since at  $V_{ds} = 0$  the source and drain Fermi levels coincide, the conductance will have a maximum. This effect can be broken by changing  $V_g$ , increasing  $V_{ds}$ , the temperature (giving the Kondo temperature  $T_K$ ) or magnetic field (giving the Kondo field  $B_K$ ).

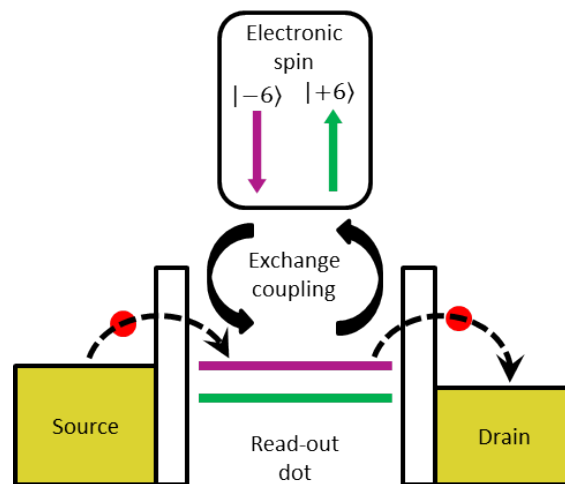


Fig. 5.1 The phthalocyanine acts as a read-out quantum dot that is exchanged coupled to the  $|\pm 6\rangle$  electronic states.

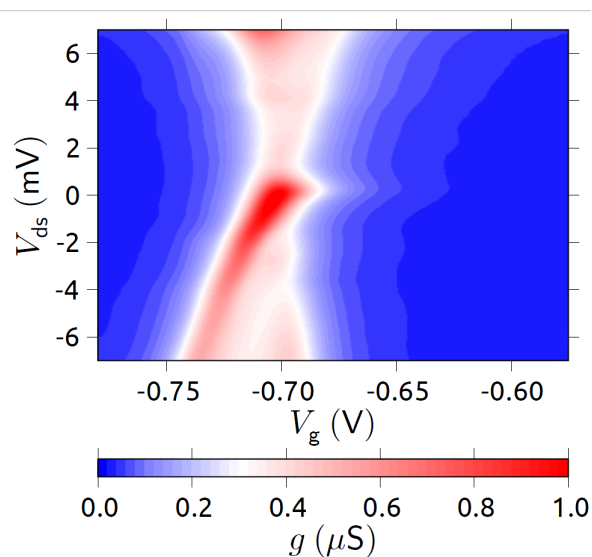


Fig. 5.2 Stability diagram of the read-out quantum dot showing the differential conductance as a function of the source-drain voltage  $V_{ds}$  and the back gate voltage  $V_g$ . The Kondo peak on the right side of the Coulomb diamond indicates an odd number of electrons on the Pc ligands read-out quantum dot.

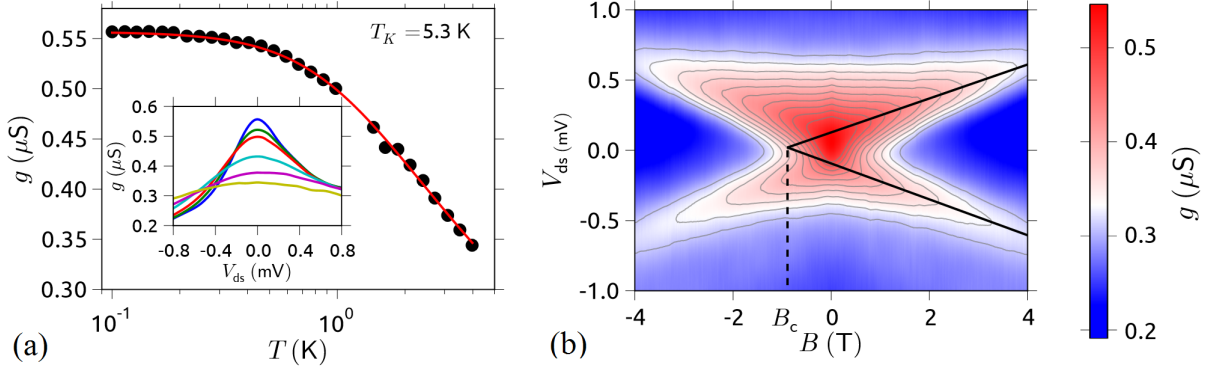


Fig. 5.3 (a) Temperature dependence of the differential conductance  $\delta I/\delta V$  at  $V_{ds} = 0$  V. Inset: Evolution of  $\delta I/\delta V$  versus  $V_{ds}$  for a different set of temperatures. The temperatures from highest to lowest conductance were 0.1K, 0.7K, 1K, 2K, 3K and 4K. (b) Differential conductance as a function of the magnetic field  $B$  and the source-drain voltage  $V_{ds}$ . The solid lines were fitted to the maxima and extrapolated to negative magnetic fields.

To characterize this Kondo peak we first determined the Kondo temperature  $T_K$  by measuring the differential conductance at  $V_{ds} = 0$  V as a function of the temperature  $T$  for a fixed gate voltage  $V_g$  figure 5.3 (a)). By fitting the results to the empirical formula:

$$g(T) = g_0 \left( \frac{T^2}{T_K^2} \left( 2^{1/s} - 1 \right) + 1 \right)^{-s} + g_c \quad (5.1)$$

where  $g_0$  is the maximum conductance,  $s = 0.22$  and  $g_c$  is the fixed background conductance, we obtained a Kondo temperature  $T_K = 5.3 \pm 0.05$  K.

Then, to determine the configuration and strength of the coupling between the read-out quantum dot and the electronic spin carried by the  $\text{Tb}^{3+}$  ion, we investigated the evolution of the Kondo peak as a function of the bias voltage  $V_{ds}$  and the applied magnetic field  $B$  (see figure 5.3(b)). A linear splitting of the Kondo peak with increasing  $B$ , at a rate of  $124 \mu\text{V/T}$ , is presented in Figure 5.3b. The slope is a direct measurement of the  $g$ -factor  $= 2.15 \pm 0.1$ , which is consistent with the usual spin  $S=1/2$  Kondo effect.

However, extrapolating the linear slopes from positive to negative magnetic fields, we observed an intersection at a negative critical magnetic field  $B_c \approx -880$  mT. This is in contrast to the classical spin  $S=1/2$  Kondo effect, where  $B_c$  is always positive and directly related to the Kondo temperature  $T_K$  via:  $2g\mu_B B_c = k_B T_K$ . To understand this behaviour, we use the analogy to the underscreened spin  $S=1$  Kondo effect [105], where the antiferromagnetic coupling between a screened spin  $S = 1/2$  and the electrons in the leads is weakened by a ferromagnetic coupling to the remaining unscreened spin  $S = 1/2$ . This ferromagnetic

coupling acts as an additional effective magnetic field, which decreases the critical field from finite values to almost zero Tesla [105]. In our device, the negative value of  $B_c$  originates from a ferromagnetic coupling between the read-out quantum dot and the terbium's electronic spin carrying a magnetic moment equal to  $9\mu_B$ . Taking into account this coupling, the relation between the critical field  $B_c$  and the Kondo temperature  $T_K$  can be modified to:

$$2g\mu_B B_c = k_B T_K + a \mu_B J_z S_z \quad (5.2)$$

where  $a$  is the coupling constant. Using the Kondo temperature  $T_K = 5.3\text{K}$  obtained from Eq.5.1 and the critical field extracted from the magnetic field dependence (figure 5.3 (b)), a coupling constant  $a = -3.91\text{T}$  is obtained. We emphasize that such a high value cannot be explained by a purely dipolar interaction due to the terbium magnetic moment. Indeed, the relative distance between the  $\text{Tb}^{3+}$  ion and the Pc read-out quantum dot is about  $0.5\text{nm}$ , giving a dipolar interaction of the order of  $0.1\text{T}$ , which is more than one order of magnitude smaller than the measured coupling constant. As an efficient exchange interaction requires an overlap of the wave functions between the electronic magnetic moment carried by the  $\text{Tb}^{3+}$  ion and the read-out quantum dot, this high coupling further validates the expected configuration for which the read-out quantum dot is the Pc.

We now present the measurements and the model to explain how the exchange coupling between the electronic spin state and the read-out quantum dot induces a modification of the read-out dot energy which makes the spin dependence of the differential conductance. We first define  $B_{\parallel}$  and  $B_{\perp}$  being the magnetic fields applied parallel and perpendicular to the easy axis of the molecule respectively. For  $V_{ds} = 0$  and  $B_{\perp} = 0$ , we recorded the differential conductance as a function of  $B_{\parallel}$  on the right side of the charge degeneracy point (figure 5.4 (a)). By repeating this measurement, we obtained two distinct magneto-conductance signals, corresponding to the two electronic spin states  $|+6\rangle$  (red) and  $|-6\rangle$  (blue). The two measurements intersect at  $B_{\parallel} = 0$  and have a constant differential conductance difference for  $B_{\parallel} > \pm 100\text{ mT}$ . To quantify the read-out fidelity of our device, we recorded the conductance values at  $B_{\parallel} = 100\text{ mT}$  for 10000 measurements. Plotting the results into a histogram yielded two distinct Gaussian like distribution as presented in figure 5.4(b). The read-out fidelity was determined to 99.5% by relating the overlap of the best fits to this two distributions.

To further characterize the signal originating from the electronic spin, we determined the difference between the spin  $|+6\rangle$  and  $|-6\rangle$  conductance as a function of  $B_{\parallel}$  and  $B_{\perp}$  figure 5.4(c)). In the red area the spin  $|+6\rangle$  conductance was larger than the spin  $|-6\rangle$  conductance whereas the blue area indicates the inverse scenario. At a particular combination of  $B_{\parallel}$

and  $B_{\perp}$  the signal goes to zero, which is indicated by the white region. The dotted line corresponds to the configuration of figure 5.4 (a).

To explain the magneto-conductance evolution as a function of  $B_{\parallel}$  and  $B_{\perp}$ , we use a semi-classical approach to describe the influence of the electronic spin  $J$  on the chemical potential of the read-out quantum dot. The model considers that the read-out quantum dot possesses a spin  $s$ , exchange coupled to  $J$  in an external magnetic field  $B$ . The Hamiltonian  $\mathcal{H}$  of the system is given by:

$$\mathcal{H} = \mathcal{H}_J + \mathcal{H}_s + \mathcal{H}_{J,s} \quad (5.3)$$

$$= \mathcal{H}_J + \mathcal{H}_{rod} \quad (5.4)$$

$$= \mu_B B \cdot g_J J + \mu_B B \cdot \bar{g}_s \cdot s + J \cdot \bar{a} \cdot s \quad (5.5)$$

with  $\bar{g}_s$  and  $g_J$  respectively the  $g$ -factor of the read-out quantum dot and of the electronic spin,  $\bar{a}$  the exchange coupling and  $\mu_B$  the Bohr magneton. To correspond to the experiment, the external magnetic field was simulated to be in the  $x$ - $z$  plane with  $B = (B_{\perp}, 0, B_{\parallel})$ , and  $J = \pm 6 e_z$  is considered as a classical vector confined on the easy axis of the TbPc<sub>2</sub> molecular magnet. Due to the axial symmetry of the system, we consider it as invariant under a rotation in the  $x$ - $y$  plan. The read-out dot Hamiltonian can be consequently defined in the  $(\perp, \parallel)$  basis as:

$$\mathcal{H}_{rod} = \mu_B \begin{pmatrix} B_{\perp} \\ B_{\parallel} \end{pmatrix} \cdot \bar{g}_s \cdot \begin{pmatrix} s_{\perp} \\ s_{\parallel} \end{pmatrix} + \begin{pmatrix} J_{\perp} \\ J_{\parallel} \end{pmatrix} \cdot \bar{a} \cdot \begin{pmatrix} s_{\perp} \\ s_{\parallel} \end{pmatrix} \quad (5.6)$$

Because the spin  $s$  of the read-out quantum dot can not be considered as a punctual electronic momentum aligned along the easy axis of terbium magnetization, the exchange interaction can not be described by a diagonal tensor. Indeed the delocalization of the electron in the ligand involves a multi-polar correction expressed in terms of coupling between the various spacial components *i.e* off-diagonal terms in the exchange tensor  $\bar{a}$ . Therefore, due to the non-symmetric coupling of the read-out quantum dot to the leads, and because no chemical environment argument can ensure an isotropic  $g$ -factor, the more general way to express the exchange tensor  $\bar{a}$  and the  $g$ -factor in the  $(\perp, \parallel)$  basis is :

$$\bar{a} = \begin{pmatrix} a & \delta a_{\parallel} \\ \delta a_{\parallel} & a \end{pmatrix} \quad \bar{g}_s = \begin{pmatrix} g_s + \delta g_s & 0 \\ 0 & g_s \end{pmatrix} \quad (5.7)$$

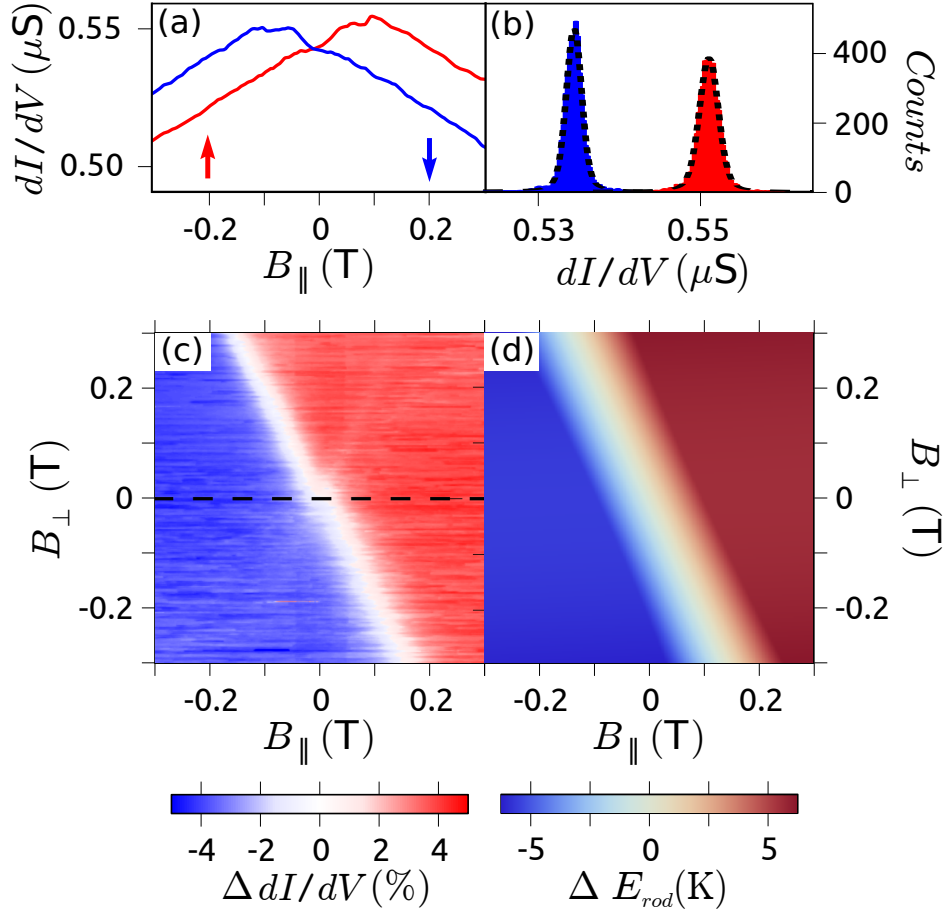


Fig. 5.4 (a) Differential conductance of the read-out quantum dot at zero bias as a function of the magnetic field  $B_{\parallel}$  parallel to the easy axis of the molecule. The exchange coupling between the read-out quantum dot and the electronic  $J = \pm 6e_z$  spin results in a different conductance signal for the two spin orientations  $|+6\rangle$  (red) and  $|-6\rangle$  (blue). (b) Histogram of differential conductance values at  $B_{\parallel} = +100$  mT for 10000 sweeps, showing two Gaussian-like distributions. From the overlap of the distributions we estimated a read-out fidelity of 99.5%. (c) Conductance difference between the spin up and down as a function of the magnetic field parallel ( $B_{\parallel}$ ) and perpendicular ( $B_{\perp}$ ) to the easy axis of the molecule. The dotted line corresponds to the configuration of (a). (d) Calculated energy difference  $\Delta E_{rod} = E_{rod}^{+6} - E_{rod}^{-6}$  between the read-out quantum dot and the source and drain potential as a function of the magnetic field  $B_{\parallel}$  and  $B_{\perp}$ .

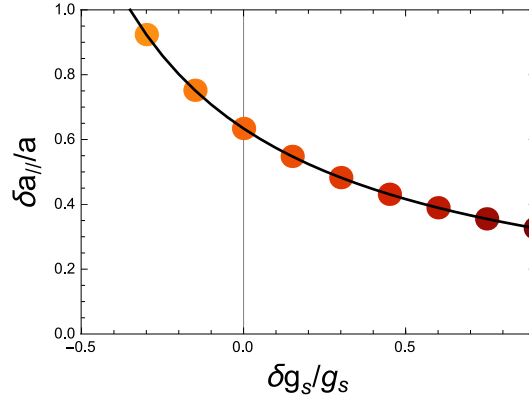


Fig. 5.5 Fitting parameter line as a function of  $(\frac{\delta g_s}{g_s}; \frac{\delta a_{\parallel}}{a})$  giving  $B_{\parallel}^{shift} = -0.6B_{\perp}$ .

where the notation "δ" is used for the anisotropic contributions. Subsequently, taking  $s_{\perp} = \hbar\sigma_x/2$  and  $s_{\parallel} = \hbar\sigma_z/2$ , the Hamiltonian  $\mathcal{H}_{rod}$  in the read-out dot electronic spin basis is given by:

$$\mathcal{H}_{rod} = \frac{\hbar\mu_B g_s B_{\parallel}}{2} \begin{pmatrix} 1 & (1 + \frac{\delta g_s}{g_s}) \frac{B_{\perp}}{B_{\parallel}} \\ (1 + \frac{\delta g_s}{g_s}) \frac{B_{\perp}}{B_{\parallel}} & -1 \end{pmatrix} + \frac{\hbar a J_z}{2} \begin{pmatrix} 1 & \frac{\delta a_{\parallel}}{a} \\ \frac{\delta a_{\parallel}}{a} & -1 \end{pmatrix} \quad (5.8)$$

The eigenenergies of the read-out dot are

$$E_{J=\pm 6} = \pm [\varepsilon_0 + 2ag_s\mu_B B_{\parallel} J_z + 2\delta a(g_s + \delta g_s)\mu_B B_{\perp} J_z]^{1/2} \quad (5.9)$$

where  $\varepsilon_0$  is function of  $J_z^2$ , meaning that the states  $J_z = \pm 6$  are degenerated for  $ag_s B_{\parallel} = \delta a(g_s + \delta g_s) B_{\perp}$ . This result in a shift of the crossing point in  $B_{\parallel}$  as the function of  $B_{\perp}$  observed in the measurement presented in Figure 5.4c, given by :

$$B_{\parallel}^{shift} = \frac{(g_s + \delta g_s)}{g_s} \frac{\delta a_{\parallel}}{a} B_{\perp} \quad (5.10)$$

In order to obtain the values of this off-diagonal term  $\delta a_{\parallel}$ , as well as the anisotropy of  $g_s$ , we calculated and present in figure 5.5 the position of  $B_{\parallel}^{shift}$  as a function of  $(\frac{\delta g_s}{g_s}; \frac{\delta a_{\parallel}}{a})$  where the model fit the experiment (figure 5.3. c). An infinite number of doublet gives a perfect agreement with the experiment ( $B_{\parallel}^{shift} = -0.6B_{\perp}$ ). The doublet ( $\frac{\delta g_s}{g_s} = 0; \frac{\delta a_{\parallel}}{a} = 0.6$ ) is plausible because it minimizes the Kondo anisotropy and gives a not so high exchange coupling anisotropy. The zero sensitivity region (in white in figure 5.4c,d), and the angle with respect to  $B_{\parallel}$  are perfectly reproduced comforting the model used to interpret the origin of the magneto-conductance signal.

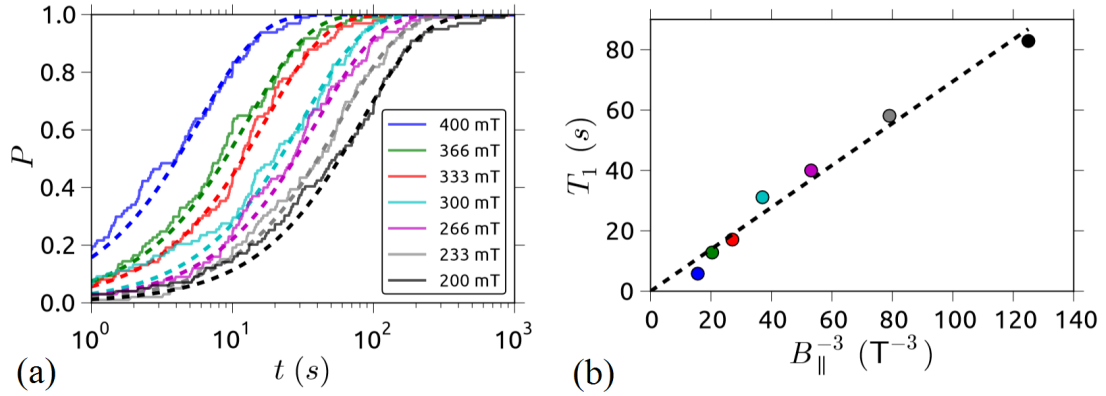


Fig. 5.6 (a) Probability of observing a direct spin relaxation after waiting a time  $t$  at different magnetic fields parallel to the easy axis of the molecule. The solid lines show the experimental data and the dashed lines a fit to the function  $P = 1 - \exp(-t/T_1)$ . (b) The characteristic relaxation times  $T_1$ , which were obtained from (a), showed an inverse cubic dependence on the parallel magnetic field, which indicated a classical relaxation behaviour mediated by phonons.

### 5.1.2 Relaxation time

I choose to present this result, obtained by Stefan Thiele [75], about the relaxation time  $T_1$  of a single electronic spin because more than illustrating the read-out technique, this  $T_1$  is an important property of the system. The process is divided in three steps:

- first, we prepare the electronic spin in its ground state  $|+6\rangle$  by applying a large negative magnetic field  $B_{\parallel} = -600$  mT (see figure 2.7. (c)).
- Second, we bring the electronic spin in its excited state by sweeping the magnetic field at 50 mT/s to  $+B_{\parallel}$  ranging from 200 mT to 400 mT. If a magnetization reversal occurred before reaching this magnetic field, the initialization was repeated.
- Third, we record the time necessary to relax back into the ground state.

Magnetic fields smaller than 200 mT were not investigated due to the onset of a competing relaxation process, making the analysis ambiguous. By repeating this procedure 100 times for each different  $B_{\parallel}$ , we obtained the probability  $P$  of observing a relaxation after a waiting time  $t$  (figure 5.1.2(a)). By fitting each measurement to an exponential function  $P = 1 - \exp(-t/T_1(B_{\parallel}))$ , we obtained the  $B_{\parallel}$  dependence of the relaxation times  $T_1(B_{\parallel})$ , ranging from 6 s to 83 s depending on the magnetic field (figure 5.5(b)).

## 5.2 Nuclear spin

Few systems managed to read-out a single nuclear spin. The difficulty lies in its tiny magnetic moment  $\mu_N$  which is three orders of magnitude smaller than an electronic spin. As for every small physical signal, one needs to amplify it to observe it. The amplification of the signal, common to all other physical systems [40, 44, 32], is based on the hyperfine interaction. Through it, the electronic spin energy is slightly changed so that a response to a certain manipulation of the electronic spin gives different answers depending on the nuclear spin states.

In NV centre, the direct read-out of the electronic spin is performed by measuring the brightness of the impurity: high for  $|0_e\rangle$  and low for  $|\pm 1_e\rangle$ ). To read-out the nuclear spin, the system is first pumped into the  $|0_e\rangle$  state using a strong laser pulse. Afterwards, a microwave pulse of precise duration and frequency is applied to inverse the population of  $|0_e, -1_n\rangle$  and  $|1_e, -1_n\rangle$ . The electronic state will change from the bright to the dark state only if the nuclear spin was in the  $|-1_n\rangle$  state. If the nuclear spin is in the  $|0_n\rangle$  or  $|1_n\rangle$  state, the luminescence signal remains large, conversely, it will decrease due to an electronic spin flip for the  $|-1_n\rangle$  state. This technique, called electron spin resonance is also used in donor impurities in silicon and is under investigation for the molecular magnet transistor (section 8).

### 5.2.1 Indirect read-out : Quantum Tunnelling of Magnetization

In our case we do not manipulate the electronic spin *via* a microwave pulse but using magnetic field sweeps. To understand the nuclear spin read-out process, we need to investigate the Quantum Tunnelling of Magnetisation (QTM) effect. We first study in details the Zeeman diagram of the molecular magnet: a perturbation calculation on the ligand field exhibits a zero field splitting of the  $|+6\rangle$  and  $|-6\rangle$  states. Then we measure the dynamic of the electronic spin when it goes through the anti-crossing by means of a magnetic field sweep. A theoretical study of this Landau-Zener effect shows that the dynamic is governed by decoherence processes. Finally we introduce the hyperfine interaction that separates the zero field splitting into four. These four anti-crossing positions in magnetic field are nuclear spin state dependent. Therefore, recording the magnetic field of QTM yields nuclear spin state.

#### Zero field splitting

We discussed in section 2.3.3 the ligand field Hamiltonian :

$$H_{LF} = B_2^0 O_2^0 + B_4^0 O_4^0 + B_6^0 O_6^0 + B_4^4 O_4^4 \quad (5.11)$$

The physics emerging from the ligands is hidden in the dependence of the Stevens operator over the electronic angular momentum  $\mathbf{J}$ . The operators  $O_m^0$  contain only integer power of the operator  $J_z$  up to the power of  $m$ . They are diagonal and introduce a strong uni-axial anisotropy in the  $z$ -direction. The operators  $O_m^m$  contain integer power of the operators  $J_+$  and  $J_-$  up to the power of  $m$ . They are off-diagonal terms and mix the states of different azimuthal quantum numbers that are the eigenstates of the operators  $O_m^0$ . The weight of these terms in the Hamiltonian is related to the structure and the geometry of the two Pc ligands. For a structural rotation of exactly  $45^\circ$  between the two Pc, the molecular magnet symmetry would have belonged to the dihedral group of order 4 ( $D_{4d}$ ), and the off-diagonal term would have vanished. The reported angle for the real  $\text{TbPc}_2$  is  $45^\circ \pm 2^\circ$ , so that the off-diagonal terms act as a perturbation in comparison with the diagonal one.

The tunnel gap in the  $|\pm 6\rangle$  ground doublet emerges solely to the third order of perturbation, because only  $J_\pm^4$  operators are involved in the perturbation. According to Messiah [106], the expression of the perturbed energy is:

$$\epsilon_3 = (B_4^4)^3 \langle \pm 6 | O_4^4 \frac{|-2\rangle \langle -2| + |2\rangle \langle 2|}{\delta} O_4^4 \frac{|-2\rangle \langle -2| + |2\rangle \langle 2|}{\delta} O_4^4 | \pm 6 \rangle \quad (5.12)$$

where  $\delta$  is the energy difference between the states  $|6\rangle \leftrightarrow |2\rangle$  and  $|-6\rangle \leftrightarrow |-2\rangle$  which are equal. Knowing that:

$$O_4^4 = (J_+^4 + J_-^4)/2 \quad (5.13)$$

$$J_+ |J, m\rangle = \sqrt{J(J+1) - m(m+1)} |J, m+1\rangle \quad (5.14)$$

$$J_- |J, m\rangle = \sqrt{J(J+1) - m(m-1)} |J, m-1\rangle \quad (5.15)$$

we get the following expression for the off-diagonal Stevens operator action on the states:

$$O_4^4 |6\rangle = 36\sqrt{55} |2\rangle = \alpha |2\rangle \quad (5.16)$$

$$O_4^4 |2\rangle = 36\sqrt{55} |6\rangle + 840 |-2\rangle = \alpha |6\rangle + \beta |-2\rangle \quad (5.17)$$

$$O_4^4 |-2\rangle = 36\sqrt{55} |-6\rangle + 840 |2\rangle = \alpha |-6\rangle + \beta |2\rangle \quad (5.18)$$

$$O_4^4 |-6\rangle = 36\sqrt{55} |-2\rangle = \alpha |-2\rangle \quad (5.19)$$

Injecting this in 5.12, results in:

$$\epsilon_3(|6\rangle \rightarrow |-6\rangle) = (B_4^4)^3 \langle 6 | \frac{\alpha}{\delta} | 6 \rangle \langle 2 | \frac{\beta}{\delta} | 2 \rangle \langle -2 | \alpha | -2 \rangle = (B_4^4)^3 \frac{\alpha^2 \beta}{\delta^2} \quad (5.20)$$

$$\epsilon_3(|-6\rangle \rightarrow |6\rangle) = (B_4^4)^3 \langle -6 | \frac{\alpha}{\delta} | -6 \rangle \langle -2 | \frac{\beta}{\delta} | -2 \rangle \langle 2 | \alpha | 2 \rangle = (B_4^4)^3 \frac{\alpha^2 \beta}{\delta^2} \quad (5.21)$$

The perturbation Hamiltonian  $B_4^4 O_4^4$  at zero applied magnetic field can be written, on the ground double  $|\pm 6\rangle$  basis, as:

$$H = (B_4^4)^3 \begin{pmatrix} 0 & \frac{\alpha^2 \beta}{\delta^2} \\ \frac{\alpha^2 \beta}{\delta^2} & 0 \end{pmatrix} \quad (5.22)$$

giving the tunnel gap energy:

$$\Delta = (B_4^4)^3 \frac{\alpha^2 \beta}{\delta^2} \quad (5.23)$$

The final step of this calculation is to find  $\delta$ :

$$\delta = 96B_2^0 + 5280B_4^0 = 598.5K \quad (5.24)$$

From the ligand field parameters reported on table 2.2, we obtain a tunnel gap of  $1\mu K$ . It clearly shows that the overlap between the  $|+6\rangle$  and  $|-6\rangle$  is usually small in comparison with the one induced by the Zeeman effect, except for longitudinal magnetic field below  $1\mu T$ . As a result, when sweeping the longitudinal magnetic field over this anti-crossing, the spin can tunnel from one state to the other with a certain probability governed by the Landau-Zener process.

### Landau-Zener model for Quantum Tunnelling of Magnetization

By applying an external magnetic field parallel to the easy axis of the molecule, we move along the lines of the Zeeman diagram as shown in figure 5.8 (a). Every time we go through an anticrossing, the electronic spin may reverse due to a process which is referred to as the Quantum Tunnelling of Magnetization (QTM). The probability of the reversal  $P_{LZ}$  is given by the Landau-Zener (LZ) formula [107, 108]:

$$P_{LZ} = 1 - \exp \left[ -\frac{\pi \Delta^2}{2 \hbar g_J \mu_0 \Delta_{m_j} \frac{dH_{\parallel}}{dt}} \right] \quad (5.25)$$

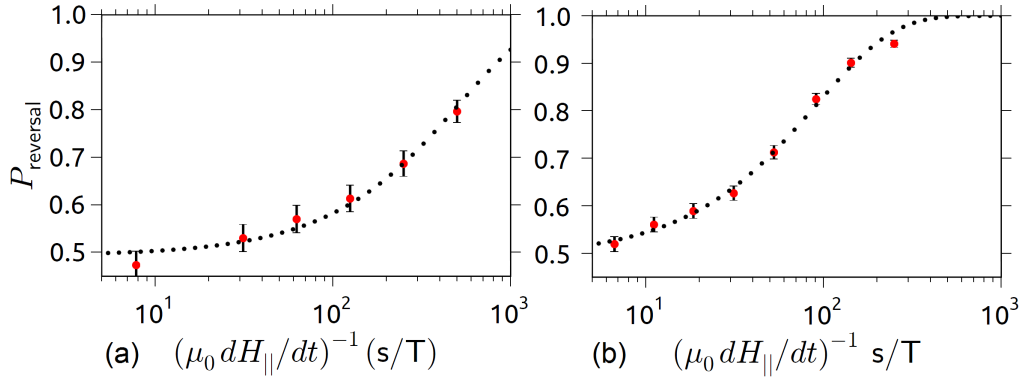


Fig. 5.7 Probability of observing a quantum tunneling of magnetization of a single electronic spin as a function of the magnetic field sweep rate  $\mu_0 dH_{\parallel}/dt$  for two different samples. The experimental results (red dots) were fitted to the function  $P_{reversal} = 1 - A \exp(BdH_{\parallel}/dt)$ .

with  $\Delta$  the tunnel gap energy,  $g_J$  the  $g$ -factor of the spin and  $\Delta_{m_J}$  the momentum difference between the two states. Here, we investigate this process for a single electronic spin. First the bias and gate voltage of the transistor are tuned to be at a working point which gives two different conductances for the two electronic spin states as explained in section 5.1.1. Then, in order to measure the reversal probability, the magnetic field is swept back and forth between  $-80$  mT and  $+80$  mT at different sweep rates. Afterwards, we calculate the probability to observe an electronic spin reversal per sweep. This measurement was performed on two samples, resulting in figure 5.7.

We found that for the smallest sweep rates the reversal probability was exponentially approaching 100 %, while it converged to 50 % for the fastest sweep rates instead of zero as expected from the Landau-Zener model. Since this phenomenon was measured for two samples independently, this behaviour is most likely device independent and originates from an underlying physical interaction. The first idea to explain the deviation from the original theory is to investigate the relaxation and decoherence processes taking place at the anti-crossing. To answer this question, we investigated the measurements. As shown in figure 5.8, we distinguish 6 different kinds of events. Starting from the  $+6$  states (conductance in the blue windows) :

- LZ1 : stay in the  $|+6\rangle$  state
- LZ2 : jump in the  $|−6\rangle$  state
- LZ3 : jump in the  $|−6\rangle$  state and jump back to the  $|+6\rangle$  state

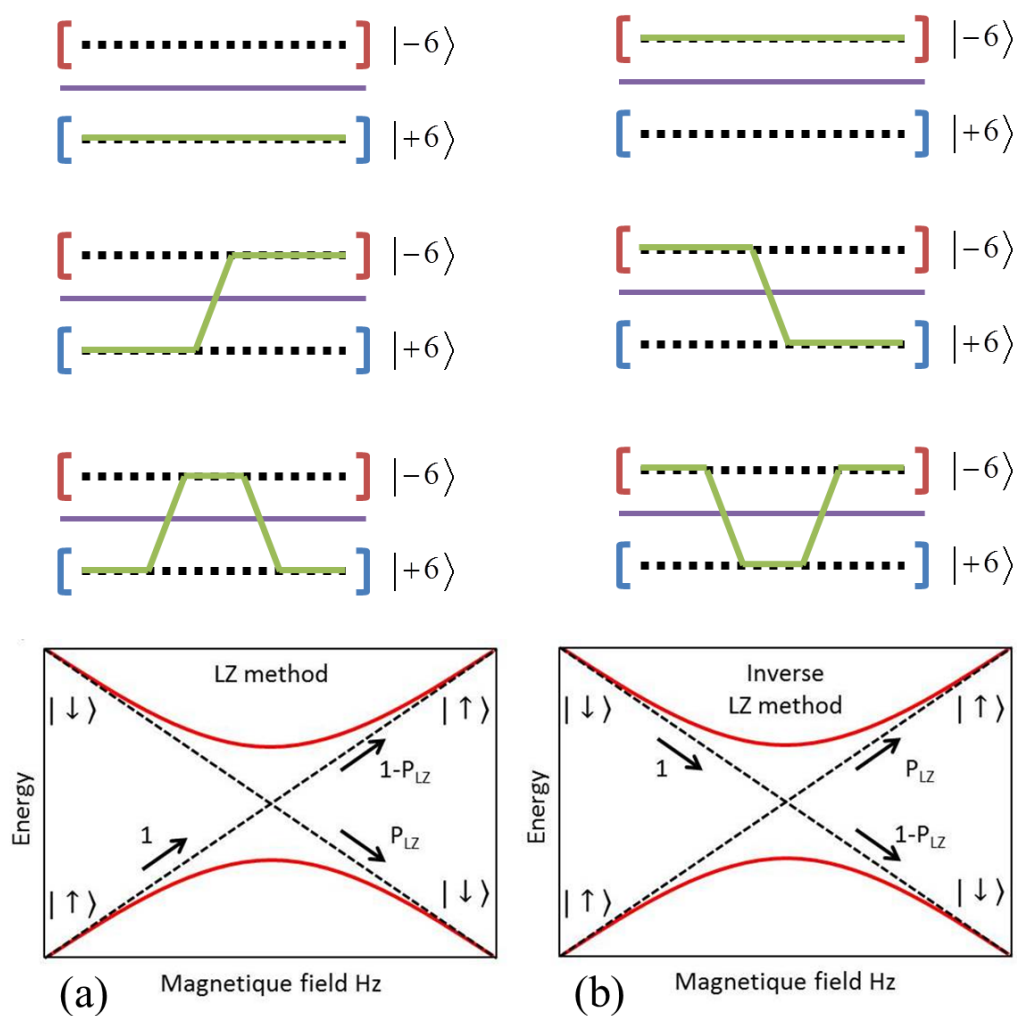


Fig. 5.8 Depending if the initial state is rather up or down, the experiment gives access to the Landau-Zener (a) or the inverse Landau-Zener probability (b). The conductance (green curve) scheme shows how the different kind of events are discriminated.

The direct relaxation time is of the order of hundreds of second for a parallel field of 80mT (see previous section 5.1.2). This is much longer than the back and forth magnetic field sweep which is of the order of two seconds so the probability of starting the sweep in the excited states is sufficiently high to be measured, giving Inverse Landau-Zener events :

- ILZ1 : stay in the  $|-6\rangle$  state
- ILZ2 : jump in the  $|+6\rangle$  state
- ILZ3 : jump in the  $|+6\rangle$  state and jump back to the  $|-6\rangle$  state

Then we define the Landau-Zener  $P_{LZ}$  and inverse Landau-Zener  $P_{ILZ}$  probabilities :

$$P_{LZ} = P_{GS \rightarrow GS} = \frac{\#LZ_2}{\#LZ_1 + \#LZ_2} \quad (5.26)$$

$$P_{ILZ} = P_{ES \rightarrow ES} = \frac{\#ILZ_2}{\#ILZ_1 + \#ILZ_2} \quad (5.27)$$

Thanks to a theoretician-experimentalist collaboration with Filippo Troiani from the university of Modena, we simulated the system dynamics by means of a master-equation in the Lindblad form [109]:

$$\dot{\rho} = \frac{i}{\hbar} [\rho, H(t)] + \sum_k \left[ 2L_k(t)\rho L_k^\dagger(t) - L_k^\dagger(t)L_k(t)\rho - \rho L_k^\dagger(t)L_k(t) \right], \quad (5.28)$$

where the time-dependent Hamiltonian associated to the sweeping magnetic field is defined as:

$$H(t) = \frac{\alpha(t - T/2)}{2} (|\uparrow\rangle\langle\uparrow| - |\downarrow\rangle\langle\downarrow|) + \frac{\Delta}{2} (|\uparrow\rangle\langle\downarrow| + |\downarrow\rangle\langle\uparrow|). \quad (5.29)$$

$\alpha$  and  $T$  being respectively the magnetic field sweep rate and duration. The Lindblad operators  $L_k$  are responsible for the incoherent components of the system dynamics. To illustrate the physical meaning of the Lindblad operator, we recall that a pure dephasing affecting the two-level system can always be described by a Lindblad operator of the form:

$$L = L(a, b) = \frac{1}{2\sqrt{\tau_d}} (|a\rangle\langle a| - |b\rangle\langle b|), \quad (5.30)$$

The main idea of this theoretical approach is to find the relevant basis in which we apply the dephasing process:

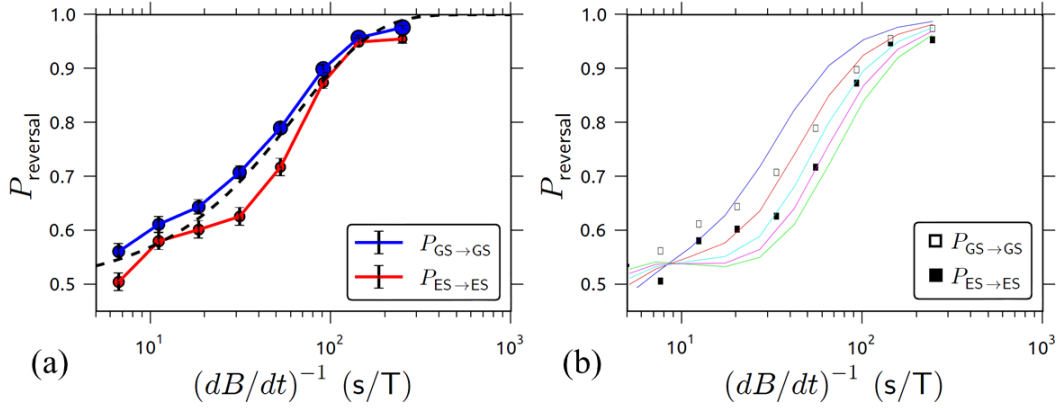


Fig. 5.9 (a) Direct and inverse Landau-Zener probabilities as a function of the  $dB/dt$ , each point correspond to 2000 sweeps to obtain the statistics. (b) Different fit obtained using the averaging Lindblad operator model, each colour correspond to a specific ratio in between the time to go through the anticrossing and the averaging time  $\frac{\tau_{ac}}{\tau_{av}}$  (40 in blue, 32 in red, 27 in turquoise, 23 in pink and 20 in green) for a dephasing time equal to  $\frac{\tau_{av}}{20}$ .

- The diabatic basis: obtained by identifying  $|a\rangle$  and  $|b\rangle$  with the states  $|\uparrow\rangle$  and  $|\downarrow\rangle$ . In this case the dephasing affects the spin-reversal probability by destroying the phase coherence between  $|\uparrow\rangle$  and  $|\downarrow\rangle$  at the avoided level crossing.
- The adiabatic basis: obtained by identifying  $|a\rangle$  and  $|b\rangle$  with the time-dependent eigenstates of the Hamiltonian ( $|\lambda_1(t)\rangle$  and  $|\lambda_2(t)\rangle$ ). In this case the dephasing affects the spin-reversal probability by destroying the phase coherence between the eigenvalues at the avoided level crossing.

We then showed that for a model where dephasing takes place with respect to the diabatic basis cannot explain the observed dependence of the spin-reversal probability on the field sweep rate and specifically the increase of  $P_{\uparrow \rightarrow \downarrow}$  from 0.5 to 1 for decreasing values of the sweeping rate. At the same time, a model where dephasing acts in the adiabatic basis is thus fully compatible with the behavior observed at low sweeping rates. However, it cannot explain the behavior observed for the saturation of  $P_{\uparrow \rightarrow \downarrow}$  to 0.5 in the opposite limit.

In order to explain the overall dependence of the spin-reversal probability, we introduced a phenomenological model, where dephasing is defined with respect to time-dependent eigenstates of the Hamiltonian  $H$ , as in the adiabatic model, but now averaged over a time interval of length  $\tau_{av}$ . Correspondingly, the Lindblad operator is given by:

$$L(t) = \frac{1}{\tau_{av}} \int_{-\tau_{av}/2}^{\tau_{av}/2} L[\lambda_1(t+\tau), \lambda_2(t+\tau)] d\tau. \quad (5.31)$$

Such expression results from the assumption that dephasing is mainly induced by the continuous measurement, which is characterized by a finite time resolution. Numerical simulations show that the effect of dephasing on the system dynamics critically depends on the value of  $\tau_{av}$  relative to  $\tau_{ac} = \Delta \frac{dt}{dB}$ , which gives the characteristic time scale over which the adiabatic states change at the anticrossing. A qualitative agreement between the experimental curves and the simulations is achieved by assuming that the system is close to adiabaticity in all the considered range of values of  $\tau_{ac}$ .

### Nuclear spin read-out signal analysis

So far, our only concern was to study the dynamic of the electronic spin. We then only measured the conductance before and after a magnetic field sweep in order to obtain the electronic spin orientation. However, as presented in figure 2.7 (c), the hyperfine interaction induces a splitting into four anti-crossings, which are nuclear spin dependent. As a result, each QTM events, which result in jumps of the read-out dot's conductance, can be assigned to the nuclear spin state by knowing where a conductance jump occurred during the magnetic field sweeps. Here we make an analysis of the conductance through the single molecular magnet transistor during the magnetic field sweep which results in the nuclear spin read-out methods.

Using a python post treatment program, the measurement of the conductance of hundreds of magnetic field sweep going from -60mT to +60mT are passed through a filter, which computed the first derivative with an adjustable smoothing over N data points. At the output of the filtered signals each jumps have been converted into peaks, which are extracted by an extrema method. To take into account only the signal corresponding the QTM events, a statistical study of the peak height of the filtered signal was performed. In results, the peaks height histogram are shown in 5.10(b), for which two distributions are clearly identifiable :

- a distribution with small jumps in the red part, corresponding to the measurement noise.
- A distribution of higher jumps in the blue part, corresponding to reversals of the magnetization.

With this histogram, we can set a threshold to filter out the jumps arising from the noise. From the selected jumps, a statistical study of the reversal fields of the magnetization is carried out. In the histogram of the magnetic field jumps value (5.10(d)), it is easy to

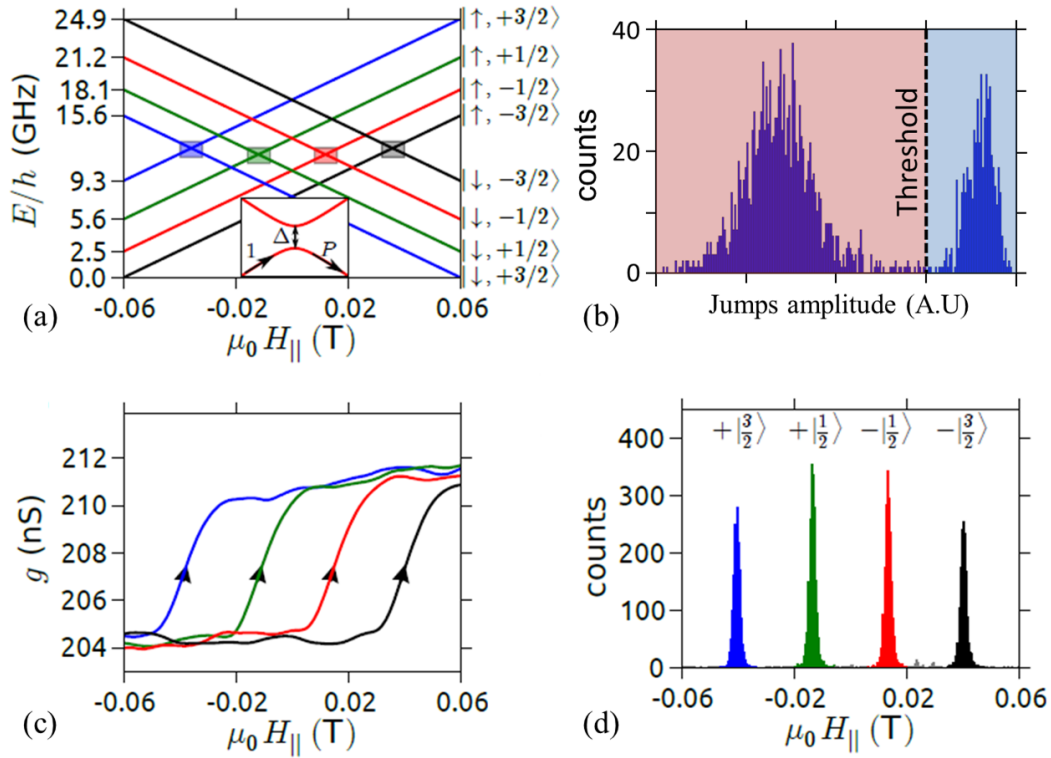


Fig. 5.10 (a) Zeeman diagram of the TbPc<sub>2</sub>, the colored rectangles indicate avoided level crossing between two states of opposite electronic spin and identical nuclear spin. (c) Raw data showing four measurements with a spin reversal (blue, green, red, and black curve). (b) Histogram of the maximum amplitudes of all filtered sweeps. Measurements without a spin reversal (red part) can be separated from measurements containing a reversal (blue part) by a threshold. (d) Histogram of the jump positions whose filtered maxima were within the blue rectangle of (b). The four peaks originate from conductance jumps in the vicinity of the four anticrossings and allow for the unambiguous attribution of each detected conductance jump to a nuclear spin qubit state.

identify four non overlapping peaks which correspond to the four high flipping probability fields of the molecular magnet magnetization. A comparison of this measurement with the Zeeman diagram of the TbPc<sub>2</sub> molecule (5.10(a)) shows that each histogram peak can be associated with one of the anti-crossings identified by squares. Because the four peaks are non overlapping, we can define four magnetic field windows corresponding to the 4 nuclear spin states. As a result, the measurement of the magnetic field at which the conductance jump makes up an indirect measurement of the terbium nucleus spin state. This latter property is used in the following of this thesis to study the nuclear spin dynamic.

### Discussion on the nuclear spin measuring time

A little discussion about the measuring time using this methods can be done. What we need is to distinguish the four peaks in the conductance jump histogram. It is first necessary to sweep the magnetic field through the four anti-crossing back and forth. The field distance between the 2 further anti-crossing is about 80mT. Because the coils have hysteresis, due to their intrinsic impedance, we need to sweep the magnetic field a bit further than the anti-crossing position. The faster we sweep, the higher the hysteresis is. Second point is that we record the QTM events, and we previously observed that the QTM probability decreases when the speed of the magnetic field sweep increases. Note that the saturation to 50% of this QTM probability for high speed sweep is a good point for us. A last point to take into account is the fact that we are using a lock-in method to measure the conductance. This technique has a certain integration time  $\tau \approx 5ms$  that limits the time resolution of the conductance jump event, so that if we sweep the magnetic field too fast we will lose the four peaks resolution. Taking into account these limitations, I swept the magnetic field over 120mT with a rate of  $100mT/s$ . In this limit, the QTM probability is of the order of 0.5 so that I need approximately 2 sweeps, in average, to make a nuclear spin measurement. As a result, the nuclear spin measurement time is of the order of 2.4 seconds. Maybe I could win few hundreds of millisecond per sweep but we are not so far from the experimental limit using this method. Others ideas will be developed in the outlook part of this thesis (chapter 8). This point is very limiting in our experiment because it takes hours to have enough statistic on the nuclear spin population, meaning that we need a great stability all over these measurements. The good point is that this measuring time is, as we will see in the next paragraph, much smaller than the life time of the nuclear spin states. This is crucial for quantum manipulation.

### 5.2.2 Nuclear spin lifetime

We sweep the magnetic field back and forth from +60mT to -60mT. If a jump occurred within a window of  $\pm 7$  mT around the avoided level crossing, then it was assigned to the corresponding nuclear spin state. If, however, a jump was recorded outside this window, the measurement was rejected. We thus obtain the real-time image of the nuclear spin trajectory (figure 5.11 (a)). In order to access the nuclear spin relaxation time  $T_1$ , we performed a bit by bit post-processing of this nuclear spin trajectory. Therefore, we extracted the different dwell times, *i.e.* the time the nuclear spin remained in a certain state before going into another one. Plotting these dwell times for each nuclear spin state in separate renormalized histograms yielded the black data points of figure 5.11 (b). Fitting to an exponential function  $y = \exp(-t/T_1)$  gave the nuclear spin dependent relaxation times  $T_1 \approx 17s$  for  $m_I = \pm 1/2$  and  $T_1 \approx 34s$  for  $m_I = \pm 3/2$ . The factor two between these 2 lifetimes comes from the number of transitions offered to the nuclear spin to relax or excite:

- if the nuclear spin is in the  $|+1/2\rangle$  ( $|-1/2\rangle$ ) state it can jump in the  $|-1/2\rangle$  ( $|+1/2\rangle$ ) or in the the  $|3/2\rangle$  ( $|-3/2\rangle$ )state.
- If the nuclear spin is in the  $|+3/2\rangle$  ( $|-3/2\rangle$ ) state it can only jump in the  $|1/2\rangle$  ( $|-1/2\rangle$ ) state.

With an equal rate for each path, the lifetime is roughly inversely proportional to the number of transition paths. As a result the relaxation time  $T_1$  shows a change of approximately a factor two.

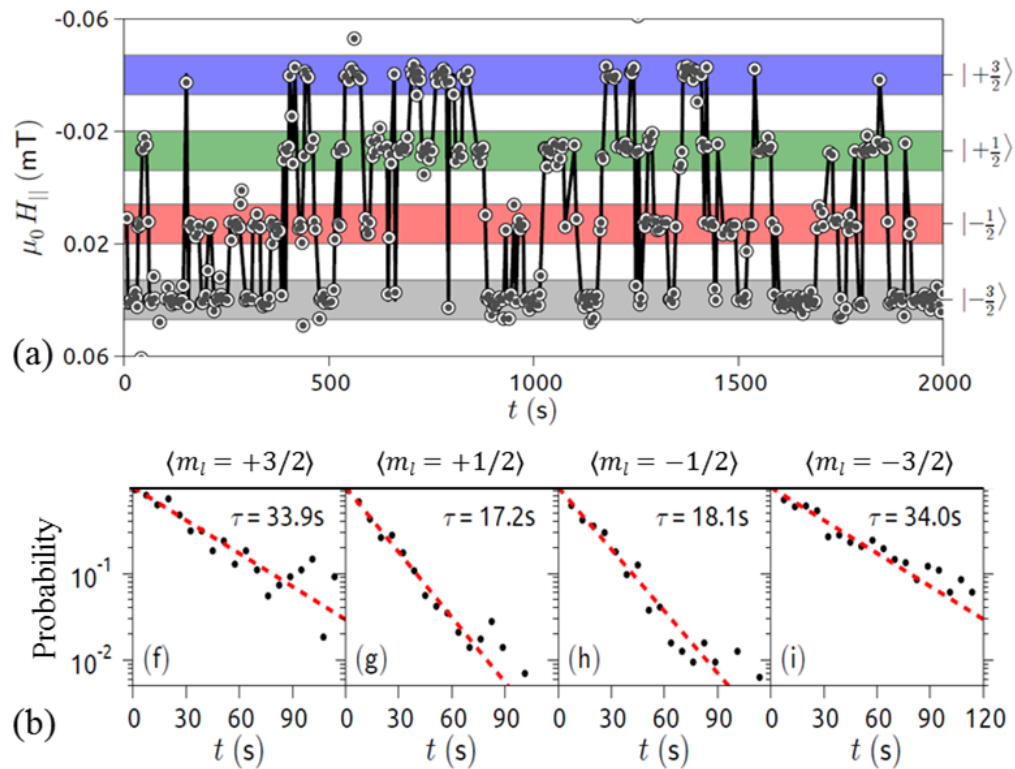


Fig. 5.11 (a) The black line show the first 2000 s of the nuclear spin trajectory. Using the signal analysis method describes in sec. 5.2.1 each conductance jump (grey dot) was assigned to the corresponding nuclear spin state. (b) Plotting the dwell times for each nuclear spin state in separate histograms led to the black data points. A further fitting to the exponential function  $y = \exp(-t/T_1)$  (red dotted line) yielded the relaxations times  $T_1$  for each nuclear spin state.



# Chapter 6

## Nuclear spin transitions coherent manipulation

So far we have discussed the steady states properties, demonstrating our ability to read-out a single nuclear spin. Now we will consider the AC regime, starting with a general discussion about the interaction of a single spin with an explicitly time-dependant magnetic field from a theoretical point of view. We will next describe a mechanism of hyperfine Stark effect, thanks to which an electric field can be used to act on the nuclear spin. The main result of this mechanism, whose formalism was worked out with Rafik Ballou, is to give rise to an effective magnetic field on the nuclear spin, which allows both the tunability of the nuclear spin resonance, by applying a DC electric field, and a coherent manipulation of the nuclear spin, using an AC electric field.

The manipulation of quantum states is said to be coherent when their phases are well controlled. To experimentally demonstrate this specific behaviour we will present the historical Rabi oscillation measurement. Then, in order to understand the mechanisms that make the system going from a quantum dynamic to a classical one, the so-called decoherence processes, we will describe two different measurements: the Ramsey fringes and the spin-echo. Finally, to slowly go from the qubit dynamic to the multi-level one, we will play with different transitions in a same pulse sequence to perform a coherent pump-probe.

### 6.1 Magnetic Field-Qubit interaction

As explained in the introduction section of this thesis, "*quantum information process is a succession of unitary matrices  $U$  describing quantum gates which are related to the physical processes by which they are achieved via the equation  $U = e^{-\frac{iHt}{\hbar}}$ ". The goal of this section*

is to make the link between this equation and my experiment. The simplest case is first to consider a two-level system  $|0\rangle$  and  $|1\rangle$  separated by an energy  $\hbar\omega_{01}$ . Due to superposition principle, a state of such a system is defined as :

$$|\psi\rangle = \alpha|0\rangle + \beta|1\rangle \quad (6.1)$$

with  $\alpha$  and  $\beta$  two complex numbers. To clarify the notation and because we will use transfer matrices, mathematically, kets stand for column vectors of a 2D Hilbert space:

$$|0\rangle = \begin{pmatrix} 1 \\ 0 \end{pmatrix} \quad |1\rangle = \begin{pmatrix} 0 \\ 1 \end{pmatrix} \Rightarrow |\psi\rangle = \begin{pmatrix} \alpha \\ \beta \end{pmatrix} \quad (6.2)$$

The normalization of the kets implies that:

$$\langle\psi|\psi\rangle = \|\alpha\|^2 + \|\beta\|^2 = 1 \quad (6.3)$$

Which is automatically satisfied if we write the states of the system in term of spherical angles (polar  $\theta$ , azimuth  $\phi$ ):

$$|\Psi\rangle = \cos(\theta/2)e^{-i\phi/2}|0\rangle + \sin(\theta/2)e^{i\phi/2}|1\rangle \quad (6.4)$$

Such a representation is very useful: a qubit state is represented by its position on a sphere of radius one (the so-called Bloch-sphere) and its time evolution can be described as the trajectory of a dot on the sphere surface.

Now, we introduce this qubit, which is a nuclear spin in our case, in an oscillating magnetic field  $\mathbf{B}$ . The Hamiltonian of the system writes then:

$$H(t) = H_{qubit} + H_{int}(t) \quad (6.5)$$

$$= \frac{\hbar\omega_{01}}{2}\sigma_z + g\mu_N\mathbf{B} \quad (6.6)$$

The magnetic field frequency is set to  $\omega_p$  with a phase  $\phi_p$  and the polarization is arbitrarily taken along the x axis. We further define  $\Omega = g\mu_NB_0/\hbar$  so that:

$$H(t) = \frac{\hbar\omega_{01}}{2}\sigma_z - \frac{\hbar\Omega}{2}[e^{i(\omega_pt-\phi_p)} + e^{-i(\omega_pt-\phi_p)}]\sigma_x \quad (6.7)$$

where  $\sigma_z$  and  $\sigma_x$  are the Pauli Matrices as defined in eq. 1.3. A fast analysis of this Hamiltonian shows that we have a constant rotation of the figurative point on the Bloch

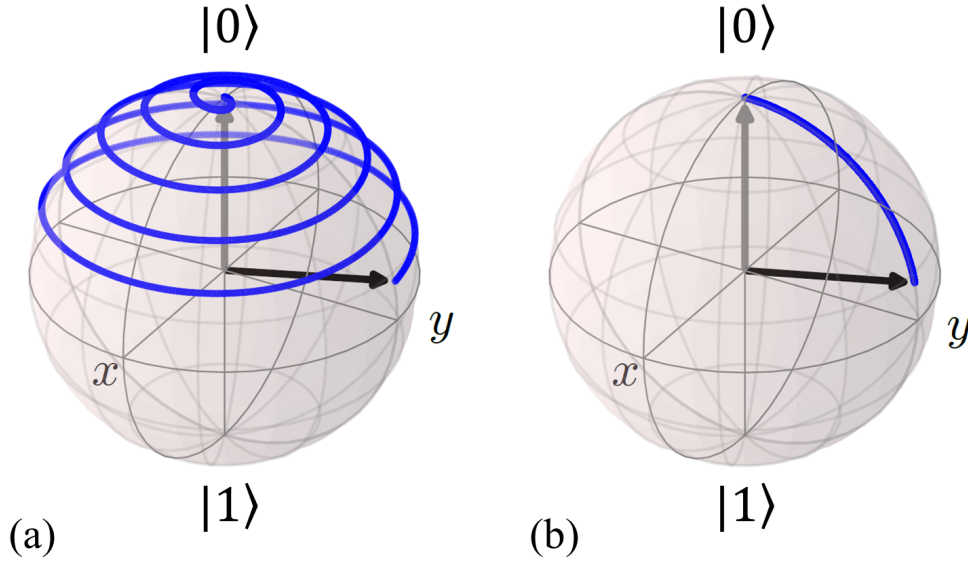


Fig. 6.1 Arbitrary trajectory of a spin qubit in the laboratory frame (a) and the rotating frame (b) illustrating the merit of this transformation.

sphere around the z axis at the constant frequency  $\omega_{01}$ . To simplify the study of the system's dynamic, we go from the laboratory frame to the rotating frame at the frequency  $\omega_p$  around the z axis. This amounts to the variable change:

$$|\hat{\Psi}\rangle = e^{i\omega_p t \sigma_z/2} |\Psi\rangle \quad (6.8)$$

The Bloch-sphere interpretation of this variable change is represented in the figure 6.1. The new Hamiltonian  $\hat{H}$  in the rotating frame becomes :

$$\hat{H} = \frac{\hbar(\omega_{01} - \omega_p)}{2} \sigma_z - \frac{\hbar\Omega}{2} [e^{i(\omega_p t - \phi_p)} + e^{-i(\omega_p t - \phi_p)}] e^{i\omega_p t \sigma_z/2} \sigma_x e^{-i\omega_p t \sigma_z/2} \quad (6.9)$$

It is hard to work out an intuitive picture with this relation. In order to understand the underlying dynamics, we will look at two particular cases, first the resonant case then the constant pulse phase case.

### Resonant interaction

In the case of a resonant interaction *i.e.*  $\omega_{01} = \omega_p$ , the  $\sigma_z$  term vanishes out and the Hamiltonian can be rewritten as:

$$\hat{H} = -\frac{\hbar\Omega}{2} [\cos \phi_p \sigma_x - \sin \phi_p \sigma_y] \quad (6.10)$$

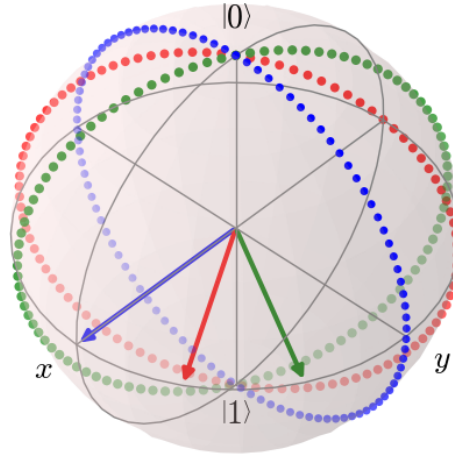


Fig. 6.2 a) Evolution of the qubit state in the Bloch sphere for different values of pulse phase ( $0$ ,  $\frac{\pi}{3}$  and  $\frac{2\pi}{3}$  respectively in blue, red and green)

The Schrödinger equation applied to this specific case of a time independent Hamiltonian results in an unitary evolution of the qubit state, fully described by the evolution operator  $U(t - t_0)$  :

$$|\hat{\Psi}(t)\rangle = U(t - t_0) |\hat{\Psi}(t_0)\rangle \quad (6.11)$$

Where  $t_0$  is the moment we switch on the field-qubit interaction. Using the Schrödinger equation, we get the expression of this evolution operator :

$$U(t - t_0) = e^{-i\Omega(t-t_0)\sigma_r/2} \quad (6.12)$$

with  $\sigma_r$  the rotation matrix around the r axis defined so that  $\sigma_r = \cos \phi_p \sigma_x - \sin \phi_p \sigma_y$ .

It is interesting to highlight two things in this resonant pulse limit. We recall that the measurement of the state is a projection on  $\sigma_z$ .

- If the qubit initial state is a polar state *i.e.*  $|0\rangle$  or  $|1\rangle$ , the experimental observable will be pulse phase independent.

$$\|\sigma_z |\Psi(t-t_0)\rangle\|^2 = \|\sigma_z U(t-t_0) |\Psi(t_0)\rangle\|^2 \quad (6.13)$$

$$= \sin^2[\Omega(t-t_0)/2] \quad (6.14)$$

Then we will observe an oscillation of the population, the so-called Rabi oscillation, at the frequency  $\Omega$ .

- If the initial state is an arbitrary state, then the dynamic that we observe is impacted. This is typically what happens during a pulse phase jump.

### Constant phase pulse interaction

The second particular case is when the phase of the pulse is constant during the whole interaction. In this limit it is much easier to see the dynamic with a certain detuning between the pulse and the two-level system. The Hamiltonian in the rotating frame is now :

$$\hat{H} = \frac{\hbar}{2} [\Delta\sigma_z - \Omega\sigma_x] \quad (6.15)$$

The evolution operator is the same as in 6.12 but the rotation axis is different:  $\sigma_r = \cos\Theta\sigma_x - \sin\Theta\sigma_z$ , with  $\Theta = \arctan \frac{\Omega}{\Delta}$  defining the angle of rotation in the (x,z) plane of the Bloch sphere. For this particular case, an ansatz for the higher energy state probability does exist :

$$P(|1\rangle) = \frac{\Omega}{\sqrt{\Omega^2 + \Delta^2}} \sin^2\left(\frac{\sqrt{\Omega^2 + \Delta^2}}{2}t\right) \quad (6.16)$$

The amplitude ( $1 \mapsto \frac{\Omega}{\sqrt{\Omega^2 + \Delta^2}}$ ) as well as the frequency of the oscillation ( $\Omega \mapsto \sqrt{\Omega^2 + \Delta^2}$ ) are affected by this detuning. Trajectories for different detuning value are represented in figure 6.3 with their associated excited state probability evolution.

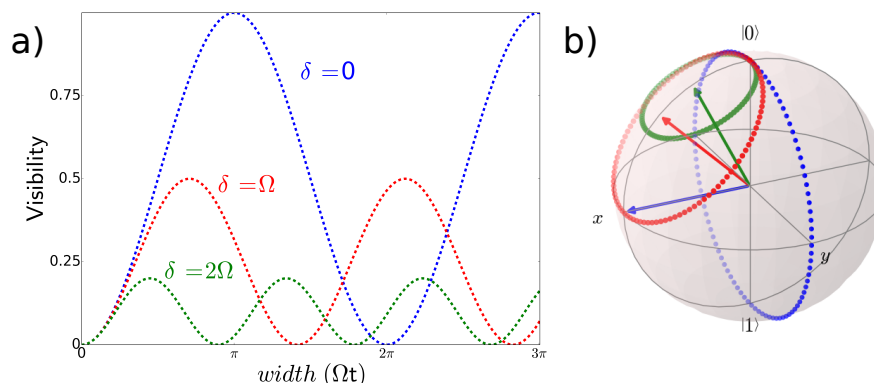


Fig. 6.3 a) Evolution of the excited state population as a function of the pulse duration for different values of detuning. b) Representation in the Bloch Sphere of the corresponding trajectory

### Qubit Manipulation

In an experimental point of view, it is important to remind this correspondence between pulse property and qubit dynamic :

- The frequency of the pulse determines the rotation angle in the (x,z) plane
- The phase of the pulse determines the rotation angle in the (x,y) plane
- The length and the power of the pulse determine the distance travelled by the state during the pulse.

## 6.2 From magnetic to electric manipulation: Stark effect

It was experimentally found out that fast manipulation of the nuclear spin can be achieved by means of an electric field. As discussed in section 6.4.2 this cannot be explained by the interaction of the nuclear magnetic moment with the magnetic field created by the antenna microbounded in the vicinity of the molecular magnet transistor nor with the tunnel current through the molecule. As a matter of fact, the physics of the fast electric manipulation of the nuclear spin relies on the hyperfine Stark effect. In its more general form this interaction writes :

$$H_{hf} = \sum_k (nT^{(k)} \cdot eT^{(k)}) = \sum_{kq} (-)^{k-q} nT_q^{(k)} \cdot eT_{-q}^{(k)} \quad (6.17)$$

where  $nT^{(k)}$  and  $eT^{(k)}$  stand for  $k$ -order tensor operator that act solely on the nuclear (n) and electronic (e) states respectively. This form arises from the multipole expansions of the electromagnetic interaction between the nuclear and electronic distribution of the stationary charges and the stationary currents inherent to both orbital motion and spins [110]. The charge contribution to  $T^{(k)}$  has parity  $(-)^k$  while the current contribution to  $T^{(k)}$  has parity  $(-)^{k+1}$ . Assuming that the stationary nuclear states have well define parity, which amounts to ignore the parity violation of the weak interaction, the matrix elements of the charge (respectively current) contributions to  $nT^{(k)}$  in a manifold of constant nuclear spin  $I$  vanishes out for  $k$  odd (respectively even). The matrix elements of  $nT_q^{(k)}$  between the states  $|I, M_I\rangle$  of a nuclear spin  $I$  are proportional to the Clebsch-Gordon coefficient  $\langle I, M_I, kq | I, M_I' \rangle$  according to the Wigner-Eckart theorem. They therefore are null if the conditions  $0 \leq k \leq 2I$  and  $M_I + q = M_I'$  are not met. In the case of the only stable isotope  $^{159}\text{Tb}$  of Terbium the nuclear spin of which is  $I = 3/2$  this implies that the multipoles expansions are limited to magnetic dipoles ( $k = 1$ ), electric quadrupoles ( $k = 2$ ) and magnetic octupoles ( $k = 3$ ). We will focus our attention in the following to the magnetic dipole hyperfine interaction ( $k = 1$ ), which for electronic states restricted to the space of constant total angular momentum  $J$ , simplify into:

$$H_{hf} = A \mathbf{I} \cdot \mathbf{J} \quad (6.18)$$

Thanks again to the Wigner-Eckart theorem. In view of our ability to manipulate the Tb nuclear spin in the  $\text{TbPc}_2$  and the lack of evident explanations it appeared of most interest to investigate to which extent the interactions  $A \mathbf{I} \cdot \mathbf{J}$  might be modified under an electric field  $\mathbf{E}$ .

The problem was approached in the Stefan Thiele thesis where it was argued that the magnetic dipole hyperfine field constant  $A$  is modified by a relative amount  $\Delta A/A$  estimated to  $10^{-3} \mathbf{E}$  (mV/nm) which provides the right magnitude of the effective magnetic field required to manipulated the nuclear spin. I will recall here this approach in an intuitive way. I will first discuss the magnetic dipolar hyperfine interaction. I will then emphasize the parity mixing of the  $\text{Tb}^{3+}$  electronic states induced by the ligand field owing to the lack of inversion center in the molecule. I will finally indicate that, although tiny, this parity mixing allows modifying the hyperfine field constant to first order in the electric field  $\mathbf{E}$ . As a matter of fact I will show that the dynamical manipulation of the nuclear spin by the electric field is fully explained by AC Stark hyperfine effect. A more numerical approach will be necessary in the case of the DC Stark hyperfine effect. I shall end this section with a few comments on the electric field dependence of the electric quadrupole hyperfine interactions.

## 6.2.1 Magnetic dipole hyperfine field Stark effect

### Magnetic dipole hyperfine interaction

The magnetic dipole hyperfine interaction arises from the interaction of the nuclear magnetic moment  $\boldsymbol{\mu}_{nuc}$  with the magnetic field  $\mathbf{B}_{elec}$  created by the surrounding electrons:

$$H_{hf} = -\boldsymbol{\mu}_{nuc}\mathbf{B}_{elec} \quad (6.19)$$

$\mathbf{B}_{elec}$  consists of two contributions. The first,  $\mathbf{B}_{orbit}$ , is due to the charge motion of the electrons about the nucleus and the second,  $\mathbf{B}_{spin}$ , is generated by the spin magnetic moment of the electron.  $\mathbf{B}_{orbit}$  is straightforwardly obtained from the Biot-Savart law, according to which the magnetic field created by a moving electron  $i$  at a certain velocity  $\mathbf{v}_i$  and a distance  $\mathbf{r}_i$  from the core is:

$$\mathbf{B}_i^0 = \frac{\mu_0}{4\pi} e\mathbf{v}_i \times \frac{\mathbf{r}_i}{r_i^3} \quad (6.20)$$

Summing this contribution over all the electrons and using the angular momentum definition  $\mathbf{l}_i = -\frac{e}{2\mu_B}\mathbf{v}_i \times \mathbf{r}_i$  give the final expression of the orbital component of the magnetic field:

$$\mathbf{B}_{orbit} = -\frac{\mu_0}{4\pi} 2\mu_B \sum_i \frac{\mathbf{l}_i}{r_i^3} \quad (6.21)$$

In evaluating  $\mathbf{B}_{spin}$  we must care about the case where the electrons move too close to the nucleus. The magnetic field will then show a singularity of order  $r_i^{-3}$ . The potential vector associated with a magnetic moment  $\boldsymbol{\mu}_s^i$  at a distance  $\mathbf{r}_i$  is

$$\mathbf{A}_i^s = \frac{\boldsymbol{\mu}_s^i \times \mathbf{r}_i}{r_i^3} = \nabla \times \frac{\boldsymbol{\mu}_s^i}{r_i} \quad (6.22)$$

Which leads to the magnetic field:

$$\mathbf{B}_i^s = \nabla \times \mathbf{A}_i^s \quad (6.23)$$

$$= \nabla \times \left( \nabla \times \frac{\boldsymbol{\mu}_s^i}{r_i} \right) \quad (6.24)$$

$$= \left[ (\boldsymbol{\mu}_s^i \cdot \nabla) \nabla - \frac{1}{3} \boldsymbol{\mu}_s^i \nabla^2 \right] \frac{1}{r_i} - \frac{2}{3} \boldsymbol{\mu}_s^i \nabla^2 \frac{1}{r_i} \quad (6.25)$$

Where the singular part has been isolated in the third term. The quantity between the hooks transform similar to a rank -2 spherical harmonic and therefore is not singular. It follows

that:

$$\mathbf{B}_{spin} = -\frac{\mu_0}{4\pi} \sum_i \frac{\boldsymbol{\mu}_s^i}{r_i^3} - \frac{3\mathbf{r}_i(\boldsymbol{\mu}_s^i \cdot \mathbf{r}_i)}{r_i^5} + \frac{8\pi}{3} \boldsymbol{\mu}_s^i \delta(\mathbf{r}_i) \quad (6.26)$$

The third contribution  $\frac{8\pi}{3} \boldsymbol{\mu}_s^i \delta(\mathbf{r}_i)$  is the one that gives rise to the hyperfine magnetic contact interaction. It is sensitive to first order to every change of the electronic density in the vicinity of the nucleus that would be induced by an electric field, provided that the nucleus is not located at a site with inversion symmetry (otherwise the sensitivity is to second order in the electric field) [111]. It is this Stark hyperfine field effect that is exploited to manipulate the Silicon qubit [112]. In our case, because the 4f electrons show zero probability density on the nucleus, this cannot work.

After summation of the different contributions and by substituting  $\mathbf{l}_i = -2\mu_B \mathbf{s}_i$  and  $\boldsymbol{\mu}_{nuc} = g_N \mu_N \mathbf{I}$ , we get the following expression of the magnetic dipole hyperfine Hamiltonian

$$H_{hf} = \frac{\mu_0}{4\pi} 2g_N \mu_N \mu_B \sum_i \left[ \frac{\mathbf{l}_i - \mathbf{s}_i}{r_i^3} + \frac{3\mathbf{r}_i(\mathbf{s}_i \cdot \mathbf{r}_i)}{r_i^5} \right] \cdot \mathbf{I} \quad (6.27)$$

$$= a \sum_i (\mathbf{N}_i / r_i^3) \cdot \mathbf{I} \quad (6.28)$$

where  $a = \frac{\mu_0}{4\pi} 2g_N \mu_N \mu_B$  is a constant and  $\mathbf{N}_i = \mathbf{l}_i - \mathbf{s}_i + 3\mathbf{r}_i(\mathbf{s}_i \cdot \mathbf{r}_i)/r_i^2$  the operator that characterizes the way the  $i^{th}$  electron of spin  $\mathbf{s}_i$  and angular momentum  $\mathbf{l}_i$  at a distance  $\mathbf{r}_i$  from the nucleus interacts with the nuclear spin  $\mathbf{I}$ .

### Ligand field perturbation on the electronic configuration

Let us point out before some useful outcomes of the parity symmetry:

- The parity  $P$  of an electronic state is defined as  $P = (-1)^{\sum l_i}$  with  $l_i = 0, 1, 2, 3, \dots$  for  $s, p, d, f, \dots$  configurations. It follows that the parity of all the states  $|\Psi\rangle$  of the ground configuration  $4f^8$  is -1 (even) and the parity of all the states  $|\Phi\rangle$  of the first excited configuration  $4f^7 5d^1$  is 1 (odd).
- The matrix elements of an operator  $O$  of even parity, *i.e.* invariant under the space inversion, are non zero solely between states with the same parity. Whereas the matrix elements of an operator  $O$  of odd parity, *i.e.* reversed under the space inversion, are non zero solely between states with the opposite parity

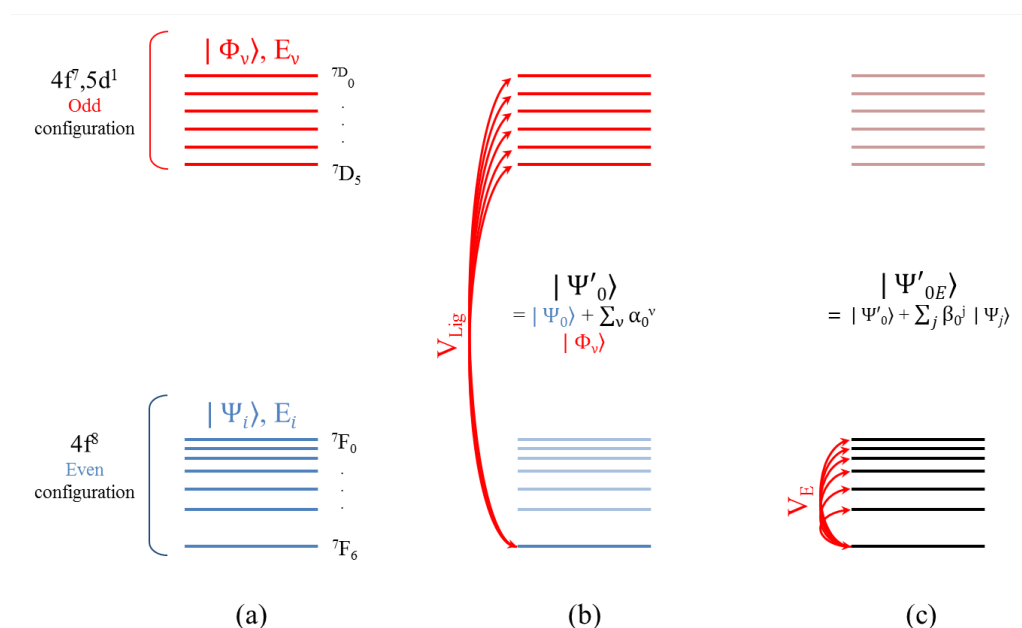


Fig. 6.4 Scheme of the Stark effect applied to the  $\text{Tb}^{3+}$  ion. The colour code indicates the parity: red for even, blue for odd and black when there is no parity. (a) Schematization of the electronic structure of the isolated  $\text{Tb}^{3+}$  ion, comprising ground state electronic configuration  $4f^8$ , composed of the states  $|\Psi_i\rangle$ , and the first excited electronic configuration  $4f^7 5d^1$ , composed of the states  $|\Phi_v\rangle$ . (b) Under the influence of odd parity components of the ligand field  $V_{\text{odd}}$ , the ground state and excited state configurations are slightly mixed. (c) As a consequence an electric field will be able to modify the electronic ground states to first order through the Stark interaction  $V_E$ .

- The position vector  $\mathbf{r}$  is reversed by space inversion (polar vector) whereas the orbital  $\mathbf{l}$  and spin  $\mathbf{s}$  moment are invariant (axial vectors). It follows that the dipole electric moment operator  $\mathbf{d}$  is of odd parity while the operator  $\mathbf{N}$  is of even parity.

We recall that the isolated  $\text{Tb}^{3+}$  ion ground state configuration is  $4f^8$ . The first excited state configuration is  $4f^7 5d^1$ . These configurations are split into spectral terms of total spin  $S = \sum_i s_i$  and orbit  $L = \sum_i l_i$  momenta by the electron correlations. Each total angular momentum  $|L - S| \leq J \leq L + S$  by the spin-orbit coupling interaction. Each of these multiplet is thus symbolized  $^{2S+1}X_J$  with  $X=S, P, D, F$  for  $L=0, 1, 2, 3\dots$  (spectroscopic notation). This is schematized in figure 6.4 which also shows the lowest energy multiplet of each configuration of equivalent electrons, namely  $^7F_6$  for the  $4f^8$  configuration and  $^7D_5$  for the  $4f^7 5d^1$  configuration which is about 5.5eV higher in energy from the ground multiplet  $^7F_6$ . Because it is of odd parity, an electric field has zero matrix elements between the states of each configuration so will have no effect in first order. When it is embedded in the  $\text{TbPc}_2$  molecule the electronic structure of the free  $\text{Tb}^{3+}$  ion is modified by electrostatic interaction with the ligand electron. This leads in particular to the splitting of the ground multiplet  $^7F_6$  into crystal field energy levels (see section 2.2). If the  $\text{TbPc}_2$  molecule were to show a centre of symmetry on the  $\text{Tb}^{3+}$  ion site ( $D_{4h}$  point group) then the ligand field will be of even parity and will preserve the parity of the electronic states so that the effect of an applied electric field will be as negligible as in the case of the free  $\text{Tb}^{3+}$  ion. As a matter of fact because the twist of the two phthalocyanine ligands encapsulating the  $\text{Tb}^{3+}$  ion in the  $\text{TbPc}_2$  is not exactly  $45^\circ$  there is no centre of inversion on the  $\text{Tb}^{3+}$  ion site ( $C_4$  point group). Accordingly to the electrostatic interaction of the  $\text{Tb}^{3+}$  ion with the electrons of the ligand will give rise to a ligand field which, in addition to the component of even parity  $V_{ligand}^{even}$  expanding over spherical harmonics  $Y_k^q$  of even rank  $k$ , will involve a component of odd parity  $V_{ligand}^{odd}$  expanding over spherical harmonics  $Y_k^q$  of odd rank  $k$ . This one mixes the states  $|\Psi_i\rangle$  of the ground configuration  $4f^8$  with those of the excited configuration  $4f^7 5d^1$ . The states  $|\Psi_i\rangle$  are modified to first order of perturbation into:

$$|\Psi'_i\rangle = |\Psi_i\rangle + \sum_{\nu} \frac{\langle \Phi_{\nu} | V_{ligand}^{odd} | \Psi_i \rangle}{E_i - E_{\nu}} |\Phi_{\nu}\rangle = |\Psi_i\rangle + \sum_{\nu} \alpha_i^{\nu} |\Phi_{\nu}\rangle \quad (6.29)$$

where  $E_i - E_{\nu}$  is the energy difference between the states  $|\Phi_{\nu}\rangle$  of the  $4f^7 5d^1$  configuration and the states  $|\Psi_i\rangle$  of the  $4f^8$  configuration.

### External electric field perturbation on the electronic structure

The strength of the Stark hyperfine effect will crucially depend on the way the electronic structure of the molecule will be sensitive to the applied electric field. An outcome to the odd parity ligand field  $V_{ligand}^{odd}$  is to induce a tiny electric dipole moment  $\mathbf{d}$ . This one will couple to an electric field  $\mathbf{E}$  through the Stark interaction  $V_E = \mathbf{d} \cdot \mathbf{E}$  which will modify the electronic states  $|\Psi'_i\rangle$  to first order of perturbation in the form

$$|\Psi'_{i\epsilon}\rangle = |\Psi'_i\rangle + \sum_j \frac{\langle \Psi'_j | V_E | \Psi'_i \rangle}{E'_i - E'_j} |\Psi'_j\rangle = |\Psi'_i\rangle + \sum_j \beta_i^j |\Psi'_j\rangle \quad (6.30)$$

Using equation 6.29 this is rewritten in the form

$$|\Psi'_{i\epsilon}\rangle = |\Psi'_i\rangle + \sum_{\nu} \alpha_i^{\nu} |\Phi_{\nu}\rangle + \sum_j \beta_i^j |\Psi'_j\rangle + \sum_j \beta_i^j \sum_{\nu} \alpha_j^{\nu} |\Phi_{\nu}\rangle \quad (6.31)$$

Which gather the combined effect of the ligand field  $V_{ligand}^{odd}$  and an external electric field  $\mathbf{E}$  on the low energy electronic states of the  $\text{Tb}^{3+}$  ion in  $\text{TbPc}_2$ . The sum over  $j$  are the sum over the  $4f^8$  states  $|\Psi\rangle$  and the sum over  $\nu$  are the one over the  $4f^7 5d^1$  states  $|\Phi\rangle$  (see figure 6.4)

### Hyperfine splitting evaluation using $|\Psi'_{i\epsilon}\rangle$

An entanglement of the electronic and nuclear degrees of freedom is in principle induced by the hyperfine interaction, but these one are in general fairly weak so that the matrix elements of the different operators can be considered separately on either the electronic or the nuclear state space for each energy level. The Hamiltonian of the magnetic dipole hyperfine interaction is:

$$H_{hf} = a \sum_i (\mathbf{N}_i / r_i^3) \cdot \mathbf{I} \quad (6.32)$$

We will then focus on the electronic operator  $\sum_i \mathbf{N}_i / r_i^3$  and its matrix elements between the electronic states  $|\Psi\rangle$  and  $|\Phi\rangle$ . On the ground state  $|\Psi_0\rangle$  we have  $\langle \Psi_0 | \sum_i \mathbf{N}_i / r_i^3 | \Psi_0 \rangle = \langle \Psi_0 | \mathbf{N} | \Psi_0 \rangle \langle 1/r_i^3 \rangle$  where  $\mathbf{N} = \sum_i \mathbf{N}_i$  and  $\langle 1/r_i^3 \rangle$  is a constant for a given electronic configuration. The operator  $\mathbf{N}$  is a vector then can be decomposed on spherical components  $N_q$  ( $q = -1, 0, 1$ ).

The influence of the Stark effect on the hyperfine coupling can be evaluated by calculating the matrix element of the operator  $\mathbf{N}$  on the first order perturbed state  $|\Psi'_{0E}\rangle$ :

$$|\Psi'_{0E}\rangle = |\Psi_0\rangle + \sum_{\nu} \alpha_0^{\nu} |\Phi_{\nu}\rangle + \sum_j \beta_0^j |\Psi_j\rangle + \sum_j \beta_0^j \sum_{\nu} \alpha_j^{\nu} |\Phi_{\nu}\rangle \quad (6.33)$$

$$\begin{aligned} \Rightarrow \langle \Psi'_{0E} | \mathbf{N} | \Psi'_{0E} \rangle &= \langle \Psi_0 | \mathbf{N} | \Psi_0 \rangle + \sum_{\nu} (\alpha_0^{\nu} \langle \Psi_0 | \mathbf{N} | \Phi_{\nu} \rangle + \alpha_0^{\nu*} \langle \Phi_{\nu} | \mathbf{N} | \Psi_0 \rangle) \\ &+ \sum_{j \neq 0} (\beta_0^j \langle \Psi_0 | \mathbf{N} | \Psi_j \rangle + \beta_0^{j*} \langle \Psi_j | \mathbf{N} | \Psi_0 \rangle) \end{aligned} \quad (6.34)$$

The contribution involving the product of the coefficients  $\alpha_i^{\nu}$  and  $\beta_i^j$  are ignored being negligible. Because  $|\Psi_0\rangle$  and  $|\Phi_{\nu}\rangle$  are of opposite parity and  $\mathbf{N}$  is an even operator, the contribution  $\sum_{\nu} \alpha_0^{\nu} \dots$  is equal to zero. We assume that the ligand field and electric field energy perturbation is much smaller than the energy split of the otherwise unperturbed electronic spectrum, *i.e.*  $E_0 - E_j \simeq E'_0 - E'_j$ , and that the energy splits of the excited configuration is much smaller than the energy difference between the ground and excited configuration, *e.i.*  $E_0 - E_{\nu} \simeq \Delta E_{4f^8 \rightarrow 4f^7 5d^1}$ . Using the closure relation  $\sum_{\nu} |\Phi_{\nu}\rangle \langle \Phi_{\nu}| = \mathbb{1}$ , coefficient  $\beta_0^j$  can be then approximated as

$$\beta_0^j = \frac{\langle \Psi'_j | V_E | \Psi'_0 \rangle}{E'_0 - E'_j} \quad (6.35)$$

$$= \frac{\left[ \langle \Psi_j | + \sum_{\tau} \langle \Phi_{\tau} | \frac{\langle \Psi_j | V_{lig}^{odd} | \Phi_{\tau} \rangle}{E_0 - E_{\tau}} \right] V_E \left[ |\Psi_0\rangle + \sum_{\nu} \frac{\langle \Phi_{\nu} | V_{lig}^{odd} | \Psi_0 \rangle}{E_0 - E_{\nu}} |\Phi_{\nu}\rangle \right]}{E'_0 - E'_j} \quad (6.36)$$

$$\simeq 2 \frac{\langle \Psi_j | V_E V_{lig}^{odd} | \Psi_0 \rangle}{(E_0 - E_j) \Delta E_{4f^8 \rightarrow 4f^7 5d^1}} \quad (6.37)$$

The matrix element of the dipole magnetic hyperfine interactions on the electric field perturbed ground state  $|\Psi'_{0E}\rangle$  writes finally

$$\langle \Psi'_{0E} | A \sum_i (\mathbf{N}_i / r_i^3) \cdot \mathbf{I} | \Psi'_{0E} \rangle = \langle \Psi_0 | A J_z | \Psi_0 \rangle \left[ I_z + \sum_j \beta_0^j \frac{\langle \Psi_0 | \mathbf{N} \cdot \mathbf{I} | \Psi_j \rangle + \langle \Psi_j | \mathbf{N} \cdot \mathbf{I} | \Psi_0 \rangle}{\langle \Psi_0 | \mathbf{N}_0 | \Psi_0 \rangle} \right] \quad (6.38)$$

Since  $\Psi_0 = |\pm 6\rangle$ , this transposed in the space of the nuclear spin states  $|IM_I\rangle$  to the additional electric field dependent Hamiltonian:

$$H_{hf}^{Stark} = \frac{\langle \Psi_0 | A J_z | \Psi_0 \rangle}{2} (\alpha_+(E) I_- + \alpha_-(E) I_+) + \alpha_0(E) I_z \quad (6.39)$$

with

$$\alpha_q(E) \approx 4 \sum_j \frac{\langle \Psi_j | V_E V_{lig}^{odd} | \Psi_0 \rangle}{(E_0 - E_j) \Delta E_{4f^8 \rightarrow 4f^7 5d^1}} \frac{\langle \Psi_j | \mathbf{N}_q | \Psi_0 \rangle}{\langle \Psi_0 | \mathbf{N}_0 | \Psi_0 \rangle} \quad (6.40)$$

The first two contributions that can also be written  $\alpha_x(E)I_x + \alpha_y(E)I_y$  with  $\alpha_x(E) = \alpha_+(E) + i\alpha_-(E)$  and  $\alpha_y(E) = \alpha_+(E) - i\alpha_-(E)$  answerable to the AC hyperfine Stark effect whereas the third contribution would account for the DC hyperfine Stark effect. It is observed that not the same excited states  $|\Psi_j\rangle$  will be involved in the two effects. The final step is to compute the matrix elements  $\langle \Psi_j | \mathbf{N}_q | \Psi_0 \rangle$ . It is a matter of standard use of the Racah algebra [113] to compute this within the Russel-Saunders coupling scheme (L-S coupling), by making use of the Wigner-Eckart Theorem.

## 6.2.2 Discussion on the Hyperfine interaction modulation

Equation 6.39 provides the relative change of the hyperfine coupling induced by applying the electric field. The challenge is now to estimate its magnitude.

- Because the expansion of the  $d$  electron wavefunction is bigger than the one of the  $f$  electrons, the crystal field experienced by the excited configuration  $4f^7 d^1$  is about ten times larger [114] than the one experienced by the electrons of the ground configuration  $4f^8$ . It is then reasonable to expect that the effect of  $V_{lig}^{odd}$  amounts to around 1 – 2 eV in energy. On the other hand, given the size of the dipole operator  $d = -er$ , the strength of  $V_E$  under an electric field  $E$  measured in mV is estimated in eV to  $(1 - 2) \cdot 10^{-4} E$ . Finally, the excited configuration is separated from the ground one by about  $\Delta E_{4f^8 \rightarrow 4f^7 5d^1} = 5.5 \text{ eV}$ . The quantity  $4 \langle \Psi_j | V_E V_{lig}^{odd} | \Psi_0 \rangle / \Delta E_{4f^8 \rightarrow 4f^7 5d^1}$  thus is estimated to  $(1.8 \pm 1.1) 10^{-4} \text{ eV E}$ , with  $E$  given in mV/nm.
- If we consider only the states of the ground multiplet ( ${}^7F_6$ ) and those of the first excited multiplet ( ${}^7F_5$ ) then only two excited states are mixed by the electric field with the ground states. Namely the states  $|\Psi_{j=1}\rangle = |J = 6, M_J = \pm 5\rangle$  at energy  $E_j - E_0 \simeq -0.06 \text{ eV}$  and the states  $|\Psi_{j=2}\rangle = |J = 5, M_J = \pm 5\rangle$  at energy  $E_j - E_0 \simeq -0.27 \text{ eV}$ . We compute the other hand  $\langle \Psi_0 | \mathbf{N}_+ | \Psi_1 \rangle / \langle \Psi_0 | \mathbf{N} | \Psi_0 \rangle = \langle \Psi_1 | \mathbf{N}_- | \Psi_0 \rangle / \langle \Psi_0 | \mathbf{N} | \Psi_0 \rangle = -1/\sqrt{6}$  and  $\langle \Psi_0 | \mathbf{N}_+ | \Psi_2 \rangle / \langle \Psi_0 | \mathbf{N} | \Psi_0 \rangle = \langle \Psi_2 | \mathbf{N}_- | \Psi_0 \rangle / \langle \Psi_0 | \mathbf{N} | \Psi_0 \rangle = -0.41576 \text{ eV}$ .

With these numbers, we may reasonably expect an electric field induced effective magnetic field parameter  $\alpha_{\pm}(E)$  of the AC hyperfine Stark effect of the order of  $10^{-3} E$  (mV/nm) times the magnetic hyperfine field of  $\approx 300 \text{ T}$ . Experimentally the AC hyperfine Stark effect will allow the coherent manipulation of the nuclear spin. As for the DC hyperfine Stark effect we need to find states in the  $4f^8$  configuration with  $M = 6$ . The first such states are only in the

multiplet  ${}^5G_6$  and  ${}^5L_6$  at about 3.3eV from the ground state. This unfortunately is too high in energy to the  $4f^75d^1$  electronic configuration. So that one cannot make use of the simplified perturbation calculation. A more quantitative quantum chemical computation is therefore required to estimate the DC hyperfine Stark effect. We end this section by indicating that the electric field modulation of the charge quadrupole hyperfine interactions can be approached in a similar way. The only difference will be that in place of a vector quantity  $\mathbf{N}$  one will have to deal with a tensor of rank 2 so that the states with the selection rules  $\Delta M = 0, \pm 1, \pm 2$  will be involved instead of  $\Delta M = 0, \pm 1$  as with the operator  $\mathbf{N}$ .

### 6.3 Experimental protocol

Classical computation follows a "Load-run-read" cycle. The quantum analog is "prepare-evolve-read". We can proceed experimentally on the nuclear spin according to the following quantum pattern:

- Preparation : Magnetic field sweep from -60 mT to +60 mT ("trace") in order to read-out the initial nuclear spin states through the position in magnetic field of the quantum tunnelling of magnetization.
- Evolution: Microwave pulse at constant magnetic field, the properties of this pulse (frequency, power, width, shape...) depend on the manipulation we want to perform.
- Reading-out: Magnetic field sweep back from +60 mT to -60 mT ("retrace") in order to read-out the final nuclear spin states.

This procedure is more than one order of magnitude faster (2.4sec) than the life time of the nuclear spin so that the relaxation probability is much shorter than the one due to the micro-wave pulse. As we will see later, the coherence time of the system is smaller than the time between the pulse and the read-out. It is thus worth keeping in mind that when we sweep the magnetic field back we are no more measuring a coherent state but a mixed state. After repeating this cycle  $x$  times, and selecting only the cycle where we get a quantum tunnelling of magnetization both in trace and retrace, it is possible to create a matrix (figure 6.5). A selection of the inverse Landau-Zener events gives the same matrix with an inversion of the states. The detected nuclear spin state during the trace sweep determined the column of the matrix, whereas the retrace sweep determined the row. As a result, this matrix contains all the informations we need : the probability of being in a certain final state knowing the initial states. In the following, all the visibility are calculated with this matrix. I was always fascinated by the amount of information we could get from this matrix. For example, if the manipulation applied between trace and retrace is reversible, the matrix will be symmetric which is necessary for a quantum gate. To familiarize ourselves with this new important tool,

figure 6.5 gives few examples for different situations.

We can now discuss the number of events recorded during a measurement. To add an event in this matrix, we need to record one jump in trace and one jump in retrace both coming from a Landau-Zener event. As we explained previously in section 5.2, the probability of measurement is approximately 0.5 for a magnetic field sweep in our experimental condition because of specific features of the quantum tunnelling of magnetization mechanism. Accordingly, because the electronic spin relaxation time is large, inverse Landau-Zener appears in 1/3 of the event. As a result, the total number of events in this matrix is approximately equal to the number of "prepare-evolve-read" cycles divided by six. To increase the statistics, we can take advantage of the Zeeman diagram symmetry. First is the electronic excited/ground state symmetry, meaning that the  $|6, i\rangle \leftrightarrow |6, j\rangle$  transition is the same as  $|6, -i\rangle \leftrightarrow |6, -j\rangle$ . Using this argument, we can also take the inverse Landau-Zener events so that the number of cycles is divided by four. A second symmetry is the parallel magnetic field inversion. We can imagine to manipulate the system with a microwave pulse in between the retrace and the trace and doing the same analysis with a nuclear spin state inversion so that the number of events goes up to the number of cycles divided by two. I never made use of this second symmetry because in the environment of the single molecular magnet there are others molecules that have random orientations that can affect the nuclear spin state. I chose to do all the manipulations of my thesis at the same magnetic parallel field. It could be interesting, to probe the molecular magnet transistor environment, to perform measurements at different parallel magnetic fields.

## 6.4 Nuclear spin dynamic

### 6.4.1 Frequency calibration

The first step before starting to play with the nuclear spin states is to find the energies differences between them. Actually, we showed in section 6.1 that a coherent manipulation is possible for a pulse frequency only in the vicinity of the resonance energy ( $\delta_f \sim \Omega_R$ ). A  $\mu$ -SQUID measurement [79] gives a value of the transition frequency but with an uncertainty of the order of 100MHz, much bigger than the expected resonance width. The energy of the transition can be also tuned through the hyperfine Stark effect (see section 6.2). It should in that case be kept in mind that the electromagnetic environment of a nuclear spin embedded in a single molecular magnet transistor is different from the one in the  $\mu$ -SQUID so that the

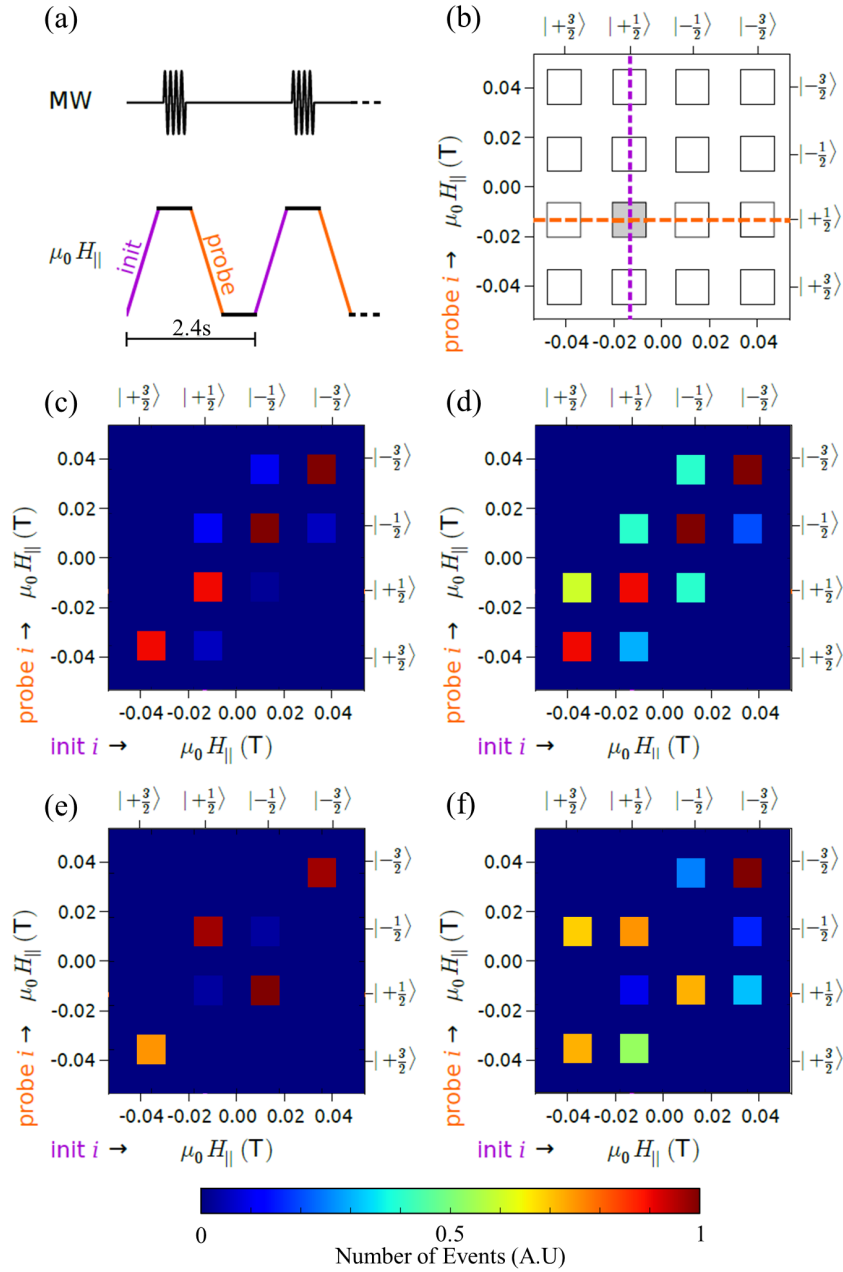


Fig. 6.5 (a) Initialize, manipulate and read-out measurement protocol scheme. To initialize the nuclear spin, the magnetic field  $\mu_0 H_{\parallel}$  is swept from negative to positive values (purple curve), while checking for QTM transition. Subsequently, we kept  $H_{\parallel}$  constant (black curve) and applied a microwave (MW) pulse of different shape depending on the desired manipulation. In the end, the final state is probed by sweeping back  $H_{\parallel}$  to negative values (orange curve). (b) Matrix representation of read-out even in trace and retrace as a function of initial (trace) and final (retrace) nuclear spin states. Experimental example of this matrix when nothing is applied to the nuclear spin system (c) and when it is heated (d). Experimental example of this matrix when the nuclear spin is subject to a reversible manipulation (e) ( $\pi$ -pulse on the second transition) and to a non reversible manipulation (f).

measurements can lead to slightly different transition energies.

The physical effect we want to probe is the increase of the transition rate  $P_{i \rightarrow j}$  and  $P_{j \rightarrow i}$  when the energy difference between the nuclear spin state  $i$  and  $j$  gets into resonance with the frequency of the applied field. Using the experimental procedure described in section 6.3, I decided to choose a pulse of constant amplitude  $A$  and a given width  $\tau$ . I repeated this measurement for different frequencies with a step  $\delta f$ . We need to find the best values for these 3 parameters :

- The pulse duration  $\tau$  : If the pulse length is smaller than the coherence time of the qubit, the manipulation will be coherent and the probabilities  $P_{i \rightarrow j}$  and  $P_{j \rightarrow i}$  might stay at zero even at resonance (for a  $n-2\pi$  pulse). To avoid this, we use a pulse width which is larger than the coherence time. At resonance, this pulse will create a mixed state giving  $P_{i \rightarrow j}$  and  $P_{j \rightarrow i}$  equal to 0.5. The maximum time duration is limited by heating effect of the sample that increases the transition probability even out of resonance. The maximum time is also related to the power of the pulse. I chose a constant width of 1 ms for all the measurements.
- The pulse frequency step  $\delta f$ : The first results obtained by S. Thiele showed a resonance shape with a width of the order of 2MHz. I chose to select a frequency step  $\delta f$  one order of magnitude smaller, namely 200kHz.
- The pulse amplitude  $A$  : it has to be high enough to be sure that the nuclear spin "sees" the pulse. On the other hand, a too high power warms the sample and decreases the life time of the nuclear spin, resulting in a high transition probability with no pulse frequency dependence which would hide the signal we are looking for. Last point about the power is that the transmission  $S_{1-2}$  of the RF line is frequency dependant. This means that, if I always send the same power in the line, the effective power at the nuclear spin vicinity will not be the same for different pulse frequencies. I chose to adjust this amplitude as a function of the applied frequency. The idea is to keep the transition probabilities of the 3 resonances typically at 0.1. A lower probability means that the nuclear spin does not "see" the pulse while a higher probability could hide the signal.

The monochromatic pulse is synthesized using the Rhode & Schwarz SMA100A signal generator with an AWG external modulation as explained in section 3.5.3. Making the assumption that the  $|i - j| = 2$  events are negligible in comparison with the  $|i - j| = 1$  ones,

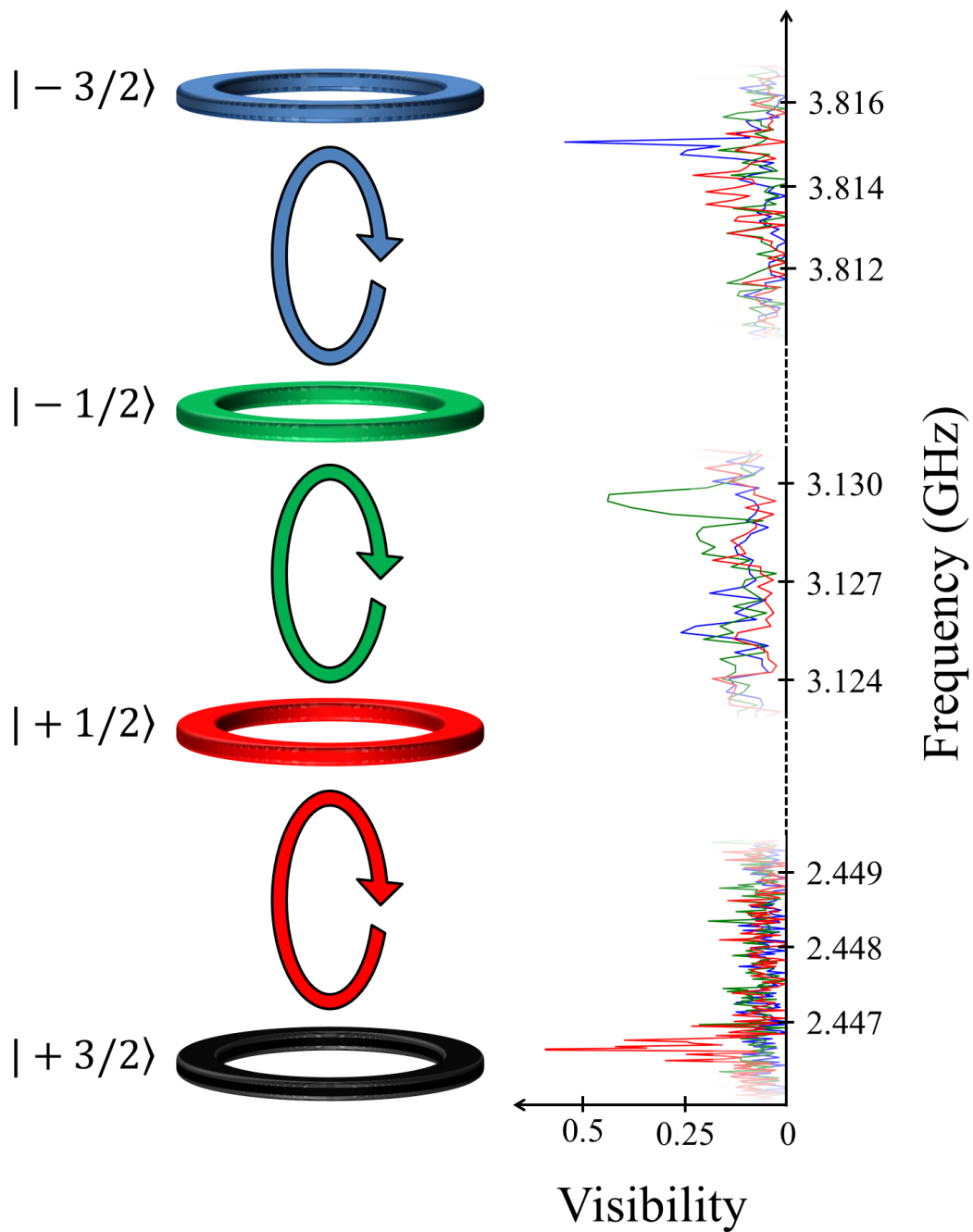


Fig. 6.6 The colour code of the four nuclear spin states is represented on the left. The visibility of each transition as a function of the applied pulse frequency is shown on the right, giving the 3 transitions energy. These three signals reach approximately a visibility of 0.5 as expected and are close to the energy previously measured using a  $\mu$ -SQUID [81].

the probability of the  $i \rightarrow j$  transition is:

$$P_{i \rightarrow j} = \frac{N_{i \rightarrow j}}{N_{i \rightarrow i} + N_{i \rightarrow j}} \quad (6.41)$$

Where  $N_{i \rightarrow j}$  is the number of events in the trace-retrace matrix corresponding to the  $i$  and  $j$  nuclear spin states. Because of the reversibility of this measurement  $P_{i \rightarrow j} = P_{j \rightarrow i}$  so that the visibility of the transition  $i \leftrightarrow j$  is defined as:

$$V_{i,j} = \frac{N_{i \rightarrow j} + N_{j \rightarrow i}}{N_{i \rightarrow i} + N_{j \rightarrow j} + N_{i \rightarrow j} + N_{j \rightarrow i}} \quad (6.42)$$

Which is the sum of  $P_{i \rightarrow j}$  and  $P_{j \rightarrow i}$ . The last thing we need to choose is the number of cycles. As I already mentioned, the probability of adding an event in the matrix (QTM during the trace and during the retrace) is approximately 25% and we have four nuclear spin states. Because we take the events of 2 states out of 4 to calculate the visibility, only one sweep over eight is used. The statistical error bar of the measurement can be estimated to  $\sqrt{8x}/x$ , where  $x$  is the number of cycles. Because I want to make the difference between a 0.1 and a 0.5 transition probability (respectively for a non resonant and a resonant signal), I chose  $x=500$ , which gives an error of about 0.12.

The results of the measurements performed on the 3 transitions are presented in figure 6.6. We clearly observe that for each case, the visibility of the expected transition goes up to 0.5 when the visibility of the others stay approximately at 0.1. This demonstrates that it is not a nuclear spin warming but really a resonant process. Here I choose to show the "historical" graphs, meaning that they are the ones where I detected the signal for the first time. Improved measurements can be performed using this method by increasing the number of cycles and by decreasing the frequency step. This has been later carried out to confirm the first measurement. However, these manipulations are not coherent. It is impossible to study the phase of the qubits because of the large pulse width. In the following, we will decrease the pulse duration, in order to be in the coherent limit.

## 6.4.2 Rabi Oscillation

Knowing the different resonances frequencies, we can measure the dynamic of the nuclear spin in the resonant limit as theoretically described in section 6.1. One needs to apply our experimental protocol with a monochromatic pulse of constant power at the frequency of the transition for different pulse duration  $\tau$ , using the same microwave generation set up (R&S SMA100A modulated by an AWG). We keep the same definition of the visibility as in the

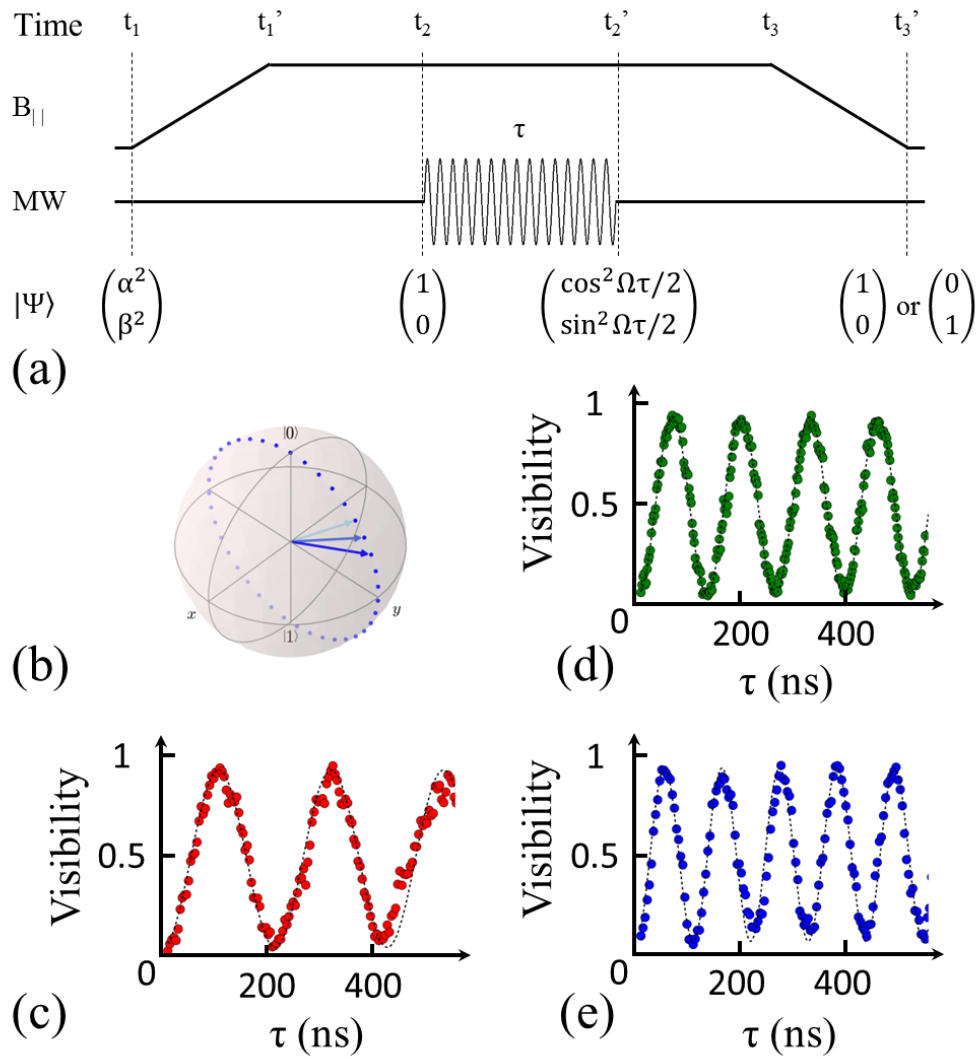


Fig. 6.7 Rabi oscillation. (a) Initialize, manipulate and read-out measurement protocol scheme for the Rabi oscillation measure. (b) Trajectory of the nuclear spin qubit state in the Bloch-sphere according to the pulse duration  $\tau$  for a resonant pulse. Rabi oscillations obtained by repeating the sequence described in (a) 1000 times for each  $\tau$  for the first (c) the second (d) and the third transition (e). The power of the pulse used to drive the different transitions is different for each transition resulting in different Rabi oscillation frequencies.

previous section (equation 6.42). As theoretically predicted, we observe an oscillation of the visibility, the so-called Rabi oscillation (figure 6.7). These measurements are performed at different powers. The respective amplitude of these oscillations are 0.88, 0.9 and 0.9 meaning that we have good control of the three nuclear spin transitions. To go up to 1, we need to decrease the nuclear spin measurement time for two reasons:

- It will reduce the relaxation probability of the nuclear spin between the initialization and the read-out. We clearly guess from equation 6.43 that even if we have a 100% efficient  $\pi$  pulse, the maximum of visibility will not go up to one because of relaxation process. Similarly from equation 6.44, even if we have a 100% efficient  $2\pi$  pulse, the minimum of visibility will not go down to 0. The result on the Rabi oscillation amplitude is  $2P_{relax} = 2(1 - e^{-t_{meas}/T_1}) \simeq 0.02$ .

$$\begin{array}{ccc} \pi \text{ pulse} & \text{relaxation} & \\ |i\rangle \longrightarrow |j\rangle & \longrightarrow & |i\rangle \\ 100\% & P_{relax} & \end{array} \quad (6.43)$$

$$\begin{array}{ccc} 2\pi \text{ pulse} & \text{relaxation} & \\ |i\rangle \longrightarrow |i\rangle & \longrightarrow & |j\rangle \\ 100\% & P_{relax} & \end{array} \quad (6.44)$$

- It will reduce the calibration time. The smaller the calibration time is in comparison with the typical stability time of the experiment, the better the parameters can be adjusted to be resonant with the nuclear spin and the better the measurement will be. In few words, it is hard to catch something that moves faster than you see.

### Power dependence: AC hyperfine Stark effect

In order to confirm the fact that we deal with the dynamic of a qubit and to calculate the effective magnetic field produced by the hyperfine AC Stark effect, I measured the frequency of these oscillations as a function of the microwave pulse power. The Rabi frequency is deduced from equation 6.7, where  $\Omega = g\mu_N B_0 / \hbar$ . Owing to the linear relation between  $B_0$  and  $\Omega$  and because the magnetic field depends on the square root of the microwave pulse power  $\sqrt{P}$ , we expect a linear dependence of  $\Omega$  with respect to  $\sqrt{P}$ . I measured this power dependence only on the second resonance by fitting the Rabi oscillation over two periods for each power. The results are displayed in figure 6.8. The linear dependence of  $\Omega$  with  $\sqrt{P}$  is respected for small powers. However, we found a deviation from the linear behaviour for injection power higher than 16mW ( $\simeq 3\mu\text{W}$  at the end of the microwave line). For multi-level

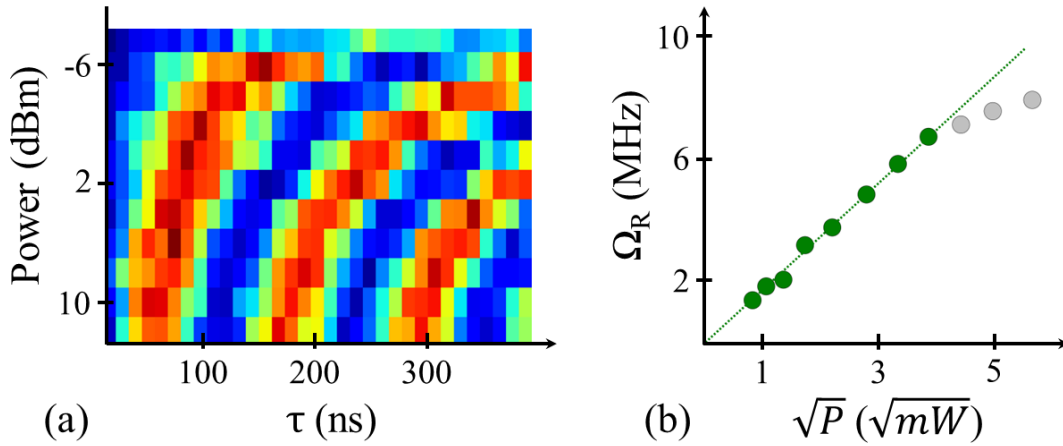


Fig. 6.8 Power dependence. (a) Map of the visibility as the function of the pulse length and power (red for high and blue for low visibility) measured on the second transition, the higher the driving power the faster the oscillation. (b) As predicted from the theory, there is a linear dependence of the Rabi frequency as a function of the square root of the pulse power  $\sqrt{P}$ . We lose this linearity for injection power higher than 12dBm ( $\approx 16mW$ ).

system with a small quadrupole term, this saturation originated from the fact that a high power pulse starts to populate the higher energy level, meaning that we are no more in the regime of a qubit dynamic. In our system, even in the limit of high injected power, the number of events related to  $|i - j| = 2$  stay unchanged and low, meaning that the qubit approximation is still verified.

One reason could be a non-linearity in the hyperfine Stark effect. To argue this, we can extract the effective magnetic field using the relation  $\Omega = g\mu_N B_0 / \hbar$ , with  $g$  being the nuclear  $g$ -factor ( $\simeq 1.354$  for Tb [82]) and  $\mu_N$  the nuclear magneton. Results reveal astonishing value, going from 50mT up to 400mT. Stefan Thiele gives a good discussion about the possible origin of such high magnetic field in his thesis [75]. Three scenarios are investigated to explain these high magnetic field value:

- The magnetic field could have been generated by the microwave antenna itself. A calculation gives a current of 10A in the antenna, 5 orders of magnitude higher than the estimated current of the experiment.
- The magnetic field could have been created by the tunnel current through the molecule. A rough estimation results in a required tunnel current of the order 1mA, 6 orders of magnitude higher than the estimated current that goes through the molecule in the experiment.

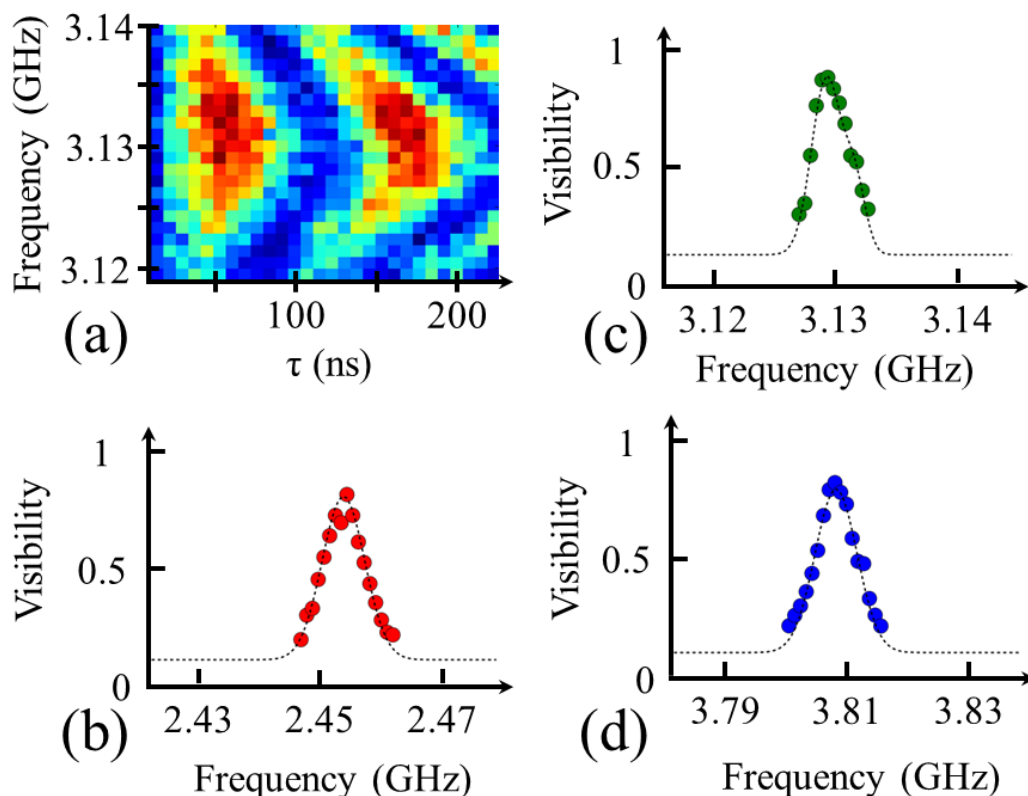


Fig. 6.9 Frequency dependence. (a) Chevron like map of the visibility as the function of the pulse length and frequency (red for high and blue for low visibility) measured on the second transition. At resonance, the oscillations are slow with a high maximum of visibility. The bigger the detuning the lower the amplitude and the faster the oscillation. The amplitude of the Rabi oscillation as a function of the pulse frequency highlights the shape of the first (b), second (c) and third (d) resonance.

- The magnetic field could have been created by the modulation of the hyperfine interaction constant as explained in section 6.2 that gives the correct order of magnitude.

This high effective magnetic field illustrates the strength of the hyperfine Stark effect and argue in favour of the saturation of the Rabi frequency due to the limit of our AC Stark model based on a perturbation calculation.

### Frequency dependence : DC hyperfine Stark effect

Similarly to the Rabi oscillations as a function of the applied microwave power, we can study the oscillation as a function of the applied microwave frequency. In section 6.1, we indicated that by changing the frequency of the pulse, in the limit of a constant phase pulse, we were

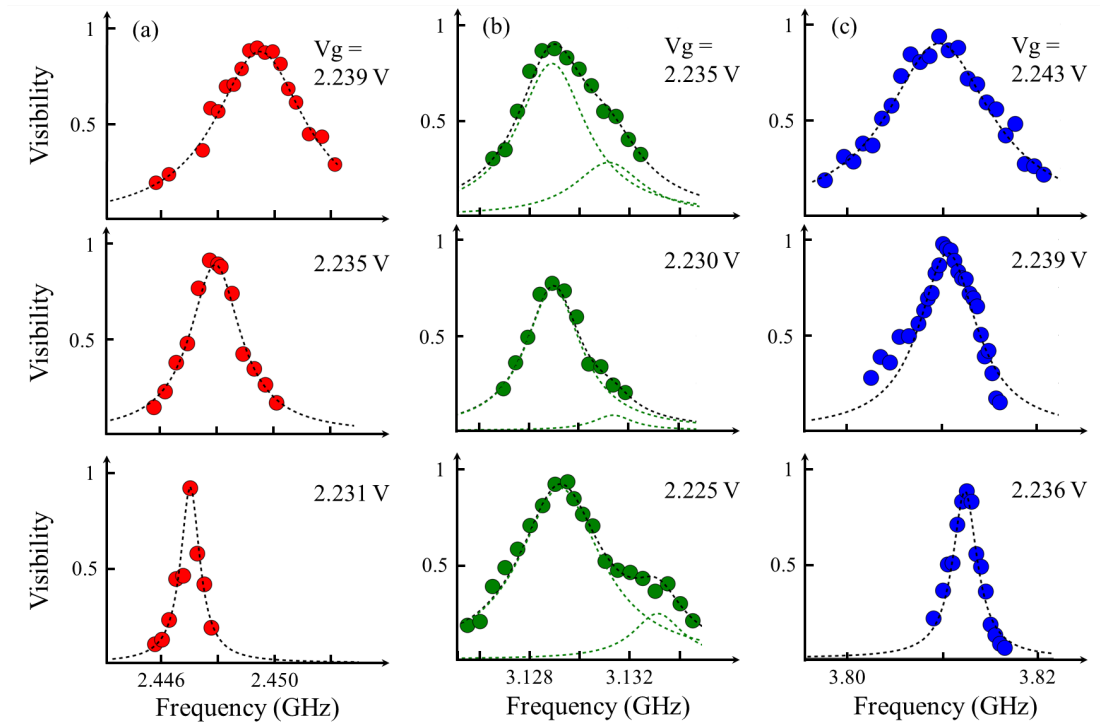


Fig. 6.10 Resonance shift induced by DC Stark effect. Rabi oscillations visibility measured at different MW frequencies for three different gate voltages and for the first second and third transition respectively (a), (b) and (c). The resonance shift of the nuclear spin qubit frequency caused by the hyperfine DC Stark effect is visible on the first and the third resonance but in opposite direction. Furthermore, the gate voltage has no effect on the second transition. We need a deeper theoretical investigation to qualitatively understand these measurements and to explain the broadening of the resonance which means that the Rabi oscillation is increasing with the gate voltage.

changing the azimuthal qubit rotation angle. As illustrated in figure 6.3, this has a direct impact on the qubit dynamic: first the amplitude of the oscillation decreases as a function of the detuning. Second the frequency of this oscillation increases. I applied the protocol by steeping the pulse with  $\tau$  over the 2 first Rabi period for different pulse frequency as shown in figure 6.9(a). By fitting the signal, I can plot in figure 6.9 (b), (c) and (d) the maximum of visibility as a function of the applied microwave pulse frequency, revealing the shape of the resonance.

More than confirming the qubit dynamic, this measure gives with a precision below 1MHz (in the low driving power limit), the spectrum of the Terbium ion nucleus. It can be fitted with the hyperfine Hamiltonian discussed in section 2.3.4, meaning that the higher order polar term of the hyperfine interaction can be neglected. Now we will use this spectroscopy technique to probe the effect of an electric field on the nuclear spin states energy by measuring the resonance shape at different gate voltages. Results of these measurements are displayed in figure 6.10. A clear dependence of the nuclear resonance frequency on the gate voltage is observed. By increasing the gate voltage the first transition shifts to higher frequencies, the third one to lower frequencies when the second seems to stay unchanged. We further observed that the higher the gate voltage the faster we drive the transition for a given pulse power. For the first transition, applying a gate voltage offset of 4 mV and 8 mV resulted in a shift of  $\Delta\nu = 1$  MHz and 3 MHz respectively. Converting this frequency shift into a change of the hyperfine constant gives  $\Delta A/A = 3.3 \times 10^{-4}$  for  $\Delta V_g = 4$  mV and  $\Delta A/A = 9.8 \times 10^{-4}$   $\Delta V_g = 8$  mV. Those values are comparable with the theoretical estimates in section 6.2.1. Namely an order of magnitude of  $\Delta A/A = 10^{-3}$  for an electric field of 1 mV/nm. The conversion of the back gate voltage into an electric field can be done using the simple formula  $E = V/d$ , a gate oxide thickness of 7 nm, and the screening factor of 0.2 (which is a typical value for devices created by electromigration). We have the same value for the 3rd transition but with an inverse effect and no effect on the 2nd. This means that only the  $|\pm 3/2\rangle$  are affected, with the same amplitude, by the DC Stark effect, when in the same time the AC Stark effect ensures a manipulation of all the transitions. This points to different origins of these effects. The AC Stark effect is however fully accounted for by the model described in section 6.2. Experimentally, it is hard to make a deeper analysis of the DC hyperfine Stark effect because the gate voltage range within which we can read-out and manipulate the nuclear spin is limited to 20mV.

## 6.5 Nuclear spin coherence time

In this section, we study the coherence of the nuclear spin transitions by considering the evolution of the qubit when it is in its equatorial plan. In the previous section, we investigated the dynamics of the qubits taking only into account the coupling of the nuclear magnetic moment to the effective magnetic field induced by the AC Stark effect. In the experiment, even if the nuclear spin magnetic moment is very low and well isolated in comparison with the electronic spin (see section 1.2), we need to investigate its coupling to the fluctuations of the environment. We consider two main sources for these fluctuations, one magnetic, through a direct coupling to the spins of the environment, and another electric, through an indirect coupling due to Stark effect. We will characterize these contributions by performing Ramsey fringes and Hahn-echo measurements.

### 6.5.1 Coherence time $T_2^R$ : Ramsey fringes

To deal with the decoherence of a quantum system, it is customary to consider the time evolution of the density matrix  $\rho = |\psi\rangle\langle\psi|$  and use the Schrödinger equation:

$$i\hbar \frac{d\rho}{dt} = [H, \rho] \quad (6.45)$$

$H$  is the Hamiltonian of the qubit in the rotating frame as described in equation 6.15. Expanding this expression for a qubit system in interaction with a microwave pulse gives the equations of motion:

$$\langle\sigma_x\rangle = \Delta\langle\sigma_y\rangle \quad (6.46)$$

$$\langle\sigma_y\rangle = -\Delta\langle\sigma_x\rangle + \Omega\langle\sigma_z\rangle \quad (6.47)$$

$$\langle\sigma_z\rangle = -\Omega\langle\sigma_y\rangle \quad (6.48)$$

Where  $\Delta$  and  $\Omega$  are respectively the detuning and the Rabi period as defined in section 6.1. In order to take into account the relaxation and decoherence processes, Felix Bloch extended this set of equations by adding empirical terms [115]. They are governed by two time scales:

- $T_1$ , the relaxation decay time of the diagonal component (z axis) of the spin density matrix.
- $T_2$ , the decoherence decay time of the off-diagonal component (x-y plan) of the spin density matrix.

These terms, illustrated in figure 6.11, result in the new equation of motion:

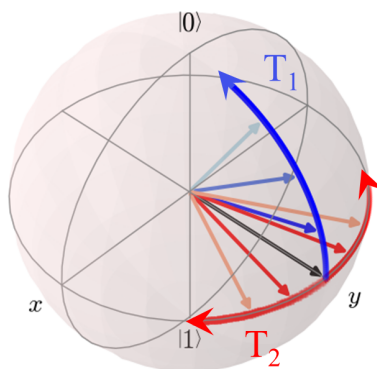


Fig. 6.11 Representation of relaxation ( $T_1$ ) and dephasing ( $T_2$ ) processes in a Bloch-Sphere.

$$\langle \sigma_x \rangle = \Delta \langle \sigma_y \rangle - \langle \sigma_x \rangle / T_2 \quad (6.49)$$

$$\langle \sigma_y \rangle = -\Delta \langle \sigma_x \rangle + \Omega \langle \sigma_z \rangle - \langle \sigma_y \rangle / T_2 \quad (6.50)$$

$$\langle \sigma_z \rangle = -\Omega \langle \sigma_y \rangle - \langle \sigma_z \rangle / T_1 \quad (6.51)$$

In case of a free evolution ( $\Omega = 0$ ) one can show that the solution to these equations is:

$$\langle \sigma_x \rangle = \langle \sigma_x \rangle_{t=0} \cos(\Delta t) e^{-t/T_2} \quad (6.52)$$

$$\langle \sigma_y \rangle = \langle \sigma_y \rangle_{t=0} \sin(\Delta t) e^{-t/T_2} \quad (6.53)$$

$$\langle \sigma_z \rangle = \langle \sigma_z \rangle_{t=0} (1 - e^{-t/T_1}) \quad (6.54)$$

In the following we make the hypothesis, which will be verified later, that the relaxation time  $T_1$  is much larger than the decoherence one  $T_2$ . We straightforwardly deduce from equations 6.53 and 6.54 that to get the information about  $T_2$  it is necessary to measure the free evolution of the operator  $\langle \sigma_x \rangle$  or  $\langle \sigma_y \rangle$ . Whereas, as explained in the experimental protocol section 5.2.1, the measurement of the nuclear spin gives access to only  $\langle \sigma_z \rangle$ , meaning that we need to apply a series of operations, illustrated in figure 6.12 (a), to perform the required measurement:

- First a magnetic field sweep prepares the spin along the z-axis, in the  $|0\rangle$  state between time  $t_1$  and  $t'_1$ .
- Second the spin is rotated into the equatorial plane using a microwave pulse. The duration of this pulse was adjusted to perform a  $\frac{\pi}{2}$  rotation around the x-axis, which is

why this type of pulse is referred to as a  $\frac{\pi}{2}$  pulse. This pulse is sent between time  $t_2$  and  $t_2 + \tau_{\pi/2}$ .

- Third the spin is let to freely evolve during a time  $\tau$ , leading to the precession of the spin according to equations 6.53 and 6.54 around the z-axis at the frequency  $\Delta$ . This free evolution occurs between time  $t_2 + \tau_{\pi/2}$  and  $t_2 + \tau_{\pi/2} + \tau$ .
- Fourth, between time  $t_2 + \tau_{\pi/2} + \tau$  and  $t_2 + 2\tau_{\pi/2} + \tau$  a second  $\frac{\pi}{2}$  pulse is applied to bring the nuclear spin back in the  $x - z$  plan. This pulse transforms the y component into z and leaves the x one unchanged.
- Fifth, at time  $t_3$  the final state is read-out by sweeping back the magnetic field.

As in the case of the Rabi oscillations, many measurements are averaged to obtain the final state probability. This sequence repeated for different values of  $\tau$  results in the measurement of  $\langle \sigma_y \rangle$  and leads to oscillations with a period of  $1/\Delta$  and an exponential decay of typical time  $T_2$  as expected from equation 6.54, the so-called Ramsey fringes.

This experimental sequence imposes the careful calibration of the  $\frac{\pi}{2}$ -pulses. We need to choose 3 parameters: the amplitude, the frequency and the length. I always performed the calibration in this order.

- Amplitude: due to DC Stark effect, an electrical noise in the nuclear spin environment might induce a little shift of the resonance. A too low amplitude will result in a thin resonance width. Accordingly, the detuning will not be sufficiently constant all over the measurement. In contrast, the slower the more accurate: a high amplitude reduces the pulse length that creates the coherent superposition. If however we drive the transition too fast, then a little error in the pulse length calibration or a noise on the pulse modulation, will have a huge impact on the state superposition quality. I chose an amplitude that ensures a Rabi frequency of the order of 5MHz.
- Frequency: the oscillation frequency of the Ramsey fringes is equal to the detuning  $\Delta/2\pi$ , as indicated in equation 6.54. Therefore, in order to adjust the oscillation period, the precise position of the resonance frequency had to be obtained. This was done by measuring the visibility of the Rabi oscillations as a function of the microwave frequency. By fitting a Lorentzian to the obtained data points, we found the maximum and we detuned the microwave source of about 1 MHz in order to see Ramsey fringes with an oscillation period of the order of  $1\mu s$ .

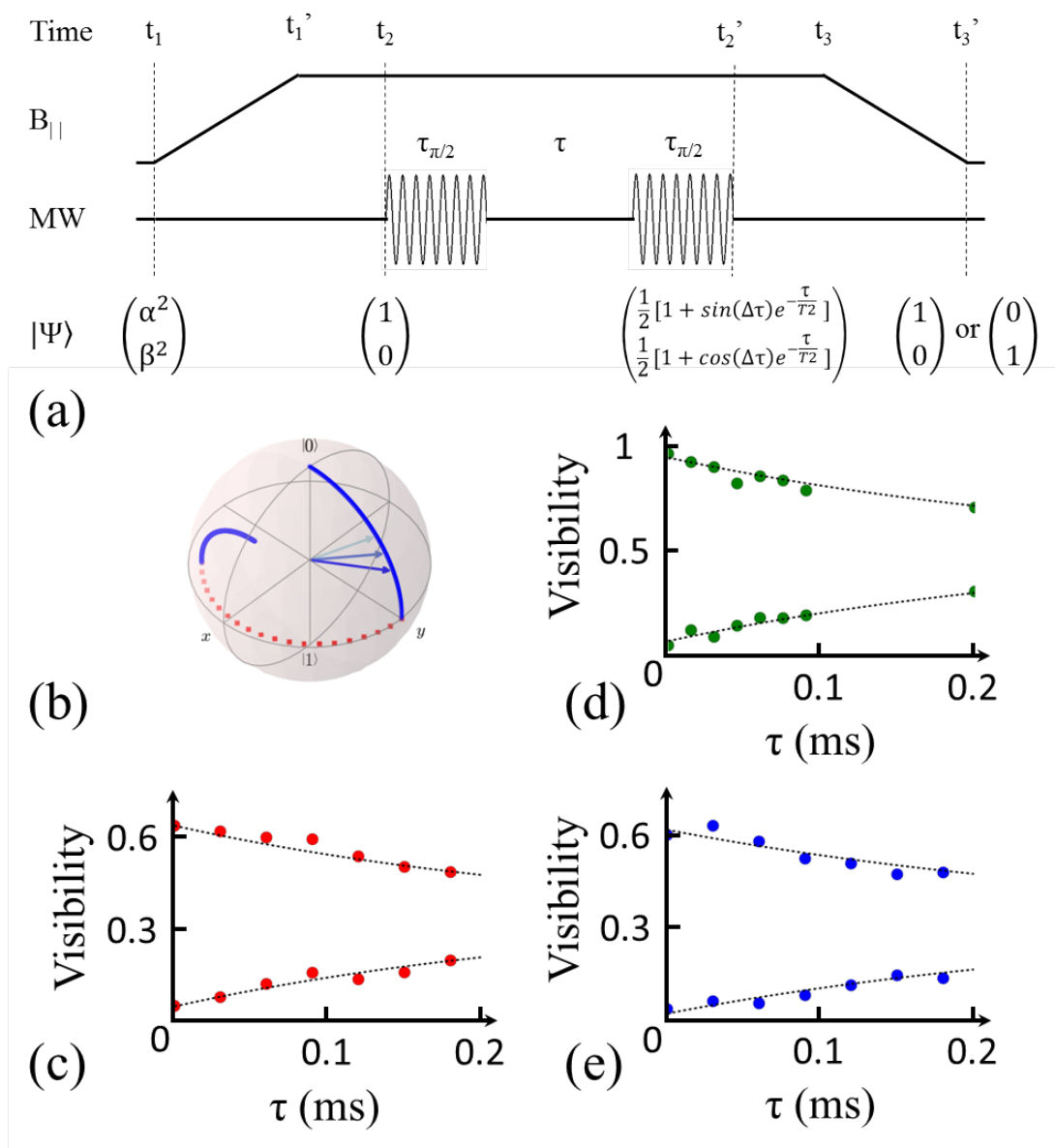


Fig. 6.12 Ramsey fringes. (a) Initialize, manipulate and read-out measurement protocol scheme for the Ramsey fringes measurements. (b) Trajectory of the nuclear spin qubit state in the Bloch-sphere during the Ramsey manipulation: The first  $\pi/2$ -pulse creates the coherent superposition. The state is then rotated according to the detuning  $\Delta$  during a time  $\tau$ . The second  $\pi/2$ -pulse finally projects the state back in the read-out basis. Ramsey fringes damping obtained by repeating the sequence described in (a) 300 times for each  $\tau$  for the first (c) the second (d) and the third transition (e). For reasons of measurement time, I only recorded the envelope of the Ramsey fringes at different  $\tau$  which reveals coherence time of respectively 0.28ms, 0.30ms and 0.32ms.

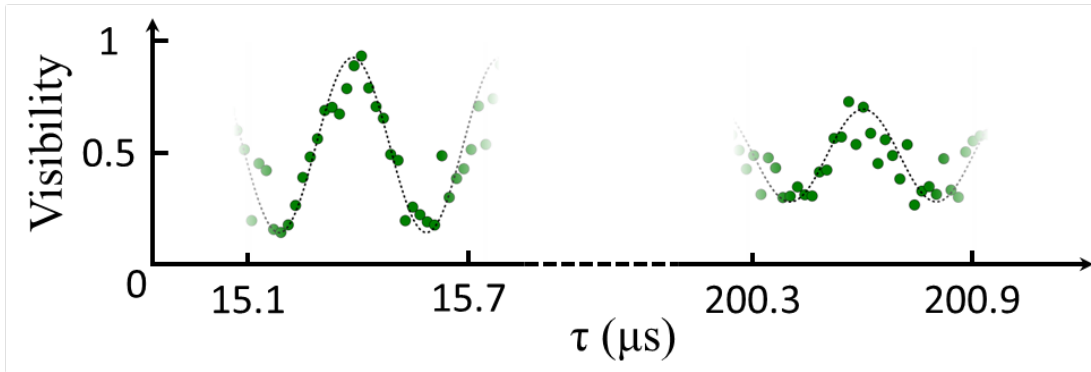


Fig. 6.13 Ramsey fringes at two different times, illustrating the damping of the fringes amplitude.

- Length: the final calibration step is the measurement of a full Rabi oscillation, given the amplitude and the frequency previously fixed, to determine the duration of the  $\frac{\pi}{2}$  pulse. Since I chose an amplitude that ensures a 5MHz oscillation, the typical time of this pulse is 50ns.

I chose a quite large detuning resulting in a fast Ramsey oscillation in comparison with the coherence time. As a result, to have the full measurement I should have recorded 300 oscillations, meaning more than 3000 points. Because of our nuclear spin measurement time scale, this would have taken more than one month. It is impossible to keep the experiment sufficiently stable all over this time so I chose to record two Ramsey fringes every 30  $\mu$ s (see figure 6.13) and to plot the maximum and minimum of visibility from the fits made on these two fringes as illustrated on figure 6.13. This method gives us the information we want in less than one week: By fitting the data to  $y = A * (0.5 + e^{-t/T_2^R})$  for the maximum of amplitude and  $y = A * (0.5 - e^{-t/T_2^R})$  for the minimum, we extracted a dephasing time  $T_2^R$  respectively equal to 0.28, 0.3 and 0.32ms. These coherence times are encouraging, in fact they exhibit a figure of merit  $\Omega_R T_2^R$  higher than 2000. However, this coherence time is really far from the theoretical limit of  $T_2 = 2T_1$ . We need to perform a deeper analysis and a new kind of measurement to understand the sources of decoherence.

### 6.5.2 Investigation of decoherence process : Hahn-echo

Decoherence process originates from the coupling of the quantum system to an external uncontrolled environment. A typical element of the environment that could break the coherence of a system is the phonon bath. In our experiment, the typical electronic temperature

is about 50mK and the energy difference between two nuclear spin states is of the order of 120 up to 180mK. Using a Boltzmann distribution, this gives non-negligible proportions of phonon that could interact with the nuclear spin going from 3 up to 10 %. A deeper study of the coherence time as a function of the environment temperature and a comparison with a model based on the Wangness-Bloch theory [116] (single spin coupled to a phonon bath) is necessary to draw a conclusion about the relevance of this source of decoherence, which would naturally explain why the coherence time is larger for higher transition energy.

Nevertheless the major contribution of the decoherence should be awaited from the electromagnetic noise of the environment. To get as much information as possible from this noise source, we distinguish in the following model:

- the magnetic noise: In the environment of the nuclear spin there are many others spins. The closest ( $\sim 0.5\text{nm}$ ) are the 8 Nitrogen nuclei that carry each a  $1/2$  spin. We can also think of the other  $\text{TbPc}_2$  molecules that are in the vicinity ( $> 0.5\text{nm}$ ) of the molecular magnet we probe by the conductance measurement. Notice that this noise source can be reduced using a better control of the molecular deposition process.
- The electric noise: The fluctuating electric field induces a modulation of the hyperfine constant through the Stark effect, resulting in an effective fluctuating magnetic field for the nuclear spin. I anticipate 3 different sources of electric noise. First, the electrons that tunnel through the Pc ligand. Second, the charges trapped in the gate oxide. Third, bit noise of the digital to analog converter at the gate terminal. All these noise sources could be lowered by using a detection scheme not based on a transport measurement but on an optical method. In a shorter term, we want to optimize the oxide layer and to increase the stability of the DA converters using a divider as explained in section 3.3.2. The use of a battery for the back gate could also be interesting but do not offer the flexibility of the DA converters which is important to find the transistor working point.

The characteristics of these noise sources will be discussed after the derivation of the model based on the Bloch-Redfield theory [117] and on a work applied to a superconducting qubit [118]. Taking into account the magnetic and electric fluctuations,  $\delta B$  and  $\delta E$ , during the free precession, the Hamiltonian of equation 6.15 modifies as:

$$\hat{H} = \frac{\hbar}{2} \left[ \Delta + \frac{\delta\omega_z}{\delta B} \delta B + \frac{\delta\omega_z}{\delta E} \delta E \right] \hat{\sigma}_z \quad (6.55)$$

We introduce two constants  $\beta_z = \delta\omega_z/\delta B$  and  $\varepsilon_z = \delta\omega_z/\delta E$  that describe the sensitivity of the nuclear spin rotation in the equatorial plan to the magnetic and electric field fluctuations. A substitution of these constants in equation 6.55 results in:

$$\hat{H} = \frac{\hbar}{2} [\Delta + \beta_z \delta B + \varepsilon_z \delta E] \hat{\sigma}_z \quad (6.56)$$

Once having incorporated the noise sources in the Hamiltonian, we need to express the random phase accumulated during the free evolution of the Ramsey sequence:

$$\Delta\phi_R = \int_0^\tau dt' [\beta_z \delta B(t') + \varepsilon_z \delta E(t')] \quad (6.57)$$

We assume a Gaussian density of the noise spectrum distribution  $S_B(\omega)$  and  $S_E(\omega)$ . The phase accumulated from these noises will be different for each measurement and will induce, as expected, the damping of the Ramsey fringes. The expression of the decay law can be calculated as follow:

$$f_R = \langle e^{i\Delta\phi} \rangle \quad (6.58)$$

$$= e^{-\frac{\langle \Delta\phi^2 \rangle}{2}} \quad (6.59)$$

$$= \exp \left[ -\frac{t^2}{2} \int_{-\infty}^{+\infty} d\omega \{ \beta_z^2 S_B(\omega) + \varepsilon_z^2 S_E(\omega) \} \text{sinc}^2 \frac{\omega t}{2} \right] \quad (6.60)$$

This expression will be compared with the experimental results later. The crucial question now is how to make a measurement that can give us more information about the noise frequency ? The answer is Hahn-echo experiments, so named in honour of Erwin L. Hahn who imagined and performed it in 1950 [119]. The idea is to reduce the low frequency noise contribution of the decay law maintaining the high frequency one unchanged. The subsequent unbalance gives, as we will see in the model, a lot of informations about the noise frequency. The sequence we now apply to the nuclear spin transition, described in figure 6.15 (a), is the same as the Ramsey one with an additional  $\pi$  pulse in the middle of the free evolution ( $t = t_2 + \tau_{\pi/2} + \tau/2$ ). This microwave pulse acts as a time reversal in the middle of the free evolution. In fact a  $\pi$  pulse along the x axis applied to an equatorial state leaves the x component unchanged and reverses the y one:

$$\langle \sigma_x \rangle = \cos(\Delta \tau/2) \quad \pi \quad \langle \sigma_x \rangle = \cos(\Delta \tau/2) = \cos(\Delta (-\tau/2)) \quad (6.61)$$

$$\langle \sigma_y \rangle = \sin(\Delta \tau/2) \quad \longrightarrow \quad \langle \sigma_y \rangle = -\sin(\Delta \tau/2) = \sin(\Delta (-\tau/2)) \quad (6.62)$$

Before approaching the calculation I will explain how I "see" this measurement. This vision is not rigorous but allowed me understanding it. Since I wish this thesis to be a helpful tool for the following Ph.D students I want to provide it. We imagine that the single spin phase is the position of an athlete on a track. This athlete runs during a time  $\tau$  and repeats this race, always starting from the starting line, N times. The time necessary to perform this N race is called  $T_{meas}$ . We will repeat this experiment considering three athletes A, B and C:

- A is very regular, he always runs at the same speed all over the N races.
- B has a constant speed over each race but tires from one race to the next so that its speed during the race n+1 is lower than the one during the race n.
- C is not regular at all, its speed is never the same during a same race and this irregular speed is not reproducible from one race to another .

Now let us examine where these athletes finish on the track depending on the race type. During a "Ramsey race" the athlete runs in the same way during time  $\tau$ . "A" always finishes at the same position related to his speed, "B" goes less and less far on the track when it is impossible to say anything about the final position of "C". In a "Hahn-echo race", in the middle of each race (at time  $\tau/2$ ) we ask the athletes to suddenly run in the opposite direction. "A" and "B" will run back on their feet with the same speed during the same time  $\tau/2$ . As a result they finish at the same position which is precisely the starting line and this all over the N races. In contrast the athlete "C" finishes once again at a random track position from one race to another. Let us now transpose this intuitive picture to the case of the nuclear spin by considering the running speed as being the detuning and the position on the track as being the nuclear spin phase.

- A is the equivalent of a spin totally isolated from noise sources. The detuning is constant so that, for the Ramsey fringes, its final position only depends on the duration of the free evolution. The fact that this is reproducible all over the N measurements means that there is no statistical broadening. As a result, because of the periodicity of the phase, we have an oscillation of the visibility without damping. In the Hahn-echo measurement, the final phase is always the same, independent from the pulse duration. As a result we have a constant visibility equal to one.
- B is the equivalent of a spin coupled to a low frequency noise source. The detuning modification is negligible during a single measurement but is not all over the N ones. The

period  $T$  of this noise can be framed by the two experimental times  $\tau$  and  $T_{meas}$  :

$$\tau \ll T \ll T_{meas} \quad (6.63)$$

Because of this low frequency noise, we loose the reproducibility over the  $N$  measurements in the Ramsey experiment, which is necessary to get the final state probability. This creates a broadening of the final spin phase, which is the origin of the damping in the Ramsey fringes visibility. However, and here is the important point, this low frequency noise has no impact on the visibility of the Hahn-echo signal. We will see latter that it is interesting also to study the limiting case  $T \approx \tau$ .

- Finally C is the equivalent of a spin coupled to a noise source which is hard to characterize. This noise has at least a high frequency component ( $T \ll \tau$ ) that broadens both Ramsey and Hahn-echo final phases. Even if the low frequency noise is filtered in the Hahn-echo measurement, the final visibility is damped in both cases.

This qualitative approach is interesting to get an intuition of the spin dynamic but needs to be deepen using a quantitative model that gives the expression of the Hahn-echo damping. In the Hahn-echo experiment, the phase acquired is the difference between the two free evolutions:

$$\Delta\phi_H = - \int_0^{\tau/2} dt' [\beta_z \delta B(t') + \varepsilon_z \delta E(t')] + \int_{\tau/2}^{\tau} dt' [\beta_z \delta B(t') + \varepsilon_z \delta E(t')] \quad (6.64)$$

Using the same model as for the Ramsey experiment, we obtain the expression of the Hahn-echo damping visibility as a function of the pulse duration for Gaussian densities of the noise spectrum distribution  $S_B(\omega)$  and  $S_E(\omega)$ .

$$f_H = \exp \left[ -\frac{t^2}{2} \int_{-\infty}^{+\infty} d\omega \{ \beta_z^2 S_B(\omega) + \varepsilon_z^2 S_E(\omega) \} \sin^2 \frac{\omega t}{4} \operatorname{sinc}^2 \frac{\omega t}{4} \right] \quad (6.65)$$

The main difference between  $f_R$  and  $f_H$  comes from the function that multiplies the density noise spectrum, that gives the weight in the integral. The density plot of these two functions (see figure 6.14) reveals the main information about the two measurements. Indeed, the amplitude of this function is maximal for  $\omega = 0$  for the Ramsey case when it is minimum for

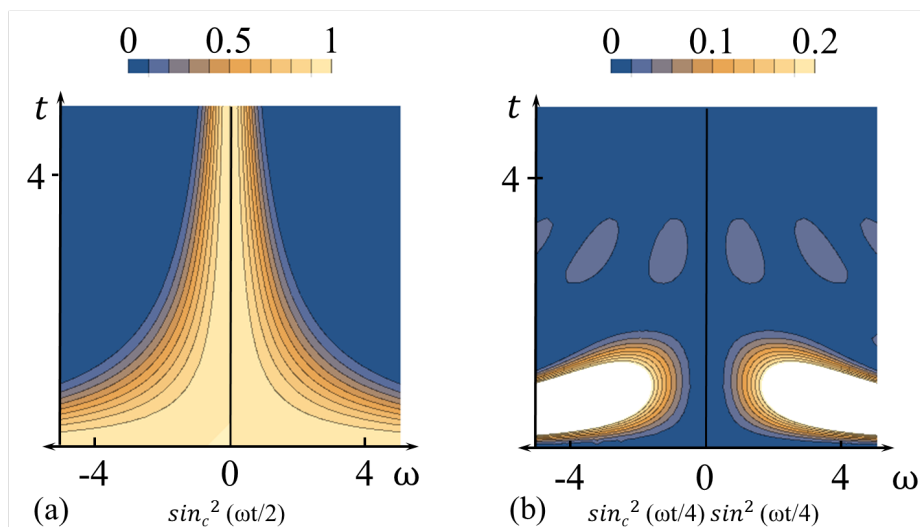


Fig. 6.14 Contour plots of the function  $\sin_c^2(\omega t/2)$  (a) and  $\sin_c^2(\omega t/4)\sin^2(\omega t/4)$  (b) as a function of  $\omega$  and  $t$ . These functions stand for the weight of the noise in the integral of the equation 6.58 and 6.65 respectively for a Ramsey and a Hahn-echo measurement. This illustrates that the low frequency noise is filtered in a Hahn-echo experiment.

the Hahn-echo case as illustrated in figure 6.14.

Because the additional  $\pi$  pulse needs to have the same frequency and amplitude as the  $\pi/2$  and to be twice its length, I measured the Hahn-echo damping using the same protocol (measurement and calibration) as the one detailed for the Ramsey fringes. Nevertheless we can notice that this measurement is easier to perform for two reasons. First, because the expression of the visibility as the function of the free evolution time is no more affected by the detuning, we don't need to pay as much attention to the frequency calibration. It is only necessary to be near resonance. Second, one needs less points to fit a decay signal than an oscillating decay signal. When I need a point every 50ns to fit the Ramsey measurement, I only need a point every  $2\mu\text{s}$  for the Hahn-echo measurement. The experimental datum are displayed in figure 6.15.

Confronting the model to the measurement we can extract the electric and magnetic Gaussian noise spectrum from the Ramsey and Hahn-echo data. Before performing the fits, we can discuss the order of magnitude of the different contributions in order to limit the fitting parameter space. The magnetic noise, as explained previously, originates from neighbouring spins. I chose to model this noise with a Gaussian (as we imposed in the model) peaked at a frequency  $\omega_B$ , close to the precession of the  $\text{Tb}^{3+}$  ion nuclear spin, meaning low frequency

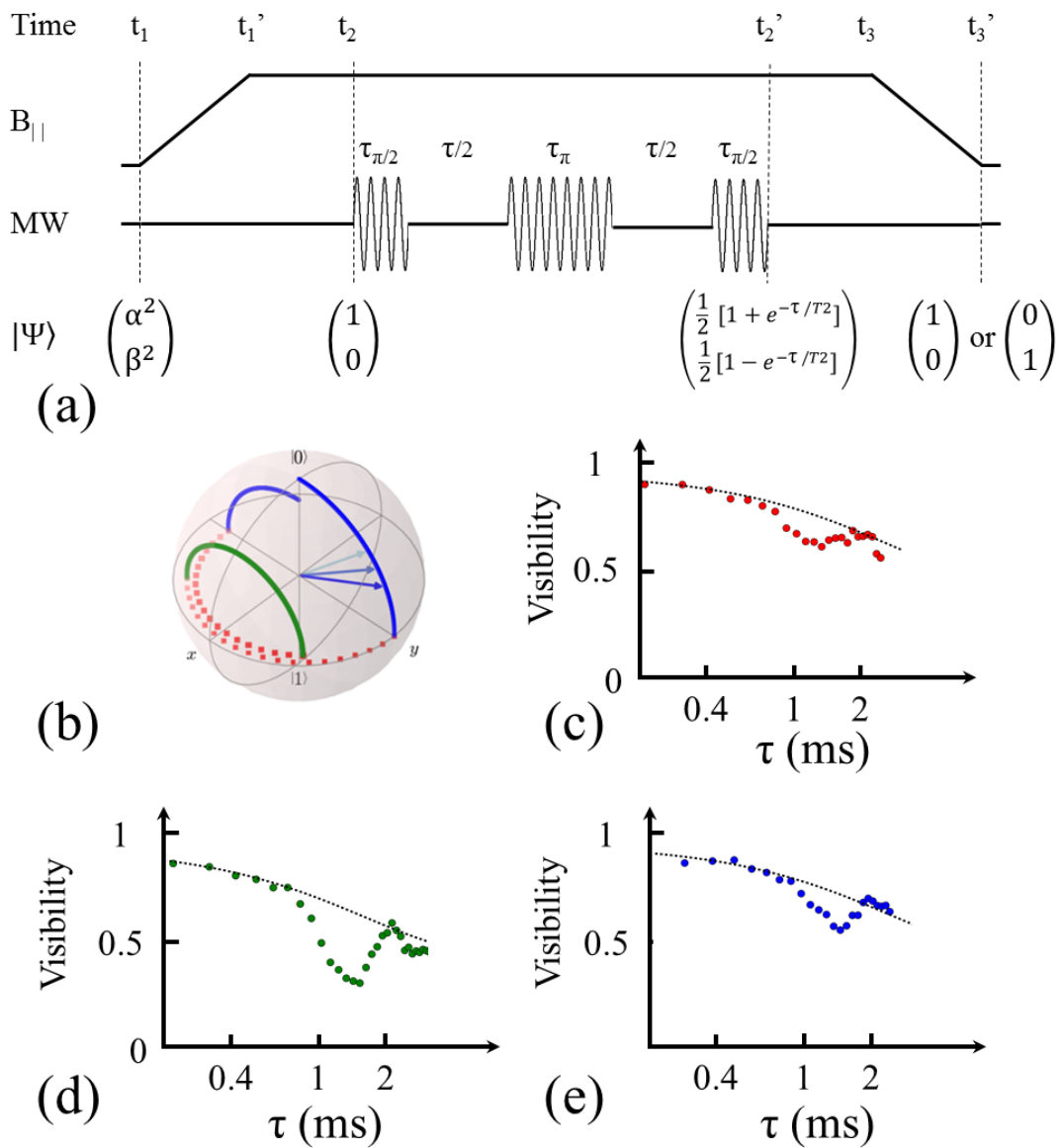


Fig. 6.15 Hahn-echo experiment. (a) Initialize, manipulate and read-out measurement protocol scheme for the Hahn-echo measurement. (b) Trajectory of the nuclear spin qubit state in the Bloch-sphere during the Hahn-echo manipulation: The first  $\pi/2$ -pulse creates the coherent superposition, then the state is rotated according to the detuning  $\Delta$  during a time  $\tau/2$ . A  $\pi$ -pulse creates a reversal of the dynamics in the equatorial plan and finally a second  $\pi/2$ -pulse projects the state in the read-out basis. Hahn-echo signal obtained by repeating the sequence described in (a) 1000 times for each  $\tau$  for the first (c) the second (d) and the third transition (e) reveal coherence time of 2.4ms, 1.6ms and 2.6ms, respectively.

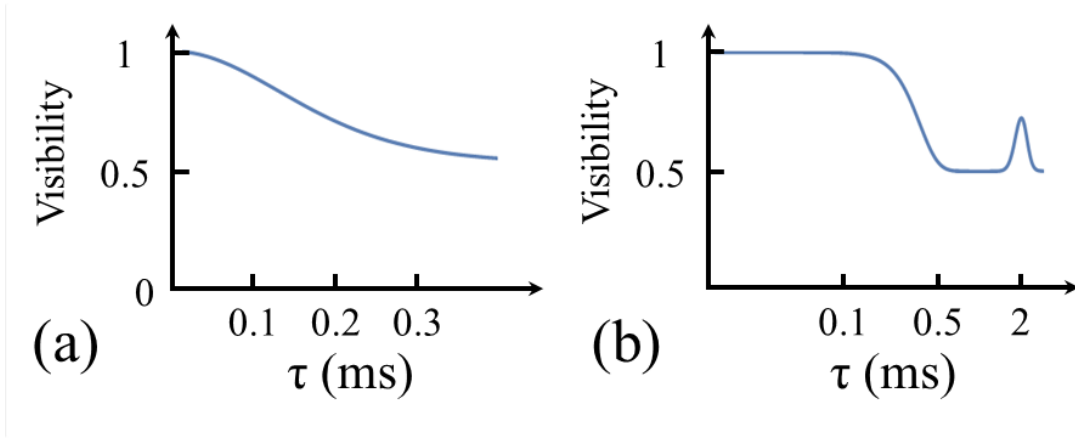


Fig. 6.16 Theoretical damping. (a) and (b) are obtained respectively from equation 6.58 and 6.65, they display the Ramsey and Hahn-echo damping.

in the rotating frame ( $\omega_B \approx 0$ ). The number of spins of the environment that couples to the nucleus might be low. This argue in favour of a narrow noise distribution for the magnetic contribution. It is harder to encircle the electric noise. As a matter of fact this originates from various phenomenon (tunnelling electron, DAC and gate oxide). The only information we have is that these noises are not coherent, resulting in a broad Gaussian. Finally, we have to access the sensitivities of the nuclear spin rotation in the equatorial plan to the magnetic and electric field fluctuation  $\beta_z$  and  $\varepsilon_z$ . Since  $\hbar\omega_z = g\mu B_z$ , we deduce that  $\beta_z$  is in the order of  $64 \text{ MHz}\cdot\text{T}^{-1}$ . In the analysis of the hyperfine Stark effect, we observed that the modulation of the hyperfine constant  $\Delta A/A$  is in the order of  $10^{-3}$  for an applied field of  $1 \text{ mV}\cdot\text{nm}^{-1}$ . This modulation results in an effective magnetic field of  $200 \text{ mT}$ . We can conclude that the order of magnitude of  $\varepsilon_z$  is  $10 \text{ MHz}\cdot\text{nm}\cdot\text{mV}^{-1}$ . Theoretical fit displayed in figure 6.16, (a) and (b) for Ramsey and Hahn-echo damping respectively, are obtained only considering the magnetic noise contribution. The detuning of this source is fixed to  $1 \text{ kHz}$  with a width of  $0.14 \text{ kHz}$  and an amplitude of  $0.8 \text{ mT}$ . This may be due to a nearby Terbium ion. I have to performed measurement with longer  $\tau$  to get more information about the electrical noise sources. Furthermore, for longer waiting time, I could measure a revival of the visibility.

The measurement of the coupling of a spin to a nuclear spin bath using the Hahn-echo sequence have been investigated with an electronic spin in GaAs structure [29] and a NV centre [120].

## 6.6 From qubit to multi level system: Coherent pump-probe

To make the transition with the final chapter where different transitions are manipulated in the same time, I want to present two measurements which I performed to make sure that different transitions can be driven in a same sequence. A great chance during the past 3 years was to be free to play as I liked with the nuclear spin device that I had in my full disposal. The measurements I am going to describe in this section are the best examples of the spirit of the scientific activity which I find important to keep in mind: doing physics for pleasure. Therefore, there is no evident applications for quantum information processing in this section. Take it just like an enjoying and pleasant little quantum game.

### 6.6.1 3 states coherent pump probe: single pump

The sequence of this measurement consists of four steps as illustrated in figure 6.17 (a). First we sweep the magnetic field to initialize the nuclear spin. Then we send a microwave pulse of duration  $\tau$  with a frequency calibration that ensures a perfect resonance between the pulse and the first qubit transition ( $\Delta = 0$ ). This pulse creates a  $|3/2\rangle \leftrightarrow |1/2\rangle$  coherent superposition. Next we pump the probability of being in the red state into the green one using a  $\pi$  pulse on the second qubit transition. The last step is to read-out the final state of the nuclear spin by sweeping back the magnetic field. We repeat this sequence 300 times for each  $\tau$ . The visibility of the different states, defined as :

$$V_i = \frac{N_{|3/2\rangle \rightarrow i}}{\sum_{n=3/2}^{-1/2} N_{|3/2\rangle \rightarrow |n\rangle}} \quad \text{§ (6.66)}$$

as a function of the first pulse length  $\tau$ , is shown in figure 6.17 (b). Thanks to this sequence, we can measure an oscillation between the states  $|3/2\rangle \leftrightarrow |-1/2\rangle$  although we are not able to directly drive this  $\Delta n = 2$  transition with a single pulse. After three oscillations, I decided to switch off the microwave generator. We clearly observe that we recover the oscillation between the 2 lowest energy states induced by the pulse  $\tau$ . Experimentally, this measurement requires two microwave generators, one for each driven transition. We used 2 channels of an AWG that switches on and off the output of generators using windows function. The calibration for this kind of measurement is twice longer in time than the one of a Ramsey or Hahn-echo because we need to tune the parameters of the two generators.

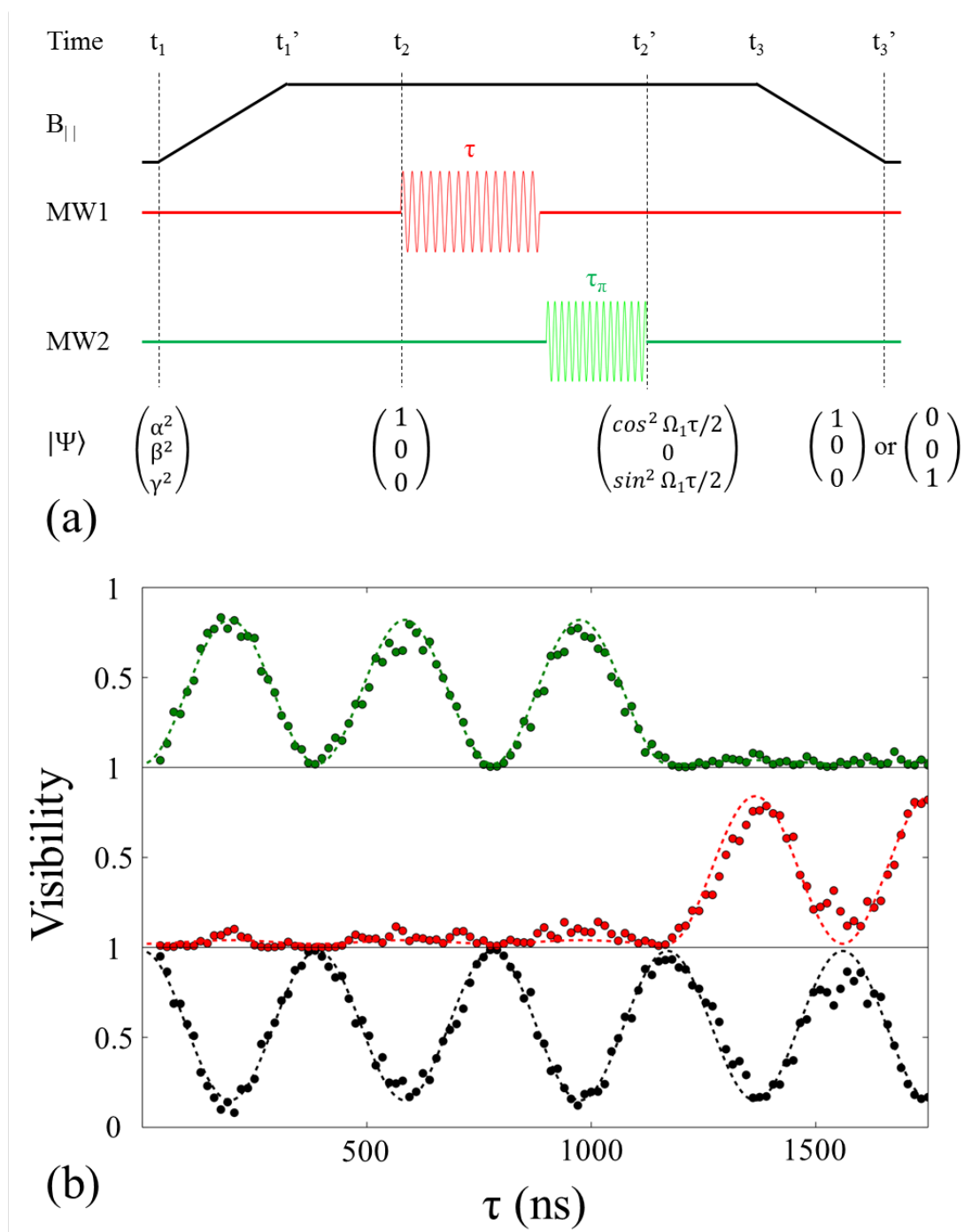


Fig. 6.17 (a) Initialize, manipulate and read-out measurement protocol scheme for the single pump-probe measure. First a pulse of duration  $\tau$  is sent on the first transition, then a  $\pi$ -pulse is sent on the second transition to create an inversion of the population in between state  $|1/2\rangle$  and  $|-1/2\rangle$ . (b) Single pump probe signal obtained by repeating sequence describe in (a) 1000 times for each  $\tau$ . We see an oscillation between the states  $|3/2\rangle$  and  $|-1/2\rangle$  until I stop the pump after three oscillations to recover the normal Rabi signal between the states  $|3/2\rangle$  and  $|1/2\rangle$ .

### 6.6.2 4 states coherent pump probe: double pump

Adding a third generator to the experimental setup and using 3 channels of the AWG allows a coherent manipulation of all the nuclear transitions in a same sequence. I thought that creating a superposition in a certain space and read-out in another one was entertaining. Here the first pulse of duration  $\tau$  is resonant with the second transition and creates a  $|1/2\rangle \leftrightarrow |-1/2\rangle$  coherent superposition. Then I sent a  $\pi$  pulse on the first and on the third transition in the same time. These pulses pump the probability of being in the  $|1/2\rangle$  onto  $|3/2\rangle$  and pump the probability of being in the  $|-1/2\rangle$  onto  $|-3/2\rangle$ . Plotting the previous visibility definition generalized to 4 states as a function of the first pulse length results in figure 6.18 (b). We clearly see, as expected, an oscillation between the states  $|3/2\rangle$  and  $|-3/2\rangle$  with a residual oscillation of the  $|1/2\rangle$  and  $|-1/2\rangle$  states because the pump pulses are not 100% efficient. This double pump probe measurement demonstrate our ability to control all the transitions in a same pulse sequence and to create a coherent superposition of  $\Delta n = 3$  transition only by means of  $\Delta n = 1$  transitions coherent manipulation.

As a physicist, when you create a coherent superposition you want to measure its coherence time. How could we get this information with our experimental setup for the  $|3/2\rangle \leftrightarrow |-3/2\rangle$  superposition we just performed ? As for the Ramsey fringes, the first thought we have to do is to create the superposition, then to let the system under a free evolution and finally bring it back to the initial base. It follows that the sequence, illustrated in figure 6.19, is the same as for the Ramsey measurement of the  $|1/2\rangle \leftrightarrow |-1/2\rangle$  transition with two additional pulses that make the projection in the  $|3/2\rangle \leftrightarrow |-1/3\rangle$  before and after the free evolution. I tried once this measurement, which is time consuming, but the obtained final plot was too noisy to be exploited due to a too fast calibration step. The time dedicated to the experiments is precious during a Ph.D. I therefore decided not to spend too much time on this ancillary measurement and to go forward to the realization of quantum gates and quantum algorithm.

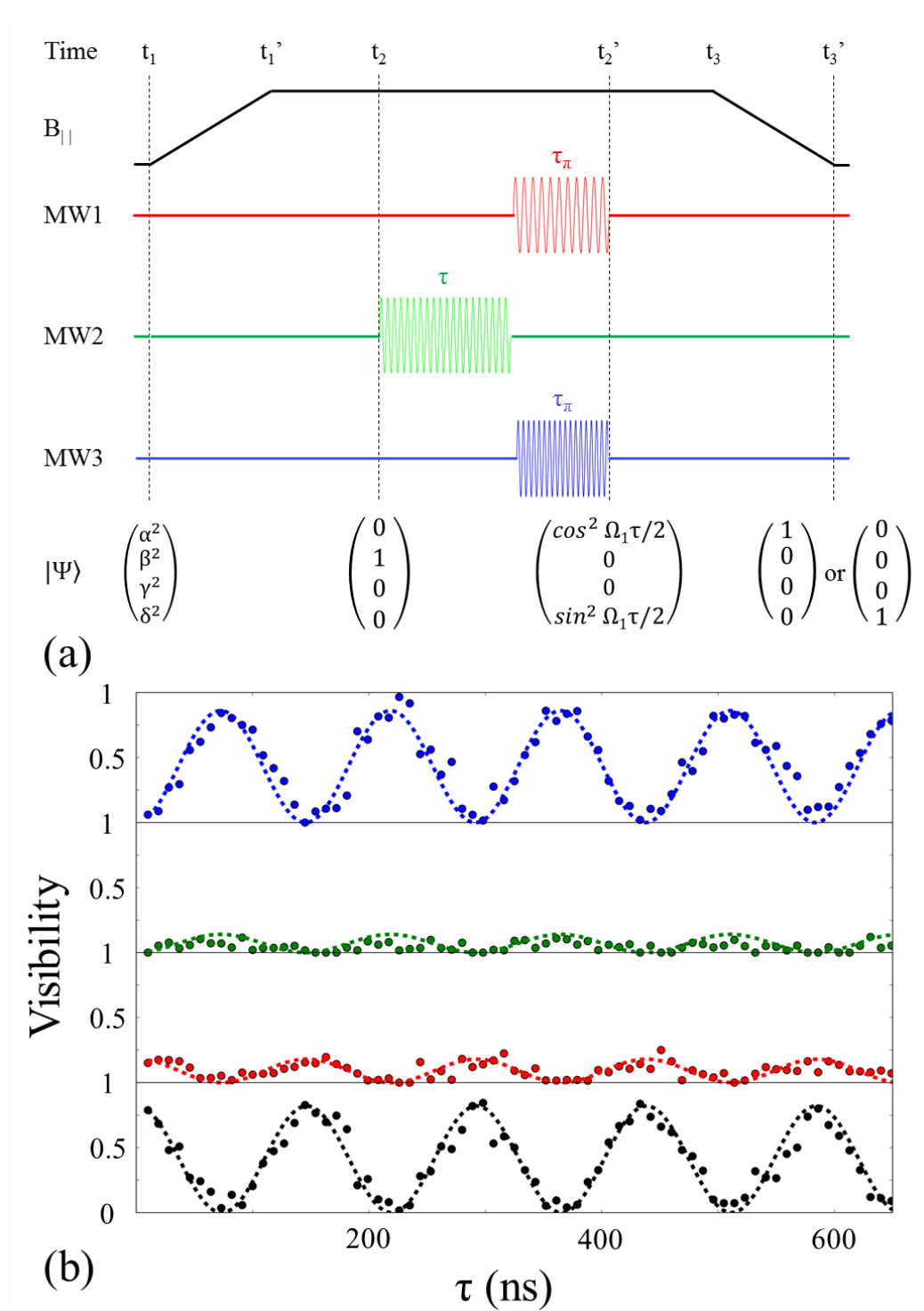


Fig. 6.18 (a) Initialize, manipulate and read-out measurement protocol scheme for the double pump-probe measurement. First a pulse of duration  $\tau$  is sent on the second transition, then a  $\pi$ -pulse is sent simultaneously on the second and the third transition to invert the population of the states  $|1/2\rangle$  and  $|3/2\rangle$  and of the states  $|-1/2\rangle$  and  $|-3/2\rangle$ . (b) Double pump probe signal obtained by repeating the sequence described in (a) 1000 times for each  $\tau$ . We observe an oscillation between the states  $|3/2\rangle$  and  $|-3/2\rangle$ . Because the pumping pulses are not perfectly calibrated, a residual oscillation is visible in between the states  $|1/2\rangle$  and  $|-1/2\rangle$ .

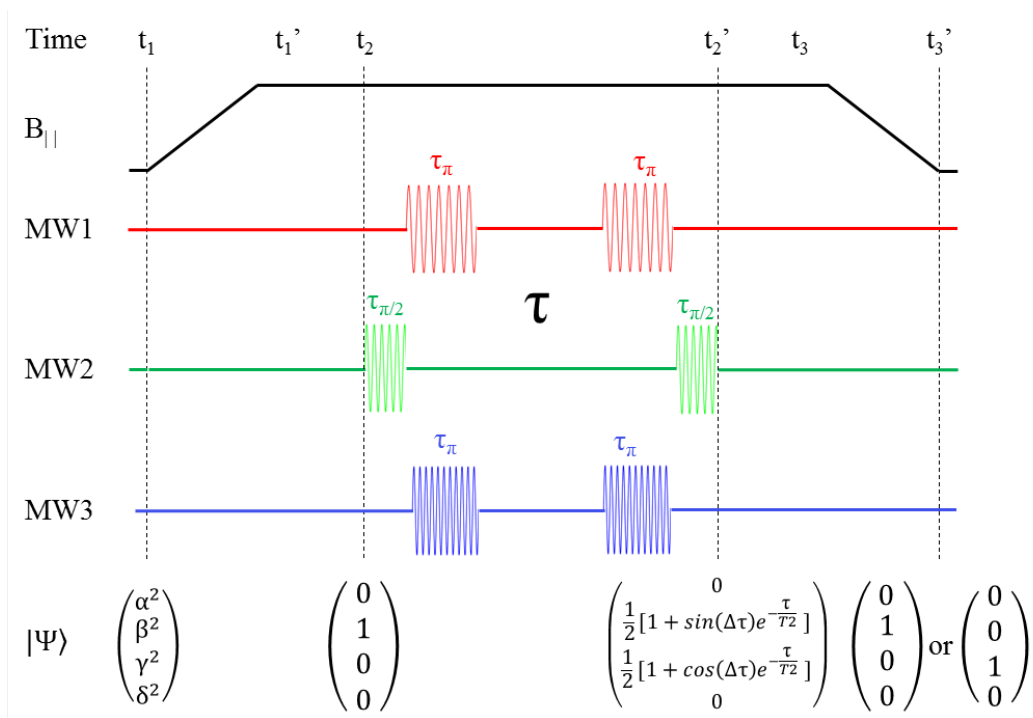


Fig. 6.19 Proposal of a protocol scheme for the  $|3/2\rangle | -3/2\rangle$  superposition coherence time measurement.



# Chapter 7

## Grover algorithm implementation

In the previous chapter, we have seen how we could coherently manipulate a single transition of the nuclear spin states by means of electric RF pulses. Using this method, we demonstrated our ability to fully control the three qubit subsystems in good agreement with the theoretical predictions. Furthermore, measurement of the coherence time of these qubits revealed that we could perform more than two thousands operation before losing the information about the phase of the qubit. Now we consider the nuclear spin in its wholeness, meaning that the RF pulses will not be monochromatic any more and will consist of a mixing of the different resonant frequencies. It has been argued that this fully coherent control of a 4 states quantum system, also called ququad, is a good candidate for the realisation of quantum gates and algorithms. In this chapter I will present my results about the experimental realization of a Hadamard gate and the first implementation of the Grover algorithm in a multi-level quantum system.

We first show how to choose the generalised rotating frame that renders the Hamiltonian of the multi-level system time independent. Operating in that context we then highlight the power of quantum information processing by demonstrating a polynomial speed-up, compared with a classical algorithm, to solve an every day problem: searching for a specific element in an unordered list. The theoretical parameters to solve this problem were derived thanks to a collaborative work with Karim Ferhat from the Néel institute. I will then present the experimental realisation of multi-states coherent superposition, the so-called Hadamard gate. The state obtained after the Hadamard gate will be subjected to an unitary evolution, increasing the population of a selected state. The succession of these two gates represents the experimental realisation of a quantum search algorithm.

## 7.1 Microwave pulse - multi-states interaction

In section 6.1 I presented the interaction of a qubit with a monochromatic RF magnetic field. Then, I detailed that in a TbPc<sub>2</sub>, through the hyperfine Stark mechanism, a large magnetic field can be produced by modulating the hyperfine constant with an electric field. Here we generalise this magnetic field-qubit interaction to a multi-level system (Qudit) coupled to a polychromatic magnetic field. We first express the dynamic of the system with a time independent Hamiltonian, convenient to describe quantum information process unitary evolution. Note that we can no longer use the Pauli matrices and that the Bloch-sphere representation is no longer applicable.

We start with the diagonal Hamiltonian  $H_{Qubit}$  of a three levels system with eigenenergies  $\varepsilon_0$ ,  $\varepsilon_1$  and  $\varepsilon_2$ . Because of RF magnetic field, a non zero transition probability  $\langle n|V|m\rangle$  between the states  $n$  and  $m$  has to be taken into account, resulting in the full Hamiltonian:

$$\hat{H} = \hat{H}_{Qudit} + \hat{H}_{Int} = \begin{pmatrix} \varepsilon_0 & \langle 0|V|1\rangle & \langle 0|V|2\rangle \\ \langle 1|V|0\rangle & \varepsilon_1 & \langle 1|V|2\rangle \\ \langle 2|V|0\rangle & \langle 2|V|1\rangle & \varepsilon_2 \end{pmatrix} \quad (7.1)$$

The RF magnetic field has to fulfill the resonant condition with  $\Delta n = 1$  transition. It then contains two frequencies  $\omega_1/2\pi$  and  $\omega_2/2\pi$  such that  $\omega_1 \approx (\varepsilon_1 - \varepsilon_0)/\hbar$  and  $\omega_2 \approx (\varepsilon_2 - \varepsilon_1)/\hbar$ . This approximation in our system is valid because of the large quadrupole term. As a result, the terms  $\langle 0|V|2\rangle$  and  $\langle 2|V|0\rangle$  vanish and we can apply the rotating wave approximation on the  $\Delta n = 1$  transition, resulting in the new Hamiltonian:

$$\hat{H}_{app} = \begin{pmatrix} \varepsilon_0 & \frac{\hbar\Omega_1}{2} e^{i(\omega_1 t + \phi_1)} & 0 \\ \frac{\hbar\Omega_1}{2} e^{i(\omega_1 t + \phi_1)} & \varepsilon_1 & \frac{\hbar\Omega_2}{2} e^{i(\omega_2 t + \phi_2)} \\ 0 & \frac{\hbar\Omega_2}{2} e^{i(\omega_2 t + \phi_2)} & \varepsilon_2 \end{pmatrix} \quad (7.2)$$

This Hamiltonian gives a good description of the dynamic of the system but is still time dependent. In the same way as for the qubit where we apply the  $U_{Qubit} = e^{i\omega_z t}$  transformation to be in the rotating frame, we need to find a unitary transformation that will hide the explicit time dependence of the Hamiltonian:

$$\hat{H}_{g.r.f} = U \hat{H}_{app} U^\dagger - i\hbar U \frac{\delta U}{\delta t} \quad (7.3)$$

We use a three parameters Ansatz:

$$U = \begin{pmatrix} e^{-i\omega_a t} & 0 & 0 \\ 0 & e^{-i\omega_b t} & 0 \\ 0 & 0 & e^{-i\omega_c t} \end{pmatrix} \quad (7.4)$$

and express  $\omega_{a,b,c}$  as a function of  $\omega_{1,2,3}$  and  $\phi_{1,2,3}$  to have a time-independent Hamiltonian. We deduce that:

$$\omega_a = (\omega_1 + \omega_2)/2 + (\phi_1 + \phi_2)/2t \quad (7.5)$$

$$\omega_b = (\omega_2 - \omega_1)/2 + (\phi_2 - \phi_1)/2t \quad (7.6)$$

$$\omega_c = -(\omega_1 + \omega_2)/2 - (\phi_1 + \phi_2)/2t \quad (7.7)$$

By injecting  $\omega_{a,b,c}$  in equation 7.3 and by renormalizing the energies we obtain a time-independent Hamiltonian in the generalized rotation frame of the 3 quantum states in interaction with the magnetic field :

$$\hat{H}_{g.r.f} = \hbar \begin{pmatrix} 0 & \frac{\Omega_1}{2} & 0 \\ \frac{\Omega_1}{2} & \delta_1 & \frac{\Omega_2}{2} \\ 0 & \frac{\Omega_2}{2} & \delta_2 \end{pmatrix} \quad (7.8)$$

The magnetic field is composed of two frequencies  $\omega_1/2\pi$  and  $\omega_2/2\pi$  with  $\delta_1 = \frac{\varepsilon_1 - \varepsilon_0}{\hbar} - \omega_1$  and  $\delta_2 = \frac{\varepsilon_2 - \varepsilon_1}{\hbar} - \omega_2$ . The magnetic field amplitude of component  $\omega_1$  (respectively  $\omega_2$ ) results in an oscillation transition probability with frequency  $\Omega_1$  (respectively  $\Omega_2$ ) between the state 0 and 1 (respectively states 1 and 2). As expected, when we switch off the second frequency component of the magnetic field ( $\Omega_2 = 0$ ) we recover the same Hamiltonian as for the qubit system. This frame rotation transformation can be easily generalized to a "N" quantum states system giving the Hamiltonian:

$$\hat{H}_{g.r.f} = \sum_{n=1}^{N-1} \delta_n |n\rangle \langle n| + \frac{\Omega_n}{2} |n+1\rangle \langle n| + \frac{\Omega_n}{2} |n\rangle \langle n+1| \quad (7.9)$$

where  $\varepsilon_0$  is set to 0. In the following, we will always use this generalized rotating frame to describe the dynamic of the nuclear spin. The experimental results will validate the rotating

wave approximation.

## 7.2 Hadamard Gate

### 7.2.1 Theory

Among all quantum algorithms, one distinguishes those specifically simulating quantum systems and those relying on quantum Fourier transforms, such as the Shor's algorithm for integer factorization. The third main category of quantum algorithms generalizes or incorporates the algorithm discovered in 1997 by L. K. Grover to search an element in an unsorted list. In this algorithm, each state of the Hilbert space is associated to an element of a list. Then, the probability of measuring the element we are looking for is equal to the probability of being in the corresponding quantum state. From this statement, we understand that this algorithm is based on state amplitude amplification.

The preliminary operation, common for all these quantum research algorithms, is to create a quantum database, such that the initial probability is an equipartition:

$$|\Psi_{sup}\rangle = \frac{1}{\sqrt{N}} \sum_{n=0}^{N-1} |n\rangle \quad (7.10)$$

The best classical analog I found to illustrate this preliminary operation is the printing of a phone number directory using the same ink intensity for each phone number. We will see in the following that the fact that there is no phase component in the sum, meaning that the phase of all the states are equal, is primordial. One can imagine systems that are in this specific state at equilibrium, so that no preliminary operation is needed. In our case we are sure of being in a given state only after the initialisation process that projects the nuclear spin in one of its eigenstate. As a result, we need to apply a unitary evolution that, starting from this eigenstate of the system, creates the state  $|\Psi_{sup}\rangle$ . This quantum operation is called a Hadamard gate.

To carry out this quantum gate, it is mandatory to drive simultaneously all transitions during a certain time  $\tau$ , with given amplitudes and detunings such that:

$$|\Psi(\tau)\rangle = \hat{U} |\Psi_i\rangle \quad (7.11)$$

$$= e^{i2\pi H_{g,r,t} \tau / \hbar} |\Psi_i\rangle \quad (7.12)$$

$$= \frac{1}{\sqrt{N}} \sum_{n=0}^{N-1} |n\rangle \quad (7.13)$$

This apparently simple equation hides a difficulty: one needs to find, for a  $N$  elements database, a combination of  $2N - 1$  parameters (1 for  $\tau$ ,  $N-1$  for the amplitudes and  $N-1$  for the detunings). At this specific moment of my thesis, I wondered how I could solved this problem.

I got the solution through discussions with Karim Ferhat from the Néel Institute. We then decided to create an application whose interface (shown in figure 7.1) is well adapted for an experimentalist. In this application I need to choose my initial eigenstate and the number of element I want in my database (2, 3 or 4). Then, to reduce the parameters space, I indicate my experimental limits on  $\tau$  and  $\Omega_n$ . Finally I press the "Hadamard Gate:  $t, \Omega_1, \Omega_2, \Omega_3$ " knob and a minimisation algorithm find the best value of the different parameters ( $\tau, \Omega_n, \delta_n$ ) to get an Hadamard state.

$$e^{i2\pi H_{g,r,t} \tau / \hbar} |\Psi_i\rangle - \frac{1}{\sqrt{N}} \sum_{n=0}^{N-1} |n\rangle = 0 \quad (7.14)$$

The population of each states are then plotted as the function of the pulse length  $\tau$  in addition with the population and phase variance (dot line). Experimentally it is necessary to know the set of parameters but it is also interesting to get an idea of the robustness of these parameters, meaning if one of the parameter is not exactly calibrated to the good value, do I have a chance to get a sufficiently nice Hadamard state at the end ? To answer this question and to find "robust" Hadamard Gate, we add the possibility of plotting the populations' variance as a function of 2 chosen parameters and to see the dynamic of this variance by creating a movie. A good set of parameters will have a large minimum area in this density plot. Last option of this application is to save in a .dat file the different parameters and populations evolution, these files are then used to plot the theoretical plot. A second window which I don't present here exists on this application. It plots the evolution of population and phase as a function of time for an arbitrary sequence. This helped me a lot during my thesis. It works on Mathematica and CDF soft, we wait that CDF becomes available on android to make it downloadable.

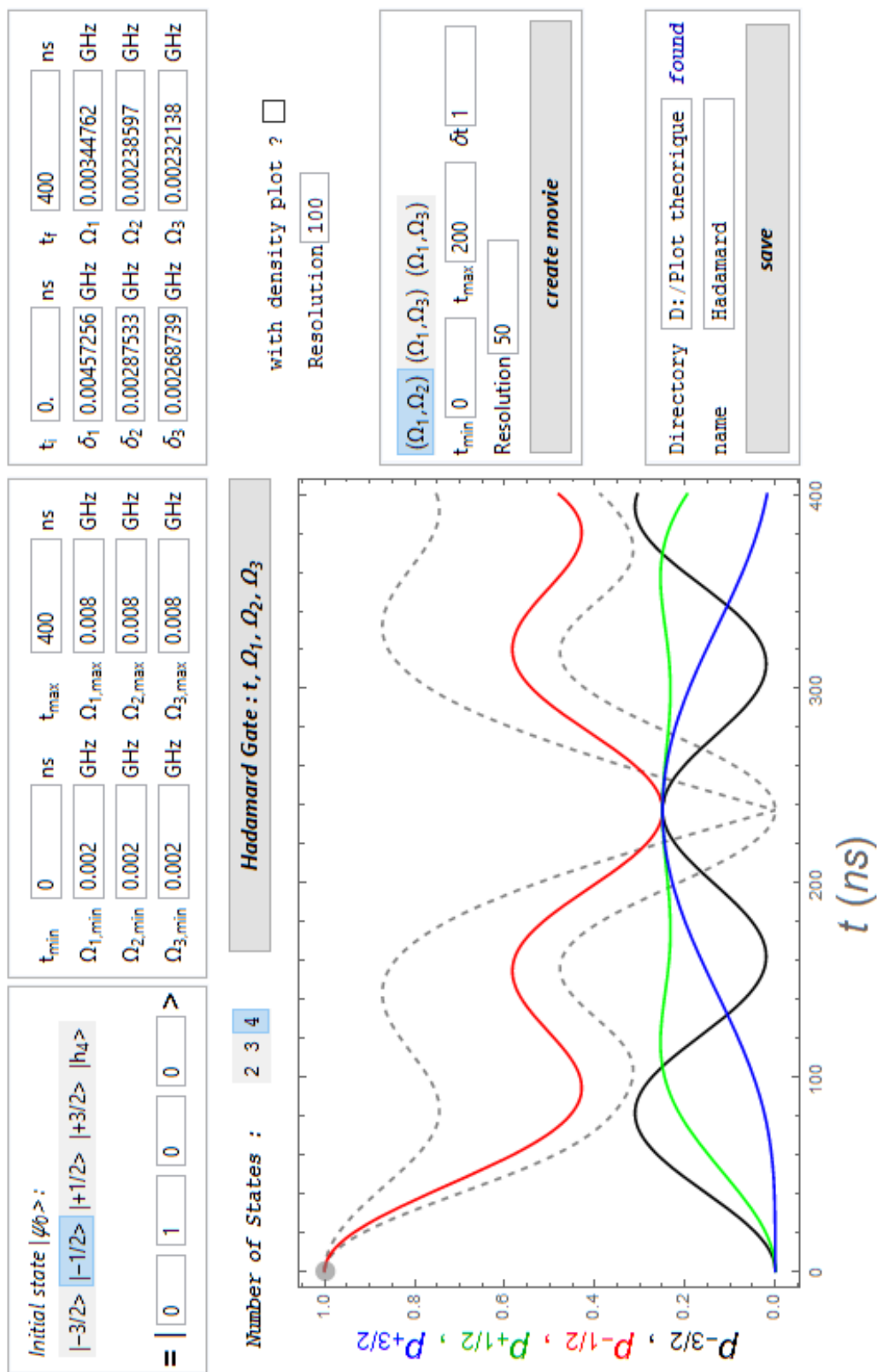


Fig. 7.1 Interface of the application developed to find the good theoretical parameters that create Hadamard gate.

### 7.2.2 Experimental realisation

To create a Hadamard state I use the microwave generation set up described in section 3.5.3. Previously, only one transition was driven in a same sequence (section 6.4 and 6.5), or several but not simultaneously for a given state (section 6.6). To perform the Hadamard gate, the Hamiltonian of equation 7.9 shows that a state  $|n\rangle$  is driven in such a way that it could, simultaneously, goes up to  $|n+1\rangle$  or goes down to the  $|n-1\rangle$ . Even a tiny de-synchronisation of the pulses of different frequencies will have a great impact on the dynamic. Thus, before the calibration step, I paid a deep attention to this synchronisation by measuring the pulse shape with a 30GHz sampling LeCroy oscilloscope (see figure 3.6) before the injection in the inverted dilution fridge.

When the microwave generation circuit has been tested, we can start the calibration step in order to tune the different pulse parameters that give the detuning and transition probability frequency calculated with the application previously presented. I always use the following method for each resonance:

- switch to "RF on" mode the microwave source that generates the expected frequency and switch to "RF off" mode the others.
- Tune the pulse frequency to find the resonance of the transition by maximizing the Rabi oscillation amplitude.
- Tune the power of the pulse to find the expected Rabi oscillation frequency at resonance.
- Measure a Rabi oscillation with previously adjusted power and frequency modified by the wanted detuning value.
- Compare this Rabi oscillation (amplitude and frequency) with the theoretical plot. If this Rabi oscillation is sufficiently close to the theoretical plot I apply this method to the next transition. Otherwise, meaning that something has changed in the experiment (charge offset in the local-back gate, transmission in the microwave circuit) I start again and check the transition previously calibrated.

The better you know the experiment the faster you can calibrate it. However the limit to have a sufficiently nice Hadamard state is about two days per resonance. When all transitions are calibrated, we can start the measurements. After switching on all the microwave sources, we record the different state populations as a function of the pulse length using the experimental

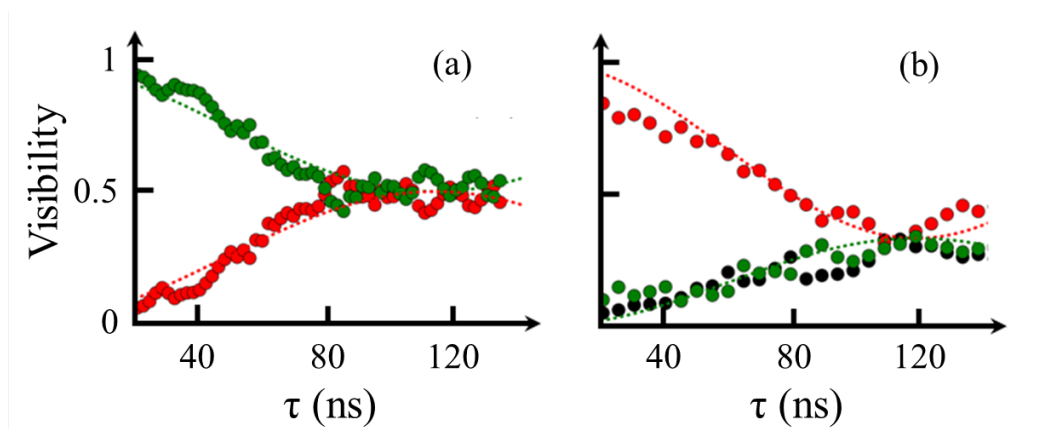


Fig. 7.2 Hadamard gate. Evolution of the nuclear spin states population as function of the microwaves pulse length for a two (a) and a three (b) states Hadamard evolution. After a pulse of duration 120ns for the two measurements, the nuclear spin is in equiprobable coherent superposition of respectively two and three states.

protocol explained in section 6.3 and the following definition of the visibility of the state  $j$  knowing that the initial state is  $i$ :

$$V_{i \rightarrow j} = \frac{N_{i \rightarrow j}}{\sum_{n=3/2} N_{i \rightarrow |n\rangle}} \quad (7.15)$$

This procedure has been repeated to create a 2 and a 3 states Hadamard gate as respectively displayed in figure 7.2 (a) and (b). In these two measurements, the phase of the states are not directly measured (which would require a tomography experiment). Indeed, the evolution of the population as a function of the pulse length can be fitted only by parameters that results in a phase variance vanishing at the specific time we obtain the coherent superposition.

Because the calibration procedure was too long to compare with the stability time of the experiment, I never succeeded to measure a nice 4 states Hadamard gate. Indeed this experiment requires the calibration of 7 parameters and is very sensitive to small lack of precision during the calibration process. To reduce the number of parameters, I decided to create a coherent superposition of 4 states forcing the detuning to be zero, only tuning the power of the three microwave sources. The drawback of this constraint is that it is impossible to find a set of driving parameter that cancels both population and phase variance. Figure 7.3 is the results of this measurement, showing a nice coherent superposition for a pulse length of 135 ns. This particular state is interesting in a fundamental point of view but cannot be

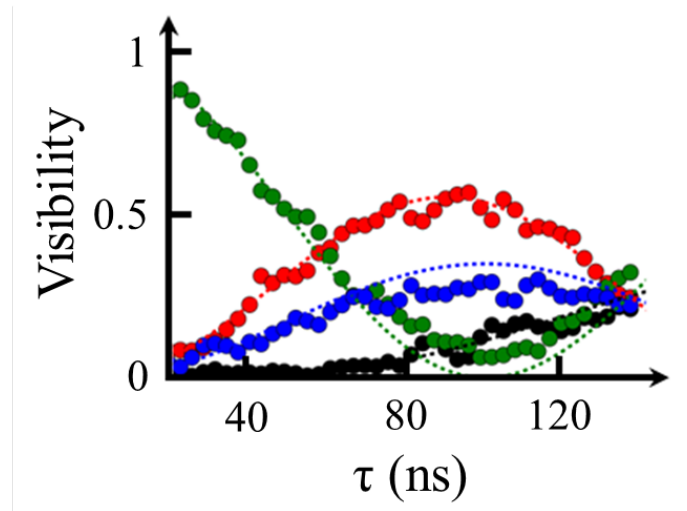


Fig. 7.3 Evolution of the nuclear spin states population according to the microwaves pulse length. After a duration of 135ns, the nuclear spin is in a coherent superposition of four states. The phase of the different states are not equal in this case. This is thus not a real Hadamard gate.

used to implement the Grover algorithm because phases of states are different. An example of 4 states Hadamard gate set of parameter and state evolution is given in figure 7.1.

### 7.2.3 Ramsey fringes generalised to N states

As already expressed in the pump probe section, in quantum physics, when a new kind of superposition is synthesized, it is interesting to find a method that gives the opportunity to measure its coherence time. In this part, I will present a generalization of the Qubit Ramsey fringes to Qudit. The main idea is the same than for a qubit: starting from an eigenstate, a coherent superposition is first created, then, we let the system free to evolve within controlled time  $\tau$ , finally, the system is projected to the eigenstate basis. I will derive in the following this generalization and present a measurement performed on a three states system  $\{|3/2\rangle, |1/2\rangle, |-1/2\rangle\}$ .

As previously explained, a superposition of N states can be obtained by applying a Hadamard gate to the system. In order to simplify the derivation, I choose  $|1/2\rangle$  as the initial state and the following Hamiltonian to maximize the symmetry of the dynamic:

$$\hat{H}_{on} = \hbar \begin{pmatrix} 0 & \Omega/2 & 0 \\ \Omega/2 & \Omega & \Omega/2 \\ 0 & \Omega/2 & 0 \end{pmatrix} \quad (7.16)$$

If we apply the unitary evolution induced by this Hamiltonian on the state  $|1/2\rangle$ , we obtain:

$$|\Psi(t)\rangle = e^{i2\pi H_{on}t/\hbar} \begin{pmatrix} 0 \\ 1 \\ 0 \end{pmatrix} = \frac{ie^{i\pi\Omega t}}{\sqrt{3}} \begin{pmatrix} \sin(\sqrt{3}\pi\Omega t) \\ \sin(\sqrt{3}\pi\Omega t) - i\sqrt{3}\cos(\sqrt{3}\pi\Omega t) \\ \sin(\sqrt{3}\pi\Omega t) \end{pmatrix} \quad (7.17)$$

This equation clearly shows that for  $t = t_{Had} = \sqrt{3}/6\Omega$  the three states have identical population and phase: we obtain a Hadamard state. The next step is to switch off the pulse and wait a certain time  $\tau$ . The Hamiltonian of the system when the microwave is off is given by:

$$\hat{H}_{off} = \hbar \begin{pmatrix} 0 & 0 & 0 \\ 0 & \Omega & 0 \\ 0 & 0 & 0 \end{pmatrix} \quad (7.18)$$

Because the global phase of a state has no physical meaning we fix it at 0, resulting in the following evolution:

$$|\Psi(\tau)\rangle = \frac{e^{i2\pi H_{off}\tau/\hbar}}{\sqrt{3}} \begin{pmatrix} 1 \\ 1 \\ 1 \end{pmatrix} = \frac{1}{\sqrt{3}} \begin{pmatrix} 1 \\ e^{i2\pi\Omega\tau} \\ 1 \end{pmatrix} \quad (7.19)$$

Taking into account the dephasing processes would require a treatment of the dynamic using the master equation, to the detriment of the global understanding, so they are not expressed here. However, as for a qubit, decoherence mainly occurs during the free evolution of time length  $\tau$ . The last step is to project the state in the eigenstate basis applying the same pulse of duration  $\tau_{Had}$  as the one used to create the coherent superposition:

$$|\Psi_f(\tau)\rangle = \frac{e^{i2\pi H_{on}\tau_{Had}/\hbar}}{\sqrt{3}} \begin{pmatrix} 1 \\ e^{i2\pi\Omega\tau} \\ 1 \end{pmatrix} = \frac{e^{i\phi}}{3} \begin{pmatrix} e^{i2\pi\Omega\tau} - 1 \\ e^{i2\pi\Omega\tau} + 2 \\ e^{i2\pi\Omega\tau} - 1 \end{pmatrix} \quad (7.20)$$

The resulting state component are plotted in figure 7.4 (a). It exhibits oscillations with frequency  $\Omega$  in between the state  $|1/2\rangle$  and the two states  $|-1/2\rangle$  and  $|3/2\rangle$ . We observe no damping in these oscillations since no decoherence was introduced in the model. As

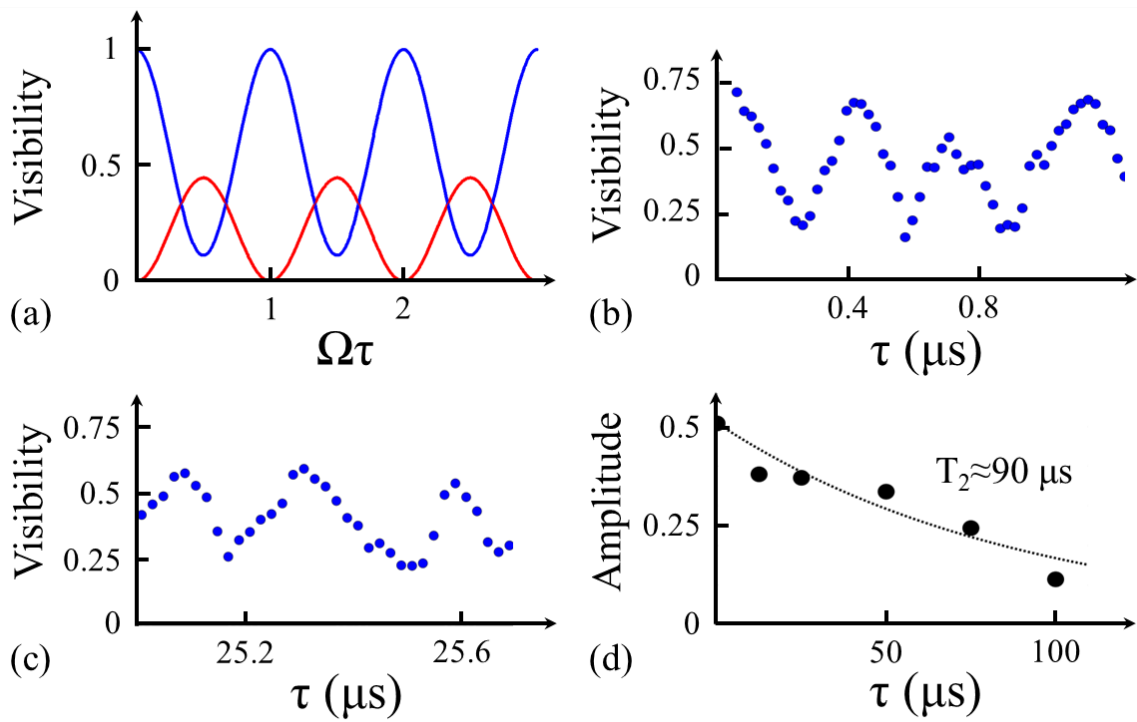


Fig. 7.4 Three states superposition coherence time measurement. (a) Theoretical evolution of the state population ( $|1/2\rangle$  in blue,  $|-1/2\rangle$  and  $|3/2\rangle$  in red) after applying two Hadamard gates separated in time by a free evolution time  $\tau$ . (b) Experimental oscillations of the  $|1/2\rangle$  population as a function of the free evolution time. (c) These oscillations are still visible for  $\tau$  of the order of  $25\mu\text{s}$  but with a damped amplitude. This amplitude damping is presented on panel (d), exhibiting a coherence time for the 3 states superposition of the order of  $90\mu\text{s}$ .

for the measurement presented in figure 7.4 (b), I apply the pulse sequence just presented. Since the aim is to measure the damping of the amplitude as a function of  $\tau$ , figure 7.4 (b) only presents the visibility of the initial state  $|1/2\rangle$ . As the oscillations are fast and the coherence time is long, I present in figure 7.4 (c) the same measurement with an offset of  $25 \mu\text{s}$  on  $\tau$ . We can clearly observe that the oscillations are still present. I then performed the same measurements with different offset and plotted the resulting oscillations amplitude as a function of  $\tau$  in figure 7.4 (d). We can extract from this measurement an approximative coherence time of  $90 \mu\text{s}$ . The main difficulty was to calibrate the microwave pulse to obtain the good condition on the detuning ( $\delta = \Omega$ ). Little mistakes on this calibration have a huge impact on the states population at the end of the sequence for waiting time corresponding to several phase oscillations. As a result it is hard to have a deeper analysis of the decoherence process because the ratio between calibration time and experiment stability time is too high, however this measurement demonstrates that:

- A succession of two Hadamard gates separated by a waiting time  $\tau$  is a good sequence to measure the coherent time of a multi-state system.
- The coherence time of a 3 states superposition is smaller than a 2 states superposition but remains of the same order.

I would like also to add that the oscillation frequency of these fringes cannot be tuned as for a Ramsey measurement but it is fixed by the probability transition frequency induced by the microwave pulse. To avoid this problem, we could implement a Hahn-echo generalization protocol that ensures the oscillating term to be constant.

### 7.3 Grover's unitary evolution

At this point we are able to build a 3 states quantum directory. The game is now to amplify the population of a desired state to increase the probability to collapse on it during the final state read-out. To achieve this, the idea of the Grover's algorithm is to create a resonant condition in between the superposed state and the searched state. Under this condition, the system will oscillate between these two states and after a half period of oscillation will be fully in the searched state. The power of this oscillating unitary evolution is the fact that its period is  $\sqrt{N}$  dependent. We will first treat this amplitude amplification gate from a theoretical point of view before demonstrating its experimental implementation.

### 7.3.1 Amplitude amplification

For a  $N$  states system, after completing a Hadamard gate, the probability of being in each state is equal to  $1/N$ : the quantum directory has therefore been built:

$$|\Psi_{had}\rangle = \frac{1}{\sqrt{N}} \sum_{n=0}^{N-1} |n\rangle \quad (7.21)$$

From this directory, the challenge is now to amplify the probability of being in a given state such that when we perform the final read-out, the system is fully in the researched state. To find a state  $|s\rangle$ , we need to label it. If in the sequential Grover's algorithm we identify the desired state by modifying its phase [58], in the present continuous version we mark it by giving it a certain energy  $E_g = 2\pi\hbar\delta_g$  in the rotating frame, such that the Hamiltonian of the system becomes:

$$\hat{H} = \hbar\delta_g |s\rangle\langle s| + \frac{\hbar\Omega_n}{2} \sum_{n=1}^{N-1} |n+1\rangle\langle n| + |n\rangle\langle n+1| \quad (7.22)$$

As explained in the article of E. Farhi and Sam Gutman [60], the main idea is to make the labelled state more visible by amplifying its population. Therefore, we aim to increase the population of  $|s\rangle$  by creating a resonant condition in between the full system and the state  $|s\rangle$ . This resonant condition is obtained by adjusting  $E_g$ , such that:

$$\langle\Psi_s|H|\Psi_s\rangle = \langle\Psi_{had}|H|\Psi_{had}\rangle \quad (7.23)$$

We can adjust the microwave powers in order to obtain the same Rabi frequency for each transition. This resonant condition results in  $\delta_g = \Omega$ . To better understand the strength of this resonant condition, it is important to study the dynamic of the system in this regime. It is clear that the dynamic of the state  $|s\rangle$  will be different from the others. To take account of this difference and to simplify the derivation of the problem, we calculate the dynamic in the Hilbert space made of  $|s\rangle$  and its perpendicular state:

$$|r\rangle = \frac{\left[ \sum_{n=0}^{N-1} |n\rangle \right] - |s\rangle}{\sqrt{N-1}} \quad (7.24)$$

The Hamiltonian of equation 7.22 in this new  $\{|s\rangle, |r\rangle\}$  basis with the resonant condition  $\delta_g = \Omega$  becomes:

$$\hat{H} = \frac{\hbar\Omega}{N} \begin{pmatrix} N+1 & \sqrt{N-1} \\ \sqrt{N-1} & N-1 \end{pmatrix} \quad (7.25)$$

Knowing that the initial state is  $|\Psi_{had}\rangle = 1/\sqrt{N}|s\rangle + \sqrt{1-1/N}|r\rangle$ , we have now all the informations to derive the unitary evolution of the system in the  $\{|s\rangle, |r\rangle\}$  basis:

$$|\Psi(\tau)\rangle = e^{i2\pi H/\hbar} |\Psi_{had}\rangle = \frac{e^{i\phi}}{\sqrt{N}} \begin{pmatrix} \cos(\frac{2\pi\Omega\tau}{\sqrt{N}}) + i\sqrt{N}\sin(\frac{2\pi\Omega\tau}{\sqrt{N}}) \\ \sqrt{N-1}\cos(\frac{2\pi\Omega\tau}{\sqrt{N}}) \end{pmatrix} \quad (7.26)$$

We can now obtain from this expression the probability of being in the researched state  $|s\rangle$  as a function of the unitary evolution time  $\tau$ . In the large N limit, we obtain :

$$|\langle s|\Psi(\tau)\rangle|^2 = \sin^2\left(\frac{2\pi\Omega\tau}{\sqrt{N}}\right) + \frac{1}{N}\cos^2\left(\frac{2\pi\Omega\tau}{\sqrt{N}}\right) \quad (7.27)$$

This "simple" equation is very convenient to understand the dynamic of the system. The resonant condition bring the system into an oscillating regime between the Hadamard state and the researched state. Indeed for  $\tau = 0 + x\frac{\sqrt{N}}{2\Omega}$  the probability of being in the research state is  $1/N$  because the system is in its Hadamard state. Whereas for  $\tau = \frac{\sqrt{N}}{4\Omega} + x\frac{\sqrt{N}}{2\Omega}$  the system is fully in the desired state. The interesting point of this oscillation is that its period increases as  $\sqrt{N}$ , meaning that the first at which we are in the researched state is:

$$\tau = \frac{\sqrt{N}}{4\Omega} \quad (7.28)$$

This clearly exhibits the square root dependence of the researched time as the function of the number of elements in the database: it is the fingerprint of the Grover's algorithm. We can also notice that the faster we drive the system (by increasing  $\Omega$ ) the faster we find the desired state.

### 7.3.2 Experimental Implementation

We previously demonstrated our ability to build up a 3 states quantum directory. Now, starting from an eigenstate of the nuclear spin, we have first to create the quantum directory *via* a Hadamard gate and second to amplify the population of a desired state using the Grover's unitary evolution. This experimental sequence is represented in figure 7.5. Thus, we will first present the needed microwave setup, then we will explain the calibration procedure to tune the pulse parameters and finally we will demonstrate the experimental Grover's algorithm implementation.

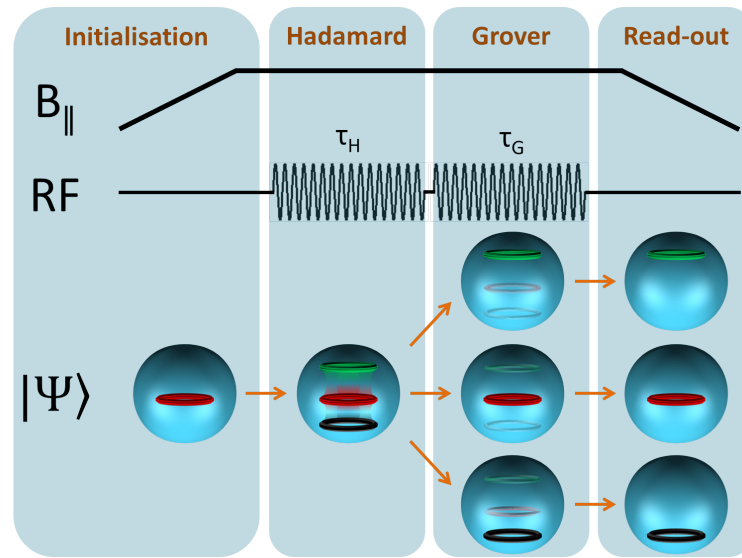


Fig. 7.5 Initialisation, Hadamard gate, Grover's unitary evolution and read-out measurement protocol scheme for Grover's algorithm implementation. First a pulse of duration  $\tau_H$  is applied to create the Hadamard state, then a second pulse of duration  $\tau_G$  is generated with a detuning that ensure a resonant condition in between the superposed and the researched state. Finally, the nuclear spin state is read-out by sweeping back the magnetic field.

### Microwave setup

As presented in figure 7.5, to perform the algorithm sequence, the microwave pulse is composed of two parts. One for the Hadamard gate and another for the unitary evolution. These two pulses have different frequencies. We first anticipated to use the microwave setup with an AWG and two RF sources (see section 3.5.3). The N-1 first outputs of the AWG are used for the amplitude modulation of the sources when the N-1 following for the frequency modulation. We experimented that, with this method, nothing worked as expected for two reasons:

- The frequency modulation is not instantaneous and takes of the order of  $1 \mu\text{s}$  per Mhz of modulation. As a result one needs to wait few  $\mu\text{s}$  in between the Hadamard and Grover evolution because detunings are typically of the order few Mhz. During this free evolution time, the phase of each state evolves (see section 7.4). Consequently, when the Grover pulse is applied, the phase of the states are no longer equal.
- During the frequency modulation of the microwave sources, all information about the phase of the pulse is lost. As explained in section 6.1, this phase has an impact on

the system dynamic. For example, for a qubit, the phase of the pulse is linked to the rotation angle of the quantum state in the (x,y) plan of the Bloch-sphere.

To summarize, in between the Hadamard and Grover gate, no time separation is allowed and the phase of the pulses have to remain constant to get the desired dynamic. In order to satisfy these constraints, we make use of one 24 GHz sampling rate AWG that directly drives all the transitions (see section 3.5.4). Indeed, the signal  $S$  is numerically defined with one point every 1/24 ns ( $\approx 41$ ps) and then converted to an analog signal:

$$S(i) = \sum_{n=1}^N A_n(\Omega_n) \left[ \sum_{i=0}^{24\tau^{Had}} \sin(2\pi\nu_n^{Had}i) + \sum_{i=24\tau^{Had}}^{24(\tau^{Had}+\tau^{Gro})} \sin(2\pi\nu_n^{Gro}i) \right] \quad (7.29)$$

with  $A_n$  the amplitude pulse's component driving the  $n^{th}$  transition,  $\tau^{Had}$  and  $\tau^{Gro}$  respectively the Hadamard and Grover unitary evolution time in nanosecond. The expression of  $\nu_n$ , the frequency that drives the  $n^{th}$  transition is defined as:

$$\nu_n = E_n/h + \delta_{n-1} - \delta_n \quad (7.30)$$

This non trivial expression originates from the dynamic in the rotating frame. Experimentally the energy of the researched state is not directly changed (which could be also done through the DC-Stark effect). To effectively give a certain energy to the researched state in the generalized rotating frame, we modify the pulses frequencies (see figure 7.6).

### Calibration process

As explained in the theoretical part, there is no condition imposed on the transition rates  $\Omega_n^{Gro}$ . For experimental reason of calibration time we will take in the following  $\Omega_n^{Gro} = \Omega_n^{Had} = \Omega_n$ . However, depending on the researched state, the detuning of the Grover's unitary evolution  $\delta_n^{Gro}$  is most of the time different from the one of the Hadamard  $\delta_n^{Had}$ .

The first calibration steps are the same as the Hadamard gate. They tune the transition rate  $\Omega_n$  and the detunings of the Hadamard gate  $\delta_n^{Had}$ . The only additional precaution to take is to control that  $\sum_{n=1}^N A_n \leq 1V_{p-p}$ , the maximum AWG output peak to peak voltage. Then, to fix  $\tau_{Had}$  and to measure the state after the Hadamard gate, I do a full measurement of the Hadamard evolution over one period. Indeed, if I only measure the population for a pulse duration  $\tau$  equal to the theoretical Hadamard gate time, I cannot get the information about

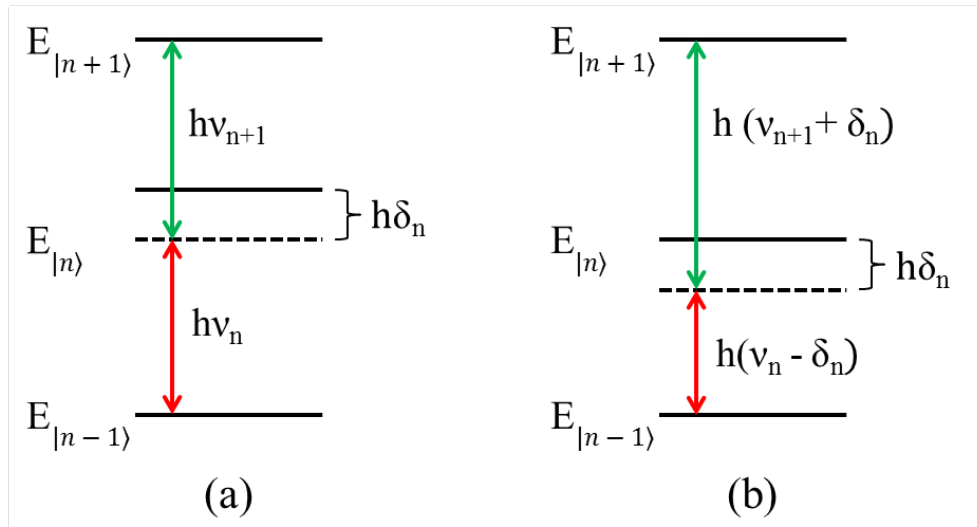


Fig. 7.6 (a) Pulse and states energy diagram for a detuning applied to the state  $n$ . (b) Experimentally, we do not change the energy of a state but we modify the frequency of the applied pulses which results in the same dynamic.

the phase of the states.

Last parameters to tune are the detuning of the Grover's gate pulse  $\delta_n^{Gro}$ . These parameters are determined by the resonant condition:  $\delta_n^{Gro} = \Omega$  if all the transitions are driven at the same speed  $\Omega$  or  $\delta = \frac{1}{N-1} \sum_{n=1}^N \Omega_n$  in the general case. This expression gives the theoretical value. However these detunings can be optimized by performing a last calibration measurement. It consists of measuring the researched state visibility as a function of the detunings of the Grover's evolution, using the pulse defined in equation 7.29 at the theoretical time  $\tau^{Gro}$ . One of these calibration measurements is presented in figure 7.7. In this case, it helps to choose the detuning value that maximizes the visibility of the third state. I did not study in details these maps but I am sure that we could spend one entire thesis on it. Now that all parameters are well tuned, the Grover's algorithm measurement can be performed.

### Grover measurements

The final and harder measurement is to prove that we can implement the Grover algorithm. To do so, we have to measure an oscillation in between the Hadamard state and the researched state. I have imposed myself to record this oscillation for the 3 different states, always

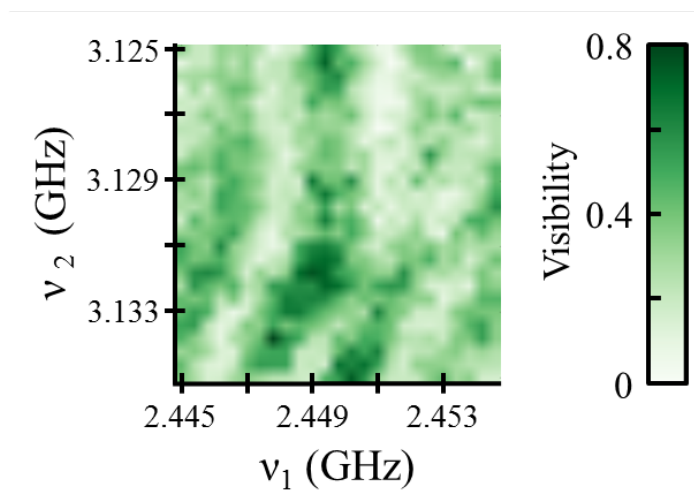


Fig. 7.7 Map of the  $|-1/2\rangle$  state visibility as a function of the frequencies of sources that drive the first and the second transition after a Hadamard gate and an unitary evolution of a fixed duration  $\tau_{Gro}$ . This measurement is performed to calibrate the two frequencies of the Grover unitary evolution. We observe that for  $(v_1 = 2.449; v_2 = 3.132)$ , the visibility of the researched state is maximized.

starting from the state  $|1/2\rangle$ . Indeed, if I start the sequence with a certain state  $|n\rangle$  and apply the Hadamard pulse, I could generate once again the same Hadamard pulse and, because of time reversibility of a unitary evolution, I will find back the  $|n\rangle$ . This is interesting but do not demonstrate the implementation of the Grover algorithm: there is no change of detuning between the Hadamard and Grover pulses.

Starting from the state  $|1/2\rangle$ , the following Hamiltonian give the desired dynamic:

$$\begin{aligned}
 H_{Gro}^{3/2} &= \hbar\Omega \begin{pmatrix} 0 & 1/2 & 0 \\ 1/2 & -1 & 1/2 \\ 0 & 1/2 & -1 \end{pmatrix} \\
 H_{Had} &= \hbar\Omega \begin{pmatrix} 0 & 1/2 & 0 \\ 1/2 & 1 & 1/2 \\ 0 & 1/2 & 0 \end{pmatrix} \\
 H_{Gro}^{1/2} &= \hbar\Omega \begin{pmatrix} 0 & 1/2 & 0 \\ 1/2 & 1 & 1/2 \\ 0 & 1/2 & 0 \end{pmatrix} \\
 H_{Gro}^{-1/2} &= \hbar\Omega \begin{pmatrix} 0 & 1/2 & 0 \\ 1/2 & 0 & 1/2 \\ 0 & 1/2 & 1 \end{pmatrix}
 \end{aligned} \tag{7.31}$$

From an experimental point of view, the sequence to apply, illustrated in figure 7.5, is the following:

- nuclear spin state initialization: Magnetic field sweep from -60mT to +60mT.
- Hadamard gate: Multi-chromatic microwave pulse with calibrated parameters that results in a transition rate  $\Omega_n^{Had}$  for the  $n^{th}$  transition and detuning  $\delta_n^{Had}$  during a pulse duration  $\tau^{Had}$ . It ensures a coherent superposition of N states.
- Grover unitary evolution: Multi-chromatic Microwave pulse with calibrated parameters that results in a transition rate  $\Omega_n^{Gro}$  for the  $n^{th}$  transition and detuning  $\delta_n^{Gro}$  during a variable pulse duration  $\tau^{Gro}$ .
- Nuclear spin state read-out: Magnetic field sweep from +60mT to -60mT.

I did not record the Hadamard evolution for each sequence in order to earn one day of measurement, which is crucial for the stability in between the calibration and the measurement. In the three cases, the population dynamic is similar to the one presented in figure 7.2. The evolution of the state population as a function of the Grover pulse length are displayed in figure 7.8 (a) (b) and (c) respectively for the Hamiltonians  $H_{Gro}^{[3/2]}$ ,  $H_{Gro}^{[1/2]}$  and  $H_{Gro}^{[-1/2]}$ . We clearly see the oscillation behaviour: starting from the coherent superposition (quantum directory) the desired state population increases to reach a maximum and finally the system goes back to the superposed state. As a result, by reading out the system at this half oscillation period time, we have an amplified probability (respectively 95%, 80% and 80%) to find the researched state.

The fact that this period is not the same for these three measurements is due to both theoretical and experimental reasons:

- in the high N limit, all periods converge to  $\frac{\sqrt{N}}{2\Omega}$  as explained in the theoretical section 7.3.1. In the low N limit, this is not the case and the period is longer for states situated on the edge of the database.
- These measurements take several weeks during which the experimental parameters changed, mainly due to charge relaxation in the back gate. As a result, these three measurements are performed at different driving speed  $\Omega$ .

Finally, we clearly observed an additional low amplitude oscillation which is about one order of magnitude faster than the Grover oscillation. A periodic modulation of about one

hour of the driving speeds can explain this signal. This may originated from the electric environment of the nuclear spin that modifies the transition energy through the DC-Stark effect. A deeper study could be of great interest and the new generation of sample discussed in section 4.1.3 should annihilate or at least lower this effect.

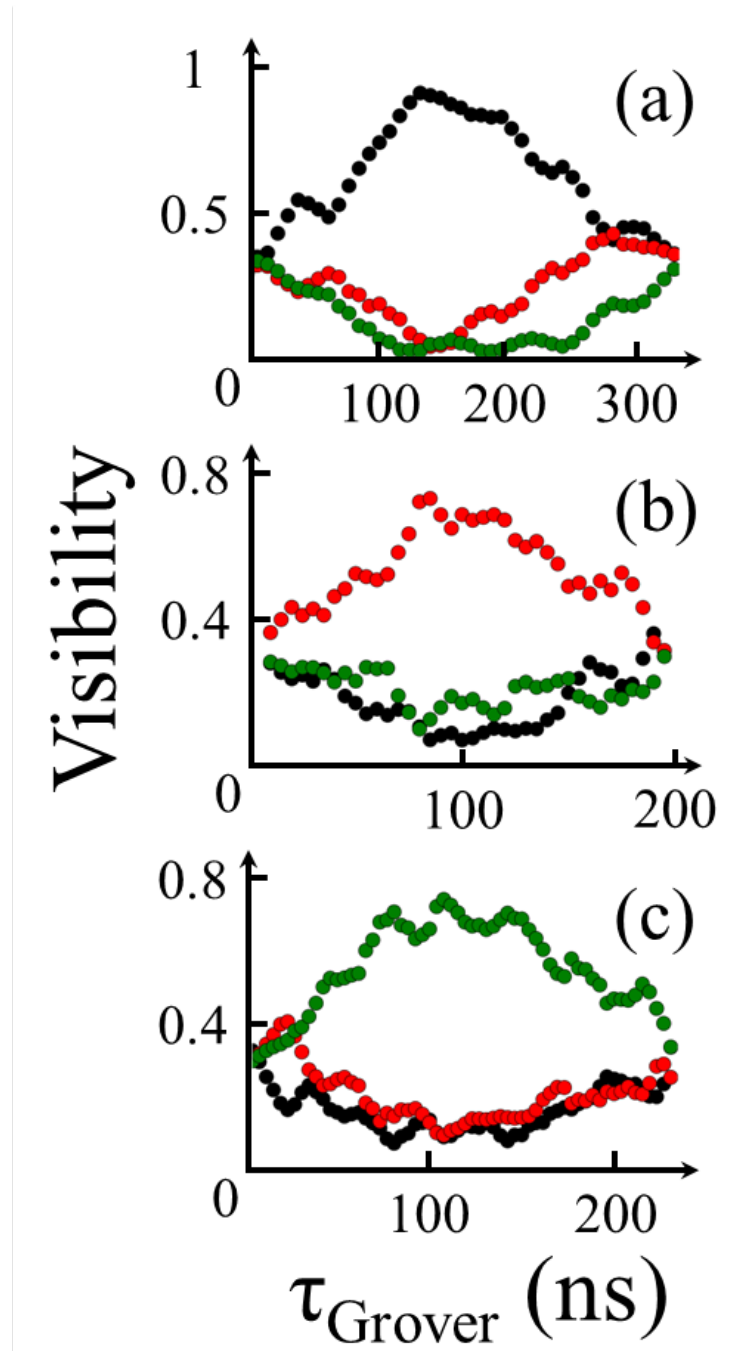


Fig. 7.8 (a) Coherent oscillations between the superposed state and the researched state of the nuclear spin. These oscillations are presented in figure (a), (b) and (c) respectively for a researched state  $|3/2\rangle$ ,  $|1/2\rangle$  and  $|-1/2\rangle$ . For a  $\tau_{\text{Grover}}$  respectively equals to 150ns, 100ns and 110ns, the probability of being in the desired state is amplified.



# Chapter 8

## Conclusion and outlook

During this thesis I measured quantum properties of a single molecular magnet transistor. Starting from an experiment, developed by Stefan Thiele, with which we can coherently manipulate one nuclear spin transition I progressed step by step until the implementation of a quantum algorithm. I first focused on the measurement of the nuclear spin states energies. Knowing this energies I could performed coherent manipulations and coherence time measurements on the three transitions *via* Rabi oscillation, Ramsey fringes and Hahn-echo protocols. These first results revealed the great potential of single molecular magnet spin transistor: we are able to manipulate each transition with a fidelity higher than 95%, Rabi frequency as high as 8MHz and coherence time of the order of 0.3ms, meaning that we have 3 qubits that could perform more than two thousand operations each. The next step was to manipulate different transitions within the same sequence. As a preliminary test, I measured single and double coherent pump probe. I finally implemented the quantum Hadamard gate and, when I understood the importance of the phase of a quantum state, the Grover algorithm. More than this implementation which is a proof of feasibility, this demonstrates that we fully and coherently control this single nuclear spin as a whole.

In parallel with these measurements, I developed a new generation of nanofabricated sample and a new sample holder. The idea was to acquire a better control of the difference microwave sequences we want to generate to the single molecular magnet spin transistor. Indeed, we could now apply AC electrical fields in two directions and AC magnetic field in one. I look forward to measure new molecules to validate this new generation.

I also collaborated with theoreticians to have a deeper understanding of the different mechanisms that occur in the experiment. First with Karim Ferhat, from the Néel Institute, to build up a theoretical model that describes, through an exchange coupling, the direct measure-

ment of a single electronic spin using a low temperature conductance measurement. Then with Filippo Troiani, from Nanosciences Institute of Modena, to characterize the electronic spin decoherence processes that induce an exotic Quantum Tunnelling of Magnetization probability. Finally with Rafik Ballou, from Néel Institute, to gather a deep understanding of the nuclear spin states manipulation with the hyperfine Stark effect.

A great favour of my thesis was to have plenty of dilution refrigerators (up to 3 at the same time !). I used them for my research, testing new sample geometries and new molecules (TbDyPc<sub>3</sub> and mononuclear trigonal bipyramidal Co(II)) but also to do fruitful collaborations. Indeed, with Andrea Candini and Stefano Lumeti, both from Nanoscience Institute of Modena, we performed low temperature transports measurement on graphene based molecular magnet transistor that exhibited magnetic signature.

As we have seen in this thesis, the two main points we need to improve to be competitive with existing quantum information processing (QIP) systems are the read-out measurement time and the system scalability. The future of molecular magnet for QIP may be conditioned on our ability to improve these two points. I classify in three time scales the perspectives for the molecular magnet QIP:

- Short term ( $\approx 1$  year): continue to "play" with the sample investigated in this thesis. During the thesis, I often thought that I could spend a whole life on this sample, here is a short list of experiments we could try in the next months.
  - ESR investigation: understand the dynamic of the electronic spin in interaction with a microwave pulse. We already demonstrated that this dynamic is not coherent but we still have to identify the mechanism that allows this electronic spin manipulation.
  - Kane: Switching on and off the resonance of a continuous microwave pulse with a nuclear spin transition through the DC stark effect [38].
  - Tomography: Control the phase of the microwave pulse in order to describe more complex nuclear spin state trajectories on the Bloch sphere.
  - Quantum chaos: In classical physic, a kicked top have a chaotic dynamic. One idea to study the quantum chaos is to study the dynamic of a spin undergoing microwave kick [121].

However, all these experiments would take too much time, we should first fabricate a new sample for which the measuring time would be much faster using the idea explained in the following.

- 
- Middle term ( $\approx 3$  years): Building up new experiments in which we use the new sample described in section 4.1.3 with new molecules. Two kind of molecular magnets would be interesting:
    - One with a smaller electronic spin to do coherent electronic spin manipulation. This manipulation will be nuclear spin dependent resulting in a microwave pulse sequence to read-out the nuclear spin, as performed with NV centres in diamond and impurity in Si experiments. This new read-out scheme would reduce by three orders of magnitude the nuclear spin measurement time, going from second to millisecond domain.
    - Another molecular system with more magnetic centres to study spins entanglement and exponentially increase our quantum database. The best candidate is the  $\text{Tb}_2\text{Pc}_3$ .
  - Long term ( $\approx 5$  years): if we want to take advantage from massive parallelism of the chemical synthesis, we have two choices:
    - control the molecular magnet deposition step, in order to put a single molecular magnet on each gap of a chip having many transistors. This can be done with a dilution refrigerator Scanning Tunnelling Microscope including a 4K preparation chamber. First, a single layer of molecular magnet would be deposited on the surface, using an electro-spray and then transfer the sample to the STM chamber to manipulate them. When the position of the molecule is optimal we could go down to 40mK to perform transport measurements. Another main advantage of this technique is that we can "see" the sample which is of great interest to have a deeper understanding of our nuclear-spin read-out scheme.
    - Second idea is to change our detection scheme to go to a low temperature optical measurement as the NV centre community. We can hybridize to the molecular magnet a function which is a photon emitter. The frequency of these photons would be "environment" dependent. So, we can think of two typical environmental lengths. A large one, of the order of the sample size (a field gradient for example), which would lift the degeneracy in between all the molecular magnets of the sample. A short one (induced by the magnetic moment of the molecule) which would lift the degeneracy in between the different magnetic states of a given molecular magnet.

The results presented in this thesis demonstrate the potential of molecular based QIP system. We demonstrated the first experimental implementation of quantum gate and algorithm using a multi-level system. The massive parallelism of their synthesis holds a lot of promises for a scalable systems which could call, maybe one day, a molecular quantum computer.



# References

- [1] R. P. Feynman, J. Hey, and R. W. Allen, *Feynman lectures on computation*. Addison-Wesley Longman Publishing Co., Inc., 1998.
- [2] M. Planck, "Ueber das gesetz der energieverteilung im normalspectrum," *Annalen der physik*, vol. 309, no. 3, pp. 553–563, 1901.
- [3] P. Benioff, "Quantum mechanical models of turing machines that dissipate no energy," *Physical Review Letters*, vol. 48, no. 23, p. 1581, 1982.
- [4] D. Z. Albert, "On quantum-mechanical automata," *Physics Letters A*, vol. 98, no. 5, pp. 249–252, 1983.
- [5] D. Deutsch, "Quantum theory, the church-turing principle and the universal quantum computer," in *Proceedings of the Royal Society of London A: Mathematical, Physical and Engineering Sciences*, vol. 400, pp. 97–117, The Royal Society, 1985.
- [6] A. Church, "An unsolvable problem of elementary number theory," *American journal of mathematics*, vol. 58, no. 2, pp. 345–363, 1936.
- [7] P. Kaye, R. Laflamme, and M. Mosca, *An introduction to quantum computing*. Oxford University Press, 2007.
- [8] R. P. Feynman, "Simulating physics with computers," *International journal of theoretical physics*, vol. 21, no. 6, pp. 467–488, 1982.
- [9] M. H. Devoret and R. J. Schoelkopf, "Superconducting circuits for quantum information: an outlook," *Science*, vol. 339, no. 6124, pp. 1169–1174, 2013.
- [10] E. Knill and R. Laflamme, "Theory of quantum error-correcting codes," *Physical Review A*, vol. 55, no. 2, p. 900, 1997.
- [11] D. P. DiVincenzo *et al.*, "The physical implementation of quantum computation," *arXiv preprint quant-ph/0002077*, 2000.
- [12] C. Monroe, D. Meekhof, B. King, and D. J. Wineland, "A "schrodinger cat" superposition state of an atom," *Science*, vol. 272, no. 5265, p. 1131, 1996.
- [13] M. Brune, E. Hagley, J. Dreyer, X. Maitre, A. Maali, C. Wunderlich, J. Raimond, and S. Haroche, "Observing the progressive decoherence of the "meter" in a quantum measurement," *Physical Review Letters*, vol. 77, no. 24, p. 4887, 1996.

- [14] D. J. Wineland, R. E. Drullinger, and F. L. Walls, "Radiation-pressure cooling of bound resonant absorbers," *Physical Review Letters*, vol. 40, no. 25, p. 1639, 1978.
- [15] M. Brune, F. Schmidt-Kaler, A. Maali, J. Dreyer, E. Hagley, J. Raimond, and S. Haroche, "Quantum rabi oscillation: A direct test of field quantization in a cavity," *Physical Review Letters*, vol. 76, no. 11, p. 1800, 1996.
- [16] Y. Nakamura, Y. A. Pashkin, and J. Tsai, "Coherent control of macroscopic quantum states in a single-cooper-pair box," *Nature*, vol. 398, no. 6730, pp. 786–788, 1999.
- [17] C. Rigetti, J. M. Gambetta, S. Poletto, B. Plourde, J. M. Chow, A. Córcoles, J. A. Smolin, S. T. Merkel, J. Rozen, G. A. Keefe, *et al.*, "Superconducting qubit in a waveguide cavity with a coherence time approaching 0.1 ms," *Physical Review B*, vol. 86, no. 10, p. 100506, 2012.
- [18] A. J. Leggett, "Macroscopic quantum systems and the quantum theory of measurement," *Progress of Theoretical Physics Supplement*, vol. 69, pp. 80–100, 1980.
- [19] M. H. Devoret, J. M. Martinis, and J. Clarke, "Measurements of macroscopic quantum tunneling out of the zero-voltage state of a current-biased josephson junction," *Physical review letters*, vol. 55, no. 18, p. 1908, 1985.
- [20] L. DiCarlo, M. Reed, L. Sun, B. Johnson, J. Chow, J. Gambetta, L. Frunzio, S. Girvin, M. Devoret, and R. Schoelkopf, "Preparation and measurement of three-qubit entanglement in a superconducting circuit," *Nature*, vol. 467, no. 7315, pp. 574–578, 2010.
- [21] M. Neeley, R. C. Bialczak, M. Lenander, E. Lucero, M. Mariani, A. O'Connell, D. Sank, H. Wang, M. Weides, J. Wenner, *et al.*, "Generation of three-qubit entangled states using superconducting phase qubits," *Nature*, vol. 467, no. 7315, pp. 570–573, 2010.
- [22] D. Kim, D. Ward, C. Simmons, J. K. Gamble, R. Blume-Kohout, E. Nielsen, D. Savage, M. Lagally, M. Friesen, S. Coppersmith, *et al.*, "Microwave-driven coherent operation of a semiconductor quantum dot charge qubit," *Nature nanotechnology*, vol. 10, no. 3, pp. 243–247, 2015.
- [23] M. D. Shulman, O. E. Dial, S. P. Harvey, H. Bluhm, V. Umansky, and A. Yacoby, "Demonstration of entanglement of electrostatically coupled singlet-triplet qubits," *Science*, vol. 336, no. 6078, pp. 202–205, 2012.
- [24] D. Loss and D. P. DiVincenzo, "Quantum computation with quantum dots," *Physical Review A*, vol. 57, no. 1, p. 120, 1998.
- [25] J. Elzerman, R. Hanson, L. W. Van Beveren, B. Witkamp, L. Vandersypen, and L. P. Kouwenhoven, "Single-shot read-out of an individual electron spin in a quantum dot," *nature*, vol. 430, no. 6998, pp. 431–435, 2004.
- [26] F. Koppens, C. Buizert, K.-J. Tielrooij, I. Vink, K. Nowack, T. Meunier, L. Kouwenhoven, and L. Vandersypen, "Driven coherent oscillations of a single electron spin in a quantum dot," *Nature*, vol. 442, no. 7104, pp. 766–771, 2006.

- [27] M. Pioro-Ladriere, T. Obata, Y. Tokura, Y.-S. Shin, T. Kubo, K. Yoshida, T. Taniyama, and S. Tarucha, “Electrically driven single-electron spin resonance in a slanting zeeman field,” *Nature Physics*, vol. 4, no. 10, pp. 776–779, 2008.
- [28] F. H. L. Koppens, K. C. Nowack, and L. M. K. Vandersypen, “Spin echo of a single electron spin in a quantum dot,” *Phys. Rev. Lett.*, vol. 100, p. 236802, Jun 2008.
- [29] H. Bluhm, S. Foletti, I. Neder, M. Rudner, D. Mahalu, V. Umansky, and A. Yacoby, “Dephasing time of gaas electron-spin qubits coupled to a nuclear bath exceeding 200 [thinsp][mu] s,” *Nature Physics*, vol. 7, no. 2, pp. 109–113, 2011.
- [30] F. Jelezko, T. Gaebel, I. Popa, M. Domhan, A. Gruber, and J. Wrachtrup, “Observation of coherent oscillation of a single nuclear spin and realization of a two-qubit conditional quantum gate,” *Physical Review Letters*, vol. 93, no. 13, p. 130501, 2004.
- [31] S. Thiele, F. Balestro, R. Ballou, S. Klyatskaya, M. Ruben, and W. Wernsdorfer, “Electrically driven nuclear spin resonance in single-molecule magnets,” *Science*, vol. 344, no. 6188, pp. 1135–1138, 2014.
- [32] J. J. Pla, K. Y. Tan, J. P. Dehollain, W. H. Lim, J. J. Morton, F. A. Zwanenburg, D. N. Jamieson, A. S. Dzurak, and A. Morello, “High-fidelity readout and control of a nuclear spin qubit in silicon,” *Nature*, vol. 496, no. 7445, pp. 334–338, 2013.
- [33] A. Gruber, A. Dräbenstedt, C. Tietz, L. Fleury, J. Wrachtrup, and C. Von Borczyskowski, “Scanning confocal optical microscopy and magnetic resonance on single defect centers,” *Science*, vol. 276, no. 5321, pp. 2012–2014, 1997.
- [34] G. Fuchs, V. Dobrovitski, D. Toyli, F. Heremans, and D. Awschalom, “Gigahertz dynamics of a strongly driven single quantum spin,” *Science*, vol. 326, no. 5959, pp. 1520–1522, 2009.
- [35] M. Veldhorst, J. Hwang, C. Yang, A. Leenstra, B. De Ronde, J. Dehollain, J. Muhonen, F. Hudson, K. M. Itoh, A. Morello, *et al.*, “An addressable quantum dot qubit with fault-tolerant control-fidelity,” *Nature nanotechnology*, vol. 9, no. 12, pp. 981–985, 2014.
- [36] R. Maurand, X. Jehl, D. K. Patil, A. Corna, H. Bohuslavskyi, R. Laviéville, L. Hutin, S. Barraud, M. Vinet, M. Sanquer, *et al.*, “A cmos silicon spin qubit,” *arXiv preprint arXiv:1605.07599*, 2016.
- [37] G. Balasubramanian, P. Neumann, D. Twitchen, M. Markham, R. Kolesov, N. Mizuochi, J. Isoya, J. Achard, J. Beck, J. Tessler, *et al.*, “Ultralong spin coherence time in isotopically engineered diamond,” *Nature materials*, vol. 8, no. 5, pp. 383–387, 2009.
- [38] B. E. Kane, “A silicon-based nuclear spin quantum computer,” *nature*, vol. 393, no. 6681, pp. 133–137, 1998.
- [39] M. G. Dutt, L. Childress, L. Jiang, E. Togan, J. Maze, F. Jelezko, A. Zibrov, P. Hemmer, and M. Lukin, “Quantum register based on individual electronic and nuclear spin qubits in diamond,” *Science*, vol. 316, no. 5829, pp. 1312–1316, 2007.

- [40] P. Neumann, J. Beck, M. Steiner, F. Rempp, H. Fedder, P. R. Hemmer, J. Wrachtrup, and F. Jelezko, "Single-shot readout of a single nuclear spin," *Science*, vol. 329, no. 5991, pp. 542–544, 2010.
- [41] W. Pfaff, T. H. Taminiau, L. Robledo, H. Bernien, M. Markham, D. J. Twitchen, and R. Hanson, "Demonstration of entanglement-by-measurement of solid-state qubits," *Nature Physics*, vol. 9, no. 1, pp. 29–33, 2013.
- [42] J. J. Pla, K. Y. Tan, J. P. Dehollain, W. H. Lim, J. J. Morton, D. N. Jamieson, A. S. Dzurak, and A. Morello, "A single-atom electron spin qubit in silicon," *Nature*, vol. 489, no. 7417, pp. 541–545, 2012.
- [43] M. Veldhorst, C. Yang, J. Hwang, W. Huang, J. Dehollain, J. Muhonen, S. Simmons, A. Laucht, F. Hudson, K. M. Itoh, *et al.*, "A two-qubit logic gate in silicon," *Nature*, 2015.
- [44] R. Vincent, S. Klyatskaya, M. Ruben, W. Wernsdorfer, and F. Balestro, "Electronic read-out of a single nuclear spin using a molecular spin transistor," *Nature*, vol. 488, no. 7411, pp. 357–360, 2012.
- [45] M. Urdampilleta, S. Klyatskaya, M. Ruben, and W. Wernsdorfer, "Landau-zener tunneling of a single  $t_{3+}$  magnetic moment allowing the electronic read-out of a nuclear spin," *Physical Review B*, vol. 87, no. 19, p. 195412, 2013.
- [46] D. J. Welsh, *Codes and cryptography*. Oxford University Press, 1988.
- [47] T. Kleinjung, K. Aoki, J. Franke, A. K. Lenstra, E. Thomé, J. W. Bos, P. Gaudry, A. Kruppa, P. L. Montgomery, D. A. Osvik, *et al.*, "Factorization of a 768-bit rsa modulus," in *Annual Cryptology Conference*, pp. 333–350, Springer, 2010.
- [48] P. W. Shor, "Algorithms for quantum computation: Discrete logarithms and factoring," in *Foundations of Computer Science, 1994 Proceedings., 35th Annual Symposium on*, pp. 124–134, IEEE, 1994.
- [49] P. W. Shor, "Polynomial-time algorithms for prime factorization and discrete logarithms on a quantum computer," *SIAM review*, vol. 41, no. 2, pp. 303–332, 1999.
- [50] C. P. Williams, *Explorations in quantum computing*. Springer Science & Business Media, 2010.
- [51] L. M. Kohnfelder, *Towards a practical public-key cryptosystem*. PhD thesis, Massachusetts Institute of Technology, 1978.
- [52] L. M. Vandersypen, M. Steffen, G. Breyta, C. S. Yannoni, M. H. Sherwood, and I. L. Chuang, "Experimental realization of shor's quantum factoring algorithm using nuclear magnetic resonance," *Nature*, vol. 414, no. 6866, pp. 883–887, 2001.
- [53] C.-Y. Lu, D. E. Browne, T. Yang, and J.-W. Pan, "Demonstration of a compiled version of shor's quantum factoring algorithm using photonic qubits," *Physical Review Letters*, vol. 99, no. 25, p. 250504, 2007.

- [54] B. Lanyon, T. Weinhold, N. Langford, M. Barbieri, D. James, A. Gilchrist, and A. White, “Experimental demonstration of a compiled version of shor’s algorithm with quantum entanglement,” *Physical Review Letters*, vol. 99, no. 25, p. 250505, 2007.
- [55] A. Politi, J. C. Matthews, and J. L. O’Brien, “Shor’s quantum factoring algorithm on a photonic chip,” *Science*, vol. 325, no. 5945, pp. 1221–1221, 2009.
- [56] E. Martín-López, A. Laing, T. Lawson, R. Alvarez, X.-Q. Zhou, and J. L. O’Brien, “Experimental realization of shor’s quantum factoring algorithm using qubit recycling,” *Nature Photonics*, vol. 6, no. 11, pp. 773–776, 2012.
- [57] A. Montanaro, “Quantum algorithms: an overview,” *arXiv preprint arXiv:1511.04206*, 2015.
- [58] L. K. Grover, “A fast quantum mechanical algorithm for database search,” in *Proceedings of the twenty-eighth annual ACM symposium on Theory of computing*, pp. 212–219, ACM, 1996.
- [59] L. K. Grover, “Quantum mechanics helps in searching for a needle in a haystack,” *Physical review letters*, vol. 79, no. 2, p. 325, 1997.
- [60] E. Farhi and S. Gutmann, “Analog analogue of a digital quantum computation,” *Physical Review A*, vol. 57, no. 4, p. 2403, 1998.
- [61] M. N. Leuenberger and D. Loss, “Grover algorithm for large nuclear spins in semiconductors,” *Physical Review B*, vol. 68, no. 16, p. 165317, 2003.
- [62] J. A. Jones, M. Mosca, and R. H. Hansen, “Implementation of a quantum search algorithm on a quantum computer,” *Nature*, vol. 393, no. 6683, pp. 344–346, 1998.
- [63] I. L. Chuang, N. Gershenfeld, and M. Kubinec, “Experimental implementation of fast quantum searching,” *Physical review letters*, vol. 80, no. 15, p. 3408, 1998.
- [64] L. M. Vandersypen, M. Steffen, M. H. Sherwood, C. S. Yannoni, G. Breyta, and I. L. Chuang, “Implementation of a three-quantum-bit search algorithm,” *arXiv preprint quant-ph/9910075*, 1999.
- [65] J. King, S. Yarkoni, M. M. Nevisi, J. P. Hilton, and C. C. McGeoch, “Benchmarking a quantum annealing processor with the time-to-target metric,” *arXiv preprint arXiv:1508.05087*, 2015.
- [66] X.-D. Cai, C. Weedbrook, Z.-E. Su, M.-C. Chen, M. Gu, M.-J. Zhu, L. Li, N.-L. Liu, C.-Y. Lu, and J.-W. Pan, “Experimental quantum computing to solve systems of linear equations,” *Physical review letters*, vol. 110, no. 23, p. 230501, 2013.
- [67] S. Barz, I. Kassal, M. Ringbauer, Y. O. Lipp, B. Dakić, A. Aspuru-Guzik, and P. Walther, “A two-qubit photonic quantum processor and its application to solving systems of linear equations,” *Scientific reports*, vol. 4, 2014.
- [68] J. Pan, Y. Cao, X. Yao, Z. Li, C. Ju, H. Chen, X. Peng, S. Kais, and J. Du, “Experimental realization of quantum algorithm for solving linear systems of equations,” *Physical Review A*, vol. 89, no. 2, p. 022313, 2014.

- [69] X.-Q. Zhou, P. Kalasuwan, T. C. Ralph, and J. L. O'Brien, "Calculating unknown eigenvalues with a quantum algorithm," *Nature Photonics*, vol. 7, no. 3, pp. 223–228, 2013.
- [70] W. Van Dam and G. Seroussi, "Efficient quantum algorithms for estimating gauss sums," *arXiv preprint quant-ph/0207131*, 2002.
- [71] T. Ralph, "Quantum computation: Boson sampling on a chip," *Nature Photonics*, vol. 7, no. 7, pp. 514–515, 2013.
- [72] S. P. Jordan, "Fast quantum algorithm for numerical gradient estimation," *Physical review letters*, vol. 95, no. 5, p. 050501, 2005.
- [73] K. Katoh, T. Komeda, and M. Yamashita, "The frontier of molecular spintronics based on multiple-decker phthalocyaninato tbi single-molecule magnets," *The Chemical Record*, vol. 16, no. 2, pp. 987–1016, 2016.
- [74] S. e. a. Stepanow, "Spin and orbital magnetic moment anisotropies of monodispersed bis(phthalocyaninato)terbium on a copper surface," *J. Am. Chem. Soc.*, vol. 132, no. 34, pp. 11900–11901, 2010.
- [75] S. Thiele, *Read-Out and Coherent Manipulation of an Isolated Nuclear Spin: Using a Single-Molecule Magnet Spin-Transistor*. Springer, 2015.
- [76] G. Ofelt, "Structure of the f6 configuration with application to rare-earth ions," *The Journal of Chemical Physics*, vol. 38, no. 9, pp. 2171–2180, 1963.
- [77] K. Thomas, S. Singh, and G. Dieke, "Energy levels of tb3+ in lacl3 and other chlorides," *The Journal of Chemical Physics*, vol. 38, no. 9, pp. 2180–2190, 1963.
- [78] A. Abragam and B. Bleaney, *Electron paramagnetic resonance of transition ions*. OUP Oxford, 2012.
- [79] N. Ishikawa, M. Sugita, T. Okubo, N. Tanaka, T. Iino, and Y. Kaizu, "Determination of ligand-field parameters and f-electronic structures of double-decker bis (phthalocyaninato) lanthanide complexes," *Inorganic chemistry*, vol. 42, no. 7, pp. 2440–2446, 2003.
- [80] K. Stevens, "Matrix elements and operator equivalents connected with the magnetic properties of rare earth ions," *Proceedings of the Physical Society. Section A*, vol. 65, no. 3, p. 209, 1952.
- [81] N. Ishikawa, M. Sugita, and W. Wernsdorfer, "Quantum tunneling of magnetization in lanthanide single-molecule magnets: Bis (phthalocyaninato) terbium and bis (phthalocyaninato) dysprosium anions," *Angewandte Chemie International Edition*, vol. 44, no. 19, pp. 2931–2935, 2005.
- [82] J. Baker, J. Chadwick, G. Garton, and J. Hurrell, "Epr and endor of tb4+ in thoria," in *Proceedings of the Royal Society of London A: Mathematical, Physical and Engineering Sciences*, vol. 286, pp. 352–365, The Royal Society, 1965.

- [83] S. Mandal, T. Bautze, R. Blinder, T. Meunier, L. Saminadayar, and C. Bäuerle, “Efficient radio frequency filters for space constrained cryogenic setups,” *Review of Scientific Instruments*, vol. 82, no. 2, p. 024704, 2011.
- [84] B. Stipe, M. Rezaei, and W. Ho, “Single-molecule vibrational spectroscopy and microscopy,” *Science*, vol. 280, no. 5370, pp. 1732–1735, 1998.
- [85] S. Müllegger, S. Tebi, A. K. Das, W. Schöffberger, F. Faschinger, and R. Koch, “Radio frequency scanning tunneling spectroscopy for single-molecule spin resonance,” *Physical review letters*, vol. 113, no. 13, p. 133001, 2014.
- [86] C. Kergueris, J.-P. Bourgoin, S. Palacin, D. Estève, C. Urbina, M. Magoga, and C. Joachim, “Electron transport through a metal-molecule-metal junction,” *Physical Review B*, vol. 59, no. 19, p. 12505, 1999.
- [87] N. Roch, *Transistors à molécule unique: des effets Kondo exotiques à la spintronique moléculaire*. PhD thesis, Université Joseph-Fourier-Grenoble I, 2009.
- [88] R. Vincent, *Spintronique moléculaire: étude de la dynamique d’un spin nucléaire unique*. PhD thesis, Grenoble, 2012.
- [89] H. Park, A. K. Lim, A. P. Alivisatos, J. Park, and P. L. McEuen, “Fabrication of metallic electrodes with nanometer separation by electromigration,” *Applied Physics Letters*, vol. 75, no. 2, pp. 301–303, 1999.
- [90] J. P. Dehollain, J. J. Pla, E. Siew, K. Y. Tan, A. S. Dzurak, and A. Morello, “Nanoscale broadband transmission lines for spin qubit control,” *Nanotechnology*, vol. 24, no. 1, p. 015202, 2013.
- [91] P. C. Magnusson, A. Weisshaar, V. K. Tripathi, and G. C. Alexander, *Transmission lines and wave propagation*. CRC Press, 2000.
- [92] J. R. Black, “Electromigration failure modes in aluminum metallization for semiconductor devices,” *Proceedings of the IEEE*, vol. 57, no. 9, pp. 1587–1594, 1969.
- [93] K. Tu, “Electromigration in stressed thin films,” *Physical Review B*, vol. 45, no. 3, p. 1409, 1992.
- [94] H. S. van der Zant, Y.-V. Kervennic, M. Poot, K. O’Neill, Z. de Groot, J. M. Thijssen, H. B. Heersche, N. Stuhr-Hansen, T. Bjørnholm, D. Vanmaekelbergh, *et al.*, “Molecular three-terminal devices: fabrication and measurements,” *Faraday discussions*, vol. 131, pp. 347–356, 2006.
- [95] M. Trouwborst, S. Van Der Molen, and B. Van Wees, “The role of joule heating in the formation of nanogaps by electromigration,” *arXiv preprint cond-mat/0510385*, 2005.
- [96] T. Taychatanapat, K. I. Bolotin, F. Kuemmeth, and D. C. Ralph, “Imaging electromigration during the formation of break junctions,” *Nano letters*, vol. 7, no. 3, pp. 652–656, 2007.
- [97] K. O’Neill, E. Osorio, and H. Van der Zant, “Self-breaking in planar few-atom Au constrictions for nanometer-spaced electrodes,” *Applied Physics Letters*, vol. 90, no. 13, p. 133109, 2007.

- [98] A. Korotkov, D. Averin, and K. Likharev, "Single-electron charging of the quantum wells and dots," *Physica B: Condensed Matter*, vol. 165, pp. 927–928, 1990.
- [99] L. P. Kouwenhoven, C. M. Marcus, P. L. McEuen, S. Tarucha, R. M. Westervelt, and N. S. Wingreen, "Electron transport in quantum dots," in *Mesoscopic electron transport*, pp. 105–214, Springer, 1997.
- [100] R. Hanson, L. Kouwenhoven, J. Petta, S. Tarucha, and L. Vandersypen, "Spins in few-electron quantum dots," *Reviews of Modern Physics*, vol. 79, no. 4, p. 1217, 2007.
- [101] S. Marocchi, A. Candini, D. Klar, W. Van den Heuvel, H. Huang, F. Troiani, V. Corradini, R. Biagi, V. De Renzi, S. Klyatskaya, *et al.*, "Relay-like exchange mechanism through a spin radical between tbpc2 molecules and graphene/ni (111) substrates," *ACS nano*, 2016.
- [102] P. Zhu, F. Lu, N. Pan, D. P. Arnold, S. Zhang, and J. Jiang, "Comparative electrochemical study of unsubstituted and substituted bis (phthalocyaninato) rare earth (iii) complexes," *European Journal of Inorganic Chemistry*, vol. 2004, no. 3, pp. 510–517, 2004.
- [103] J. Park, A. N. Pasupathy, J. I. Goldsmith, C. Chang, Y. Yaish, J. R. Petta, M. Rinkoski, J. P. Sethna, H. D. Abruña, P. L. McEuen, *et al.*, "Coulomb blockade and the kondo effect in single-atom transistors," *Nature*, vol. 417, no. 6890, pp. 722–725, 2002.
- [104] W. Liang, M. P. Shores, M. Bockrath, J. R. Long, and H. Park, "Kondo resonance in a single-molecule transistor," *Nature*, vol. 417, no. 6890, pp. 725–729, 2002.
- [105] N. Roch, S. Florens, T. A. Costi, W. Wernsdorfer, and F. Balestro, "Observation of the underscreened kondo effect in a molecular transistor," *Physical review letters*, vol. 103, no. 19, p. 197202, 2009.
- [106] A. Messiah, "Mecanique quantique," 1995.
- [107] C. Zener, "Non-adiabatic crossing of energy levels," in *Proceedings of the Royal Society of London A: Mathematical, Physical and Engineering Sciences*, vol. 137, pp. 696–702, The Royal Society, 1932.
- [108] L. D. Landau, "Zur theorie der energieubertragung. ii," *Physics of the Soviet Union*, vol. 2, no. 2, pp. 46–51, 1932.
- [109] H.-P. Breuer, "Non-markovian generalization of the lindblad theory of open quantum systems," *Physical Review A*, vol. 75, no. 2, p. 022103, 2007.
- [110] C. Schwartz, "Theory of hyperfine structure," *Physical Review*, vol. 97, no. 2, p. 380, 1955.
- [111] S. P. Karna, "Theory of electric-field effects on electron-spin-resonance hyperfine couplings," *Physical review letters*, vol. 79, no. 3, p. 379, 1997.
- [112] A. Laucht, J. T. Muhonen, F. A. Mohiyaddin, R. Kalra, J. P. Dehollain, S. Freer, F. E. Hudson, M. Veldhorst, R. Rahman, G. Klimeck, *et al.*, "Electrically controlling single-spin qubits in a continuous microwave field," *Science advances*, vol. 1, no. 3, p. e1500022, 2015.

- [113] B. Judd, "Operator techniques in atomic spectroscopy mcgraw-hill book company," *Operator Techniques in Atomic Spectroscopy McGraw-Hill Book Company*, 1963.
- [114] R. M. Macfarlane, "Optical stark spectroscopy of solids," *Journal of luminescence*, vol. 125, no. 1, pp. 156–174, 2007.
- [115] F. Bloch, "Nuclear induction," *Physical review*, vol. 70, no. 7-8, p. 460, 1946.
- [116] R. K. Wangness and F. Bloch, "The dynamical theory of nuclear induction," *Physical Review*, vol. 89, no. 4, p. 728, 1953.
- [117] A. G. Redfield, "On the theory of relaxation processes," *IBM Journal of Research and Development*, vol. 1, no. 1, pp. 19–31, 1957.
- [118] G. Ithier, E. Collin, P. Joyez, P. Meeson, D. Vion, D. Esteve, F. Chiarello, A. Shnirman, Y. Makhlin, J. Schrieffer, *et al.*, "Decoherence in a superconducting quantum bit circuit," *Physical Review B*, vol. 72, no. 13, p. 134519, 2005.
- [119] E. L. Hahn, "Spin echoes," *Physical review*, vol. 80, no. 4, p. 580, 1950.
- [120] L. Childress, M. G. Dutt, J. Taylor, A. Zibrov, F. Jelezko, J. Wrachtrup, P. Hemmer, and M. Lukin, "Coherent dynamics of coupled electron and nuclear spin qubits in diamond," *Science*, vol. 314, no. 5797, pp. 281–285, 2006.
- [121] S. Chaudhury, A. Smith, B. Anderson, S. Ghose, and P. S. Jessen, "Quantum signatures of chaos in a kicked top," *Nature*, vol. 461, no. 7265, pp. 768–771, 2009.



# Appendix A

## Stevens operators

Diagonal

$$O_2^0 = 3J_z^2 - J(J+1)$$

$$O_4^0 = 35J_z^4 - 30J(J+1)J_z^2 + 25J_z^2 - 6J(J+1) + 3J^2(J+1)^2$$

$$O_6^0 = 231J_z^6 - 315J(J+1)J_z^4 + 735J_z^4 + 105J^2(J+1)^2J_z^2 - 525J(J+1)J_z^2 + \\ + 294J_z^2 - 5J^3(J+1)^3 + 40J^2(J+1)^2 - 60J(J+1)$$

Off-diagonal

$$O_4^4 = \frac{1}{2}(J_+^4 + J_-^4)$$

$$O_6^4 = \frac{1}{4} [(11J_z^2 - J(J+1) - 38)(J_+^4 + J_-^4) + (J_+^4 + J_-^4)(11J_z^2 - J(J+1) - 38)]$$

